AN EXPERIMENTAL STUDY OF FLOW CONTROL USING BLOWING FOR A LOW-PRESSURE TURBINE AIRFOIL

by

Brian McAuliffe

A thesis submitted to the Faculty of Graduate Studies and Research
in partial fulfillment of the requirements for the degree of

Master's of Applied Science

in Aerospace Engineering

Ottawa-Carleton Institute for Mechanical & Aerospace Engineering

Department of Mechanical & Aerospace Engineering
Carleton University
Ottawa, Ontario, Canada

December 2003

Your file Votre référence
ISBN: 978-0-494-23321-4
Our file Notre référence
ISBN: 978-0-494-23321-4

Dedicated to the memory of

Terry McAuliffe

His strength is an inspiration to us all.

Abstract

Recent developments in low-pressure turbine design for aero-engines have resulted in highly-loaded blades with strong adverse pressure gradients over the aft suction surface. At low Reynolds numbers, typical of high-altitude cruise conditions, much of the suction surface boundary layer remains laminar and is prone to separation. In some cases, the separated shear layer does not reattach to the surface resulting in stall of the airfoils. This thesis describes two aerodynamic investigations of a low-pressure turbine airfoil. The first investigation examines the influence of freestream turbulent length scale on the performance and separated-flow transition process of a low-pressure turbine airfoil. The second examines a method of active flow control using localized blowing for suppressing stall in high-lift low-pressure turbines.

Measurements were made in a low-speed linear cascade wind tunnel. The low-pressure turbine cascade was examined with steady inflow conditions at levels of Reynolds number and freestream turbulence intensity typical of those encountered in an actual engine. The influence of turbulent length was examined using passive turbulence generating grids located upstream of the cascade. For the flow control investigation, the three middle blades of the cascade included a slot through which air could be injected for flow control.

Two levels of freestream turbulent length scale, with similar levels of freestream turbulence intensity, were examined over a range of Reynolds numbers. There was no significant influence of length scale on the separated-flow transition process over the airfoil. Flow control was examined at various levels of Reynolds number and freestream turbulence intensity. The method of flow control examined was effective at preventing stall and reducing the profile losses of the low-pressure turbine airfoil.

Acknowledgements

First and foremost, I would like to thank my research advisor Dr. Steen Sjolander, for his gracious support and encouragement throughout course of the present work.

Most of all I would like to thank my family. My wife, Rakhi, for her undying love, encouragement, and tolerance over the last few years. Her support has been my foundation throughout the course of this research. I would also like to thank my mother, Marguerite, my father, Sean, and my sister, Lisa, who have provided love and support throughout my years of study.

I would like to acknowledge the financial support of Pratt & Whitney, East Hartford, Connecticut, as well as the Natural Sciences and Engineering Research Council of Canada (NSERC) for a post-graduate scholarship. Without their support, this research would not have been possible.

This work could not have been completed without the technical support of many people. I would like to thank Terry Goodwin, Alex Proctor, and Jim Sliwka for their technical assistance in the laboratory and in the machine shop of the Department of Mechanical and Aerospace Engineering. I would also like to acknowledge Ashish Nedungadi and Greg Tillman of the United Technologies Research Center (UTRC), East Hartford, Connecticut, for designing the slot and plenum arrangement of the flow control airfoils.

Of course, I could not have tolerated the long hours and late nights in the laboratory without the presence of my colleagues and friends. I am indebted to Ali Mahallati for his generous friendship and help in the laboratory. Many of the insights into the current measurements came about through long discussions with him over coffee. Also, I would like to thank Xuefeng Zhang for his help during the initial stages of the work, and Martin Conlon for the many coffee breaks required to alleviate the stress during the preparation of this manuscript.

Table of Contents

List of Tables

List of Figures

List of Symbols

a	King's law coefficient
A	Area
AVR	Axial velocity ratio $\left(\dfrac{\int_0^s \dot{m}_e dy}{\int_0^s \dot{m}_i dy}\right)$
b	Slot width; King's law coefficient
B	Blowing ratio $\left(\dfrac{U_{j_{max}}}{U_e}\right)$
B_x	Blade axial chord
c	Transducer calibration coefficient
C	Blade true chord; Empirical coefficient for turbulence decay rate
C_{Pb}	Plenum pressure coefficient $\left(\dfrac{P_b - P_{c2}}{P_{c1} - P_{c2}}\right)$
C_{P0}	Total pressure loss coefficient $\left(\dfrac{P_{0_{ref}} - P_0}{P_{0_{ref}} - P_{S_{ref}}}\right)$
C_{PL}	Loading coefficient $\left(\dfrac{P_{0i} - P_L}{P_{0i} - P_{Si}}\right)$
C_{Pp}	Three-hole probe port pressure coefficient $\left(\dfrac{P_p - P_{S_{ref}}}{P_{0_{ref}} - P_{S_{ref}}}\right)$
C_{PS}	Static pressure coefficient $\left(\dfrac{P_S - P_{S_{ref}}}{P_{0_{ref}} - P_{S_{ref}}}\right)$
$\overline{C_{PS}}$	Reference static pressure coefficient $\left(\dfrac{\overline{P_S} - P_{c2}}{P_{c1} - P_{c1}}\right)$
C_V	Velocity ratio $\left(\dfrac{U}{U_{ref}}\right)$

C_Q	Dynamic pressure coefficient $\left(\frac{P_0 - P_S}{P_{0_{ref}} - P_{S_{ref}}}\right)$
$\overline{C_Q}$	Reference dynamic pressure coefficient $\left(\frac{\overline{P_0 - P_S}}{P_{c1} - P_{c1}}\right)$
$C_{\tau'}$	Normalized mean quasi-wall shear stress $\left(\frac{\tau'_{mean} - \tau'_{min}}{\tau'_{max} - \tau'_{min}}\right)$
d	Turbulence grid bar width or rod diameter
e	Specific energy
E	Voltage; Energy
E_0	Wind-off hot-film voltage
E_{offset}	Anemometer offset voltage
E_{out}	Anemometer output voltage
E_{TOB}	Anemometer top-of-the-bridge voltage
$f(\Delta x)$	Longitudinal correlation function
$\vec{F}$	Force vector
g	Gravitational constant
G	Anemometer gain
H	Blade span
H'	Shear layer shape factor $\left(\frac{\delta^{*\prime}}{\theta'}\right)$
i	Incidence angle $(\alpha_i - \beta_i)$
I	Empirical coefficient for integral length scale growth rate
K	Three-hole probe calibration coefficient
$\dot{m}$	Mass flow rate per unit span
M	Mass flow ratio $\left(\frac{\int_0^b d\dot{m}_j}{\int_0^S d\dot{m}_i}\right)$; Turbulence grid mesh length
n	King's law coefficient
OHR	Overheat ratio $\left(\frac{R_w}{R_r}\right)$

P_0	Total pressure
P_b	Flow control blade plenum pressure
P_{c1}	Wind tunnel contraction inlet pressure
P_{c2}	Wind tunnel contraction exit pressure
P_p	Three-hole probe port pressure ($p = 1, 2, 3$)
P_S	Static pressure
P_{SL}	Surface static pressure
ΔP	Transducer pressure difference
Q	Heat transfer
R_r	Hot-wire/hot-film resistance at reference temperature
R_w	Hot-wire/hot-film resistance at operating temperature
Re	Cascade Reynolds number $\left(\frac{U_i B_x}{\nu}\right)$
Re_d	Turbulence grid Reynolds number $\left(\frac{U_i d}{\nu}\right)$
Re_p	Three-hole probe Reynolds number $\left(\frac{U_i w}{\nu}\right)$
$Re_{\delta^{*\prime}}$	Displacement thickness Reynolds number $\left(\frac{U_e \delta^{*\prime}}{\nu}\right)$
$Re_{\theta'}$	Momentum thickness Reynolds number $\left(\frac{U_e \theta'}{\nu}\right)$
$R(\Delta t)$	Autocorrelation function
S	Blade pitch
SSL	Suction surface length
t	Time
t_0	Starting time
T	Total sampling time
T_0	Hot-wire calibration flow temperature
T_r	Heated hot-wire/hot-film sensor temperature
T_{test}	Hot-wire measurement flow temperature

T_w	Cold hot-wire/hot-film sensor temperature
tet	Blade trailing edge thickness
U	Mean velocity
u	Instantaneous velocity; Specific internal energy
u'	Root-mean-square (RMS) of fluctuating velocity $\sqrt{\overline{(u-U)^2}}$
V	Volume
w	Three-hole probe width
W	Work
x	Axial location; Streamwise distance
y	Pitchwise location; Distance from blade surface
Y_m	Mixed-out profile loss coefficient $\left(\frac{P_{0i}-P_{0m}}{P_{0m}-P_{Sm}}\right)$
z	Height
α	Flow angle
α_r	Hot-wire/hot-film sensor coefficient of thermal resistance
β	Blade metal angle
γ	Blade stagger angle
Γ	Intermittency
δ	Deviation angle $(\beta_e - \alpha_m)$; Shear layer thickness
$\delta^{*\prime}$	Shear layer displacement thickness $\left(\int_0^\delta (1-\left\lvert\frac{U}{U_e}\right\rvert)dy\right)$
θ'	Shear layer momentum thickness $\left(\int_0^\delta \left\lvert\frac{U}{U_e}\right\rvert (1-\left\lvert\frac{U}{U_e}\right\rvert)dy\right)$
Λ	Calculated integral length scale
Λ_x	Longitudinal integral length scale
ν	Kinematic viscosity
ρ	Air density
σ	Standard deviation

τ_w	Wall shear stress
τ'	Quasi-wall shear stress
τ'_{mean}	Mean of quasi-wall shear stress
τ'_{RMS}	Root-mean-square of quasi-wall shear stress
τ'_{skew}	Skewness of quasi-wall shear stress
ϕ	Flow angle; Angle of hot-wire traverse plane relative to surface
ψ	Zweifel coefficient $\left(2(\frac{S}{B_x})\cos^2\alpha_m\,\lvert\tan\alpha_i - \tan\alpha_m\rvert\right)$
ζ	Flow control effectiveness coefficient $\left(\frac{[(\frac{1}{2}\rho u_m^2\,Y_m)_{BAS} - (\frac{1}{2}\rho u_m^2\,Y'_m)_{AFC}]S}{\rho\overline{u_j}^2 b}\right)$

Subscripts

AFC	Flow control airfoil
BAS	Baseline airfoil
e	Cascade exit; Edge of shear layer
i	Cascade inlet
j	Jet
LBL	Laminar boundary layer
m	Mixed-out
MD	Maximum displacement
s	Separation
t	Transition onset
T	Transition completion
tot	Total cascade inlet value
TBL	Turbulent boundary layer
ref	Reference condition
R	Reattachment
x	Axial component

y	Pitchwise component

Superscripts

$'$	Fluctuation; Corrected for jet momentum
—	Average

Abbreviations

AVR	Axial velocity ratio
CS	Control surface
CV	Control volume
FS	Full scale
FSTI	Freestream turbulence intensity
LPT	Low-pressure turbine
LSTL	Low-Speed Turbomachinery Laboratory
K-H	Kelvin-Helmholtz
SVGJ	Synthetic vortex generator jet
T-S	Tollmien-Schlichting
VGJ	Vortex generator jet

Chapter 1

Introduction

1.1 Motivation

The low-pressure turbine of a turbofan engine is required to drive the fan and some of the low-pressure compressor stages of the engine. In high bypass ratio turbofan engines, such as the Pratt & Whitney PW4084, the low-pressure turbine can have up to seven stages and account for as much as one third of the total engine weight. At high-altitude cruise conditions, it has been observed that low-pressure turbine efficiency can drop by almost 3% compared to take-off and landing conditions (Lord *et al.*, 2000). This efficiency drop occurs due to laminar separation of the airfoil suction surface boundary layer at the low Reynolds numbers encountered during high-altitude flight. In many low-pressure turbines, laminar separation is present over most of the operating envelope (Mayle, 1991). At Reynolds numbers typical take-off and landing conditions, transition promotes reattachment of the separated shear layer well ahead of the trailing edge, and the resulting small separation bubble has relatively little effect of the blade row pressure losses. At the low Reynolds numbers encountered at high-altitude flight, transition occurs late in the separated shear

layer and the airfoil can stall, resulting in higher losses and the observed efficiency drop. It is therefore important to understand the transition process in low-pressure turbines, in particular the effects of Reynolds number and freestream turbulence on transition.

At the current state of turbomachinery aerodynamic design, limits are being reached where significant jumps in performance can no longer be achieved. For instance, minute increases in the efficiency of gas turbine compressors and turbines now require a great deal of research and development (Lord *et al.*, 2000). Much of the effort in current gas turbine aerodynamic design is geared towards reducing engine weight while maintaining current performance levels, i.e. reducing the number of stages, while maintaining the same aerodynamic efficiency. Increased stage loading results in increased blade loading, which in a low-pressure turbine increases the susceptibility of the boundary layers to separation and stall. Current trends in aerodynamic research include manipulating the flow field to achieve a desired performance improvement (Gad-el-Hak, 2000). This manipulation is known as flow control.

Flow control is not a new concept. In Ludwig Prandtl's classic paper of 1904, which introduced the concept of the boundary layer, he showed how suction applied to the aft side of a circular cylinder could prevent flow separation and reduce drag. Since then, many applications of flow control have been realized. All aircraft manufacturers use vortex generators to varying degrees to delay stall. The X-21 research demonstrator aircraft used distributed suction to delay transition, and reduce drag, up to a chord Reynolds number of 4.7×10^7. Even in sports, flow control has made its mark. The dimples on the surface of a golf ball have been designed to promote transition which in turn delays separation and reduces drag, making the ball travel a greater distance. The need to prevent stall of low-pressure turbine airfoils at high-altitude cruise conditions makes them an ideal candidate for flow control.

1.2 Thesis Objectives

There are two main objectives to the present investigations. Both are concerned with the performance of a low-pressure turbine airfoil at low Reynolds numbers.

The first objective is to examine the performance of a low-pressure turbine airfoil with levels of freestream turbulence intensity and freestream turbulent length scale comparable to those found in the low-pressure turbine of an actual engine, and to examine the influence of freestream turbulent length scale on the airfoil performance.

The second objective of the present investigation is to examine the use of blowing flow control for improving the performance of a low-pressure turbine airfoil at low Reynolds numbers.

1.3 Approach

The objectives of this thesis were achieved through experimental measurements. Low-pressure turbines are characterized by long blades with high aspect ratios. This results in essentially two-dimensional flow over most of the blade surface, with small regions of secondary flow near the end-walls. The linear cascade provides an effective environment for studying the two-dimensional behaviour of low-pressure turbine airfoils. The measurements for the present investigations were performed in a low-speed linear cascade wind tunnel using the Pak-B low-pressure turbine profile. This profile was designed by Pratt & Whitney specifically for use in low-speed experimental investigations, and has been documented to stall at low Reynolds numbers (Mahallati, 2003).

Several types of measurements have been used for the investigations. Surface static pressure measurements have been used to examine the loading distribution over the airfoil

surface. Three-hole pressure probes have been used to measure the flow field upstream and downstream of the cascade and to examine the pressure losses and flow turning of the airfoil. Hot-wire probes have been used to measure the turbulence levels of the cascade inlet flow and to examine the development of the shear layer over the aft suction surface of the airfoil. Also, surface-mounted hot-film sensors have been used to examine the transition process over the baseline (non-flow control) airfoil suction surface.

1.4 Overview of Thesis

This thesis presents results from an experimental investigation that has examined the influence of freestream turbulent length scale on the performance of a low-pressure turbine airfoil, and has examined a method of separation control using blowing for a low-pressure turbine airfoil at low Reynolds numbers.

A review of the literature most pertinent to the present investigation is given in Chapter 2. The chapter is divided into three main sections. The first section discusses transition in turbomachinery. The second section discusses issues associated with low-pressure turbines and reviews some of the most pertinent experimental investigations. The third section discusses some flow control goals and methods, and reviews some experimental investigations of flow control applied to axial compressor and turbine airfoils.

The experimental investigations were performed in a low-speed cascade wind tunnel. Chapter 3 describes the experimental apparatus, measurement procedures, and data reduction procedures used for the investigations.

Chapters 4 through 6 present the results from the baseline (non-flow control) Pak-B experiments. Chapter 4 presents the aerodynamic performance of the Pak-B cascade with a level of freestream turbulence intensity and length scale typical of a low-pressure turbine

environment. During the investigation, it was determined that detailed measurements of the aft-suction surface shear layer could be made successfully using a hot-wire. Chapter 5 presents these hot-wire traverse measurements for two levels of freestream turbulence intensity, at one Reynolds number. Chapter 6 examines the influence of turbulent length scale on the aerodynamic performance of the Pak-B airfoil by comparing the measurements described in Chapter 4 with measurements made by Mahallati (2003) for a similar level of turbulence intensity but with a larger turbulent length scale.

The results of the Pak-B flow control study are presented in Chapter 7. The flow control measurements are compared to those for the baseline airfoil, showing the effects that flow control can have on the performance of a low-pressure turbine airfoil at low-Reynolds number.

Finally, the conclusions of the present investigation and recommendations for future work are presented in Chapter 8.

Chapter 2

Literature Review

2.1 Introduction

The present research is concerned with the performance of a low-pressure turbine airfoil at low-Reynolds numbers and a method of flow control applied to the airfoil for stall prevention. This chapter presents a review of previous literature concerned with low-pressure turbines and separated flow control.

The first few sections of this chapter (Sections 2.2 through 2.5) present a review of transition in turbomachinery. Section 2.6 discusses some relevant issues and experimental studies related to low-pressure turbines. The last major part of the chapter, Section 2.7, discusses flow control and some strategies for controlling stall. The most pertinent literature to the current research will be discussed in more detail in the results chapters of the thesis (Chapters 4 through 7).

2.2 Modes of Transition

2.2.1 Classification of Modes

In most engineering applications concerning fluid flow, transition from laminar to turbulent flow occurs in the shear layer between a solid object and the freestream flow. This can occur through various modes which depend on factors such as the Reynolds number, the level of freestream turbulence, the pressure gradient, and the roughness of the solid surface. In turbomachinery flows, a substantial portion of the compressor or turbine airfoil surfaces can be covered by transitional flow (Mayle, 1991), as compared to aircraft wings where the assumption of "point transition" is often accepted. The various modes of transition in turbomachinery flows, according to Mayle (1991), are natural, bypass, separated-flow, periodic-unsteady, and reverse transition, of which the first three are considered the "primary" modes of transition. The following sections describe these three primary modes of transition.

2.2.2 Natural Transition

In a boundary flow with low-freestream disturbances and mild pressure gradient, transition from laminar to turbulent flow typically occurs through a process called "natural transition". The following description of the natural transition process is from Schlichting and Gersten (2000), where a more detailed description can be found. Figure 2.1, taken from White (1991), shows the development of the transition region over a flat plate with negligible streamwise pressure gradient.

As the laminar boundary layer develops downstream of the leading edge, a point is reached where amplification of two-dimensional instability waves within the shear layer

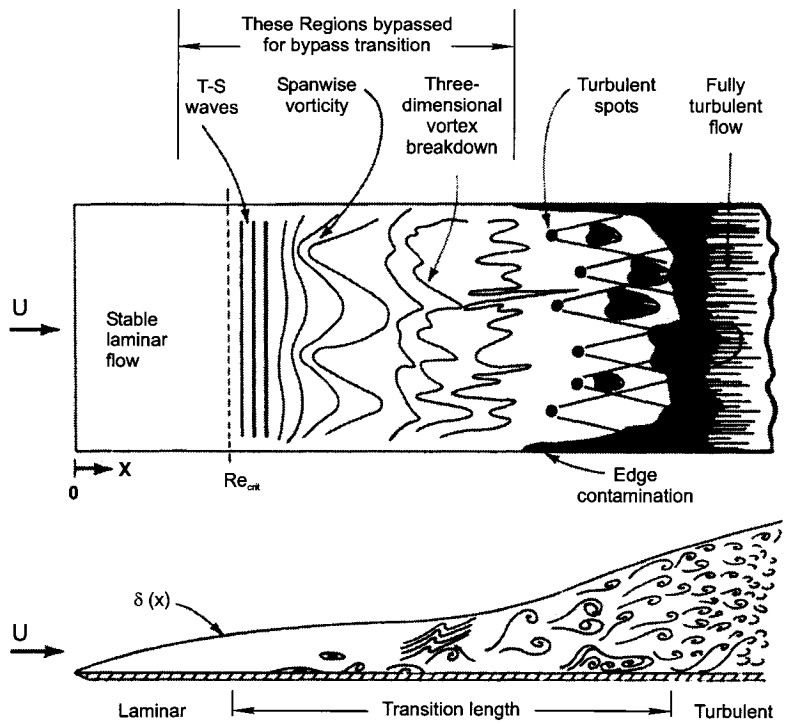

Figure 2.1: **Schematic of Natural Transition Process**

(reproduced from White, 1991)

begins. This occurs at a critical Reynolds number, Re_{crit}, which defines the earliest location at which the waves can be amplified, based on linear stability theory. These instability waves are known as Tollmien-Schlichting (T-S) waves and their frequency can also be predicted from stability theory. As these instability waves grow, secondary instabilities lead to the development of streamwise vorticity, from which three-dimensional disturbances grow in the form of vortex loops. These vortex loops eventually breakdown into turbulent spots which appear irregularly over the surface, spread downstream in a wedge-shaped pattern and eventually coalesce forming a fully-turbulent boundary layer.

2.2.3 Bypass Transition

In flows with high freestream turbulence, the freestream disturbances can lead to a bypass of the first and possibly the second stages of natural transition (Mayle, 1991), these stages being the formation of T-S waves and the formation of vortex loops, respectively. In this bypass mode of transition, turbulent spots start to appear once the boundary layer becomes receptive to disturbances. The main concerns are with the production, growth and convection rates of these turbulent spots. Johnson and Dris (2000) propose a theory for the formation of turbulent spots during bypass transition. In a follow-up paper to that of Mayle (1991), Walker (1993) states that although T-S waves are not observed in bypass transition, primary linear stability, from which the onset of T-S waves can be predicted, should still be relevant for predicting the rate of spot production and hence the length of the transitional region.

2.2.4 Separated Flow Transition

Separation of a laminar boundary layer is a common occurrence in aerodynamic flows. This occurs in regions of adverse pressure gradient where the near-wall momentum cannot overcome the pressure rise and the flow separates from the surface. Once a laminar boundary layer separates from the surface, transition may occur in the resulting free shear layer and may lead to reattachment of a turbulent boundary layer to the surface. A more detailed description of separation bubbles is given in Section 2.3. Although separated-flow transition has been considered a separate mode of transition by Mayle (1991), it can occur through either a natural or a bypass mode and Walker (1993) suggests that the "separated-flow" transition mode be abandoned in favour of a unified approach to transition in attached and separated shear layers, for both the natural and bypass modes.

2.3 Laminar Separation Bubbles

As a laminar boundary layer develops in a region of increasing pressure, an inflection point becomes present in the boundary layer profile. If the laminar boundary layer does not possess sufficient momentum to overcome the pressure rise, the flow adjacent to the surface may be brought to rest and the boundary layer will separate from the surface. This process is shown in Figure 2.2. Once the boundary layer separates from the surface, at X_S, a free shear layer is formed that cannot support a transverse pressure gradient and a plateau in the surface pressure distribution is normally seen. Initially, the region under the separated shear

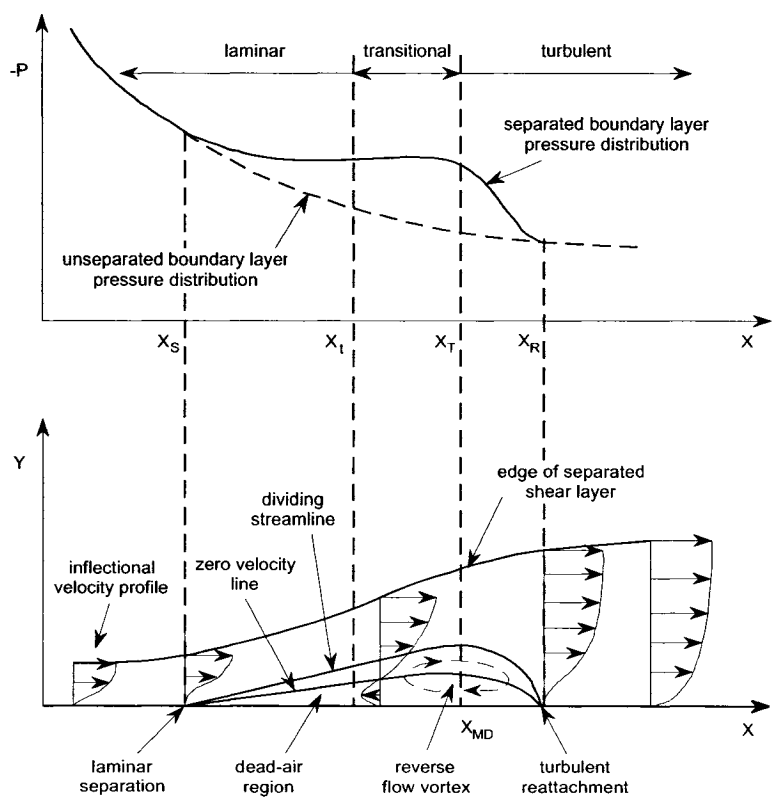

Figure 2.2: **Schematic of a Separation Bubble**

(modified from Zhang, 2002)

layer is stagnant, as described by Ward (1963) and Tani (1964), and is sometimes referred to as the "dead-air" region. The separated shear layer, which contains an inflectional velocity profile, is susceptible to an inviscid-type instability known as the Kelvin-Helmholtz (K-H) instability, which causes the shear layer to roll-up (Muti Lin and Pauley, 1996, Malkiel and Mayle, 1996). Hatman and Wang (1999) have also observed the apparent growth of Tollmien-Schlichting (T-S) instabilities in separation bubbles. Once these instabilities begin to grow, at X_t, transition begins in the separated shear layer. Downstream of transition onset, a reverse-flow vortex forms underneath the separated shear layer. Transition is said to be complete at the location of maximum bubble displacement, $X_T = X_{MD}$, after which the separated shear layer reattaches to the surface, at X_R, accompanied by a region of strong pressure recovery. Hatman and Wang (1999) and Mahallati (2003) have observed some cases in which transition completion appears to occur downstream of the reattachment point ($X_T > X_R$).

Separation bubbles have typically been classified into two categories, "short" and "long", each defined by their effects on the airfoil pressure distribution (Mayle, 1991). Short bubbles have only a local effect on the airfoil surface pressure distribution, as shown in Figure 2.2, whereas long bubbles significantly alter the pressure distribution over the entire airfoil. The transition from a short to a long bubble is referred to as "bursting" and is sometimes the process to which airfoil stall is attributed.

2.4 Transition Prediction in Turbomachinery Flows

2.4.1 Attached-Flow Transition

As described in the previous sections, transition can occur through three primary modes: natural, bypass, or separated-flow. Apart from the fan and first few stages of the

low-pressure compressor, the turbomachinery components of gas turbine engines typically operate in an environment with elevated levels of freestream turbulence due to disturbances and flow unsteadiness generated by the upstream components (Mayle, 1991). This suggests that, as long as laminar separation does not occur, bypass transition is the primary mode observed in gas turbines. In the last several decades, many researchers have examined the attached-flow transition process in turbomachinery and have developed prediction methods for use in design. This section presents a brief review of some of these studies.

One of the first comprehensive studies of attached-flow transition, for turbomachinery applications, was that of Abu-Ghannam and Shaw (1980), for which the focus was the natural transition mode. Correlations were developed for predicting the onset and length of transition based on experimental measurements with varying levels of freestream turbulence and pressure gradients. The momentum thickness Reynolds number at the onset of transition was found to depend on both turbulence intensity and pressure gradient, and a correlation was proposed which accounts for these two effects. This correlation is still in use (Roberts and Yaras, 2003), despite the fact that it has been artificially forced to correspond with the natural transition stability limit and does not accurately predict the onset of bypass transition. The length of transition on the other hand was not correlated with turbulence intensity and pressure gradient, presumably due to the lack of understanding of the various modes of transition. A correlation based on the "concentrated breakdown" model of Dhawan and Narasimha (1958) was developed which relates the transition length Reynolds number to the Reynolds number at transition onset. A similar study to that of Abu-Ghannam and Shaw (1980) was performed by Fraser *et al.* (1988), who were successful at correlating the transition length with changes in turbulence intensity and adverse pressure gradient. Their correlation is purely empirical and was used to predict the transition length over the suction surface of an aft-loaded turbine blade reasonably well. The main deficiency in this correlation is that it is based on measurements in low freestream turbulence conditions

(FSTI $< 1.4\%$), which is much lower than values typically found in gas turbines.

As the physical understanding of transition developed, modelling of transition length based on this understanding became more commonplace. Throughout the 1990's, much of the work in transition length prediction for attached-flow transition came from the work of Walker and Gostelow (Walker and Gostelow, 1990, Gostelow *et al.*, 1994, Gostelow *et al.*, 1996, Solomon *et al.*, 1996). The work culminated with a prediction model for the length of transition (Solomon *et al.*, 1996) based on experimentally observed turbulent spot propagation characteristics (Gostelow *et al.*, 1996). The model was evaluated for five experimental test cases, two of which approximate the pressure distribution observed over turbine airfoils. The predictions were in very good agreement with the test cases and the model was recommended for engineering use. Recently, Roberts and Yaras (2003) proposed a modification to the model of Solomon *et al.* (1996) based on experiments in which systematic variations in the flow Reynolds number, streamwise pressure distribution, and freestream turbulence intensity were made. These models account for the effects of freestream turbulence and pressure gradient history.

2.4.2 Separated-Flow Transition

Separated-flow transition is also a common occurrence in gas turbines. Compressor airfoils operate with regions of strong adverse pressure gradients over their surfaces, particularly at off-design operating conditions, which can lead to laminar boundary layer separation. Low-pressure turbine airfoils, which typically operate at low-Reynolds numbers, are susceptible to boundary layer separation due to the large regions of laminar flow over the airfoil surfaces. In recent years, several tools have been developed to predict the onset and length of separated-flow transition in turbomachinery flows. Hatman and Wang (1999) have performed a comprehensive study of separated-flow transition at low freestream turbulence

levels, and Yaras (2001 and 2002) has examined the effects of freestream turbulence and pressure gradient history on separated flow transition. Both Hatman and Wang (1999) and Yaras (2001 and 2002) have proposed correlations for predicting separated flow transition.

In the study by Hatman and Wang (1999), three modes of separated-flow transition have been observed, defined as *transitional separation*, *laminar separation/short bubble mode*, and *laminar separation/long bubble mode*. *Transitional separation* is characterized by the onset of transition upstream of the separation point and can occur at high Reynolds numbers and low levels of adverse pressure gradient. In this mode, natural transition begins in the boundary layer shortly upstream of separation, attributed to Tollmien-Schlichting (T-S) instabilities, and Kelvin-Helmholtz (K-H) instabilities develop within the separated shear layer. Transition completion typically occurs shortly downstream of the reattachment point. For the *laminar separation/short bubble mode* and *laminar separation/long bubble mode*, transition occurs in the separated shear layer downstream of separation. In the *laminar separation/short bubble mode*, which can occur at moderate Reynolds numbers and mild adverse pressure gradients, transition is induced by inflectional instability at the location of maximum bubble displacement and is characterized by quick transition completion due to the interaction between the separated shear layer and the reverse-flow vortex. Transition completion may occur at or before reattachment but in many cases occurs shortly downstream of reattachment. Both T-S instabilities and K-H instabilities have been observed for this *short bubble* mode. In the *laminar separation/long bubble mode*, which can occur at low Reynolds numbers and strong adverse pressure gradients, transition onset occurs in the same manner as for the *short bubble mode* but due to the locally low Reynolds number, mixing is reduced and the bubble fails to reattach immediately. As transition progresses and the separated shear layer becomes fully turbulent, the bubble eventually reattaches to the surface, much further downstream than in the *short bubble mode*. In some cases in which very strong adverse pressure gradients are present, the bubble may fail to

reattach resulting is an open bubble and stall of the airfoil. Hatman and Wang (1999) have developed tools for predicting the mode of transition, as well as the corresponding location of transition onset and transition length, for low levels of freestream turbulence.

Yaras (2001 and 2002) has examined the effects of freestream turbulence and pressure gradient history on separated-flow transition and has noted that both play an important role in both the onset and length of transition within the separated shear layer. The cases examined by Yaras can be classified as the *laminar separation/short bubble mode* of Hatman and Wang (1999), but the effects of elevated freestream turbulence changes the general characteristics of this mode. In particular, Yaras found that with elevated freestream turbulence, transition onset occurs ahead of the maximum displacement location. This is due to instability growth promoted by disturbances in the freestream flow. Yaras (2002) proposed correlations for the location of transition onset and the location of bubble reattachment, based on conditions at separation, which account for pressure gradient history and freestream turbulence. The correlations of Yaras provide better predictions than those of Hatman and Wang (1999), at least for the cases examined.

2.5 Effects of Turbulent Length Scale in Turbomachinery

Freestream turbulence is characterized not only by the intensity of the turbulent fluctuations but also the length scales, and time scales, associated with the turbulent structures in the flow (Schlichting and Gersten, 2000). The length scales of a turbulent flow define the size of the important turbulent eddies within the flow. The integral, or macro, length scale defines the size of the dominant energy-containing eddies in the flow and the micro length scale defines the size of the energy-dissipating eddies. The effects of freestream turbulence intensity on transition are relatively well known, while the effects of freestream turbulent length scale are not well understood.

In a series of three papers, Dullenkopf and Mayle (1995), Mayle and Schultz (1997), and Mayle *et al.* (1998) examined both theoretically and experimentally the effects of turbulent length scale on laminar heat transfer and transition onset. The growth of laminar fluctuations in a pre-transitional boundary layer are caused by fluctuations in the freestream and, as discussed by Johnson and Dris (2000), these laminar fluctuations are primarily responsible for turbulent spot initiation during bypass transition. Mayle *et al.* (1998) show that the growth of pre-transitional laminar fluctuations is promoted in a narrow band of frequencies, with a corresponding band of freestream length scales proportional to the scale of the energy-dissipating eddies in the boundary layer. The band of length scales responsible for promoting laminar heat transfer, on the other hand, depends on the scale of the larger energy containing eddies in the boundary layer.

The effects of turbulent length scale on heat transfer in gas turbines has been known for some time (Dullenkopf and Mayle, 1995). The literature describing the effects of length scale on transition are scarce and scattered. Butler *et al.* (2001) describe a study with systematic changes in Reynolds number, turbulence intensity and turbulent length scale, in which the heat transfer distribution and transition were examined over a low-pressure turbine airfoil. At a freestream turbulence intensity of 10%, three levels of integral length scale were examined, varying from 20%-70% of axial chord. For this range of length scales, there was no appreciable difference in the location of transition onset. Chapter 6 compares the separated-flow transition process over a low-pressure turbine airfoil for two freestream turbulent length scales, at nearly identical levels of freestream turbulence intensity.

2.6 Low-Pressure Turbines

2.6.1 Operating Environment

The low-pressure turbine (LPT) is the last component through which the core flow of a turbofan engine passes. The main purpose of the LPT is to produce shaft power for the fan, and in some cases a number of low-pressure compressor stages. The fan of a high bypass ratio turbofan engine produces up to 80% of the engine thrust and in some engines the LPT comprises one third of the total engine weight (Howell *et al.*, 2001).

Due to the highly turbulent flow produced in the combustion chamber, and the relative motion of the upstream blade rows, the flow through an LPT is highly disturbed. The freestream turbulence intensity is typically between 3-7% and the integral length scale of the freestream turbulence is typically 10% of blade axial chord or smaller (private communication, Pratt & Whitney Aircraft, East Hartford, Connecticut, 2002). Turbulence intensity within the incoming wakes from upstream blade rows can exceed 10% (Mahallati, 2003). The current study considers steady inlet flow conditions; therefore unsteady-wake effects will not be discussed. A detailed review of these effects and a complimentary experimental study is presented by Mahallati (2003).

As discussed by Mayle (1991), the blade-chord Reynolds numbers in LPTs is low, particularly at high altitude cruise conditions where the ambient density is very low. This results in significant regions of laminar flow over LPT airfoils, despite the high levels of freestream turbulence. Laminar separation and subsequent stall of the airfoils has been observed, which can significantly decrease the LPT efficiency and work output.

In modern turbofan engines, the desire to continually increase the stage performance and decrease the weight of LPTs has led to the design of high-lift airfoils. Increasing the lift, or

loading, of these airfoils will however increase the strength of the adverse pressure gradients over the airfoil surface. This in turn leads to higher susceptibility to flow separation and stall. The next section discusses some design philosophies for LPT airfoils, followed by a discussion of some experimental studies concerning LPTs with steady inflow conditions.

2.6.2 High-Lift Design Philosophy

In the quest to reduce the number of blades in an engine, the lift produced by low-pressure turbine blades has increased significantly over the years. This has resulted in several design philosophies for high-lift blading. Hourmouziadis (1989) was the first to describe a set of systematic guidelines for designing LPT blades. These guidelines relate to the boundary layer development over the blade surfaces, which is directly influenced by the loading distribution. For LPTs operating at cruise conditions, the blade Reynolds numbers are low enough that a significant portion of the blade surface is covered by laminar flow. One goal of high-lift design is to control the transition process.

Papers by Curtis *et al.* (1997) and Howell *et al.* (2001) discuss the development and design philosophies involved in the design of LPT blading for the Rolls-Royce BR700 series of engines. They have found that aft-loading the suction surface pressure distribution is beneficial in keeping the losses to a reasonable level while increasing the spacing between blades. Harvey *et al.* (1999) also discuss the need to keep pressure surface separation bubbles to a minimum size. It was found that the location of minimum pressure on the suction surface should be moved rearward as far as possible without an open separation bubble forming in the strong deceleration region ahead of the trailing edge.

In a non-separated boundary layer, the location of transition onset varies as the blade Reynolds number changes. Since current LPTs operate at low-Reynolds numbers, it is desired to design blades that are insensitive to Reynolds number. This has led designers to

enforce separation at a specified location on the blade suction surface. This is part of the current high-lift design philosophy of Rolls-Royce (Howell *et al.*, 2001).

2.6.3 Experimental Studies of Low-Pressure Turbine Airfoils

This section reviews some experimental investigations of the aerodynamic performance of LPTs. Only investigations with steady inflow conditions are discussed. Table 2.1 presents a summary of some of the most relevant investigations that will be discussed within this section. The abbreviations used in Table 2.1 are listed below:

Type of experiment:	**FP**	**flat plate experiment with imposed pressure gradient**
	LCS	**linear cascade experiment**
	RR	**rotating rig experiment**
	SA	**single airfoil experiment**
	SPC	**single passage cascade experiment**
	WTT	**water tow-tank experiment**
Measurement locations:	**BL**	**measurements made in boundary layer**
	DS	**measurements made downstream**
Type of measurements:	**3HP**	**three-hole pressure probe**
	HFP	**hot-film probe**
	HW	**hot-wire probe**
	PIV	**particle image velocimetry**
	FPP	**flattened pitot probe**
	SFV	**smoke flow visualization**
	SHF	**surface-mounted hot-film**
	SP	**surface pressure taps**
Parameters investigated:	**i**	**incidence variation**
	LD	**loading distribution**
	Re	**Reynolds number**
	Ma	**Mach number**
	Tu	**freestream turbulence intensity**

Table 2.1: **Summary of Experimental Low-Pressure Turbine Studies**

Reference	Type	Measurement Details										Parameters Inverstigated					Conditions		Comments
		Location		3HP	HFP	HW	PIV	FPP	SFV	SHF	SP	i	LD	Re	Ma	Tu	Re x 10^{-3}	Tu [%]	
		BL	DS																
Hoheisel et al. (1987)	LCS	x	x	x				x		x	x	x	x	x	x	x	100-1100[1]	0.8-7.1	- examined 3 cascades with same duty but different LD - BL measurements used to examine transition length - aft-loaded airfoil has lowest losses and most insensitive to Tu
Qui and Simon (1997)	SPC	x				x					x			x		x	50-300[2]	0.5-10	- appears to be Pak-B profile - examined separation and transition characteristics
Lake et al. (1999)	LCS	x	x	x		x								x		x	50-200[3]	1-4	- Pak-B profile - examined separation and transition characteristics - recessed surface dimples used for control of separation
Murawski and Vafai (1999)	LCS	x	x	x		x					x		x	x			50-300[2]	1	- appears to be Pak-B profile - examined effects of variable axial chord (LD) on separation and transition
Dorney et al. (2000)	LCS	x	x	x		x					x			x			43-172[3]	1	- Pak-B profile - examined separation and transition characteristics
Murawski and Vafai (2000)	LCS		x		x						x			x		x	50-300[2]	1.1-8.1	- appears to be Pak-B profile - examined momentum deficit and turbulence levels in downstream wakes
Shyne et al. (2000)	FP	x				x			x	x	x			x		x	100-250[2]	0.8-3	- Pak-B suction-surface pressure distribution - typical LPT suction-surface pressure distribution - examined separation and transition characteristics
Solomon (2000)	RR	x								x			x			x	400[2]	1-5	- exained 2 different LPT airfoils in a RR - separation apparent over high-lift airfoil - transition moves forward with increased loading
Hollon and Jacob (2001)	WTT/ LCS	x					x		x					x			13-38/ 30-70[4]	-	- examined Pak-B cascade in two different facilities at low Tu - PIV demonstrated for WTT with 3-blade linear cascade - smoke-flow visualization used to identify separation and transition in LCS
Volino and Hultgren (2001)	FP	x				x								x		x	50-300[2]	0.2-7	- Pak-B suction-surface pressure distribution - examined separation and transition characteristics
Volino (2002)	SPC	x				x					x			x		x	25-300[2]	0.5-9	- Pak-B profile - examined separation and transition characteristics
Mahallati (2003)	LCS	x	x	x						x	x			x		x	25-150[3]	0.4-4.5	- Pak-B profile - examined separation and transition characteristics

1 *Re* based on exit velocity and true chord
2 *Re* based on exit velocity and suction surface length
3 *Re* based on inlet velocity and axial chord
4 *Re* based on inlet velocity and suction surface length

The aerodynamics of LPT's with unsteady incoming wakes, also known as rotor-stator interaction, has also been studied extensively. The LPT group from the Whittle Laboratory at Cambridge University, headed by Howard Hodson, perform almost all of their investigations with unsteady incoming wakes. For a review of unsteady effects in LPTs, and a complimentary experimental study, see Mahallati (2003).

Of the twelve experimental investigations summarized in Table 2.1, ten have studied the Pratt & Whitney Pak-B profile. It is worth noting that the present experimental study is also concerned with the Pak-B profile. The Pak-B profile is typical of an in-service high-lift LPT airfoil. The blade surface shape has been inverse-designed to achieve the same non-dimensional pressure distribution at low-speed as is encountered in the compressible flow conditions of the actual engine (private communication, Pratt & Whitney Aircraft, East Hartford, Connecticut, 2002). Lake *et al.* (1999), Murawski and Vafai (1999), Murawski and Vafai (2000), Dorney *et al.* (2000), Hollon and Jacob (2001), and Mahallati (2003) have all presented experimental measurements for the Pak-B profile performed in a linear cascade wind tunnel. Although Murawski and Vafai do not explicitly state that they have used the Pak-B profile, it is assumed based on the descriptions and schematics of their cascade. Hollon and Jacob (2001) also present PIV measurements for a three-blade cascade in a water tow tank facility. Qui and Simon (1997) and Volino (2002) have performed their experiments in a single-passage cascade setup, using the Pak-B profile. This type of arrangement consists of a single passage between two large-scale airfoils. The main deficiency of this type of arrangement is that flow periodicity cannot be achieved. Shyne *et al.* (2000) and Volino and Hultgren (2001) have performed measurements on a flat plate with an imposed pressure gradient from a flexible opposing wall. The flexible wall was adjusted until the pressure distribution over the flat plate matched that on the suction surface of the Pak-B airfoil. Although a flat plate experiment does not capture the curvature and downstream periodicity effects of a cascade, very detailed measurements of the developing boundary layer can be

made in a larger-scale facility. The focus of most of the above cited studies has been the separation and transition characteristics of the Pak-B profile under varying levels of Reynolds number and freestream turbulence intensity.

In most of the experimental investigations of the Pak-B profile, cited in the previous paragraph, a separation bubble was present over the airfoil suction surface and separated flow transition has been observed as the primary mode of transition. It has been found that as the Reynolds number is decreased, transition onset moves downstream and causes a lengthening of the separation bubble. If the Reynolds number becomes low enough, transition begins too far downstream and the separated shear layer fails to reattach to the surface, resulting in stall of the airfoil. Increasing the freestream turbulence intensity promotes transition within the separated shear layer, resulting in a shorter separation bubble. Mahallati (2003) compared the estimated locations of separation, transition onset, reattachment, and transition completion of his experiments with those from Qui and Simon (1997), Volino and Hultgren (2001), and Volino (2002), and found reasonably good agreement despite the different experimental configurations. The separation and transition length characteristics affect the performance of the the Pak-B profile. In general, profile losses decrease with decreasing separation length and therefore decrease with increasing Reynolds number and increasing turbulence intensity. In Chapters 4 through 6, an additional experimental investigation of the Pak-B airfoil will be presented. Chapter 7 presents a experimental study of flow control applied to the Pak-B profile.

Table 2.1 also lists two experimental studies of LPT configurations that do not use the Pak-B profile. Hoheisel *et al.* (1987) examined the effects of freestream turbulence, Reynolds number, Mach number, and incidence on the performance of three low-pressure turbine cascades. The three cascades were designed for the same duty but each had a different pressure distribution over the airfoil surface. One cascade was forward-loaded

(T104) while the other two were aft-loaded (T105 and T106). The T105 cascade had a stronger adverse pressure gradient than the T106 cascade over the aft suction surface. The T106 cascade performed best at both design and off-design conditions, which was attributed to the aft-loaded pressure distribution. Although the T105 cascade behaved similarly to the T106 cascade, the stronger adverse pressure gradient resulted in a thicker suction surface boundary layer at the trailing edge and higher profile losses. The T106 profile has been the subject of many experimental and numerical studies, and is the European equivalent of the Pak-B profile. Solomon (2000) also examined the effects of LPT loading distribution, but in a two-stage low-speed rotating rig experiment. Two airfoils were used, one with higher overall loading than the other. Solomon found that movement in the transition onset point was least sensitive for the more highly loaded airfoil, which is desired for off-design operating conditions.

As seen in many of the studies concerned with LPTs, separation can have a detrimental effect on blade row performance. The current study is concerned with controlling the separation over the Pak-B airfoil. The remainder of this chapter reviews flow control concepts and their application to control separation in turbomachinery flows.

2.7 Flow Control

2.7.1 Flow-Control Goals

There are many goals one can aim to achieve using flow control. For example, one can aim to reduce drag, enhance lift, suppress flow-induced noise, or promote/reduce heat transfer. To achieve a specific goal, transition may have to be delayed or advanced, flow separation may have to be prevented or provoked, and turbulence levels may have to be reduced or enhanced. In general, there is no ideal method of flow control for any specific

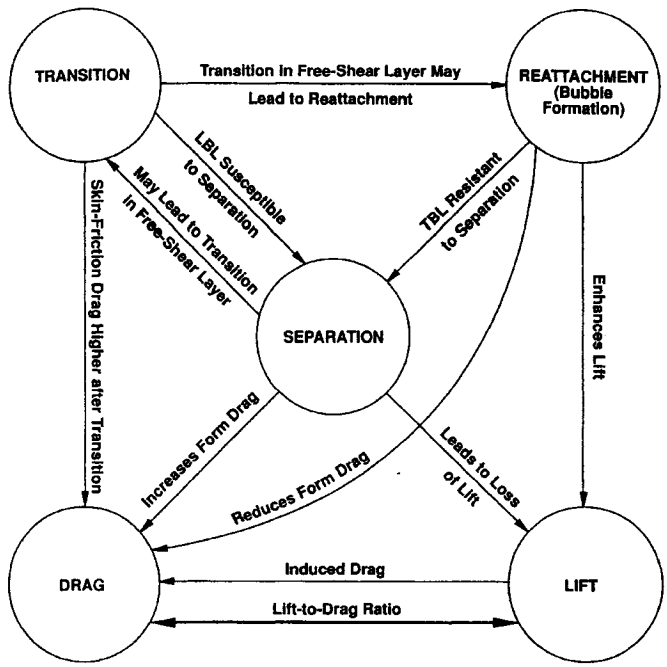

Figure 2.3: **Interrelation Between Flow-Control Goals (reproduced from Gad-el-Hak, 2000)**

goal and compromises must always be made (Gad-el-Hak, 2000).

Some examples of the interrelationship between flow-control goals are given by Gad-el-Hak (2000) and are discussed here using Figure 2.3 as a guide. One of the primary goals for designing a lifting surface is to achieve the highest lift-to-drag ratio possible. This requires maximizing the lift and minimizing the drag. Lift can be increased by advancing transition and preventing separation, but skin-friction drag and induced drag may be increased. Skin-friction drag can be decreased by delaying transition (extend laminar boundary layer), but separation may occur resulting in loss of lift and increased form drag. Form drag can be reduced by advancing transition, hence preventing separation, but skin-friction drag will be increased. Induced drag can be decreased only by decreasing lift. These few examples show the conflict between flow-control goals.

2.7.2 Flow Control Concepts

Gad-el-Hak (2000) describes many ways of classifying flow-control methods. The classification scheme adopted by the present author considers the energy expenditure and the control loop involved. Figure 2.4 shows this classification scheme. If no energy input is required, the control method is considered *passive* and there is no control loop involved. If energy input is required, the control method is considered *active* and involves a control loop. *Active* flow control is further sub-divided, depending on the control loop and controlled flow variable. If steady or unsteady energy input is used without regard for the state of the flow (fixed-input), then the method is considered *predetermined* and uses open-loop control, whereas if the control input is continually adjusted based on a measured flow variable (variable-input), then the method is considered *reactive*. Two different types of control loop can be used for reactive control. In a *feedforward* control loop, the measured and controlled flow variables differ. In a *feedback* control loop, the measured and controlled variables are the same. Chapter 7 presents measurements for a predetermined active flow

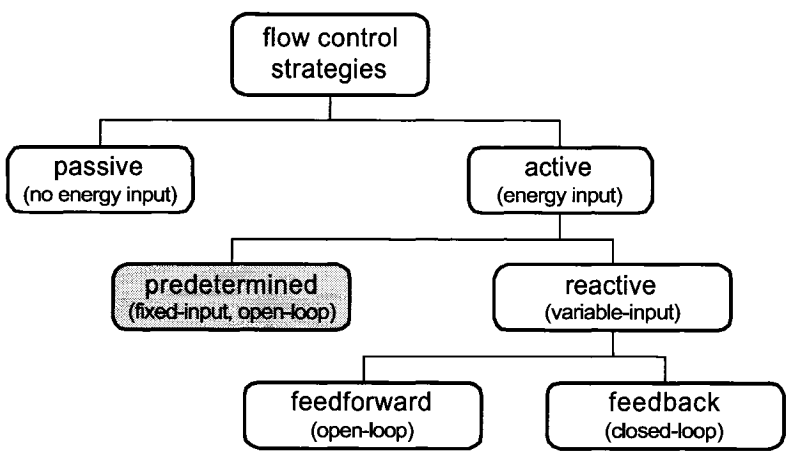

Figure 2.4: **Classification of Flow Control Concepts (adapted from Gad-el-Hak, 2000)**

control concept (shaded concept in Figure 2.4) applied to a low-pressure turbine airfoil for stall control.

2.7.3 Passive Methods of Flow Control

Passive flow control methods have been used for many years to prevent separation over wings, the afterbody of aircraft fuselages and in diffusers (Gad-el-Hak, 2000). This section briefly reviews some of the methods of passive separation flow control described in the literature.

The primary method of passive separation control has been vortex generators, which consist of surface protrusions that generate vortical entrainment of freestream fluid down to the surface. When these devices are used to prevent separation at off-design conditions, parasitic drag is typically increased at design conditions unless the devices can be retracted into the surface (Gad-el-Hak, 2000). This effect is seen for many types of separation control devices. In studies by Lake *et al.* (2000) and Volino (2003a), the use of boundary layer trip wires on the Pak-B LPT airfoil reduced low-Reynolds number separation losses, but generated higher losses at higher Reynolds numbers typical of take-off and landing conditions. Lin *et al.* (1989) and Lin *et al.* (1990) examined various passive methods of turbulent-flow separation control over a backward facing ramp. They found that vortex generators, transverse grooves, longitudinal grooves, large-eddy breakup devices, and arches were all effective at either preventing or reducing the length of turbulent separation. Lin (2002) describes the development of "low-profile" vortex generators that generate lower losses than conventional vortex generators, while effectively suppressing or reducing separation of turbulent boundary layers. Recessed surface dimples are also an effective method of separation control. The dimples on a golf ball have been designed to promote transition and thereby delay separation, which results in lower drag.

2.7.4 Active Methods of Flow Control

Active flow control methods have also been used for separation control over airfoils and in diffusers. This section briefly reviews some of the methods of active separation control described in the literature.

One of the first demonstrations of active separation control was presented by Ludwig Prandtl in his classic paper introducing the concept of the boundary layer (Schlichting and Gersten, 2000). Prandtl showed how suction applied to the aft side of a circular cylinder could prevent flow separation and reduce drag. Suction, also known as aspiration, is used to remove the near-wall low-momentum fluid of a boundary layer. In some cases, such as over the wing of the X-21 research demonstrator aircraft, distributed suction is used to delay transition by keeping the momentum thickness of the boundary layer below the critical value at which transition begins (Gad-el-Hak, 2000). Localized suction through a spanwise slot has been used by Merchant (2002) to increase the loading capability and decrease the profile losses of compressor and turbine airfoils. The same technique, using slots on the endwall, has been used by Funazaki *et al.* (1996) to reduce secondary losses in a turbine cascade.

Flow control via fluid injection is also a common method of separation control. This is the method used for the present experiments. The primary goal of fluid injection is to re-energize the low-momentum near-wall boundary layer and thereby delay separation. Turbulent wall jets have been studied extensively for this purpose, and a review concerning all major contributions up to 1981 has been given by Launder and Rodi (1981). A wall jet, as defined by Launder and Rodi (1981), is a shear flow directed along a wall where at any station the streamwise velocity over some region within the shear flow exceeds that in the external stream. Wall jets show characteristics similar to a boundary layer in the inner, near-wall, region and similar to a jet in the outer region. More recent investigations

of wall jets are given by Kobayashi and Fujisawa (1982), Zhou and Wygnanski (1993), and Eriksson *et al.* (1998), just to name a few, and most are concerned with the turbulence characteristics within the complex shear layer. The wall jet used in the present study differs from that described by Launder and Rodi (1981) in that the injection slot of the present study is inclined to the surface, and the levels of fluid injection examined result in rapid mixing of the jet and the freestream flows, with no distinct jet profile apparent over the airfoil surface downstream of the injection slot. Wall jets have also been used in wide-angle diffusers to prevent stall and increase pressure recovery (Fielder and Gessner, 1972, Back and Cuffel, 1982, Kwong and Dowling, 1994) and have been used on STOL (short take-off and landing) aircraft wings to increase circulation and lift (Chin *et al.*, 1975, and Loth and Boasson, 1984).

Recent developments in active flow control, particularly separation control, are concerned with unsteady excitation of the boundary layer. Pack and Roslin (1998) review some of the active flow control methods under investigation at the NASA Langley Research Center in the late-90's. They discuss methods such as oscillatory blowing through a spanwise slot (unsteady wall jet), "on-demand" vortex generators which have no parasitic drag when deactivated, and zero-net-mass flux (or synthetic jet) actuators which combine the effects of suction and blowing without requiring an internal plumbing system.

The next, and final, section of this chapter reviews experimental studies of flow control applied to turbomachinery, particularly those that affect the profile losses.

2.7.5 Flow Control in Turbomachinery

This section reviews some experimental investigations of flow control applied to turbomachinery, in particular investigations of passive and active-blowing methods in axial compressors and turbines for gas turbine engines. Table 2.2 presents a summary of these

investigations. The abbreviations used in Table 2.2 are the same as those used in Table 2.1 (listed in Section 2.6.3 on page 19), except for those describing the method of flow control, which are listed below:

Flow control (FC) method:	**P**	**passive flow control**
	AP	**active-predetermined flow control**
	AR	**active-reactive flow control**

Recently, Lord *et al.* (2000) presented a paper discussing flow control opportunities in military and civilian aircraft gas turbines. They show how maximum performance levels are now being reached using existing gas turbine technology and discuss the benefits that could be realized with flow control technology. The general design goal of modern compressors and turbines is to reduce the number of stages while maintaining or increasing the stage efficiency. Increased stage loading is typically associated with increased blade loading which, as discussed in Section 2.6.1, can lead to stall and significant performance degradation. Some flow control concepts that have been investigated for separation/stall suppression in turbomachinery blade rows are discussed below.

The use of blowing for stall suppression was recognized early on in the development of gas turbine engines. Brocher (1961) examined the effects of using a trailing edge jet-flap on a compressor cascade. He found that injection of fluid through a slot in the trailing edge could prevent stall at high incidence. An incidence limit was reached above which no amount of blowing could prevent stall. Lord *et al.* (2000) discuss how this jet-flap technique could be used to remove the complex variable-geometry flap system used on the inlet guide vanes (IGVs) of military engines, and thereby reduce engine weight.

One technique of preventing stall over a compressor or turbine airfoil is to introduce momentum to the near-wall region of the boundary layer just upstream of separation. This can be accomplished passively by exploiting the pressure difference between the pressure

Table 2.2: **Summary of Experimental Flow Control Studies for Turbomachinery**

Reference	Type	FC Method			Measurement Details							Parameters Inverstigated				Conditions		Comments
		P	AP	AR	Location		3HP	HW	FPP	SFV	SP	i	Re	Ma	Tu	Re x 10^{-3}	Tu [%]	
					BL	DS												
Brocher (1961)	LCS		x			x	x					x				300_1	-	- jet-flap compressor cascade - examined stall characteristics with blowing level
Mikolajczak et al. (1970)	LCS	x			x	x	x				x	x				200_1	-	- slotted and tandem compressor cascades - examined losses with incidence for various slot configurations
Fottner (1979)	LCS	x	x		x	x	x		x		x	x	x	x		-	-	- through-slot and slot blowing for compressor cascade - examined blowing level required to minimize losses
Sturm et al. (1992)	SA		x		x				x		x					620_1	4.7	- simulated compressor with blowing slot - examined blowing level required to minimize losses
Bons et al. (1999)	LCS		x		x	x	x	x		x	x		x		x	$25\text{-}100_2$	1-4	- Pak-B profile with vortex generator jets (VGJs) - examined effects of steady blowing on separation characteristics
Lake et al. (1999)	LCS	x				x	x	x					x		x	$50\text{-}200_2$	1-4	- Pak-B profile with recessed surface dimples - examined downstream wake and loss characteristics with flow control
Lake et al. (2000)	LCS	x			x	x	x	x			x		x		x	$43\text{-}172_2$	1-4	- Pak-B profile with recessed surface dimples, V-grooves, and trip-wire - examined separation and loss characteristics with flow control
Bons et al. (2001a)	LCS		x		x	x	x	x			x		x		x	$25\text{-}100_2$	1	- Pak-B profile with vortex generator jets (VGJs) - examined effects of pulsed blowing on separation characteristics
Bons et al. (2001b)	LCS		x		x	x		x								25_2	1	- Pak-B profile with vortex generator jets (VGJs) - examined effects of pulsed blowing on BL and DS flow fields
Carter et al. (2001)	LCS		x			x	x									2000_1	-	- compressor cascade with suction/blowing flow control concept - examined effects of additional blowing level on losses and flow turning
Culley et al. (2003)	RR		x	x		x	x				x	x	x			160_1^*	-	- compressor vane with 2 blowing configurations - examined effects of steady and unsteady blowing on losses - demonstrated two methods of reactive control for stall suppression
Volino (2003a)	SPC	x			x			x			x		x		x	$25\text{-}300_3$	0.5-8.5	- Pak-B profile with rectangular spanwise bars on suction surface - examined separation and transition characteristics with BL trip
Volino (2003b)	SPC		x		x			x			x					25_3	0.5	- Pak-B profile with synthetic vortex generator jets (SVGJs) - examined effects of SVGJs for one demonstration case

1 *Re* based on inlet velocity and true chord
2 *Re* based on inlet velocity and axial chord
3 *Re* based on exit velocity and suction surface length
* estimated nominal *Re*

and suction surfaces of the airfoil. Mikolajczak *et al.* (1970) and Fottner (1979) examined the use of a slot between the pressure and suction surface to introduce fluid from the pressure surface flow to the low-momentum suction surface boundary layer on a compressor airfoil. Mikolajczak *et al.* (1970) showed that this technique can increase the useful range of incidence of a compressor cascade. Fottner (1979) also examined the use of blowing through a slot on the suction surface of a compressor airfoil using a secondary air supply. This technique is similar to that used in the present flow control experiment, presented in Chapter 7. Fottner found that this active "blowing" technique is more effective at reducing losses and widening the useful incidence range than the passive through-slot technique. The advantage of this blowing technique is that the level of momentum injection can be controlled and adjusted for different operating conditions. Sturm *et al.* (1992) also present an experimental study of slot blowing, with a similar configuration and similar results to those of Fottner (1979).

More recently, due to a renewed interest in flow control for gas turbine turbomachinery components, several new methods of stall suppression have been investigated for compressor airfoils. Carter *et al.* (2001) examined a flow control design for a high-turning compressor cascade (blade turning angle of 69°) that uses suction and blowing developed from a secondary air supply. The design uses a row of suction holes located slightly downstream of the nominal separation point and a row of blowing holes further downstream. The mass flow removed through the suction holes is combined with the secondary air supply, and the resulting flow is used for blowing. The general results of the study showed that at zero-incidence, where stall occured near the trailing edge, a secondary flow rate of 1.6% of the passage through-flow resulted in a 65% reduction in profile loss and a 4.5° increase in flow turning.

Culley *et al.* (2003) examined various methods of blowing flow control for a compressor

stator vane. Three blowing configurations were used: a "slot-vane" design which uses a spanwise inclined slot, a "hole-vane" design which uses a spanwise row of discrete injection holes inclined in the downstream direction, and an "embedded-fluidic vane" design which uses a double-row of discrete injection holes which are driven by embedded micro-fluidic devices that alternate the injection flow between the two rows. The "slot-vane" and "hole-vane" designs were tested with both steady and periodic-unsteady injection. The "embedded-fluidic vane" design is inherently unsteady and therefore was tested with periodic-unsteady injection only. Stagger of the compressor vane was increased by 3° to force separation. Although all blowing configurations resulted in decreased losses, the unsteady "slot-vane" configuration was found to be the most effective. Culley *at al.* also investigated a method of closed-loop reactive control using the "slot-vane" design, and found that the new control system could activate the injection flow only when stall was detected.

So far the discussions of flow control in turbomachinery have focused on methods applied to compressor airfoils. Several flow control investigations have been performed using the Pak-B low pressure turbine airfoil and are discussed in the following. The Pak-B airfoil stalls at low Reynolds numbers, as discussed in Section 2.6.3. Any quoted Reynolds numbers are based on inlet velocity and axial chord.

Passive methods of separation control for the Pak-B airfoil have been investigated by Lake *et al.* (1999), Lake *et al.* (2000), and Volino (2003a). Lake *et al.* (1999) examined the performance of the Pak-B airfoil with a spanwise row of recessed surface dimples located on the suction surface at 55% axial chord (41% suction surface length). They observed a 40% reduction in losses at low Reynolds number (50000) and low freestream turbulence intensity (1%) without any adverse effects at higher levels of Reynolds number and freestream turbulence, where the airfoil behaves well. In a follow-up study, Lake *et al.* (2000) observed that separation could be fully suppressed and losses could be further reduced

with dimples located at 65% axial chord (53% suction surface length). Lake *et al.* (2000) also examined the effects of streamwise V-grooves and boundary layer trip wires on the performance and separation characteristics of the Pak-B airfoil, but found that surface dimples were most effective at suppressing separation and reducing losses. Volino (2003a) placed two-dimensional rectangular bars on the suction surface of the Pak-B airfoil at 53% suction surface length to promote transition and suppress separation. Although separation length and suction surface losses were minimized with the smallest bar size considered (bar height 0.2% of suction surface length), a small increase in suction surface losses from the baseline (clean blade) configuration was observed. For most cases examined by Volino, suction surface losses were increased by the presence of the bars, indicating that surface protrusions may not be the most effective method of flow control for low-pressure turbines.

Vortex generator jets (VGJs) have also been used as a method of separation control for the Pak-B airfoil (Bons *et al.*, 1999, Bons *et al.*, 2001, Bons *et al.*, 2002, and Volino, 2003b). VGJs behave similarly to passive vortex generators in that they generate vortical entrainment of freestream fluid into the boundary layer, but have the added advantage of being able to be turned off when they are not needed. VGJs consist of discrete jets inclined from the surface in the spanwise direction which generate a single dominant slowly-decaying streamwise vortex. Bons *et al.* (1999) examined the effects of VGJs on the separation characteristics of the Pak-B airfoil with steady blowing, with the jets inclined 30° from the surface and located at 73% of axial chord (61% of suction surface length). They observed a significant reduction in separation at low Reynolds number and all levels of freestream turbulence examined. A minimum level of blowing was required to effectively reduce separation and profile losses. Bons *et al.* (2001) examined the same VGJ configuration as Bons *et al.* (1999) but with pulsed VGJs located at 45% and 63% of axial chord (37% and 51% of suction surface length). They observed that the same level of separation and loss reduction could be achieved using the pulsed jets but with an order of

magnitude reduction in the required secondary mass flow rate. The VGJs located at 63% axial chord provided the highest loss reduction for the lowest required secondary mass flow rate. Bons *et al.* (2001) found that the impulse at the start and end of the pulse provided the means for influencing the boundary layer, which led to the study of Bons *et al.* (2002) which examined the relaxation period of the suction surface boundary layer and downstream wake after each pulse (63% axial chord VGJ location). The timescale of the relaxation period was found to be relatively constant for the operating condition examined and it was found that reducing the duty cycle (fraction of pulse period for which the jet is activated) could reduce the required secondary mass flow rate even further. Volino (2003b) investigated the effects of using synthetic vortex generator jets (SVGJs) to control the separation characteristics of the Pak-B airfoil. SVGJs are geometrically identical to standard VGJs but provide oscillatory blowing and suction with zero net mass flux. Volino used the same VGJ configuration and location as Bons *et al.* (2002) and used a speaker inside the blade plenum to generate the periodic oscillations. Volino observed that the pulses generated by the SVGJs had similar characteristics to a turbulent spot, and suppressed separation of the laminar boundary layer.

The present investigation examines blowing through a slot located just upstream of separation on the suction surface of the Pak-B airfoil. The flow control configuration is similar to that of Fottner (1979) and Sturm *et al.* (1992), and the results of the study are presented in Chapter 7.

Chapter 3

Experimental Setup and Procedures

3.1 Introduction

The current research project was performed in the Low-Speed Turbomachinery Laboratory (LSTL) at Carleton University. All measurements were made in a variable-incidence linear cascade test section attached to an open-circuit wind tunnel. Two cascades were used during the course of the project, each consisting of nine Pratt & Whitney Pak-B airfoils. One of the cascades includes blades with active flow control.

This chapter describes the experimental setup and the measurement procedures used throughout the current experiments. The first section describes the wind tunnel, test section and cascade configurations, followed by a brief description of the calibration facilities used in the LSTL. The instrumentation, data acquisition system, and traversing mechanism are then described. The chapter concludes with a discussion of the data reduction and

uncertainty analysis procedures used.

3.2 Low-Speed Wind Tunnel

3.2.1 Wind Tunnel

A low-speed open-circuit wind tunnel has been used for the current experiments, and is shown schematically in Figure 3.1, taken from Mahallati (2003).

A radial blower fitted with a bellmouth is located at the inlet of the wind tunnel, and supplies the tunnel with a maximum flow rate of approximately 5 kg/s with a total pressure rise of about 1.2 kPa. The blower is driven by a 4-pole AC motor which is controlled by a solid-state variable-frequency controller. A honeycomb is used at the outlet of the blower to remove any swirl in the flow. The flow is then diffused through a square diffuser with an area ratio of 5.6 and a divergence angle of 19°. Five evenly spaced screens are located in the diffuser to prevent or reduce the extent of boundary layer separation. A settling chamber is located downstream of the diffuser in which 4 evenly spaced screens are used to improve the flow uniformity and to promote the dissipation of large-scale turbulence. A square-to-rectangular contraction with an area ratio of 14:1 then accelerates the flow into the test section. Additional details of the wind tunnel are given by Rodger (1992).

Static pressure taps, P_{c1} and P_{c2}, are located at the inlet and outlet of the contraction respectively and are used to monitor the wind tunnel operating condition. These taps provide reference pressures for all differential pressure transducers. With the test section in place, the maximum attainable velocity at the outlet of the wind tunnel is approximately 35 m/s, and thus the flow is essentially incompressible. The turbulence intensity at the entrance to the test section is approximately 0.4% (Mahallati, 2003).

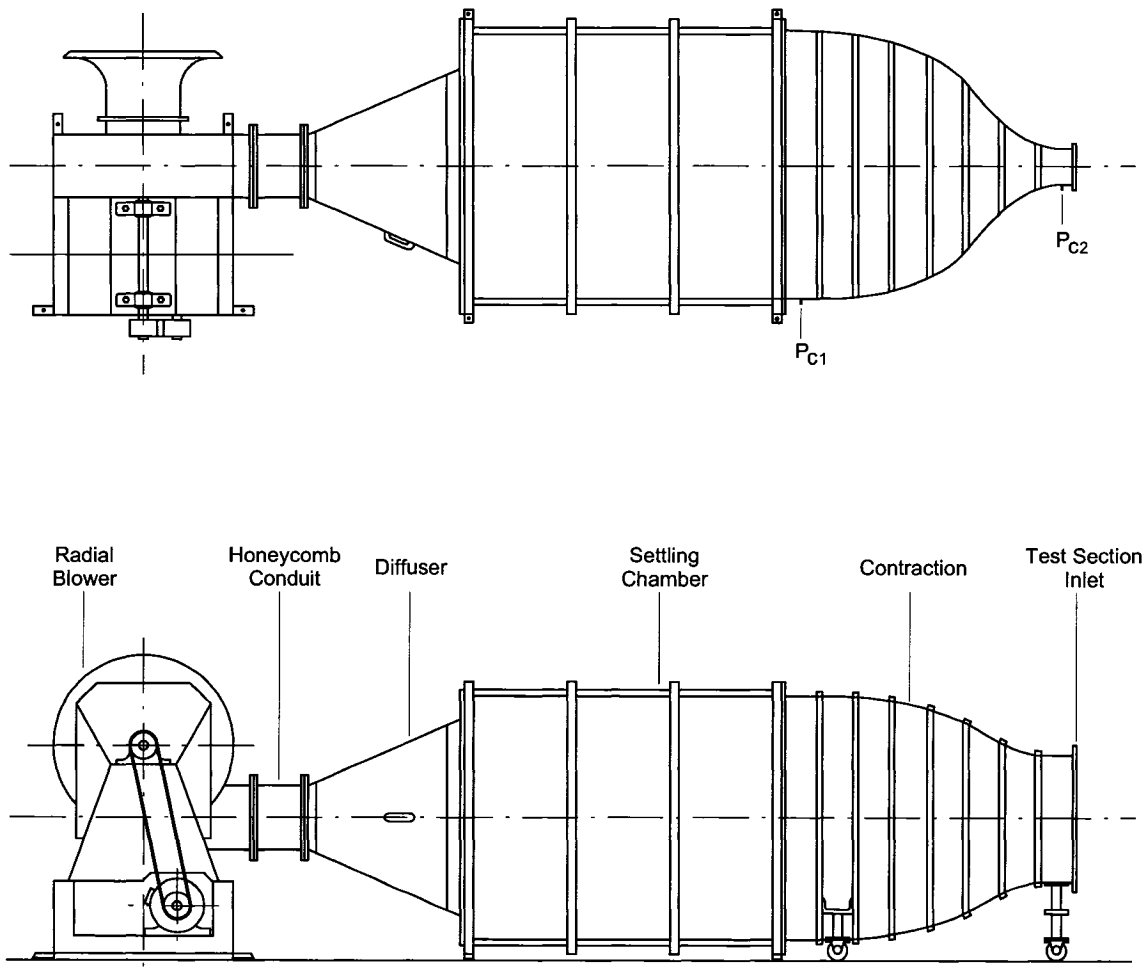

Figure 3.1: **Schematic of Low-Speed Open-Circuit Wind Tunnel (reproduced from Mahallati, 2003)**

3.2.2 Test Section

A variable-incidence linear cascade test section has been used for the current experiments, and is shown in Figure 3.2. The test section was designed by Goobie (1989).

The inlet to the test section has a rectangular cross-section 67.3cm high and 20.0cm wide. Two boundary layer bleed slots, one on each endwall, are located downstream of

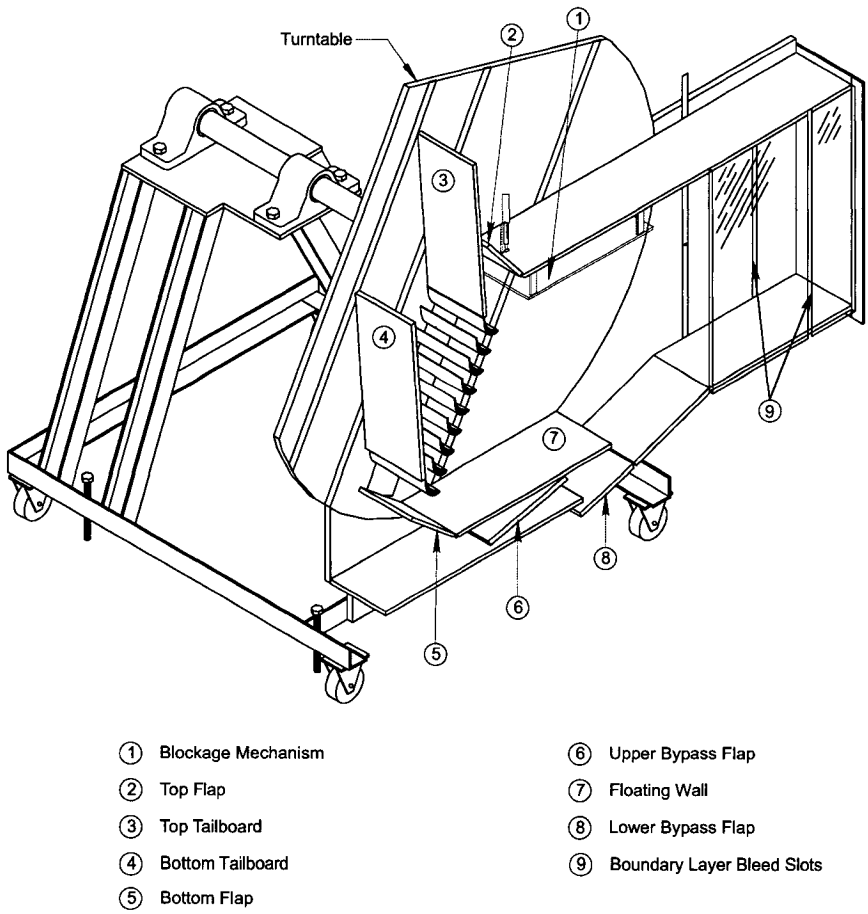

Figure 3.2: **Schematic of Variable-Incidence Linear Cascade Test Section**

the inlet to reduce the thickness of the contraction boundary layers. A linear cascade is mounted on a turntable which allows incidence variations over a range of 60°. The turntable serves as the back endwall and a removable plexiglass wall serves as the front endwall (not shown). Eight flow control devices are used to adjust the flow in and out of the cascade and are depicted in Figure 3.2. The top flap and bottom flap are primarily used to control the inlet flow uniformity, whereas the top and bottom tailboards are primarily used to adjust the outlet flow periodicity. The blockage mechanism is a suspended plate and gate arrangement that gives additional flow control at the top of the cascade, and was designed

by Mahallati (2003). The bypass flaps control the mass flow rate through the cascade. The floating wall is attached to the turntable and is adjusted to maintain a constant area flow channel entering the cascade when the turntable is rotated to vary the incidence for the cascade. However, all the present measurements were conducted at the design incidence. Traverse mechanisms are mounted to the backside of the turntable to allow movement of measurement probes across the blade span and pitch, both upstream and downstream of the cascade.

3.2.3 Baseline Cascade

The airfoil used for the baseline study, that is without flow control, is the Pratt & Whitney Pak-B profile, which represents the mid-span section of a typical high-lift low-pressure turbine blade. The Zweifel coefficient for the airfoil is 1.08. The blade surface shape has been inverse-designed to achieve the same pressure distribution at low-speed as is encountered in the compressible flow conditions of the actual engine. The cascade consists of nine blades with a solidity (B_x/S) of 1.13 and an aspect ratio (H/C) of 2.4. Details of the Pak-B cascade geometry are given in Figure 3.3.

3.2.4 Flow Control Cascade

The flow control cascade also consists of nine Pak-B blades. The middle three blades of the cascade include a slot through which air can be injected for flow control, as shown in Figure 3.4. Pressurized air is supplied to the "air supply pipe" at both ends of the blade. There are 19 holes along the upstream side of the pipe, spaced approximately 1 cm apart, that discharge air into the blade plenum. The plenum serves as a settling chamber for the flow control slot which injects air into the blade passage at approximately 52% of suction surface length ($\sim$ 64% axial chord). The slot has a width of 0.3mm (0.3% of suction surface

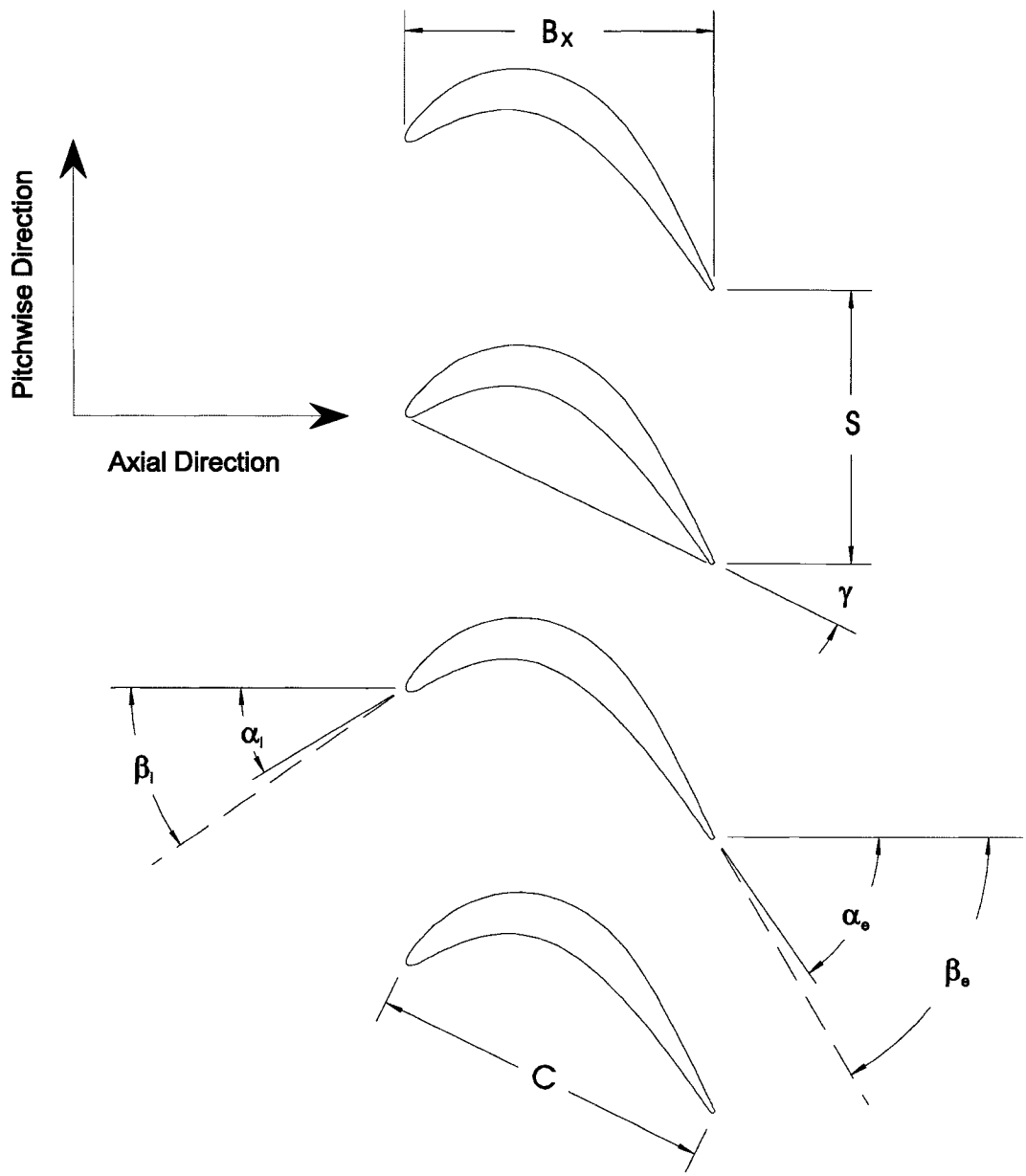

Inlet metal angle	$\beta_i = 35°$	Chord length	$C = 83.3\,\text{mm}$
Exit metal angle	$\beta_e = 60°$	Axial chord length	$B_x = 75.4\,\text{mm}$
Inlet flow angle	α_i	Blade spacing (Pitch)	$S = 66.8\,\text{mm}$
Exit flow angle	α_e	Blade span	$H = 203\,\text{mm}$
Stagger angle	$\gamma = 26°$	Trailing edge thickness	$tet = 1.1\,\text{mm}$

Figure 3.3: **Geometry of Baseline Pak-B Cascade**

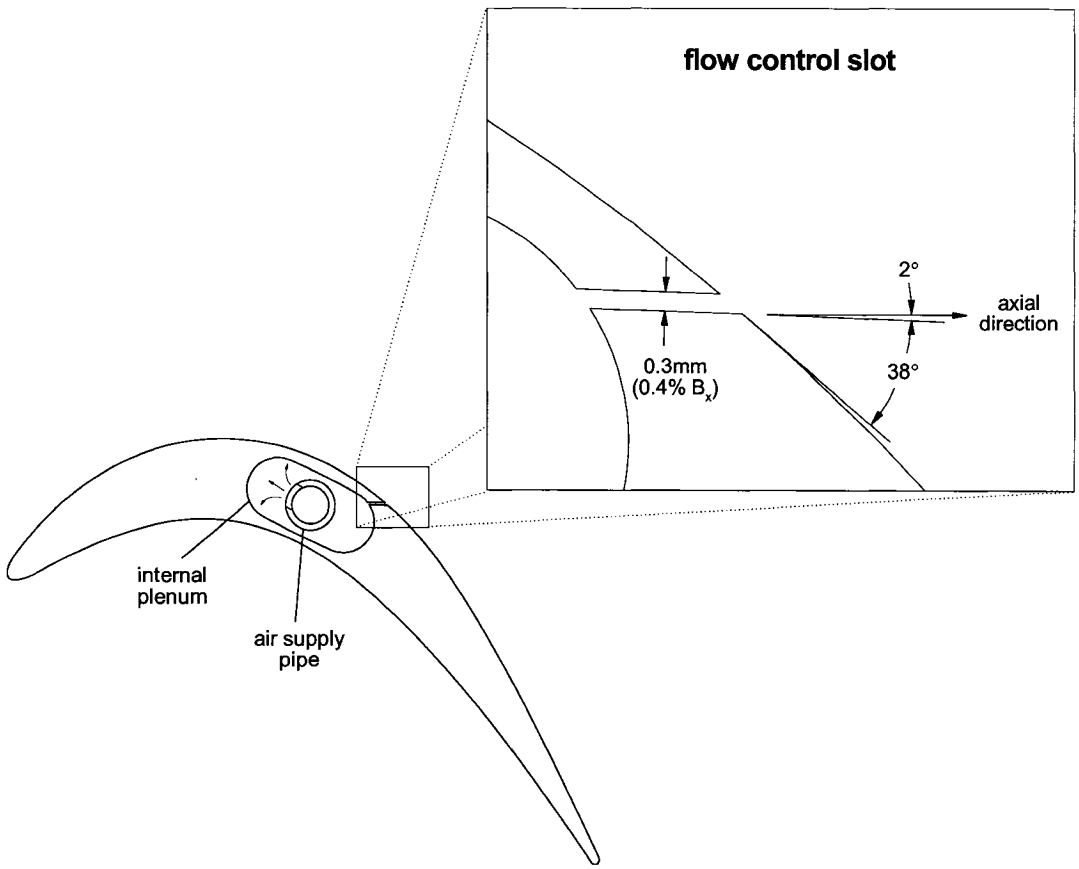

Figure 3.4: **Geometry of Active Flow Control Configuration**

length, 0.4% of axial chord), is inclined approximately 38% from the airfoil surface, and spans the middle 78% of the blade span.

3.2.5 Flow Control Air Supply System

A distribution system was designed to deliver shop air to the flow control blades. Shop air first passes through a Schrader model 3533-1000 filter/water trap to remove any impurities or moisture from the flow, followed by a Schrader model 3566-2000 pressure regulator used to control the flow rate of air to the blades. A utility hose then delivers the air to a manifold, shown in Figure 3.5. The manifold has six Swagelok model B-1RS6-A needle valves to adjust

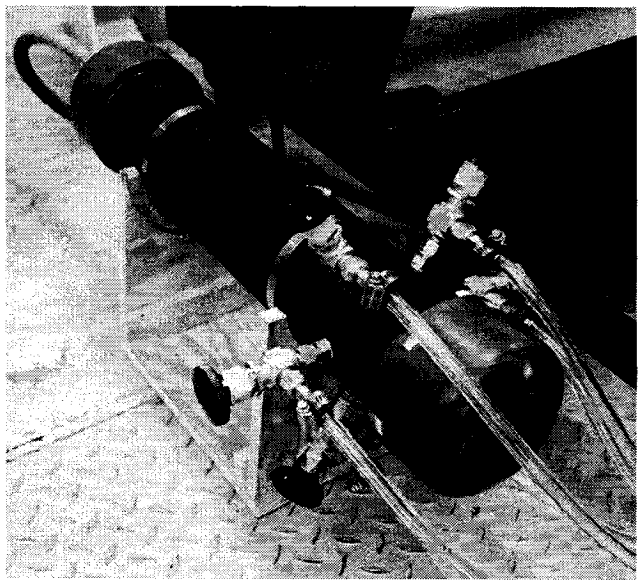

Figure 3.5: **Air Supply Manifold**

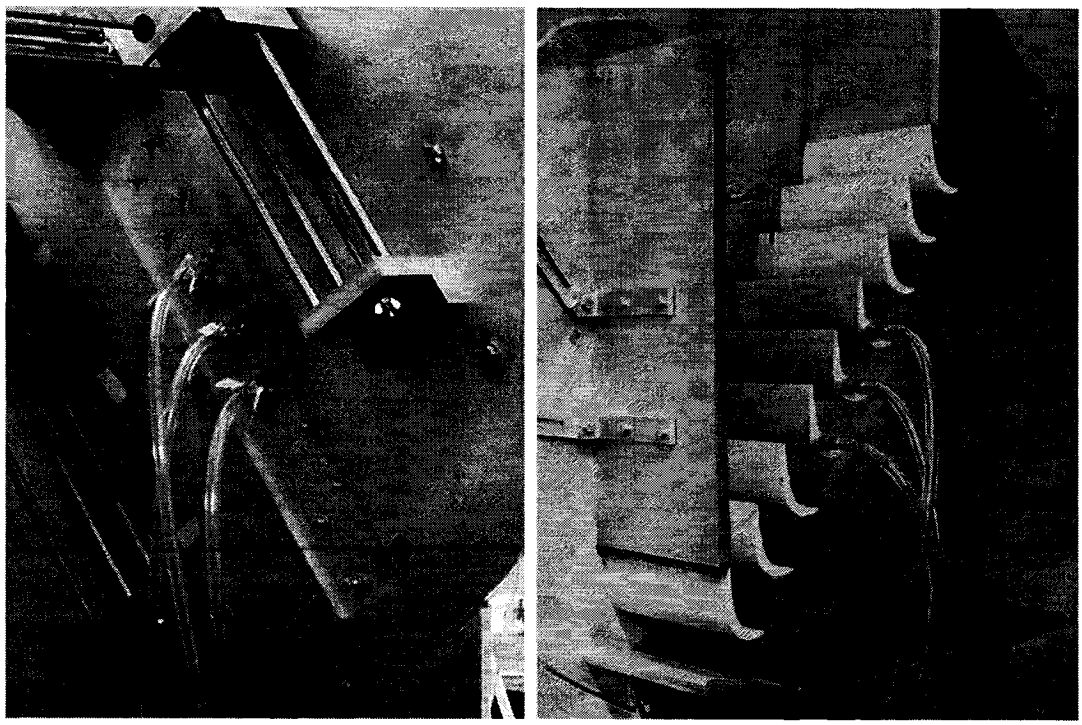

Backside Frontside

Figure 3.6: **Air Supply Line Connections**

the flow rates to each blade. Tygon vinyl tubing connects the manifold valves to the flow control blades. Figure 3.6 shows the supply line connections to the flow control blades.

3.2.6 Turbulence Generating Grids

Freestream turbulence levels in a low-pressure turbine are greater than the background turbulence level present in the wind tunnel. Turbulence generating grids are used in the LSTL to elevate the level of freestream turbulence intensity entering the cascade. The Pak-B study of Mahallati (2003) considered two separate grids, with cascade inlet turbulence intensities of 1.5% and 4.5%. For the current study, a new turbulence generating grid was designed and manufactured to produce a freestream turbulence intensity similar to the high-intensity grid of Mahallati but with a smaller turbulent length scale. The details of this new grid are deferred to Chapter 4, where a description of the grid design and resulting turbulence field are given.

3.3 Probe Calibration Apparatus

All pressure and hot-wire probes used in the current experiments were calibrated in an in-house calibration rig, shown schematically in Figure 3.7. The apparatus is a suction-type device driven by a radial vacuum blower with a throttle valve.

Filtered air enters the calibration rig through a nozzle for which the exit velocity can be varied up to 42m/s. The pressure or hot-wire probes are mounted on the arm of a two-axis turntable mechanism, which allows movement in the pitch and yaw directions. A range, in both pitch and yaw, of more than 50° can be achieved in the calibration rig. For all calibrations, the probe head was positioned at the centres-of-rotation of the two turntables. The reference pressures are measured downstream of the inlet filter panels (P_{c1}) and near

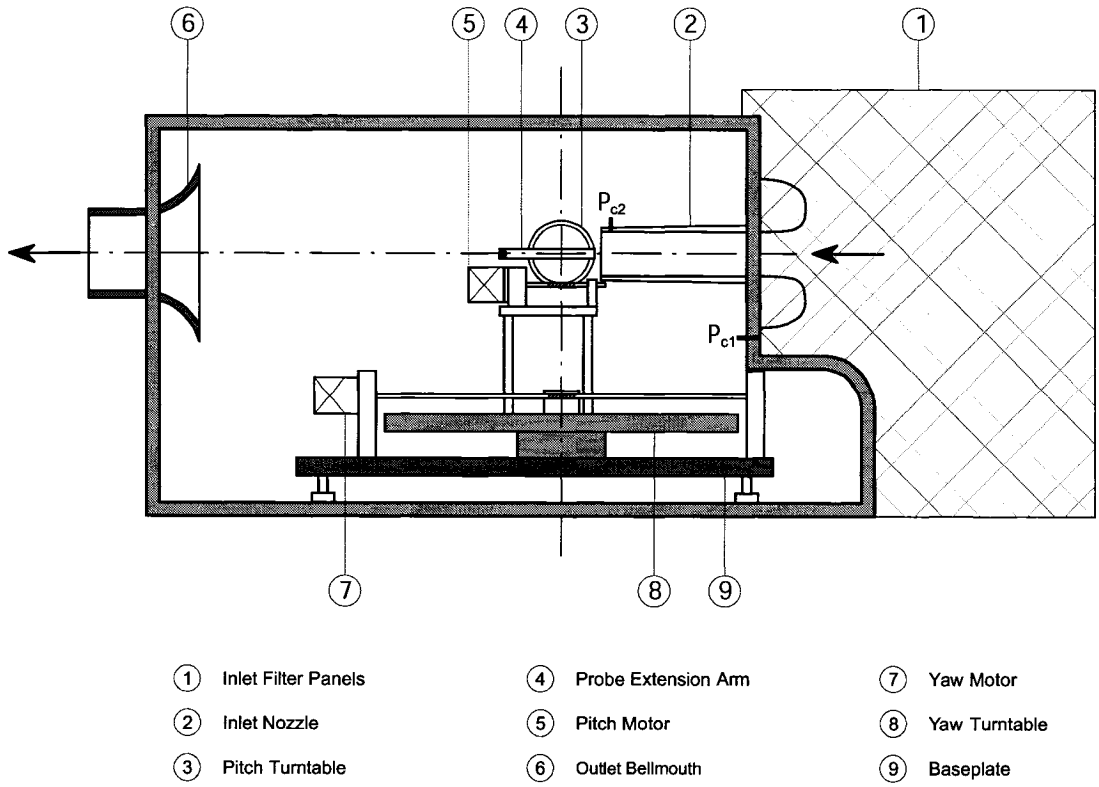

Figure 3.7: **Schematic of Probe Calibration Rig**

the exit plane of the nozzle (P_{c2}). More details of the calibration rig and nozzle flow quality are given by Benner (2003) and Mahallati (2003).

3.4 Instrumentation

3.4.1 Pressure Transducers

Differential pressure transducers were used for all pressure measurements in the current experiments. Two types of Data Instrument transducers were used, models DRAL501DN and DRAL505DN, which have operating ranges of ±250Pa and ±1250Pa, respectively.

Higher pressure ranges were measured using SensorTechnics model 113LU20D-PCB transducers, which have an operating range of ±5000Pa. All pressure transducers used have a linear relationship between the measured pressure difference, ΔP, and the output voltage, E, given by

$$\Delta P = c_1 E + c_2.$$

where c_1 and c_2 are calibration coefficients. Over a period of six months the c_1 coefficient varied by no more than 0.2%, for all transducers used. The c_2 coefficient was observed to drift from day-to-day and was adjusted for each measurement run. Calibration of the pressure transducers is described in Appendix A.

3.4.2 Hot-Wire and Hot-Film Anemometer

Thermal anemometry is based on the principles of forced-convection heat transfer. By heating a sensor to a temperature greater than the flow temperature, characteristics of the flow field can be inferred from the measured heat transfer characteristics of the sensor. For the current study, hot-wire probes have been used to measure the velocity and turbulence field downstream of turbulence generating grids, and to examine the boundary layer development over the airfoil suction surface. Surface mounted hot-film sensors have also been used to examine the state of the suction surface boundary layer by relating the heat transfer from the sensors to the surface shear stress. One of the benefits of thermal anemometry is the high frequency response, which can capture turbulent fluctuations in the flow field. A 10-channel A.A. Lab System, model AN-1003, constant-temperature anemometry system has been used.

A constant-temperature anemometer operates on the principle of keeping the sensor resistance constant. The sensor resistance, R_w, is proportional to the sensor temperature,

T_w, according to

$$R_w = R_r[1 + \alpha_r(T_w - T_r)]$$

where r refers to a reference temperature, typically $20°C$, and α_r is the sensor temperature coefficient of resistance. A feedback circuit continually adjusts the current through the sensor to keep the resistance, and hence the temperature, constant. The overheat ratio, OHR, defines the ratio of cold-to-hot sensor resistance:

$$OHR = \frac{R_w}{R_r} = 1 + \alpha_r(T_w - T_r)$$

The sensitivity of the sensor is determined by the OHR.

The basic circuitry of a constant-temperature anemometer is shown in Figure 3.8. The sensor is one leg of the Wheatstone bridge, which constitutes part of the feedback circuit. The top-of-the-bridge voltage, E_{TOB}, passes through a set of signal conditioners (Zero-Offset, Gain, and Low-Pass Filter) and the output voltage, E_{out}, is measured by the data acquisition system. From the measured output voltage, the top-of-the-bridge voltage is

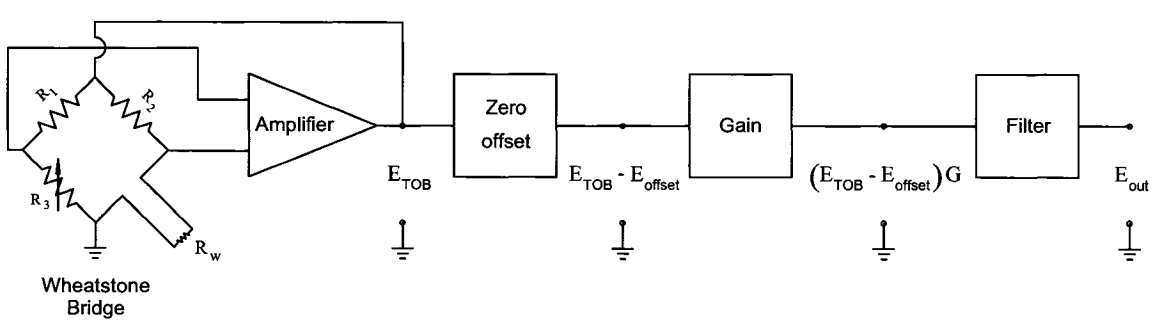

Figure 3.8: **Schematic of Constant-Temperature Anemometer Circuit (reproduced from Mahallati, 2003)**

calculated by

$$E_{TOB} = \frac{E_{out} + E_{offset}}{G}$$

where E_{offset} is the zero-offset voltage and G is the gain.

3.4.3 Digital Barometer

The ambient pressure was measured and logged in all experiments by a digital barometer. The barometer is an Omega model DPI740, which incorporates a pre-calibrated 77 to 115kPa absolute pressure transducer. The transducer has an accuracy of ±0.02% FS, a resolution of 1.016 Pa and sampling frequency of 2 Hz. The ambient pressure was used along with the wind tunnel contraction pressure and test section flow temperature to set and maintain the cascade Reynolds number.

3.4.4 Temperature Monitor

The test section operating temperature, measured inside the bypass duct, was recorded for all experiments. The recorded temperature was used to correct hot-wire measurements for temperature effects and was used along with the measured contraction pressure and ambient pressure to set the cascade operating condition. The temperature monitor used is a Omega i-series temperature/process meter, model DPi8-C24, connected to a type-T (Copper-Constantan) thermocouple.

3.5 Data Acquisition System

The data acquisition system used for the current experiments consists of a data acquisition board and a Windows-based software system.

A United Electronic Industries (UEI) model PD2-MFS-8-800/14 PowerDAQ data acquisition board was used to sample the electronic signals from the pressure transducers and anemometer. The board is a simultaneous sample-and-hold PCI card installed in an Intel Pentium II powered personal computer, and has the ability to sample at a rate of 800kHz. Eight 14-bit analog channels were used to sample the data acquisition instruments. More details of the board are given by Mahallati (2003).

The PowerDAQ board is controlled by an in-house data acquisition software system, TurboDAQ, developed by Mahallati (2003). The software is an object-oriented program designed to bring device setup, control, data acquisition, instrument calibration, and data reduction under one Windows-based environment. Details of the software are given by Mahallati (2003).

3.6 Probe Traversing Mechanism

A two-axis linear traverse mechanism is used to move measurement probes in the spanwise and pitchwise directions relative to the cascade. Two of these mechanisms are mounted on the backside of the test section turntable, one upstream and one downstream of the cascade. Each axis is driven by a 4-phase stepper motor attached to a $^1/_4-20$ threaded rod. The stepper motors are driven by a motor controller, which receives TTL signals from the host computer. The minimum attainable step size for the traverse mechanism is 0.00635 mm.

3.7 Measurement Procedures

3.7.1 Three-Hole Pressure Probe Measurements

A three-hole pressure probe has been used to characterize the mid-span flow field upstream and downstream of the cascade. The probe used for the current experiments was manufactured by Mahallati (2003) and its geometry is shown in Figure 3.9. The probe consists of three stainless steel hypodermic tubes, soldered side-by-side in a single plane. The tips of the two outer tubes are machined at a 45° angle relative to the centre tube. By virtue of the inclined pressure ports, the flow angle, dynamic pressure and static pressure can be inferred from the three measured pressures. The width of the probe tip is 3% of the blade pitch.

The measurements from a three-hole pressure probe are reduced to flow angle, ϕ, dynamic pressure coefficient, C_Q, velocity ratio, C_V, static pressure coefficient, C_{PS}, and total pressure loss coefficient, C_{P0}. These coefficients are defined as follows:

$$
\begin{aligned}
C_Q &= \frac{P_0 - P_S}{P_{0ref} - P_{Sref}} \\
C_V &= \frac{U}{U_{ref}} \\
C_{PS} &= \frac{P_S - P_{Sref}}{P_{0ref} - P_{Sref}} \\
C_{P0} &= \frac{P_{0ref} - P_0}{P_{0ref} - P_{Sref}}
\end{aligned}
$$

where ref refers to a reference condition.

For both calibration and wind tunnel measurements, the three ports were connected to three separate pressure transducers, with the reference being the contraction, or nozzle, outlet pressure, P_{c2}. Each measured port pressure, P_p (p = 1,2,3), was converted to a port

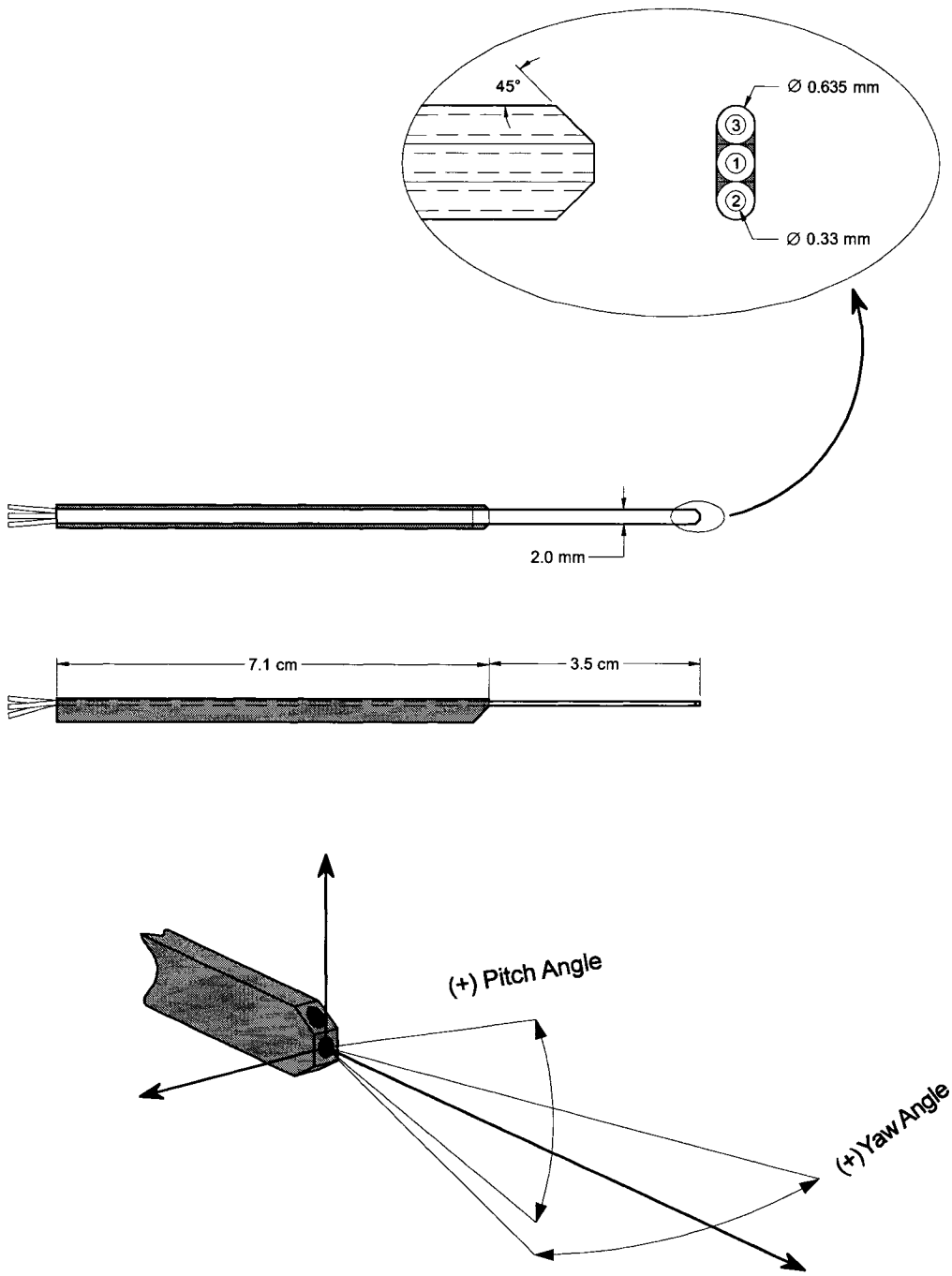

Figure 3.9: **Schematic Three-Hole Pressure Probe**

pressure coefficient, C_{Pp}, relative to a reference measurement plane, as follows:

$$C_{Pp} = \frac{P_p - P_{Sref}}{P_{0ref} - P_{Sref}} = \frac{P_p - P_{c2}}{\overline{C_Q}(P_{c1} - P_{c2})} - \frac{\overline{C_{PS}}}{\overline{C_Q}}$$

For calibration of the three-hole probe, reference dynamic and static pressure coefficients, $\overline{C_Q}$ and $\overline{C_{PS}}$, were measured in the calibration rig using pitot and static pressure probe, as described by Mahallati (2003). These reference coefficients are defined as:

$$\begin{aligned} \overline{C_Q} &= \frac{P_{0ref} - P_{Sref}}{P_{c1} - P_{c2}} \\ \overline{C_{PS}} &= = \frac{P_{Sref} - P_{c2}}{P_{c1} - P_{c2}} \end{aligned}$$

For wind tunnel experiments, the pre-calibrated three-hole probe is used to measure these reference pressure coefficients at the inlet plane of the cascade.

The three-hole probe has been calibrated using the form of calibration coefficients defined by Lewis (1966), the details of which can be found in Appendix B. For the current experiments, the probe has been calibrated in increments of 0.5° over a range of −10° to +15° of pitch. The result is a set of 6 calibration coefficients for each calibration angle, as follows:

$$\begin{aligned} K_1 &= \frac{P_1 - P_S}{P_0 - P_S} = C_{P1} \\ K_{12} &= \frac{P_1 - P_2}{P_0 - P_S} = C_{P1} - C_{P2} \\ K_{13} &= \frac{P_1 - P_3}{P_0 - P_S} = C_{P1} - C_{P3} \\ K_{23} &= \frac{P_2 - P_3}{P_0 - P_S} = C_{P2} - C_{P3} \\ K_{\phi 2} &= \frac{P_1 - P_2}{P_1 - P_3} = \frac{K_{12}}{K_{13}} \\ K_{\phi 3} &= \frac{P_1 - P_3}{P_1 - P_2} = \frac{K_{13}}{K_{12}} \end{aligned}$$

For the three-hole probe data reduction, these calibration coefficients are used in a look-up table format. Linear interpolation is used to extract data between the calibration points.

The first step of the three-hole probe data reduction procedure is to extract the flow angle, ϕ, relative to the probe axis. The flow angle coefficients, $K_{\phi 2}$ and $K_{\phi 3}$, are calculated and the smaller of the two is used to extract the flow angle from the calibration data. The flow angle is then used to extract the corresponding K_1 and K_{12} (or K_{13}) calibration coefficients. If $K_{\phi 2}$ is used to determine the flow angle, then K_{12} is used to calculate the dynamic pressure coefficient, C_Q, as follows:

$$C_Q = \frac{C_{P1} - C_{P2}}{K_{12}}$$

If $K_{\phi 3}$ is used to determine the flow angle, then K_{13} is used to calculate the dynamic pressure coefficient:

$$C_Q = \frac{C_{P1} - C_{P3}}{K_{13}}$$

The velocity ratio, C_V, is calculated from the dynamic pressure ratio as follows:

$$C_V = \sqrt{C_Q}$$

since the flow can be considered incompressible. The static pressure coefficient, C_{PS}, is then calculated using K_1, as follows:

$$C_{PS} = C_{P1} - K_1 C_Q$$

In some instances the total pressure loss coefficient, C_{P0}, is desired, and is calculated by:

$$C_{P0} = 1 - C_Q - C_{PS}$$

The reduced three-hole probe data (ϕ, C_Q, C_V, C_{PS}, and C_{P0}) are used in the data reduction procedures for the cascade performance, described in Chapter 4.

3.7.2 Blade Loading Measurements

Surface static pressure measurements, or loading measurements, have been made over the surfaces of both the baseline and flow control airfoils. For the baseline loading measurements, the cascade middle blade was replaced with an instrumented blade, which had 40 static pressure taps distributed over the airfoil surface. Of the 40 taps, 24 taps were located on the suction surface, 15 on the pressure surface, and 1 tap on the blade trailing edge. For the flow control loading measurements, the middle flow control airfoil was instrumented with 14 static pressure taps, the modifications for which were done after all the three-hole probe and hot-wire measurements were completed. Of the 14 taps, 1 tap was located upstream of the blowing slot on the suction surface, 12 were located downstream of the slot on the suction surface, and 1 tap was located on the trailing edge. The locations of the taps, which were positioned at mid-span, are shown and tabulated in Figure 3.10 for both airfoils. The suction surface location, s/SSL, is only tabulated for those taps located on the suction surface of the airfoils.

The loading data is presented in the form of a loading coefficient, C_{PL}, defined as

$$C_{PL} = \frac{P_{0i} - P_{SL}}{P_{0i} - P_{Si}}.$$

where P_{SL} is the surface static pressure, P_{0i} is the total pressure at the cascade inlet plane, and P_{Si} is the static pressure at the cascade inlet plane. In order to minimize the uncertainty associated with the loading measurements, it is desired to use the largest span of the lowest range pressure transducer possible, without exceeding the respective operating limits. Based

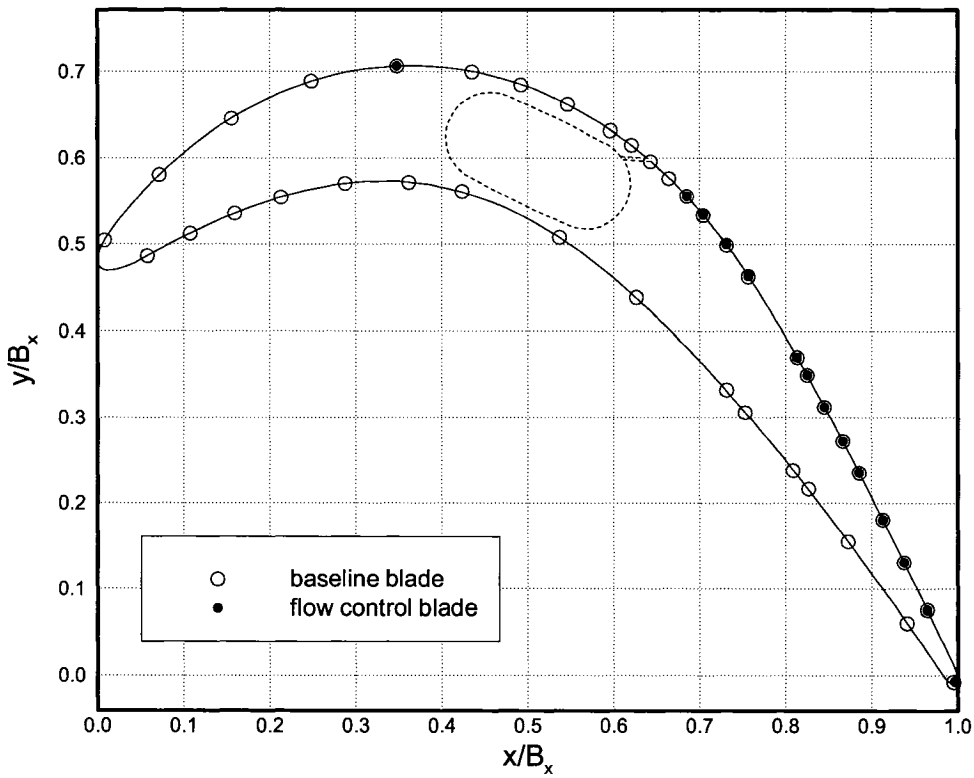

Baseline Blade

tap	x/B$_x$	s/SSL	tap	x/Bx	s/SSL
1	0.008	0.023	21	0.885	0.815
2	0.072	0.090	22	0.913	0.856
3	0.155	0.162	23	0.938	0.894
4	0.248	0.231	24	0.964	0.937
5	0.348	0.300	25	0.995	1.000
6	0.435	0.360	26	0.941	-
7	0.492	0.399	27	0.872	-
8	0.546	0.439	28	0.827	-
9	0.596	0.479	29	0.809	-
10	0.620	0.499	30	0.753	-
11	0.643	0.518	31	0.731	-
12	0.664	0.538	32	0.626	-
13	0.685	0.558	33	0.537	-
14	0.704	0.578	34	0.424	-
15	0.731	0.608	35	0.362	-
16	0.756	0.638	36	0.288	-
17	0.813	0.711	37	0.213	-
18	0.825	0.727	38	0.159	-
19	0.845	0.755	39	0.108	-
20	0.866	0.787	40	0.058	-

Flow Control Blade

tap	x/B$_x$	s/SSL
1	0.348	0.309
2	0.685	0.566
3	0.704	0.585
4	0.731	0.616
5	0.756	0.647
6	0.813	0.705
7	0.825	0.735
8	0.845	0.766
9	0.866	0.797
10	0.885	0.825
11	0.913	0.865
12	0.938	0.906
13	0.964	0.943
14	0.995	1.000

Figure 3.10: **Location of Surface Static Pressure Taps**

on this requirement, two procedures have been used to measure the loading coefficient, each of which uses a different reference pressure for the differential pressure transducers. For the first procedure, the pressure difference $P_{c1} - P_{SL}$ was measured, and the loading coefficient is then given by

$$C_{PL} = 1 - \frac{1}{\overline{C_Q}} + \frac{\overline{C_{PS}}}{\overline{C_Q}} + \frac{P_{c1} - P_{SL}}{\overline{C_Q}(P_{c1} - P_{c2})}.$$

$\overline{C_Q}$ and $\overline{C_{PS}}$ are the inlet flow reference pressure coefficients, extracted from inlet flow three-hole probe measurements and defined in Section 3.7.1. For the second procedure, the pressure difference $P_{SL} - P_{c2}$ was measured, and the loading coefficient is then given by

$$C_{PL} = 1 + \frac{\overline{C_{PS}}}{\overline{C_Q}} - \frac{P_{SL} - P_{c2}}{\overline{C_Q}(P_{c1} - P_{c2})}.$$

For a given Reynolds number, one of the procedures described above was used to allow use of the lowest range pressure transducer possible.

3.7.3 Hot-Wire Measurements

In the current experiments, single normal hot-wire probes have been used to measure the turbulence characteristics downstream of turbulence generating grids (Section 4.2) and to measure the boundary layer development over the blade suction surface (Chapter 5 and Section 7.6). Dantec type 55P01 hot-wire probes have been used, which have a 5 μm diameter, 3 mm long platinum-plated tungsten wire with gold-plated ends. The active sensor length is 1.25 mm.

The flow velocity, U, is related to the measured top-of-the-bridge voltage, E_{TOB}, by King's Law:

$$E_{TOB}^2 = a + bU^n$$

This equation stems from the relationship between the Nusselt number and the Reynolds number for forced convection heat transfer (Hinze, 1975). The coefficients a, b, and n are determined from calibration of the hot-wire. A description of the hot-wire calibration procedure is given in Appendix C.

For all hot-wire measurements, the wire temperature was kept constant at $200°C$ by the constant-temperature anemometer, which corresponds to an overheat ratio, OHR, of approximately 1.6. An anemometer gain, G, of 2 was used and the frequency response was greater than 100 kHz. To correct for any differences in flow temperature between the calibration and wind tunnel tests, the temperature correction of Bearman (1971) has been applied, as follows:

$$\left(\frac{T_w - T_0}{T_w - T_{test}}\right) E_{TOB}^2 = a + bU^n$$

where T_w is the wire temperature, T_0 is the calibration flow temperature, and T_{test} is the flow temperature during the experiments.

3.7.4 Surface-Mounted Hot-Film Measurements

An array of surface-mounted hot-film sensors has been used to examine the transition process over the suction surface of the baseline Pak-B airfoil. This was accomplished by relating the convective heat transfer from the sensors to the surface shear stress. The measured signals can be used to infer the state of the surface shear layer.

For the hot-film measurements, the middle blade of the cascade was replaced with an instrumented blade on which a TAO Systems 9010 hot-film array was placed. The hot-film array is shown schematically in Figure 3.11. The array consists of 40 evenly-spaced Nickel elements, each with a width of 0.1 mm, a length of 0.635 mm, and thickness of less than 20 μm. The sensors have been electron beam deposited onto a 50 μm thick Upilex polymide

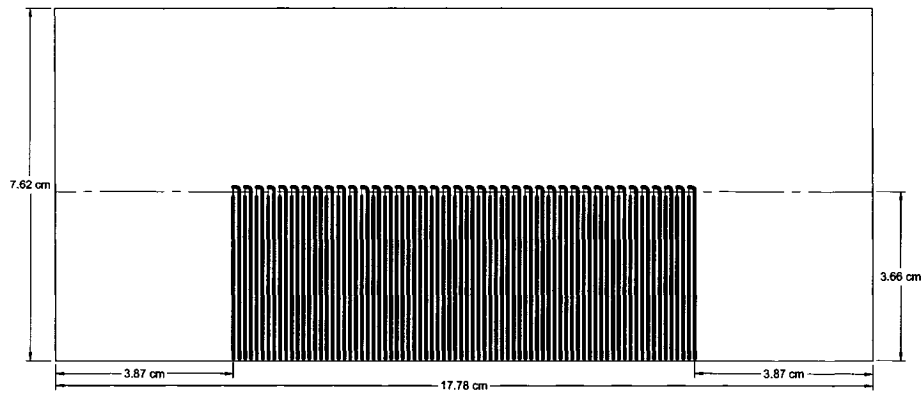

Figure 3.11: **Schematic of Surface-Mounted Hot-Film Array**

foil. The sensors are located at mid-span of the blade and are distributed over the aft 90% of the suction surface. Sensor locations over the blade surface are shown and tabulated in Figure 3.12. One of the sensors (#29) is defective, and hence was inactive for the current measurements.

Based on arguments for localized heating in a zero-pressure gradient laminar flow, Hodson (1985) argued that the wall shear stress measured with a hot-film sensor takes the form

$$\tau_w \propto \left(\frac{E^2 - E_0^2}{E_0^2} \right)^3 = \tau' \tag{3.1}$$

where τ' is referred to as the "quasi-wall shear stress", and where E and E_0 are the anemometer top-of-the-bridge voltages for wind-on and wind-off conditions, respectively. The constant of proportionality between τ_w and τ' is a function of the sensor geometry and the sensor thermal characteristics. These characteristics are slightly different for each sensor but, as described by Mahallati (2003), calibration of hot-film sensors to determine this constant of proportionality is extremely difficult and subject to large errors. For this reason, un-calibrated sensors have been used to obtain semi-quantitative results. Mahallati has used the quasi-wall shear stress to interpret the state of the surface shear layer.

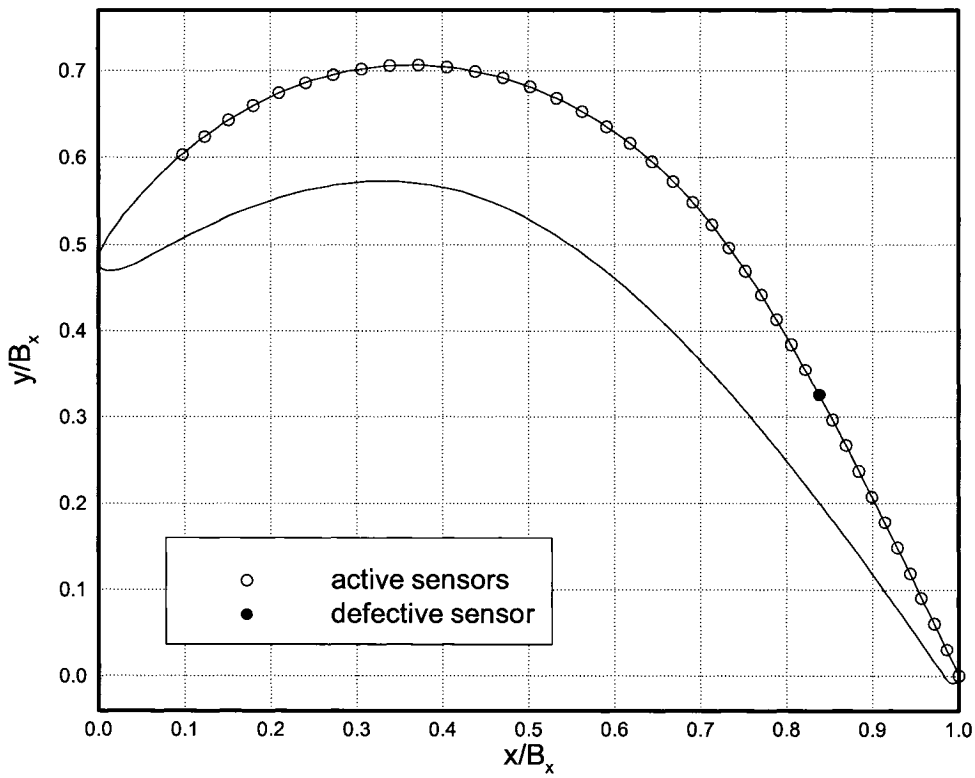

sensor	x/B_x	s/SSL	sensor	x/Bx	s/SSL
1	0.098	0.113	21	0.691	0.564
2	0.124	0.136	22	0.713	0.587
3	0.151	0.158	23	0.733	0.610
4	0.180	0.181	24	0.752	0.632
5	0.210	0.203	25	0.771	0.655
6	0.241	0.226	26	0.788	0.677
7	0.273	0.249	27	0.805	0.700
8	0.306	0.271	28	0.822	0.722
9	0.339	0.294	29*	0.838	0.745
10	0.372	0.316	30	0.854	0.768
11	0.405	0.339	31	0.869	0.790
12	0.438	0.361	32	0.884	0.813
13	0.471	0.384	33	0.899	0.835
14	0.502	0.407	34	0.914	0.858
15	0.533	0.429	35	0.929	0.880
16	0.562	0.452	36	0.944	0.903
17	0.591	0.474	37	0.957	0.925
18	0.618	0.497	38	0.972	0.948
19	0.644	0.519	39	0.986	0.971
20	0.668	0.542	40	1.000	0.993

* defective sensor

Figure 3.12: **Location of Hot-Film Sensors**

Only eight anemometer channels were available for the hot-film measurements. Therefore five sensors were used with each anemometer channel, requiring five sets of measurements for each operating condition. Ideally, each anemometer channel should be readjusted for each sensor in order to achieve the desired overheat ratio. This requires an excessive amount of time. Mahallati observed that the cold resistances of the sensors were not significantly different, and adjusted each anemometer channel to an average setting for the five sensors for which the channel was used, significantly reducing the time required to perform the measurements. The same procedure has been used for the current measurements. The sensors were grouped so that five sensors with very close cold resistances were used with a given channel. This was done to minimize differences in the overheat ratio between sensors. Table 3.1 lists the sensor groupings used and the cold resistance of each sensor prior to the measurements. These groupings are different than those used by Mahallati, who grouped sensors so that the active sensors for one measurement set were evenly spaced over the hot-film array. It was also desired to have at least one deactivated sensor between active sensors to minimize any residual heating effects from upstream sensors. For each hot-film sensor, 20480 samples were collected at a sampling rate of 40kHz and low-pass filtered at 10.4kHz. Each anemometer channel was adjusted to achieve a frequency response of 25kHz or greater for each sensor. A sensor operating temperature of approximately $200°C$ was used, which resulted in an overheat ratio of approximately 1.5. The anemometer gain was set to 1.0.

In addition to the instantaneous traces of quasi-wall shear stress, statistical quantities of the quasi-wall shear stress were used to interpret the state of the suction surface shear layer. The mean value of quasi-wall shear stress is defined as:

$$\tau'_{mean} = \frac{1}{N}\sum_{n=1}^{N}\tau'_n \tag{3.2}$$

Table 3.1: **Hot-film Array Arrangement**

	CTA channel	**1**	**2**	**3**	**4**	**5**	**6**	**7**	**8**
Bank	Sensor	1	4	9	33	27	15	19	40
1	R (Ω)	5.45	5.95	6.31	6.36	6.42	6.46	6.54	6.70
Bank	Sensor	2	7	11	32	20	38	35	28
2	R (Ω)	5.82	5.93	6.32	6.33	6.43	6.44	6.52	6.82
Bank	Sensor	6	12	14	37	22	18	25	-
3	R (Ω)	5.90	6.08	6.28	6.37	6.41	6.45	6.56	-
Bank	Sensor	31	26	17	39	10	3	23	34
4	R (Ω)	5.85	6.25	6.32	6.35	6.43	6.45	6.58	6.70
Bank	Sensor	36	24	21	16	5	8	30	13
5	R (Ω)	5.86	6.10	6.31	6.39	6.44	6.45	6.49	6.65

where N is the total number of samples collected. This mean value was normalized to eliminate an observed Reynolds number dependence. The mean quasi-wall shear stress coefficient is defined as:

$$C_{\tau'} = \frac{\tau'_{mean} - \tau'_{min}}{\tau'_{max} - \tau'_{min}} \tag{3.3}$$

where τ'_{min} and τ'_{max} are the minimum and maximum values observed over the entire hot-film array for each flow condition. The level of fluctuations in the quasi-wall shear stress signal is defined by the root-mean-square (RMS) of the signal, and is calculated by:

$$\tau'_{RMS} = \sqrt{\frac{1}{N}\sum_{n=1}^{N}(\tau'_n - \tau'_{mean})^2} \tag{3.4}$$

Although a Reynolds number dependence was observed for τ'_{RMS}, the dependence was not as pronounced as for τ'_{mean}. Also, the interpretation of τ'_{RMS} is based on the trend of the distribution over the surface, and not the magnitude. Therefore, normalization of τ'_{RMS} was not performed. The skewness of a dynamic signal represents the asymmetry of the

fluctuations about the mean. The skewness of quasi-wall shear stress is calculated by:

$$\tau'_{skew} = \frac{1}{N(\tau'_{RMS})^3} \sum_{n=1}^{N} (\tau'_n - \tau'_{mean})^3 \tag{3.5}$$

The distributions of mean, RMS, and skewness of quasi-wall shear stress have been used to interpret the state of the surface shear layer, and hence examine the transition process over the suction surface of the Pak-B airfoil.

3.8 Uncertainty Analysis

All experimental measurements are subject to errors. Although we can minimize these errors through careful design of an experiment and careful selection of instrumentation, we cannot eliminate them completely. We can however estimate the uncertainty associated with a measured value. This section describes the Single-Sample Uncertainty Analysis of Moffat (1982), which has been used to estimate the uncertainties associated with the present experimental results.

There are generally two types of errors associated with experimental measurements. Bias, or fixed, errors result when an instrument consistently measures a wrong value. Bias errors can be minimized by proper design and calibration of experimental equipment. Precision, or random, errors arise when a measured value differs under repeated measurements at the same condition. In the Single-Sample Uncertainty Analysis of Moffat, bias and precision errors are treated the same and are introduced in the form of instrument calibration errors.

The uncertainty of any measured value, f, can be estimated from instrument calibration data such that

$$\delta f = \pm 2\sigma$$

where σ is the standard deviation of the calibration data. Provided the scatter in the calibration data is normally distributed, then δf represents the uncertainty with 95% confidence. If δf is estimated for each measurement, then the uncertainty associated with any calculated value can be estimated.

Any calculated parameter, F, is a function of various fundamental parameters, f_i, such that

$$F = F(f_1, f_2, \cdots, f_N)$$

where N is the total number of fundamental parameters. Assuming that the individual f's are independent from one another, the uncertainty in F due to an uncertainty in f_i is then

$$\delta F_i = \left(\frac{\partial F}{\partial f_i}\right) \delta f_i. \tag{3.6}$$

The combined uncertainty in F due to all δf_i's is

$$\delta F = \pm\sqrt{\sum_{i=1}^{N} (\delta F_i)^2} \tag{3.7}$$

with 95% confidence.

In the present investigations, the partial derivatives in Equation 3.6 were approximated by individually perturbing the fundamental parameters within their error bands. The resulting change in the calculated parameter, ΔF_i, is the uncertainty due to f_i ($\delta F_i = \Delta F_i$). The total uncertainty, δF, is then calculated using Equation 3.7. The estimated uncertainties of the three-hole pressure probe and hot-wire measurements are presented in Appendices B and C, respectively. Uncertainties associated with any calculated results are quoted in their respective sections.

Chapter 4

Discussion of Pak-B Cascade Performance

4.1 Introduction

One of the important goals in experimental cascade studies is to simulate the important effects of the working environment in an actual engine. As stated in Chapter 2, previous low-speed investigations on the Pak-B airfoil at Carleton University matched the Reynolds numbers and inlet freestream turbulence intensities (FSTI) typically found in the low-pressure turbines (LPT) of high-bypass ratio turbofan engines. Another parameter that is believed important to the performance of LPTs is the length scale of the freestream turbulence, which is a measure of the size of the dominant energy-containing turbulent eddies. The size of these eddies may affect the boundary layer development, in particular the transition characteristics, over LPT airfoils.

The turbulence intensities and length scales present in LPTs are generated by the

upstream turbine blade rows, as well as the high turbulence produced in the combustion chamber. Typical values found in LPTs are FSTIs of 3% to 7% and length scales smaller than 10% of blade axial chord (private communication, Pratt & Whitney Aircraft, East Hartford, Connecticut, 2002). The previous study of Mahallati (2003) using the Pak-B cascade considered high FSTI (approximately 4%) with turbulent length scales larger than those found in LPTs. The turbulence generating grid used by Mahallati for his study is designated grid H1 for the current investigations. Near the completion of his work, Mahallati designed and manufactured a new turbulence generating grid, designated grid H2, to obtain the desired lower length scales at a level of FSTI similar to that for grid H1. This new grid was positioned much closer to the cascade than had previously been done. This was required to obtain the desired length scales. It was subsequently determined that grid H2 resulted in spatially non-uniform inlet flow to the cascade, due to the close proximity, which was deemed unacceptable for the current investigations. The present author designed and manufactured a new turbulence generating grid, designated grid H3, to obtain the desired lower length scales while minimizing the problems associated with a close proximity grid.

This chapter presents the results for the high-FSTI, small-length scale investigation, including the turbulence characteristics downstream of grid H3, and the performance of the Pak-B cascade using this new grid. The Pak-B study considers cases of steady inlet flow for Reynolds numbers, based on axial chord and inlet velocity, of 25000, 50000, 100000 and 150000. The turbulence characteristics of grid H3 are first presented, followed by discussions of the mid-span three-hole pressure probe measurements, surface static pressure measurements, and surface mounted hot-film measurements. The chapter concludes with a summary of the high-FSTI, small-length scale study of the Pak-B airfoil. The comparison of the grid H3 measurements with those of Mahallati (2003) using grid H1 is presented in Chapter 6, which examines the influence of turbulent length scale on the Pak-B cascade.

4.2 Grid Generated Turbulence Characteristics

4.2.1 Background

Wind tunnels are typically designed to minimize the turbulence level in the mean flow through the test section. The wind tunnel used in the current study produces an FSTI of approximately 0.4% at the entrance of the test section. The turbomachinery of gas turbine engines, particularly the turbines, experience elevated levels of freestream turbulence due to the complex flow paths, relative blade row motion, and combustion processes present upstream. Since the transition characteristics of LPTs at low Reynolds numbers are dependent on freestream turbulence levels, as described in Chapter 2, an elevation of the mean-flow turbulence level is required in linear cascade experiments. The most effective means of increasing the FSTI in a wind tunnel is by introducing a turbulence generating grid into the test section. Turbulence generating grids can be designed to obtain both a specified FSTI and a particular length scale associated with the turbulence.

Turbulence intensity is a measure of the magnitude of random fluctuations in the velocity field. At a spatial location in a turbulent flow, the instantaneous velocity can be written as

$$u(t) = U + u'(t) \tag{4.1}$$

where U is the mean velocity and $u'(t)$ is the time varying fluctuating component, from which the turbulence intensity ($FSTI$) of the velocity trace is

$$FSTI = \frac{u'}{U} \times 100\%$$

where u' is the root-mean-square of the fluctuating component of the velocity. The mean

velocity, U, is calculated by averaging the instantaneous velocity trace, and is defined as

$$U = \frac{1}{T}\int_{t_0}^{t_0+T} u(t)dt$$

which for a discrete velocity trace is

$$U = \frac{\sum_{j=1}^{N} u_j}{N}.$$

By definition, the mean of the fluctuating velocity component is zero. The velocity fluctuation level, u', is calculated as the root-mean-square (RMS) of the velocity trace, defined as

$$u' = \sqrt{\overline{u'(t)^2}} = \sqrt{\frac{1}{T}\int_{t_0}^{t_0+T} (u(t) - U)^2\, dt}$$

which for a discrete velocity trace is

$$u' = \sqrt{\frac{\sum_{j=1}^{N} (u_j - U)^2}{N-1}}.$$

The turbulent length scale of importance for the current study is the integral length scale, which represents the average size of the dominant energy-containing eddies in the flow. The longitudinal, or streamwise, integral length scale of turbulence, as defined by Hinze (1975), is

$$\Lambda_x = \int_0^{\infty} f(\Delta x) d\Delta x$$

where

$$f(\Delta x) = \frac{\overline{u'(x)u'(x+\Delta x)}}{\overline{u'^2}} \tag{4.2}$$

is the longitudinal correlation coefficient function. This correlation coefficient requires that

simultaneous measurements be made at separate locations in the flow field, which is not very practical due to interference effects and can be time consuming. For homogeneous turbulence, the longitudinal correlation coefficient function (Equation 4.2) is equivalent to the autocorrelation coefficient function, as described by Hinze (1975), which is given by

$$R(\Delta t) = \frac{\overline{u'(t)u'(t+\Delta t)}}{\overline{u'^2}}$$

and requires only data from a single measurement location.

Due to the close proximity of the grid to the cascade inlet plane, it is expected that the measured turbulence field will not be homogeneous. Taylor's Frozen-Eddy hypothesis, which assumes that the energy-containing eddies change very little in the time that it takes to be convected the distance Λ_x, allows an estimate of the integral length scale. By assuming that the flow field is a frozen structure moving at the mean velocity, Taylor's Frozen-Eddy hypothesis states that $R(\Delta t) \approx f(\Delta x)$, where $\Delta x = -U\Delta t$. The longitudinal integral length scale is then given by

$$\Lambda_x = U \int_0^\infty R(\Delta t) d\Delta t. \tag{4.3}$$

Although the turbulence level is decaying in space downstream of a grid, and the measured velocity trace from a hot-wire contains both longitudinal and lateral velocity fluctuations, Equation 4.3 is generally used to calculate the integral length scale downstream of turbulence generating grids (Roach, 1987). A typical autocorrelation function for the current study is shown in Figure 4.1. The upper limit of integration for the integral length scale calculation is taken where the autocorrelation function first reaches zero, as shown in Figure 4.1.

As described in the introduction to this chapter, an FSTI on the order of 3% to 7%, with an integral length scale smaller than 10% of blade axial chord is desired for LPT cascade studies. To obtain these desired turbulence characteristics, the method of Roach (1987) was

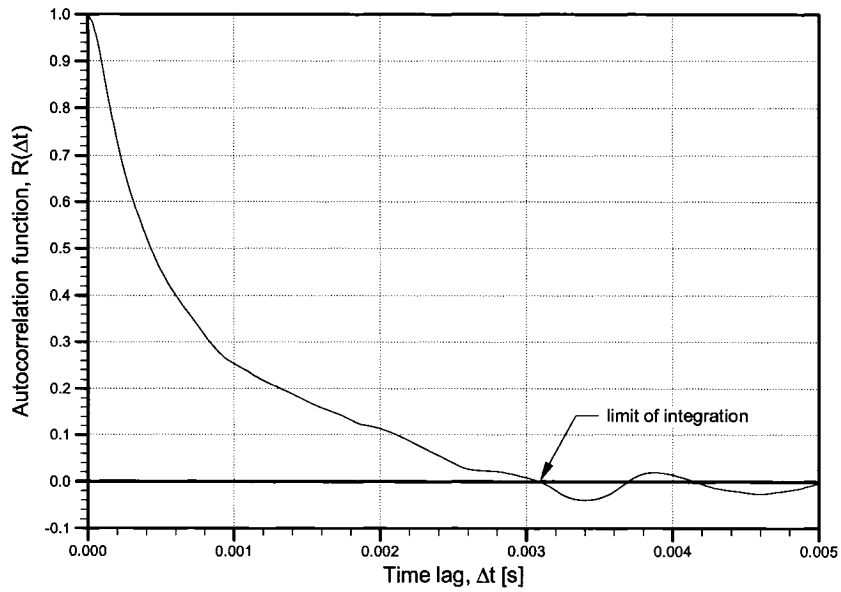

Figure 4.1: **Typical Autocorrelation Function**

used to design a new turbulence generating grid.

As described by Roach (1987), the introduction of a grid into a uniform flow has two effects on the flow field. The first is a manipulation effect that alters the turbulence spectrum by changing the scale of turbulent eddies as they pass through the grid. The second effect is a wake effect which contributes turbulent energy to the downstream flow field. The level of turbulence generated is proportional to the pressure drop across the grid. Roach found that the FSTI downstream of a grid varies as

$$FSTI = C\left(\frac{x}{d}\right)^{-5/7} \tag{4.4}$$

and the integral length scale varies as

$$\frac{\Lambda_x}{d} = I\left(\frac{x}{d}\right)^{1/2} \tag{4.5}$$

where Λ_x is the longitudinal, or streamwise, integral length scale, C and I are experimentally determined constants based on the grid type, and d is a representative grid dimension. For the types of grids used in the current experiments, the appropriate dimension, d, is the rod diameter or bar width of the grid material. The types of grids used in the Low-Speed Turbomachinery Laboratory are of the "square mesh array of square bars" (SMS) and "square mesh array of round rods" (SMR) types which, according to Roach (1987), have values of C of 0.80 and 1.13, respectively. Roach suggests that the constant I has a value of 0.20 for both grid types. The configurations of the grids used in the LSTL (grids H1, H2 and H3) are shown in Figure 4.2 as compared to the bi-planar configurations of the SMR and SMS types considered by Roach (1987). Grids H1 and H2 have a tri-planar configuration, the details of which can be found in Mahallati (2003), and grid H3 consists of a woven bi-planar arrangement.

Another, more recent set of correlations useful for the design of turbulence generating grids are those proposed by Praisner (private communication, 2003) which are

$$FSTI = 1.12\left(\frac{x}{d}\right)^{-0.675} \tag{4.6}$$

and

$$\frac{\Lambda_x}{d} = \left(\frac{x}{d}\right)^{0.20}. \tag{4.7}$$

These correlations do not distinguish between grid types, and have been correlated based on data from round-rod and square-bar grids.

Roach suggests that the grid mesh length, M (shown in Figure 4.2), should be less than 10% of the smallest test section dimension (width or height) to obtain uniform downstream flow, and the grid porosity should be greater than 50% to avoid flow instabilities. Roach also states that at least 10 mesh lengths downstream of the grid are required to obtain

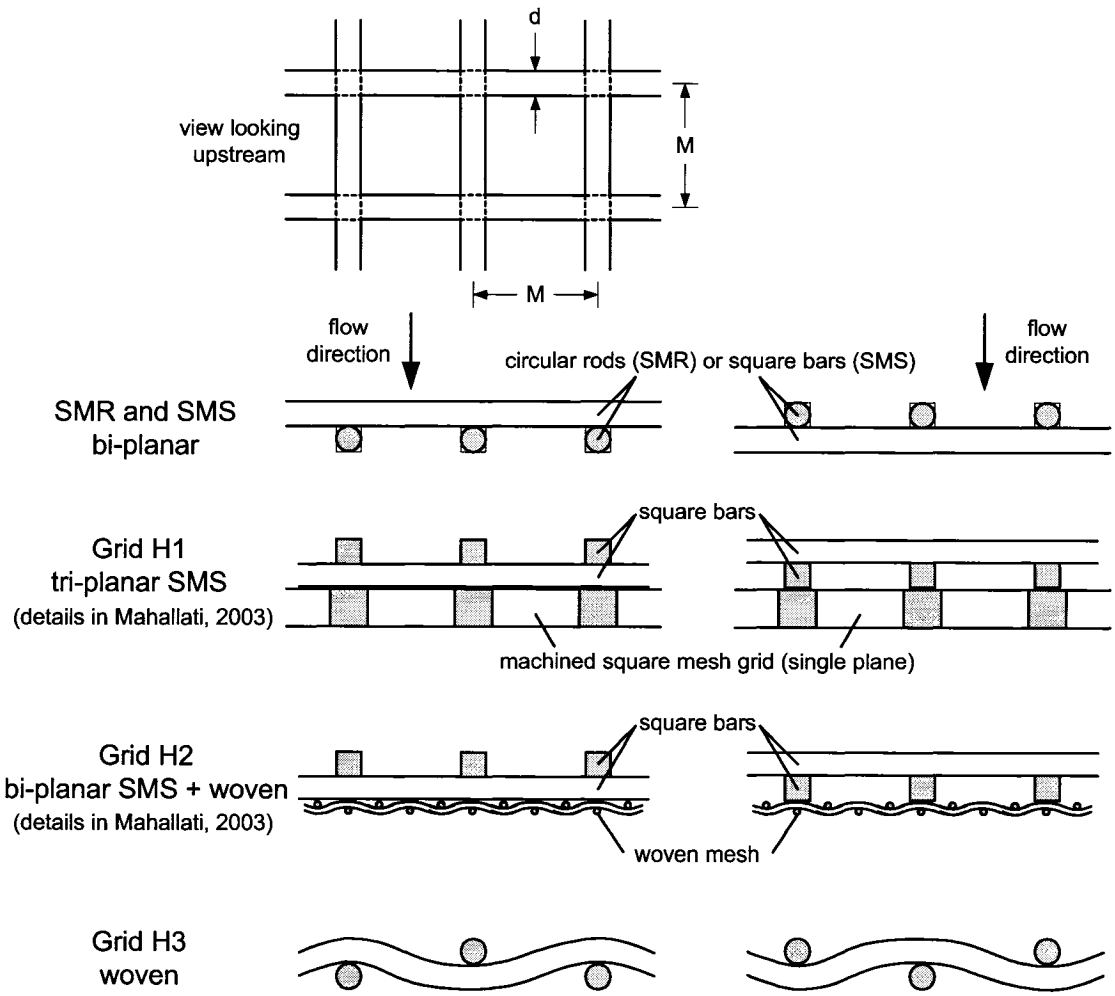

Figure 4.2: **Configurations of Turbulence Generating Grids**

homogeneous flow. The measurements described in the next section show that more than 10 mesh lengths may be required for certain grid arrangements.

Based on the above correlations and design guidelines, it was found that to achieve the desired levels of FSTI and integral length scale the grid must be placed closer to the cascade than had previously been done. The locations within the test section of the various turbulence generating grids are shown in Figure 4.3. The initial low-length scale grid of

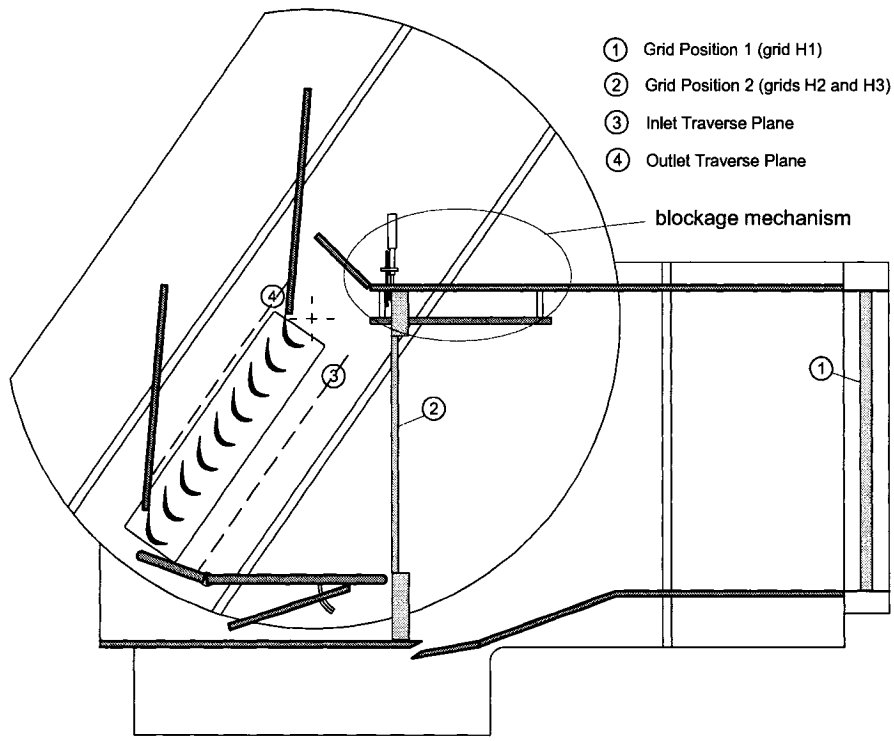

Figure 4.3: **Location of Turbulence Generating Grids Within Test Section**

Mahallati (grid H2) had strong non-uniformities in the downstream flow field which did not have adequate distance to mix out before entering the cascade. Also, the test section blockage mechanism, used to adjust the flow uniformity near the top of the cascade (shown in Figure 4.3), had been removed. The non-uniformity of the flow downstream of grid H2 is documented in Appendix D. The new low-length scale grid (grid H3) was intended to reduce the flow uniformity problems associated with grid H2 by using a smaller mesh size and by incorporating the test section blockage mechanism into the design. Details of the geometry for grid H3 are shown in Figure 4.4. Hot-wire measurements have been made to characterize the turbulence intensity and length scale downstream of grid H3, and are described in the following sections.

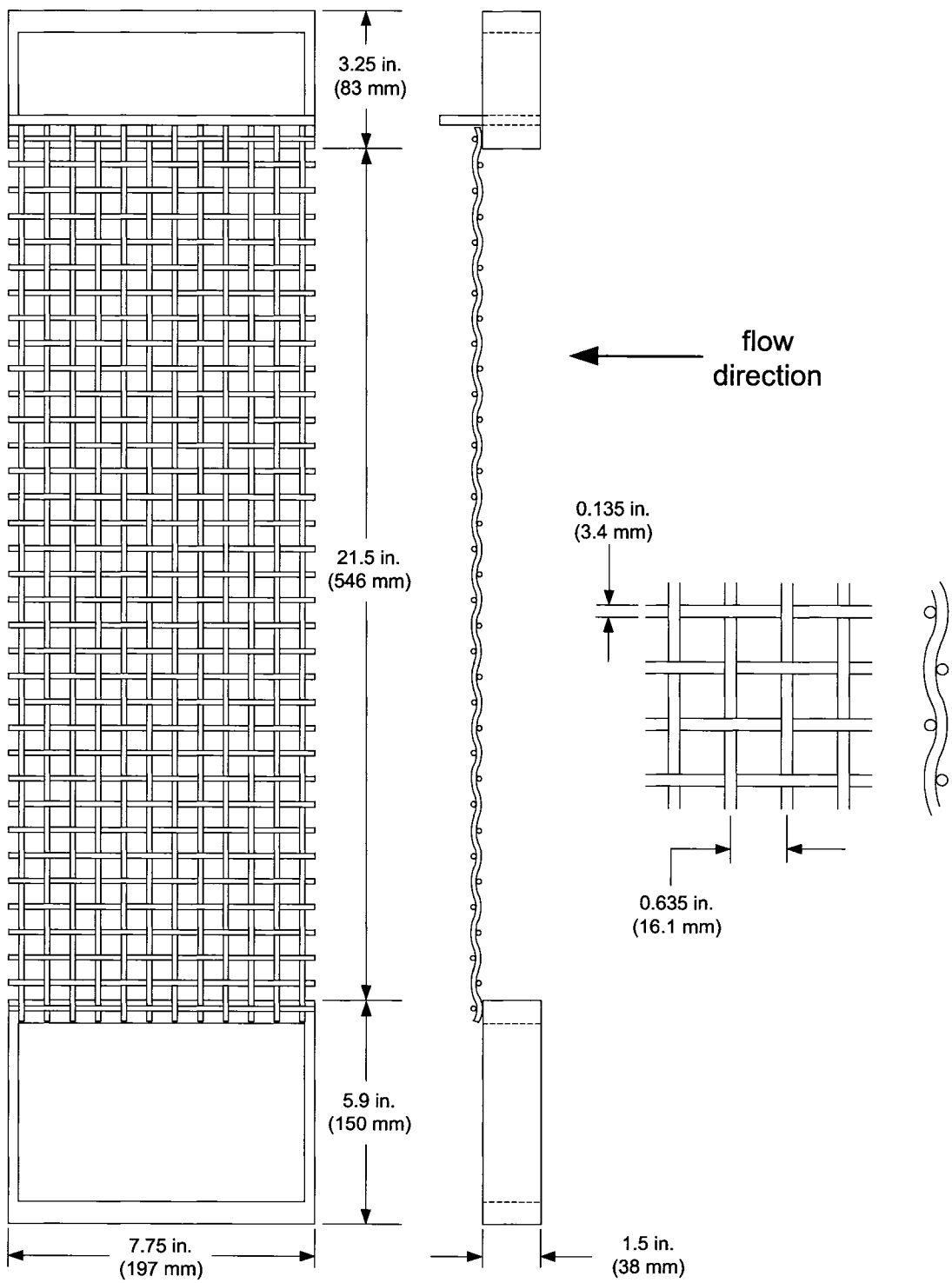

Figure 4.4: **Schematic of Turbulence Generating Grid H3**

4.2.2 Freestream Turbulence Intensity Measurements

The freestream turbulence intensity characteristics of grid H3 have been measured using a single normal hot-wire at several measurement planes downstream of the grid. During the development of grid H3, measurements were made with the grid located at the test section inlet plane (designated Grid Position 1 in Figure 4.3). The final position of grid H3 (designated Grid Position 2) is located closer to the cascade, and is also shown in Figure 4.3. Figures 4.5 and 4.6 show the decay of FSTI downstream of the grid, where the cascade middle blade leading edge is located at approximately 100 x/d (or 21 x/M) downstream of Grid Position 2. Figure 4.5 shows the FSTI measurements made downstream of grid H3 with it mounted in both positions 1 and 2. The circular symbols in Figure 4.5 show measurements made with the grid at the test section inlet (Grid Position 1) while the "+" symbols, along with the data shown in Figure 4.6, were made with the grid in its final location (Grid Position 2). The traverse planes for the "Grid Position 2" measurements (parallel to the Inlet Traverse Plane shown in Figure 4.3) were inclined 55° from the streamwise/horizontal direction. Traverses along these planes result in measurements for a range of streamwise locations downstream of the grid. The scatter in the "Grid Position 2" measurements is partly due to slight non-uniformity of the flow entering the cascade, and due to the potential effect of the blades near the cascade inlet plane. The "Grid Position 2" location is very near the cascade and does not allow for complete mixing ahead of the cascade. This suggests that Roach's guideline for grid proximity (minimum 10 mesh lengths) is not adequate for woven-mesh type grids, seeing as non-uniformities are present at the cascade middle blade leading edge (approximately 21 mesh lengths downstream of the grid). Three-hole pressure probe measurements presented in Section 4.3.3 also show non-uniformities due to the close proximity of grid H3 to the cascade.

The decay of FSTI downstream of grid H3, for mean velocities of 5m/s and 10m/s,

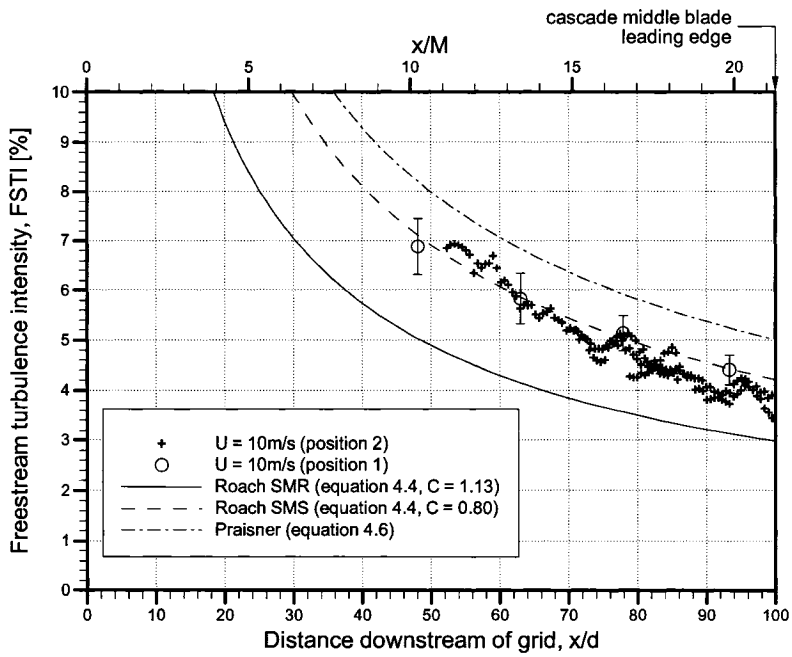

Figure 4.5: **Turbulence Intensity Characteristics of Grid H3 (a)**

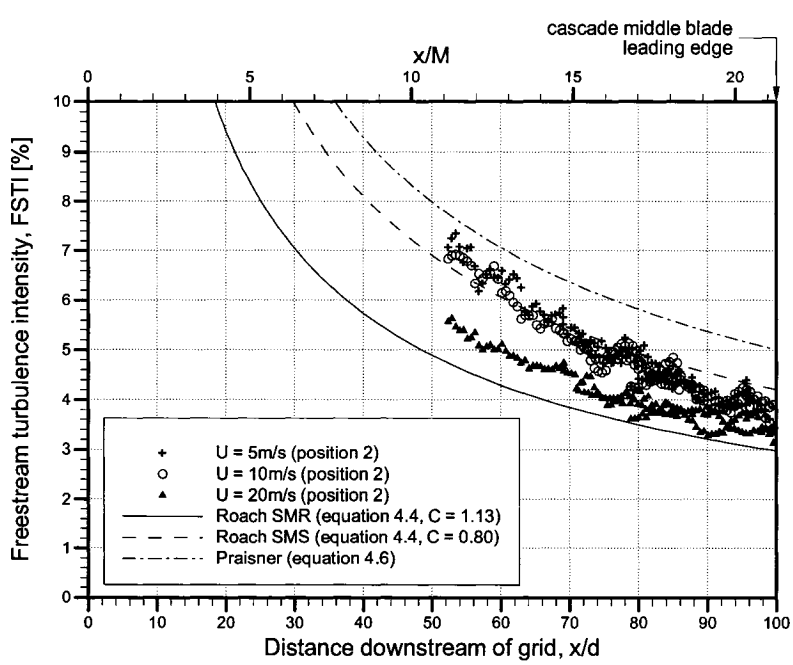

Figure 4.6: **Turbulence Intensity Characteristics of Grid H3 (b)**

follows more closely Roach's square bar correlation (SMS) than that for round rods (SMR) of which the grid consists. This is likely due to the woven-mesh style of the grid, as opposed to the bi-planar style described by Roach (1987) for SMR grids (shown in Figure 4.2).

In Figure 4.6, it is clear that there is a Reynolds number dependence for the FSTI. The FSTI at the leading edge of the cascade middle blade is approximately 3.9% for cascade inlet velocities of 5m/s and 10m/s, which correspond to grid Reynolds numbers based on rod diameter, Re_d, of approximately 1150 and 2300, respectively. The FSTI for 20m/s inlet velocity ($Re_d = 4600$) is approximately 3.5%. The grid Reynolds numbers encountered in the current experiments are greater than those for which Roach (1987) presents a Reynolds number dependence ($Re_d < 1000$). Other factors that may affect the Reynolds number dependence of grid H3 are the grid porosity (62%) and the close proximity of the grid to the test section flow control surfaces, which have different settings for different Reynolds numbers. The uncertainty in FSTI at the leading edge of the cascade middle blade is estimated at ±0.5%.

4.2.3 Integral Length Scale Measurements

The integral length scale characteristics of grid H3 have been calculated using the method described in Section 4.2.1 and are shown in Figures 4.7 and 4.8. Again, the circular symbols in Figure 4.7 indicate measurements taken with the grid in "Grid Position 1" and the "+" symbols indicate measurements taken with the grid in "Grid Position 2". Despite the scatter in the data, Praisner's correlation (Equation 4.7) appears to give the best agreement for this grid. The large scatter in the data is believed to result from the non-uniformity and non-homogeneity of the flow downstream of the grid.

Figure 4.9 shows two autocorrelation functions calculated from the same velocity trace, each of which uses a different subset of the velocity trace data. The solid line autocorrelation

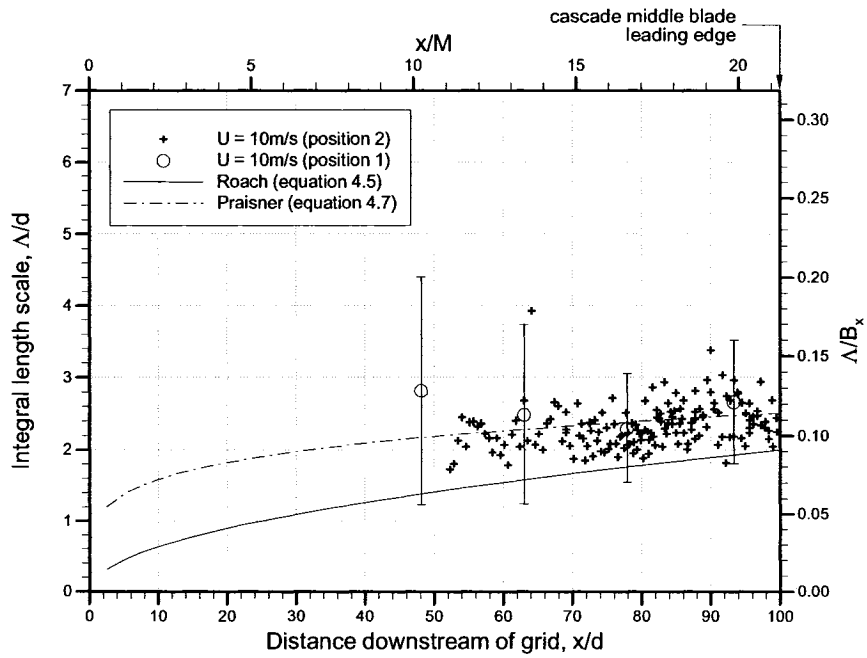

Figure 4.7: **Integral Length Scale Characteristics of Grid H3 (a)**

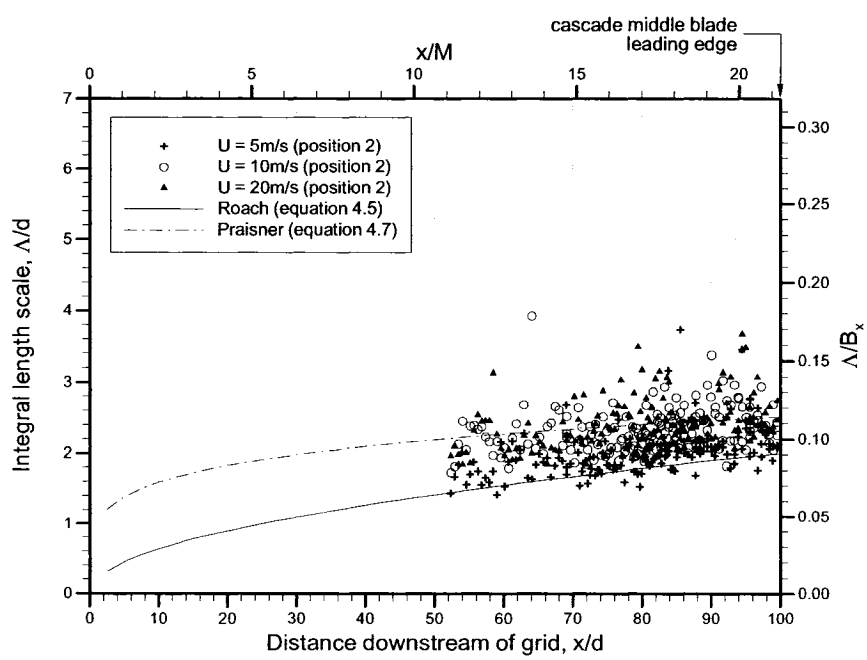

Figure 4.8: **Integral Length Scale Characteristics of Grid H3 (b)**

function smoothly decreases to zero, which is typical of a well behaved (correlated) turbulent flow. The dashed line autocorrelation function indicates that the velocity trace data is correlated over a much longer period of time, which results in an integral length scale almost double that of the solid line autocorrelation function (Λ/d of 3.55 compared with 1.95 for the solid line curve). It is reminded that the integral length scale is calculated by integrating the autocorrelation curve. The shape of the dashed line autocorrelation curve suggests a numerical problem due to non-homogeneity and possibly due to organized vortex shedding from the grid bars. It was found that using a smaller set, or window, of data alleviated this problem. For the data presented in Figures 4.7 and 4.8, the velocity trace measured at a single point was sub-divided, with the integral length scale being calculated for each sub-set and subsequently averaged. Each measurement point consisted of 65536 samples (2^{16}) which were divided into 8 windows of 8192 samples (2^{13}). This size of window resulted in similar integral length scales for each window of data within a single velocity

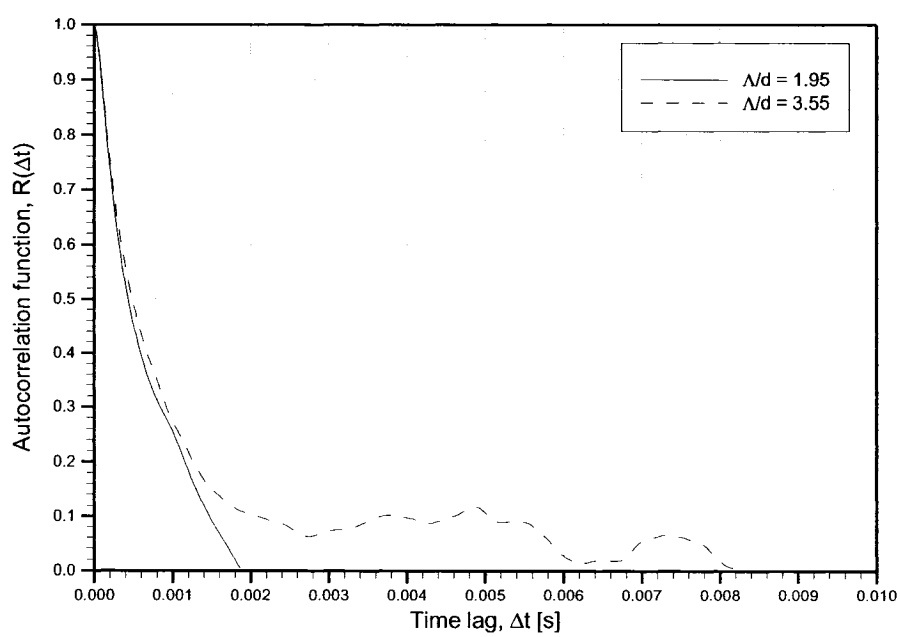

Figure 4.9: **Autocorrelation Function Comparison**

trace.

The goal of grid H3 was to obtain turbulent length scales on the order of 10% of axial chord, or lower. As seen in Figures 4.7 and 4.8, the integral length scale at the leading edge of the cascade middle blade ($x/d = 100$) is approximately 11% of axial chord, with an uncertainty estimated at $\pm 4\%$ of axial chord. Turbulence characteristics of grid H1 (high FSTI, large length scale grid) were also measured for comparison to grid H3. It was found that the FSTI for grid H1 is approximately 3.8% at the cascade inlet, with an integral length scale of approximately 32% of axial chord. The similar values of FSTI allow a comparison of the Pak-B cascade performance for different turbulent length scales. Cascade measurements using grids H1 and H3 have been used to study the performance of the Pak-B airfoil for relatively high FSTI, while isolating the effect of integral length scale. These measurements are presented in Chapter 6.

4.3 Cascade Pressure Measurements

4.3.1 Introduction to Pressure Probe and Loading Measurements

For the current study, a three-hole pressure probe was traversed upstream and downstream of the cascade to examine the mid-span behavior of the Pak-B airfoil. From these measurements, the pressure losses across the cascade have been calculated. Surface static pressure measurements have also been made over both the pressure and suction surfaces of the cascade middle blade. The surface static pressure distribution over the airfoil shows differences in blade lift, or load, between different operating conditions.

The following sections describe the cascade pressure measurement results for the Pak-B airfoil using the new small length scale turbulence generating grid (grid H3). As described

in the previous section, grid H3 produces an FSTI of approximately 3.9% and an integral length scale of approximately 11% of axial chord at the leading edge of the cascade middle blade. First, the data reduction procedures for the mid-span blade performance is presented, followed by discussions of the cascade flow quality, the surface loading distributions, the downstream wake profiles, the mixed-out profile losses, and the mixed-out outlet flow deviation angles.

4.3.2 Data Reduction Procedures for Mixed-Out Flow Conditions

4.3.2.1 Mixing Analysis

The following sections describe the performance calculation procedures for mid-span three-hole pressure probe measurements in a low-speed turbine cascade. Three-hole pressure probes measurements have been made at 1.2 axial chord lengths upstream and 0.5 axial chord lengths downstream of the cascade, at mid-span (see Figure 4.10 for traverse plane locations). From these measurements, the flow angle, ϕ, the dynamic pressure coefficient, C_Q, and the static pressure coefficient, C_{PS}, have been calculated based on the method described in Section 3.7.1. Downstream of the outlet measurement plane, the wakes produced as a result of the boundary layer development over the airfoil surfaces continue mixing until they reach a fully mixed-out condition. This mixing is due to viscous shear and turbulence. The mixed-out flow parameters are calculated using a constant-area mixing analysis and the following sections will present the derivation of mixed-out flow angle (α_m), mixed-out pressure coefficients (C_{Qm}, C_{PSm}, and C_{P0m}), mixed-out profile loss coefficient (Y_m), and axial-velocity ratio (AVR).

The calculation of mixed-out flow parameters is based on the analysis of a control volume extending between the downstream measurement plane (e) and the far-downstream

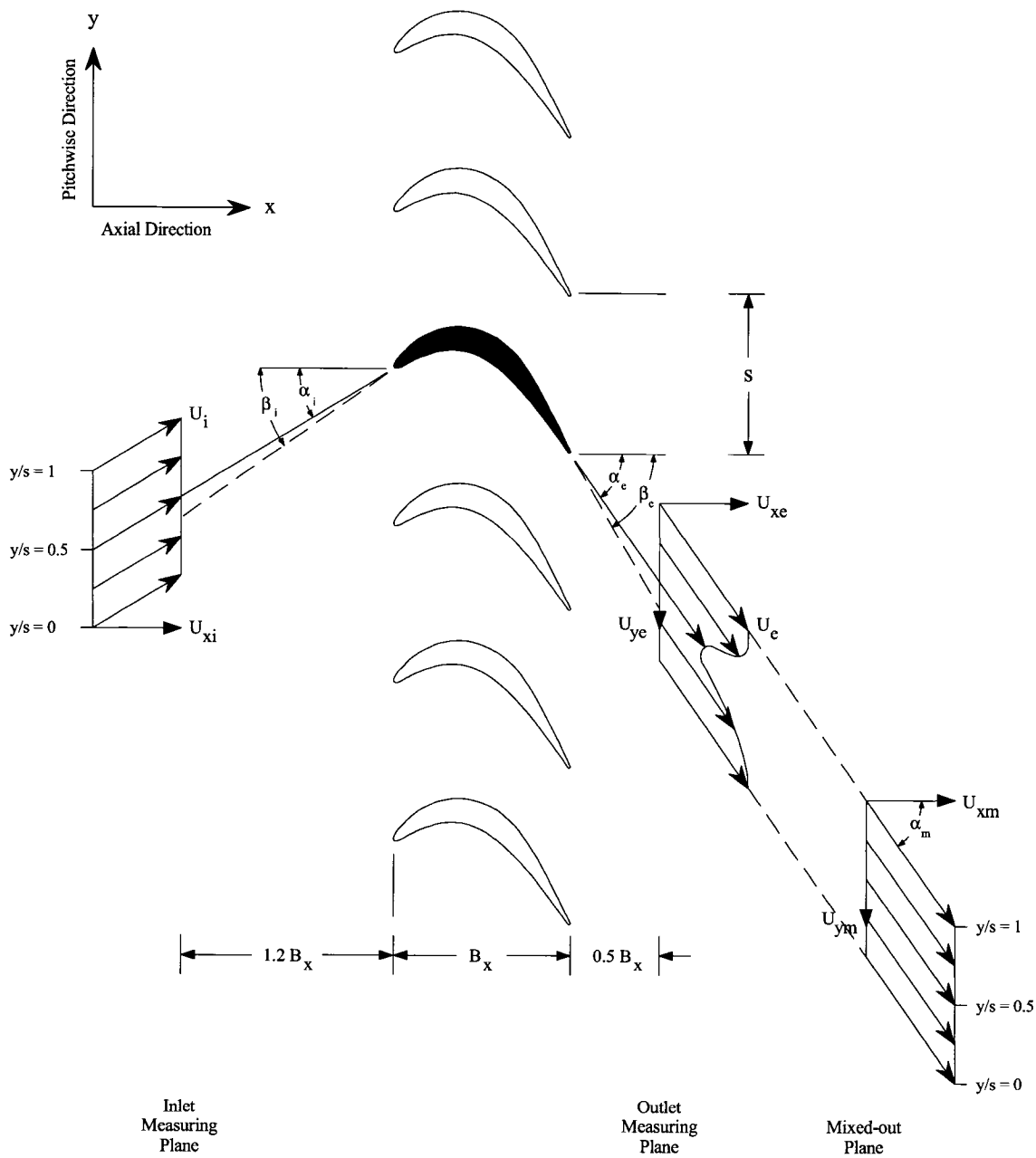

Figure 4.10: **Nomenclature For Mixing Analysis**

mixed-out plane (m). The locations of the measurement planes, along with the co-ordinate directions and sign conventions used in the analysis, were shown in Figure 4.10. As described by Denton (1993), the process by which the mixing occurs does not need to be known. As long as the mixed-out plane is assumed far-downstream where the flow has become uniform, the result is independent of the details of the mixing process. The control volume extends one blade spacing in the pitchwise direction, as shown in Figure 4.10. Absolute flow angles are required for the analysis, and are obtained from

$$\alpha_i = \beta_i + i \tag{4.8}$$

$$\alpha_e = \beta_e + \delta_e \tag{4.9}$$

where i is the inlet flow incidence angle, δ_e is the outlet flow deviation angle, $\beta_i = 35°$ and $\beta_e = -60°$ are the blade inlet and outlet metal angles, respectively.

4.3.2.2 Control Volume Relations

For the constant-area mixing analysis between the outlet measurement plane and the mixed-out plane, the mass conservation and linear momentum equations are applied. The energy equation is not required since the flow is assumed incompressible and adiabatic. The flow is assumed incompressible since the maximum flow velocity encountered in the current experiments is approximately 48m/s, which corresponds to a Mach number of approximately 0.14. White (1994) shows that density variations are negligible if the flow velocity is below 30% of the speed of sound (Mach number of 0.3).

The mass conservation equation for a control volume is

$$\int_{CV} \frac{\partial \rho}{\partial t}\, dV + \int_{CS} \rho(\vec{U} \cdot \vec{n})\, dA = 0 \tag{4.10}$$

and the linear momentum equation is

$$\sum \vec{F} = \frac{d}{dt}\left(\int_{CV} \vec{U}\rho\, dV\right) + \int_{CS} \vec{U}\rho(\vec{U}\cdot\vec{n})\, dA \tag{4.11}$$

where CV and CS refer to "control volume" and "control surfaces", respectively. The derivation of these relations, based on the Reynolds Transport Theorem, can be found in White (1994).

4.3.2.3 Mass Conservation

The control volume used for the mixed-out flow calculation is assumed to have periodic streamwise control surfaces. The mass conservation equation for the control volume (Equation 4.10), assuming two-dimensional steady-state flow, becomes

$$\int_0^S \rho u_{xm}\, dy - \int_0^S \rho u_{xe}\, dy = 0.$$

By virtue of the definition of mixed-out values, and assuming incompressible flow, the mixed-out axial velocity is

$$u_{xm} = \int_0^1 u_e \cos\alpha_e\, d(\frac{y}{S}). \tag{4.12}$$

For the purpose of applying the measured downstream data, which are in coefficient form, Equation 4.12 is divided by the cascade inlet velocity, resulting in

$$C_{Vxm} = \int_0^1 C_{Ve} \cos(\alpha_e)\, d(\frac{y}{S}). \tag{4.13}$$

4.3.2.4 Axial Momentum Balance

The axial, or x-direction, momentum balance consists of momentum fluxes through the outlet measurement and mixed-out planes only. By definition, there is no momentum flux through the upper and lower control volume surfaces, and the pressure forces on these surfaces are assumed identical due to the periodicity of the flow. From Equation 4.11, the linear momentum balance in the axial direction is

$$\int_0^S P_{Se}\,dy - \int_0^S P_{Sm}\,dy = \int_0^S u_{xm}\rho u_{xm}\,dy - \int_0^S u_{xe}\rho u_{xe}\,dy.$$

Recalling that the flow is incompressible and that the mixed-out values are constant, and inserting Equation 4.12 for the mixed-out axial velocity, the mixed-out static pressure is

$$P_{Sm} = \int_0^1 P_{Se}\,d(\frac{y}{S}) - \rho\left[\int_0^1 u_e\cos\alpha_e\,d(\frac{y}{S})\right]^2 + \rho\int_0^1 (u_e\cos\alpha_e)^2 d(\frac{y}{S}). \tag{4.14}$$

Dividing through by the cascade inlet dynamic pressure, Equation 4.14 becomes

$$\frac{P_{Sm}}{\frac{1}{2}\rho u_i^2} = \int_0^1 \frac{P_{Se}}{\frac{1}{2}\rho u_i^2}\,d(\frac{y}{S}) - 2\left[\int_0^1 C_{Ve}\cos\alpha_e\,d(\frac{y}{S})\right]^2 + 2\int_0^1 C_{Qe}\cos^2\alpha_e\,d(\frac{y}{S}). \tag{4.15}$$

4.3.2.5 Pitchwise Momentum Balance

The pitchwise, or y-direction, momentum balance is the third, and last, governing equation required to calculate the mixed-out flow parameters. Recalling that the pressure forces on the upper and lower surfaces of the control volume are identical due to the flow periodicity assumption, the pitchwise momentum equation is

$$0 = \int_0^S u_{ym}\rho u_{xm}\,dy - \int_0^S u_{ye}\rho u_{xe}\,dy.$$

For incompressible flow and constant mixed-out values, and inserting Equation 4.12 for the mixed-out axial velocity, the mixed-out pitchwise velocity becomes

$$u_{ym} = \frac{\int_0^1 u_e^2 \sin(2\alpha_e) d(\frac{y}{S})}{2\int_0^1 u_e \cos\alpha_e d(\frac{y}{S})}. \tag{4.16}$$

Normalizing by the inlet flow velocity, u_i, Equation 4.16 can then be written as

$$C_{Vym} = \frac{\int_0^1 C_{Qe} \sin(2\alpha_e) d(\frac{y}{S})}{2\int_0^1 C_{Ve} \cos\alpha_e d(\frac{y}{S})}. \tag{4.17}$$

4.3.2.6 Mixed-Out Flow Angle

The mixed-out flow angle is calculated from the resulting mixed-out axial and pitchwise velocities. The mixed-out flow angle is

$$\alpha_m = \tan^{-1}\left(\frac{u_{ym}}{u_{xm}}\right) = \tan^{-1}\left(\frac{C_{Vym}}{C_{Vxm}}\right)$$

and inserting Equations 4.13 and 4.17 for C_{Vxm} and C_{Vym}, respectively, the mixed-out flow angle becomes

$$\alpha_m = \tan^{-1}\left(\frac{\int_0^1 C_{Qe} \sin(2\alpha_e) d(\frac{y}{S})}{2\left[\int_0^1 C_{Ve} \cos\alpha_e d(\frac{y}{S})\right]^2}\right). \tag{4.18}$$

4.3.2.7 Mixed-Out Pressure Coefficients

From the control volume analysis described above, the mixed-out dynamic pressure coefficient (C_{Qm}), mixed-out static pressure coefficient (C_{PSm}), and mixed-out total pressure loss coefficient (C_{P0m}) can be calculated.

The dynamic pressure coefficient is the square of the mixed-out velocity ratio (C_{Vm}),

$$C_{Qm} = \frac{\frac{1}{2}\rho u_m^2}{\frac{1}{2}\rho u_i^2} = C_{Vm}^2 = C_{Vxm}^2 + C_{Vym}^2$$

resulting in

$$C_{Qm} = \left[\int_0^1 C_{Ve}\cos\alpha_e\, d(\frac{y}{S})\right]^2 + \left[\frac{\int_0^1 C_{Qe}\sin(2\alpha_e)\, d(\frac{y}{S})}{2\int_0^1 C_{Ve}\cos\alpha_e\, d(\frac{y}{S})}\right]^2 . \tag{4.19}$$

The static pressure coefficient is calculated by subtracting $P_{Si}/\frac{1}{2}\rho u_i^2$ from both sides of Equation 4.15, resulting in

$$C_{PSm} = \frac{P_{Sm} - P_{Si}}{\frac{1}{2}\rho u_i^2}$$

$$C_{PSm} = \int_0^1 C_{PSe}\, d(\frac{y}{S}) - 2\left[\int_0^1 C_{Ve}\cos\alpha_e\, d(\frac{y}{S})\right]^2 + 2\int_0^1 C_{Qe}\cos^2\alpha_e\, d(\frac{y}{S}) \tag{4.20}$$

The total pressure loss coefficient is related to the dynamic and static pressure coefficients by

$$\begin{aligned}
C_{P0m} &= \frac{P_{0i} - P_{0m}}{\frac{1}{2}\rho u_i^2} \\
C_{P0m} &= \frac{P_{Si} + \frac{1}{2}\rho u_i^2}{\frac{1}{2}\rho u_i^2} - \frac{P_{Sm} + \frac{1}{2}\rho u_m^2}{\frac{1}{2}\rho u_i^2} \\
C_{P0m} &= \frac{\frac{1}{2}\rho u_i^2}{\frac{1}{2}\rho u_i^2} - \frac{\frac{1}{2}\rho u_m^2}{\frac{1}{2}\rho u_i^2} - \frac{P_{Sm} - P_{Si}}{\frac{1}{2}\rho u_i^2} \\
C_{P0m} &= 1 - C_{Qm} - C_{PSm}
\end{aligned}$$

which results in

$$C_{P0m} = 1 - \int_0^1 C_{PSe}\, d(\frac{y}{S}) + \left[\int_0^1 C_{Ve} \cos\alpha_e\, d(\frac{y}{S})\right]^2 - \ldots$$

$$2\int_0^1 C_{Qe} \cos^2\alpha_e\, d(\frac{y}{S}) + \left[\frac{\int_0^1 C_{Qe} \sin(2\alpha_e)\, d(\frac{y}{S})}{2\int_0^1 C_{Ve} \cos\alpha_e\, d(\frac{y}{S})}\right]^2 . \tag{4.21}$$

4.3.2.8 Mixed-Out Profile Loss Coefficient

The mixed-out profile loss coefficient relates the total pressure loss across the cascade to the outlet dynamic pressure,

$$Y_m = \frac{P_{0i} - P_{0m}}{\frac{1}{2}\rho u_m^2}$$

and relates to the mixed-out total pressure loss coefficient by

$$Y_m = \frac{C_{P0m}}{C_{Qm}} \tag{4.22}$$

where C_{P0m} is obtained from Equation 4.21 and C_{Qm} from Equation 4.19.

4.3.2.9 Axial-Velocity Ratio

For the mixing analysis described above, it is assumed that the mid-span flow measurements and reduced data are two-dimensional. Since the test section has a finite width, the end-wall boundary layer growth and secondary flows can have an impact on the blade mid-span boundary layers, by either expanding or contracting the mid-span streamtubes in the spanwise direction.

The axial-velocity-density ratio ($AVDR$) is a measure of the two-dimensionality of the

mid-span flow, being the ratio of outlet-to-inlet unit-span mass flow rates.

$$AVDR = \frac{\int_0^s (\rho u_{xe})_{MS} dy}{\int_0^s (\rho u_{xi})_{MS} dy} = \frac{\int_0^1 (\rho_e u_e \cos\alpha_e)_{MS}\, d(\frac{y}{s})}{\int_0^1 (\rho_i u_i \cos\alpha_i)_{MS}\, d(\frac{y}{s})}$$

A value of $AVDR$ of 1 implies that the mid-span flow is approximately two-dimensional. A value lower than 1 suggests there is an expansion in the spanwise direction, whereas a value greater than 1 suggests a contraction in the spanwise direction.

In gas turbines, density changes and meridonial expansions or contractions across a blade row are present, which can have an effect on the blade boundary layers, as described by Cumpsty (1989). For cascade studies, unless these effects are being studied directly, as in the study of Rodger *et al.* (1992), it is desirable to keep the streamtube expansion or contraction to a minimum. Rodger *et al.* (1992) studied the effects of AVR on profile losses and outlet flow deviation angles of a low-speed turbine cascade.

For incompressible flows, the densities at inlet and outlet are the same and the axial-velocity ratio (AVR) is the parameter of importance. Assuming uniform inlet flow angle and velocity, the axial velocity ratio is:

$$AVR = \frac{\int_0^1 u_e \cos\alpha_e\, d(\frac{y}{S})}{\int_0^1 u_i \cos\alpha_i\, d(\frac{y}{S})} = \frac{1}{\cos\alpha_i} \int_0^1 C_{Ve} \cos\alpha_e\, d(\frac{y}{S}) \tag{4.23}$$

As mentioned in the introduction to this chapter, the original high-FSTI, small-length scale turbulence generating grid (grid H2) resulted in flow uniformity problems. Another serious problem with grid H2 was that the AVR across the cascade was low, around 0.90, which was suspected to be caused by a thickening of the inlet end-wall boundary layers due to the presence of the supporting frame for the grid. Grid H3 was intended to minimize

both the non-uniform flow and low-AVR problems.

4.3.3 Cascade Flow Quality

In turbomachinery cascade studies, it is important to simulate as closely as possible the most important conditions under which a compressor or turbine airfoil operate. Since the airfoils of an axial compressor or turbine are distributed circumferentially around a rotor axis, the blades essentially operate in an infinite blade row. To simulate the periodic effects of an infinite blade row, a cascade of evenly spaced blades is used, along with inlet and outlet flow control surfaces, to achieve identical flow patterns around the middle blades of the cascade. In the current experimental study, the control surfaces of the test section were positioned to achieve uniform inlet flow and periodic outlet flow over the middle five blades of the cascade, with emphasis on the middle three blades over which detailed downstream three-hole probe measurements were made. Figure 4.11 shows the cascade inlet and outlet flow measurements for a Reynolds number of 50000 and an FSTI of 3.9%. These measurements are typical of all the cases examined using grid H3. The figure shows the flow angle, static pressure coefficient, dynamic pressure coefficient, and total pressure loss coefficient distributions at 1.2 axial chord lengths upstream and 0.5 axial chord lengths downstream of the middle three blades of the cascade.

The inlet flow measurements, in the left-hand plots of Figure 4.11, show that spatial non-uniformities in the flow are present due to the close proximity of the turbulence generating grid. The decay in non-uniformities from the top of the cascade to the bottom of the cascade is due to the inclination of the cascade to the streamwise flow direction, with the upper blades closer to the grid than the lower blades, as shown in Figure 4.3. Although Figure 4.11 only shows the non-uniformities at mid-span, spanwise measurements showed similar non-uniformities across the test section width. Therefore, the mid-span measurements were used

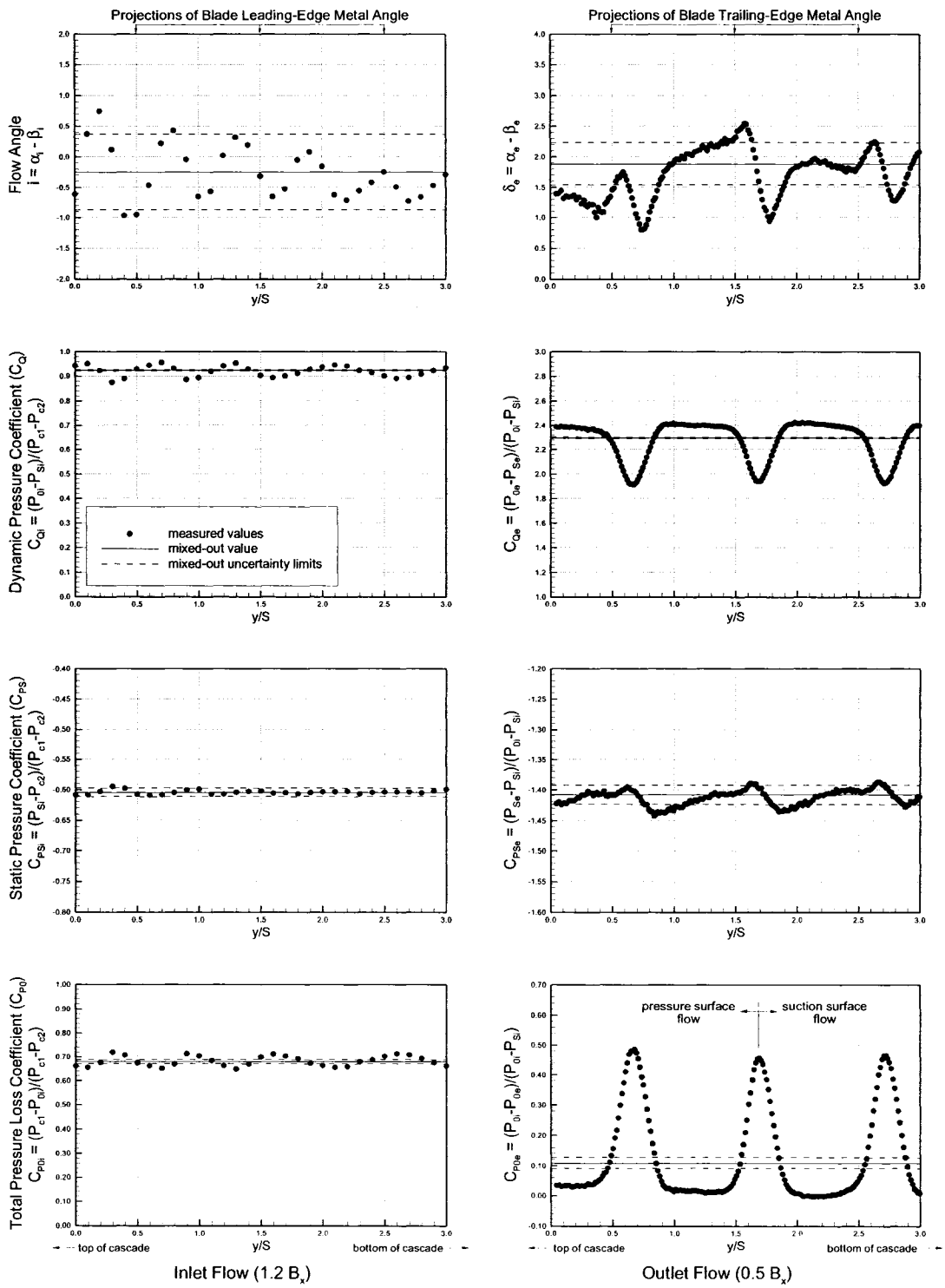

Figure 4.11: **Cascade Flow Quality for** $Re = 50000$, $FSTI = 3.9\%$, $\Lambda/B_x = 0.11$

to obtain averaged inlet flow angles and pressure coefficients, which are required to reduce the downstream three-hole probe measurements into coefficient form (described in Section 3.7.1). To obtain these averaged reference values, a mixed-out calculation, as described in Section 4.3.2, was performed on the inlet flow measurements for the middle two blade passages (y/S=0.5 to y/S=2.5) since these blade passages most influence the flow around the cascade middle blade. The mixed-out flow angle and pressure coefficients are presented in Figure 4.11 by solid horizontal lines, with their respective uncertainty limits shown by dashed lines. The mixed-out analysis of the inlet flow accounts for pressure losses associated with mixing-out of the gross flow non-uniformities.

The right-hand graphs of Figure 4.11 present the detailed downstream three-hole probe measurements, and show the periodicity achieved for this case. The traverse grid for these measurements consists of 65 points per blade pitch. The non-uniformities present in the inlet flow cause a slight non-periodicity in the downstream flow. This non-periodicity is present in the distribution of flow deviation angle, δ_e, for which each of the blade passages has a slightly different mixed-out value. The mixed-out values shown are based on the flow distribution downstream of the cascade middle blade.

The downstream total pressure loss distribution (C_{P0e}) shows another effect of the non-uniform inlet flow. The upper blade passage has positive values of total pressure loss in the region between the wakes. Measurements for uniform inlet flow conditions (Mahallati, 2003) show loss-free fluid in the regions between the wakes. It is believed that since the grid generated non-uniform flow has not completely mixed-out ahead of the inlet measurement plane, losses due to turbulent mixing of the grid wakes and jets continue through the blade passages. Since the upper blades of the cascade have stronger inlet non-uniformities, and the inlet reference pressure coefficients are taken for the middle two blade passages, the turbulent mixing losses through the upper blades show up as pressure losses in the

downstream measurements. For this reason, all quoted performance characteristics for the Pak-B airfoil with grid H3 are calculated from the measurements downstream of the middle blade only, whereas the data of Mahallati (2003) for grid H1 are based on an average of the downstream measurements for the middle three blades.

The axial-velocity ratios (AVR) for the current experimental study, using grid H3, are shown in Figure 4.12. The AVR is slightly low ($\sim$ 0.97 to 0.99), which corresponds to a spanwise divergence of the mid-span flow through the cascade. As discussed in Section 4.3.2, the AVR for the first low-length scale grid (grid H2) was approximately 0.90. The data in Figure 4.12 show that a significant improvement in AVR has been achieved with grid H3. Data of Rodger *et al.* (1992) show that losses and deviation angle are a function of AVR, with losses increasing as AVR drops below 1, and flow deviation angle decreases slightly with decreasing AVR. Rodger *et al.* (1992) observed an increase in losses of approximately

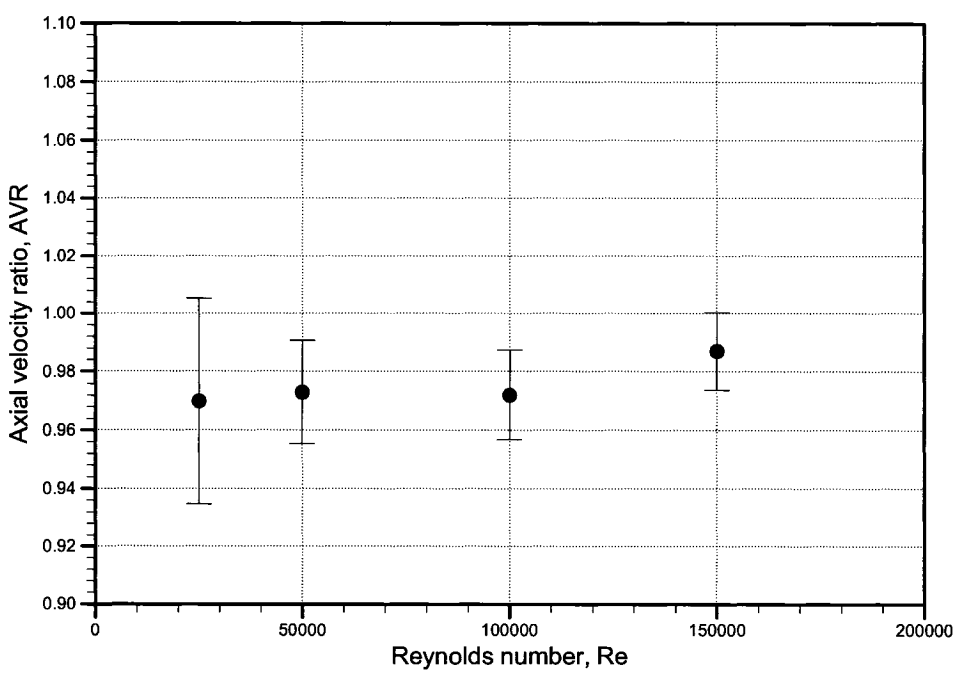

Figure 4.12: **Axial-Velocity Ratios for** $FSTI = 3.9\%$ **and** $\Lambda/B_x = 0.11$

50% between $AVR = 1.0$ and $AVR = 0.97$. This suggests that the low AVR of the current study may have an undesired effect on the losses when comparing against the data of Mahallati (2003) for grid H1, for which the AVR is slightly greater than 1. The airfoil used by Rodger *et al.* (1992) had an aspect ratio of approximately 1 and the aspect ratio for the current airfoil is 2.4. The endwall boundary layers and secondary flows affect the mid-span flow more so when the aspect ratio is small, therefore any difference in losses between the current study and that of Mahallati (2003) are not expected to be as significant as for the case of Rodger *et al.* (1992). The comparison between the current study, using grid H3, and the study of Mahallati, using grid H1, will be presented in Chapter 6.

4.3.4 Loading

4.3.4.1 Loading Measurements

The blade static pressure distribution is important in characterizing the airfoil performance. This distribution is directly related to the lift produced by the blade, which in turn relates to the blade row torque in an engine. The surface pressure distribution also has a direct influence on the state of the boundary layer. In the quest to reduce the number of blades in an engine, the lift produced by LPT blades has increased significantly over the years and has resulted in regions of strong adverse pressure gradient over the aft suction surface. For LPTs operating at cruise conditions, the blade Reynolds numbers are low enough that a significant portion of the blade surface is covered by laminar flow which, in regions of adverse pressure gradient, is susceptible to separation. The main focus of the Pak-B study at Carleton University is the separated-flow transition process over the suction surface of the airfoil (Zhang, 2002 and Mahallati, 2003). This section presents the surface static pressure, or loading, distributions over the Pak-B airfoil using grid H3.

Figures 4.13 and 4.14 show the loading distributions over the Pak-B airfoil with an FSTI of 3.9% and turbulent length scale of 11% of axial chord, for Reynolds numbers ranging from 25000 to 150000. The surface static pressure is presented in the form of the loading coefficient:

$$C_{PL} = \frac{P_{0i} - P_{SL}}{P_{0i} - P_{Si}}.$$

The estimated measurement uncertainties in the loading coefficient are tabulated in Table 4.1 and represent both random and bias errors. Figure 4.13 presents the loading distribution over both the suction and pressure surfaces based on axial location through the blade passage. Figure 4.14 presents the suction surface loading distributions based on suction surface location, which represents the pressure distribution experienced by the boundary layer developing over the suction surface.

The pressure surface loading distributions shown in Figure 4.13 are relatively well behaved for the higher Reynolds numbers (100000 and 150000), but at low Reynolds numbers (25000 and 50000) a separation bubble appears to be present, starting at approximately 20% axial chord and reattaching before 40% of axial chord. As discussed in Chapter 2, flow separation is indicated by a pressure plateau followed by a sudden rise in pressure. Although it is difficult to see the pressure surface pressure plateau in Figure 4.13, this trend is very similar to the data of Mahallati (2003) using grid H1 (similar FSTI with larger integral length scale). Details of the Pak-B pressure surface separation characteristics are given by

Table 4.1: **Maximum Uncertainty for Loadings at** $FSTI = 3.9\%$ **and** $\Lambda/B_x = 0.11$

Re	δC_{PLmax}
25000	0.20
50000	0.08
100000	0.04
150000	0.02

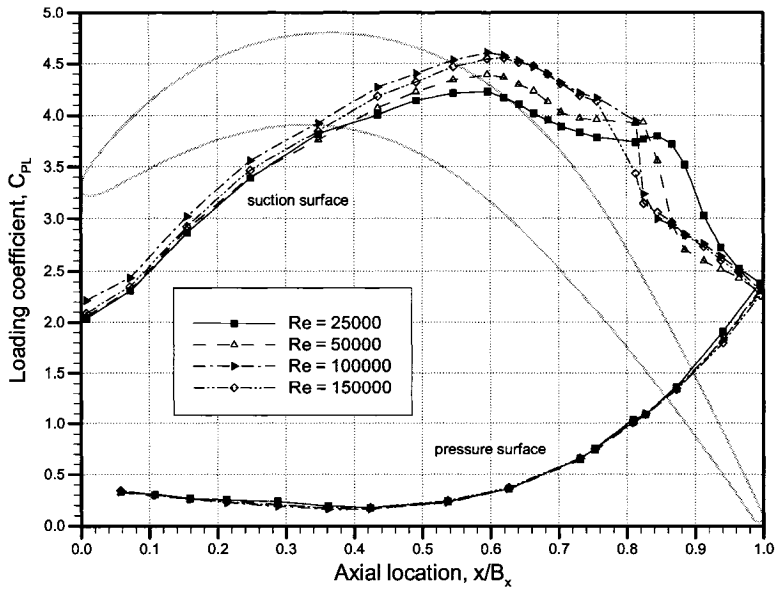

Figure 4.13: **Blade Loading Distributions for** $FSTI = 3.9\%$ **and** $\Lambda/B_x = 0.11$

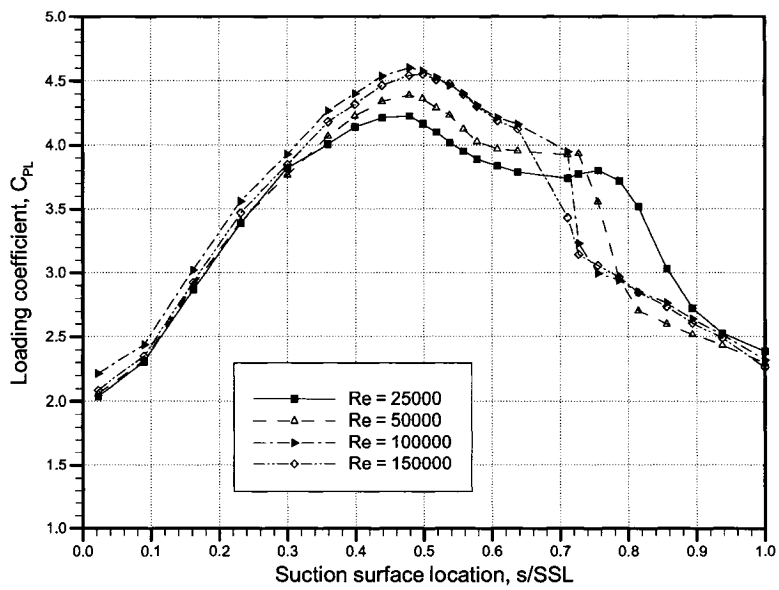

Figure 4.14: **Suction Surface Loading Distributions for** $FSTI = 3.9\%$ **and** $\Lambda/B_x = 0.11$

Mahallati (2003).

The suction surface pressure distribution shows a Reynolds number dependence. The suction peak for all Reynolds numbers occurs at approximately 60% of axial chord (48% of suction surface length). Downstream of the suction peak, the adverse pressure gradient causes the flow to separate from the surface. This occurs at approximately 70% to 73% of axial chord (58% to 61% of suction surface length). The presence of separation soon after the suction peak suggests that the boundary layer remains laminar up to the separation point, downstream of which a laminar separation bubble forms. Due to the highly-unstable free-shear layer over the separation bubble, the flow eventually undergoes transition and reattaches to the surface, resulting in a region of strong pressure recovery. A turbulent boundary layer then continues to develop to the trailing edge. Table 4.2 lists the estimated locations of separation (s), maximum bubble displacement (md), and reattachment (r), within the resolution of the pressure tap locations. The "maximum bubble displacement" location (md) refers to the knee of the separated region where entrainment of freestream fluid is high enough to initiate reattachment of the separated shear layer. In a simulated LPT flat-plate experiment, Yaras (2002) notes that the knee of a separation bubble occurs at the position of maximum displacement thickness, and for low-FSTI, the knee is the streamwise location where transition begins in the free-shear layer. At high-FSTI, Yaras notes that transition is initiated ahead of the knee. Table 4.2 shows that the locations of

Table 4.2: **Separation Bubble Characteristics Based on Loading Measurements**

Re	$(x/B_x)_s$	$(s/SSL)_s$	$(x/B_x)_{md}$	$(s/SSL)_{md}$	$(x/B_x)_r$	$(s/SSL)_r$
25000	0.70 – 0.73	0.58 – 0.61	0.85 – 0.87	0.76 – 0.79	0.94 – 0.96	0.89 – 0.94
50000	0.70 – 0.73	0.58 – 0.61	0.82 – 0.85	0.73 – 0.76	0.87 – 0.89	0.79 – 0.81
100000	0.70 – 0.73	0.58 – 0.61	0.81 – 0.82	0.71 – 0.73	0.82 – 0.85	0.73 – 0.76
150000	0.70 – 0.73	0.58 – 0.61	0.76 – 0.81	0.64 – 0.71	0.81 – 0.82	0.71 – 0.73

maximum bubble displacement and reattachment move upstream with increasing Reynolds number. This indicates that transition within the separated shear layer is promoted with increasing Reynolds number, resulting in a smaller separation bubble.

The extent of the suction surface separation bubble has an effect on the overall loading of the blade, as seen in Figure 4.13. As the length of the separation bubble increases, the loading coefficient corresponding to the suction peak decreases, resulting in lower blade loading and hence less flow turning.

The development of the suction surface boundary layer is also discussed in Section 4.4 with regards to surface-mounted hot-film measurements.

4.3.4.2 Zweifel Coefficient

In the design of axial-flow turbines, especially for high-lift blades, it is desired to achieve the highest blade spacing possible without promoting fully-separated flow and high losses. For large pitch-to-chord ratios (low solidity), fewer blades are required but there is an increased likelihood of fully separated flow. For small pitch-to-chord ratios, frictional losses are high due to the increased wetted-surface area of the blade passages. Zweifel (1945) proposed an optimum blade loading value useful for design purposes. This optimum blade loading value corresponded to minimum profile losses for the state-of-the-art designs of the time. Through many experiments and an analytical treatment of cascade flows, Zweifel found that a loading coefficient based on the tangential, or pitchwise, lift of the blade was approximately constant for optimum blade spacing. This coefficient, known as the Zweifel Coefficient, is

$$\psi = 2(\frac{S}{B_x})\cos^2\alpha_m\,|\tan\alpha_i - \tan\alpha_m| \tag{4.24}$$

and can be interpreted as the ratio of actual tangential blade lift to a representative blade lift for the desired flow turning. The sign conventions for flow angles are shown in Figure 4.10 on page 80. The representative blade lift is calculated by assuming a rectangular pressure distribution over the blade, where the entire pressure surface is at the inlet total pressure and the entire suction surface is at the exit static pressure. For the Pak-B airfoil, this rectangular loading distribution for a Reynolds number of 50000 is shown in Figure 4.15, compared to the actual loading distribution. The representative suction surface pressure shown is the mixed-out downstream static pressure as determined from three-hole pressure probe measurements. Zweifel suggested that a value of 0.8 for the Zweifel Coefficient results in minimum losses for a given tangential loading, from which an optimum pitch-to-chord ratio can be found. Japikse and Baines (1994) state that when designing highly-loaded blades, it is often necessary to increase the lift by overexpanding the flow on the forward part of the suction surface, so that the pressure over the rearward portion of the suction

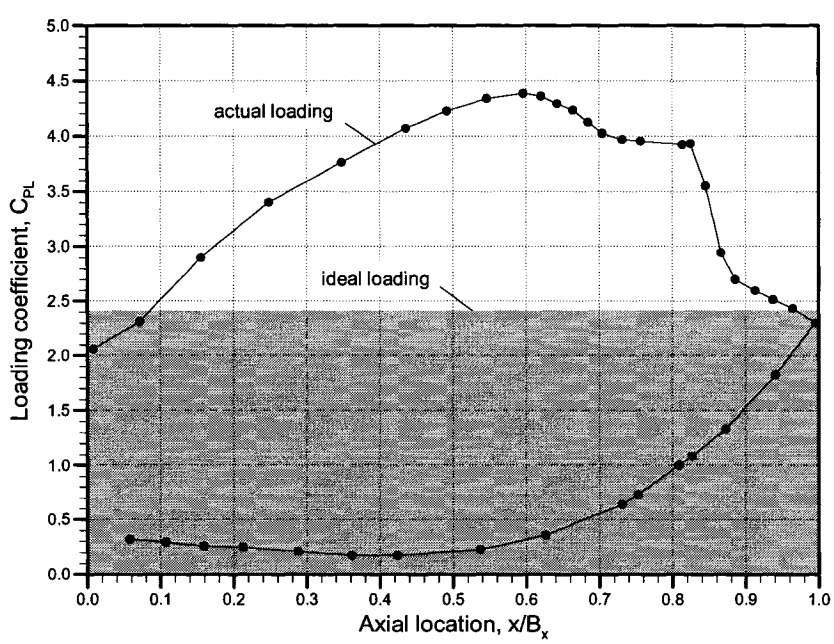

Figure 4.15: **Ideal Zweifel Loading Compared with Actual Loading for** $Re = 50000$

surface is lower than that downstream of the blade row. This results in increased diffusion between the throat and the trailing edge, and usually results in Zweifel Coefficients greater than 0.8. The Zweifel Coefficient for the Pak-B cascade is approximately 1.08.

The high Zweifel Coefficients obtained by current high-lift designs are a result of increased understanding of the boundary layer development over the airfoil. Current blades are often designed by prescribing a loading distribution that is tailored to meet the required boundary layer development, and by using inverse design methods to obtain the corresponding profile geometry (Japikse and Baines, 1994). At the time this manuscript was being written, a new generation of high-lift blades were being studied in the LSTL at Carleton University (Pak-D-A and Pak-D-F). These blade have been designed by Pratt & Whitney for the same duty as Pak-B but have Zweifel Coefficients of approximately 1.36.

The next section presents the wake profiles downstream of the Pak-B cascade using grid H3.

4.3.5 Wake Profiles

Downstream of the Pak-B cascade of airfoils, the boundary layers from the pressure and suction surfaces merge into a wake of low-momentum fluid. The momentum deficit within the wake is due to the total pressure loss across the cascade. Figure 4.16 shows the wake profiles for the 3.9% FSTI and 11% of axial chord length scale cases, measured at 0.5 axial chords downstream of the middle blade in the cascade. The wake distribution is presented in terms of the total pressure loss coefficient:

$$C_{P0} = \frac{P_{0i} - P_{0e}}{P_{0i} - P_{Si}}.$$

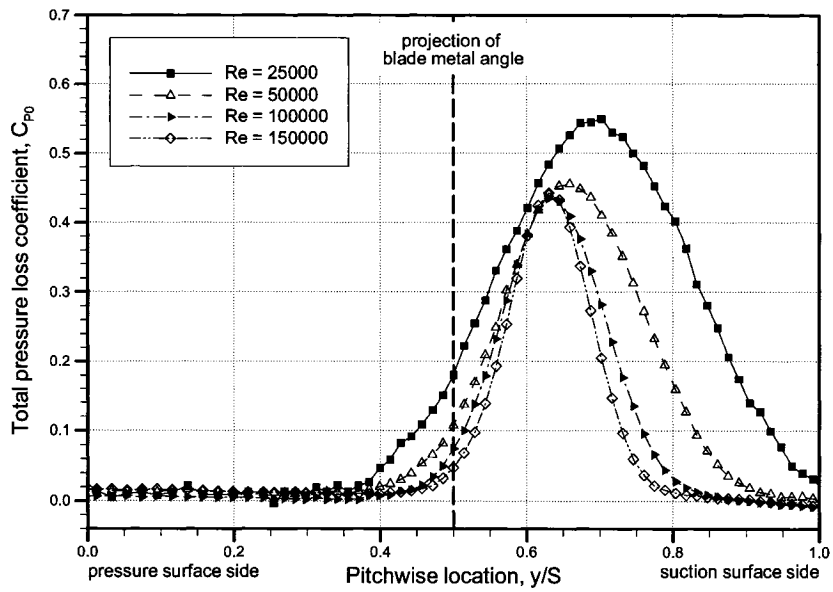

Figure 4.16: **Wake Profiles for** $FSTI = 3.9\%$ **and** $\Lambda/B_x = 0.11$

Position $y/S = 0.5$ corresponds to the blade metal angle extended from the trailing edge. The offset of the wake center from $y/S = 0.5$ is a result of flow deviation from the trailing edge metal angle, and shows a decrease in deviation angle with increasing Reynolds number.

The effect of Reynolds number on the momentum deficit in the wake is clearly seen in Figure 4.16. As the Reynolds number is decreased, the wake becomes wider and deeper due to the thicker boundary layers that develop over the blade surfaces, particularly the suction surface. This thickening of the boundary layers is due to two effects. The first effect is the size of the separation bubbles over the blade surfaces. Larger separation bubbles lead to larger displacement and momentum thicknesses downstream of the reattachment point. This is clearly shown for LPT conditions in the studies of Volino and Hultgren (2001), Volino (2002), Yaras (2001), and Yaras (2002). The second, less dominant effect, is the Reynolds number dependence on the growth rate of the boundary layers. As described by White (1991), the boundary layer growth rate increases as the Reynolds number is decreased.

Denton (1993) shows that the total pressure loss of a cascade airfoil is proportional to the trailing edge momentum thickness and proportional to the square of the trailing edge displacement thickness.

The wake profiles in Figure 4.16 are relatively symmetric. Based on arguments by Denton (1993) that the entropy generation, or total pressure loss, in a boundary layer is proportional to the cube of the local freestream velocity, it is expected that the wake would be asymmetric with a higher momentum deficit on the suction side. The symmetry visible in the wakes of Figure 4.16 is due to the mixing that occurs between the trailing edge and the measurement plane. Data of Ames and Plesniak (1995) for a cascade of high-pressure turbine nozzles show that although the downstream total pressure profile of a wake is relatively symmetric, the turbulent fluctuations and shear stresses are not always symmetric. A study by Murawski and Vafai (2000) in an LPT cascade showed that asymmetry is present in wake profiles measured at 25% axial chord downstream of the trailing edge, with a larger momentum deficit on the suction side. Although not stated explicitly, the airfoil used by Murawski and Vafai (2000) appears to be the Pak-B profile.

As the Reynolds number is decreased in the current study, the wakes become deeper and wider due to the thickening of the trailing edge boundary layers. As already mentioned, the momentum deficit downstream of a cascade airfoil is a measure of the total pressure losses across the cascade. The following section discusses the mixed-out profile losses for the current investigation.

4.3.6 Profile Losses

Losses in turbomachinery blade rows have a direct impact on the component efficiencies in the engine. It is desired to minimize the losses to obtain high component and engine efficiency. As described by Denton (1993), the pressure loss across a turbine has historically

been broken down into "profile loss," "end-wall loss," and "tip leakage loss". Although these loss sources are not independent of one another, their separation into components makes the development, and use, of loss correlations much easier. This separation of the losses into components is used in the turbine loss correlation system of Kacker and Okapuu (1982), which is a development of the well-known Ainley and Mathieson (1951) loss system. In LPTs of modern engines, the blade aspect ratios are high, typically 4-5, and the blades are shrouded resulting in primarily two-dimensional flow across the blade span. Therefore, the profile losses are particularly important in LPTs.

Profile losses arise from entropy generation within the blade boundary layers, from expansion at the trailing edge, and from mixing within the downstream wakes. The mechanism by which entropy is generated is viscous shear. The profile loss coefficient is defined in Section 4.3.2.8, and is presented for the current measurements in Figure 4.17. The losses increase as Reynolds number is decreased due to the thicker boundary layers and larger separation bubbles. This trend is expected based on the wake profiles discussed in Section 4.3.5. The large uncertainties in the profile loss coefficients at low Reynolds numbers are due to the low pressure differences encountered during the experiments. For example, for a Reynolds number of 25000, the total pressure loss across the cascade is approximately 2 Pa, while for a Reynolds number of 150000, the total pressure loss is approximately 20 Pa. Measurement uncertainties were minimized as much as possible by using low-range differential pressure transducers, as described in Section 3.4.1. As the separation bubble decreases in size with increasing Reynolds number, the losses appear to plateau. As discussed by Hourmouziadis (1989), if the Reynolds number was increased further, transition will eventually occur before the separation point and from there, the losses will be expected to increase with Reynolds number due to increased turbulent wetted surface area.

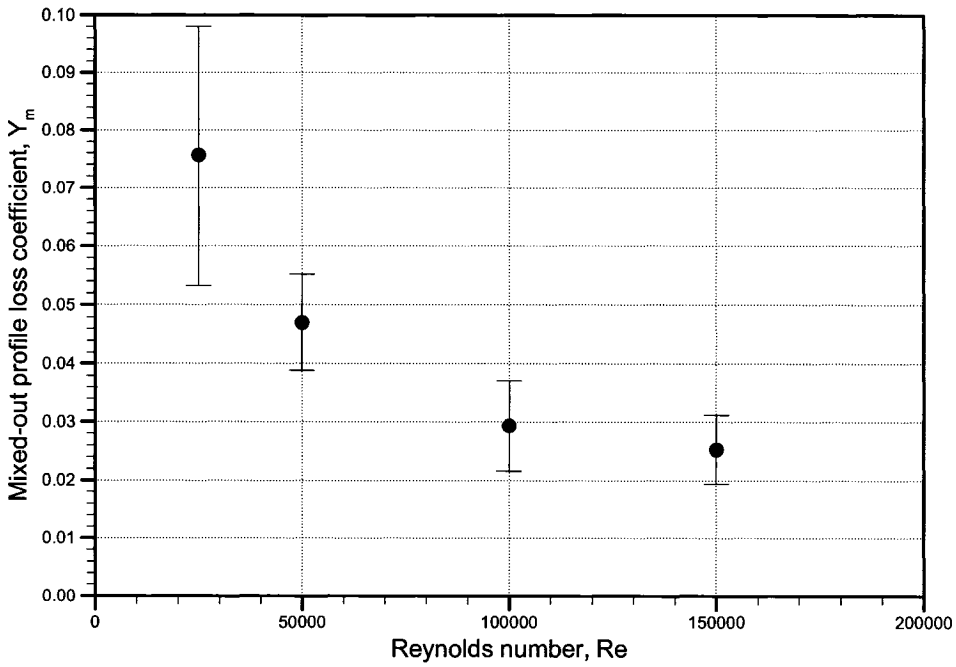

Figure 4.17: **Mixed-Out Profile Losses for** $FSTI = 3.9\%$ **and** $\Lambda/B_x = 0.11$

Apart from pressure losses through the blade passage, the flow deviation angle is also an important performance parameter in cascade studies. The deviation angle results for the current study are presented in the next section.

4.3.7 Mixed-Out Deviation Angles

In the vicinity of the trailing edge, the pressure field set up by the tangential force on the blades causes the streamlines leaving the blade passage to curve towards the suction side (Japikse and Baines, 1994). This results in decreased flow turning. The difference between the outlet flow angle and the blade metal angle is known as deviation. Deviation must be accounted for in the design of a blade row in order to meet the flow turning requirements. The mixed-out deviation angles for the current study are shown in Figure 4.18. These

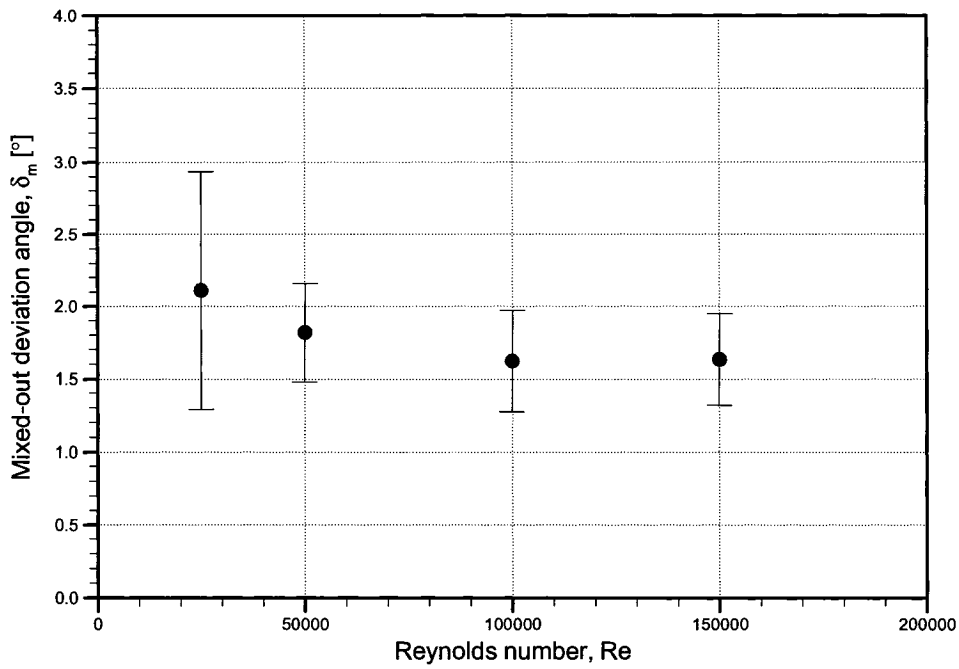

Figure 4.18: **Mixed-Out Deviation Angles for** $FSTI = 3.9\%$ **and** $\Lambda/B_x = 0.11$

mixed-out deviation angles were calculated using Equation 4.18. As Reynolds number is decreased, flow turning is reduced, indicated by the increase in the deviation angle. This is expected based on the decreased loading observed at low-Reynolds numbers in Section 4.3.4.

4.4 Discussion of Hot-Film Measurement Results

4.4.1 Hot-Film Measurements

The previous sections described the pressure measurements from which overall cascade performance characteristics were obtained. The surface static pressure measurements gave an indication of the separation bubble characteristics, from which the regions of laminar,

separated, transitional, and turbulent flow could only be estimated. A means by which these regions can be distinguished is through surface-mounted hot-film measurements.

Surface-mounted hot-film sensors behave, and are operated, in the same manner as hot-wires. The measured voltage across the sensor is directly related to the heat transfer rate from the sensor. As described in Section 3.7.4, this heat transfer rate gives an indirect indication of the shear stress at the surface. Although the sensors are not calibrated to give a direct measure of the wall shear stress, the trends observed in the statistical quantities of the quasi-wall shear stress signals allow interpretation of the boundary layer state.

The following sections present the suction surface hot-film measurements for an FSTI of 3.9% with an integral length scale of 11% of axial chord (grid H3).

4.4.2 Identification of Boundary Layer State

4.4.2.1 Hot-Film Measurement Interpretation

The state of the Pak-B suction surface boundary layer, including regions of laminar, separated, transitional, and turbulent flow, have been identified by means of surface-mounted hot-film measurements. The analysis presented here is based on the method developed by Mahallati (2003) for hot-film measurements in the presence of separated-flow transition under steady inflow conditions. This method will be briefly reviewed as a basis for the discussion of the current measurements.

The voltages measured by the hot-film sensors are converted to quasi-wall shear stresses by means of Equation 3.1 in Section 3.7.4. From the resulting quasi-wall shear stress traces, the mean (Equation 3.2), the root-mean-square (RMS, Equation 3.4), and the skewness (Equation 3.5) of the signals are calculated and represent the time-average, the fluctuation level, and the fluctuation asymmetry of the signals, respectively. For comparison

of measurements at different Reynolds numbers, the mean quasi-wall shear stress has been normalized using Equation 3.3 and the resulting term is called the mean quasi-wall shear stress coefficient.

The interpretation of hot-film signals with respect to natural transition will be discussed briefly, with reference to Figure 4.19 reproduced from Mahallati (2003), but originally from Anderson *et al.* (1991). This interpretation is the basis for the interpretation method of Mahallati (2003). In the laminar region, the mean and RMS of the quasi-wall shear stress are both low and the skewness of the signal is zero. The intermittency (Γ), which represents the fraction of the time the signal is turbulent, is zero in the laminar region. Transition begins when instability waves begin to grow in the laminar boundary layer. These instability waves

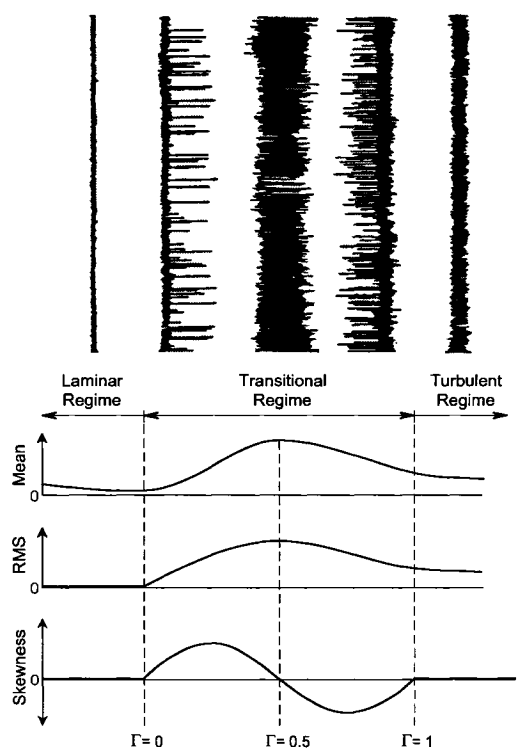

Figure 4.19: **Hot-Film Signals and Statistical Moments in Natural Transition (signal traces reproduced from Anderson *et al.*, 1991)**

develop into loop vortices with large fluctuations, and eventually give rise to the formation of turbulent spots. The turbulent spots coalesce downstream and a fully developed turbulent boundary layer results. As transition begins, both the mean and RMS increase. As the position of maximum skewness is approached ($\Gamma = 0.25$), turbulent spots begin to form which results in intermittently high quasi-wall shear stresses. Once the turbulent spots begin to coalesce, the mean and RMS reach their respective maxima and the skewness returns to zero. This position, at $\Gamma = 0.5$, is referred to as mid-transition. Downstream of mid-transition the mean and RMS decrease continually until the fully developed turbulent boundary layer is formed. At the position corresponding to $\Gamma = 0.75$, the skewness reaches a minimum due to intermittently laminar regions of flow, after which the skewness returns to zero when the fully developed turbulent boundary layer is formed. Although transition occurs within the separated shear layer in the current study, the interpretation of hot-film signals for natural transition allows insight into the shear-layer transition process.

The hot-film signal interpretation method of Mahallati (2003), for separated flow transition, follows that for natural transition in the high-FSTI cases. This interpretation method appears to work well for short bubbles, where the separation bubble affects the flow field, and in particular the blade loading, only in the vicinity of the bubble, as discussed by Tani (1964). For fully separated flow, which is encountered by the Pak-B airfoil at low-Reynolds number and low-FSTI, this interpretation technique is not reliable.

Figure 4.20 shows the distributions of statistical quantities of the quasi-wall shear stress over the suction surface length (SSL) for the current measurements, along with the surface static pressure measurements discussed in Section 4.3.4.1. The following discussions use the method of Mahallati (2003) to infer the boundary layer state over the Pak-B airfoil.

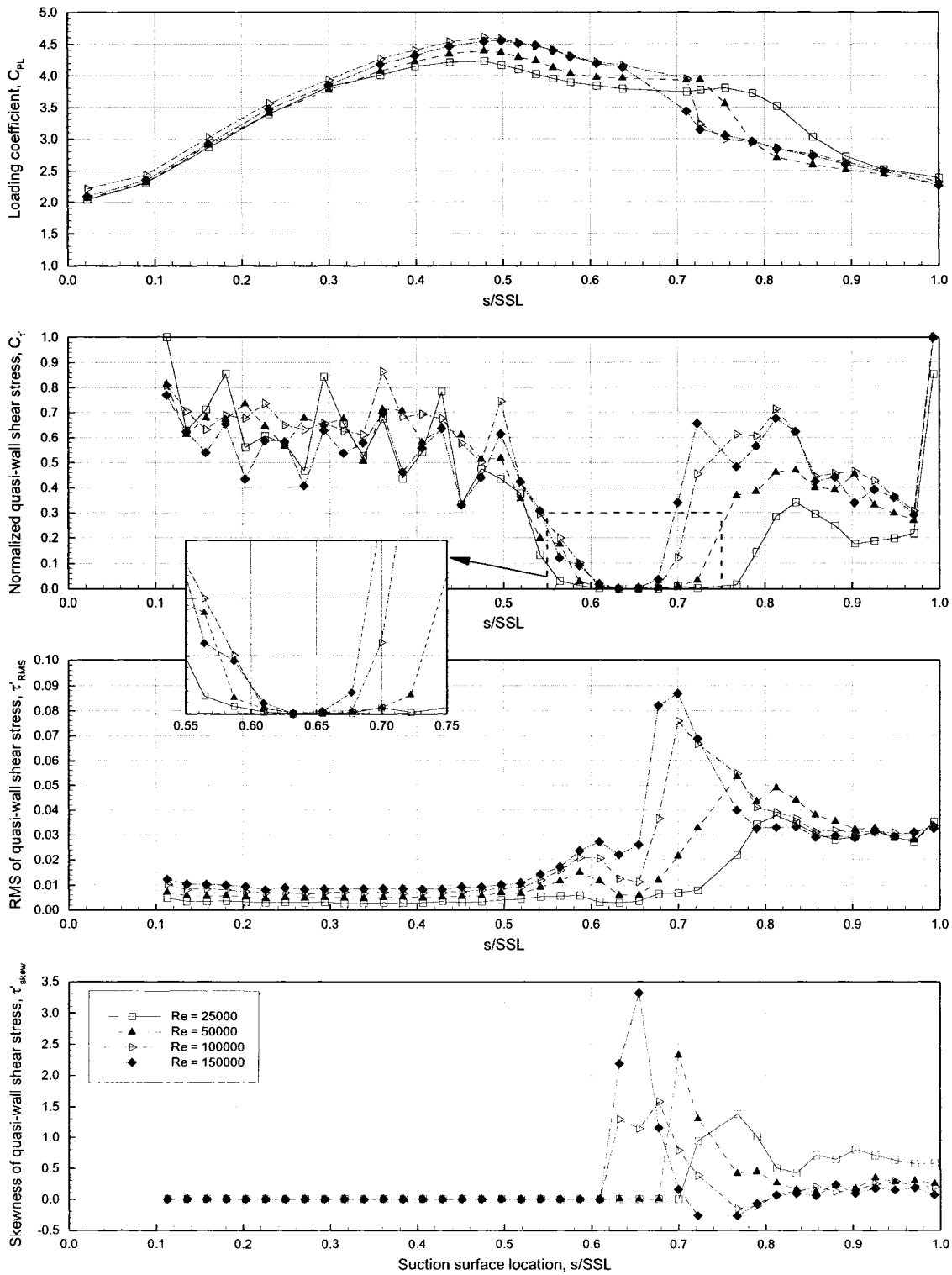

Figure 4.20: **Hot-Film Data for** $FSTI = 3.9\%$ **and** $\Lambda/B_x = 0.11$

4.4.2.2 Laminar Boundary Layer

The mean quasi-wall shear stress over the forward portion of the blade, up to the suction peak (approximately s/SSL=0.50), is relatively constant despite the scatter in the data. This trend is similar to that predicted from the corresponding pressure distribution using the method of Thwaites for laminar boundary layer growth, as described in White (1991) (not presented). In this region the RMS is low and relatively constant. The low level of fluctuations are probably due to freestream turbulence. The skewness of quasi-wall shear stress is zero over the forward part of the suction surface, indicating symmetric fluctuations about the mean. The low fluctuations and zero skewness indicate a laminar boundary layer.

Downstream of the suction peak, the mean quasi-wall shear stress decreases due to the adverse pressure gradient. In this region, the RMS grows as a result of laminar fluctuation growth. The skewness remains zero for all Reynolds numbers examined.

4.4.2.3 Separation Point

The separation point is inferred from the mean of the quasi-wall shear stress. Data of Tani (1964) for separation bubbles over NACA airfoils, show that a pressure plateau does not necessarily result when a separation bubble is formed, and that it can be difficult to interpret the exact location of separation from pressure distributions with a plateau. A better criteria for separation is that of zero wall shear stress, which indicates a stagnation point where the boundary layer lifts-off the surface. From the enlarged section of the C_τ graph in Figure 4.20, the first sensor within the separation bubble is at approximately 63% of SSL for all Reynolds numbers examined.

4.4.2.4 Start of Transition

The start of transition, where instability waves develop and loop vortices form within the shear layer, is indicated by an increase in the skewness of the quasi-wall shear stress from zero. From visual inspection of the quasi-wall shear stress traces, this increase in skewness results from positive spikes in the signal. Figure 4.21 shows the quasi-wall shear stress traces at 68% and 70% of SSL for the Reynolds number of 50000 case, which clearly shows the positive spikes in the latter trace. These spikes are due to the appearance of local high shearing regions, as described by Schlichting and Gersten (2000). The appearance of the spikes, interpreted as the location of transition onset, occurs at approximately 72% and 70% of SSL for Reynolds numbers of 25000 and 50000, respectively, and at approximately 63% of SSL for Reynolds numbers of 100000 and 150000.

4.4.2.5 Location of Maximum Bubble Height

Shortly downstream of the transition onset location, entrainment of freestream fluid increases, leading to the start of reattachment. Due to the increased entrainment, the fluctuations within the shear layer increase significantly with maximum RMS occurring

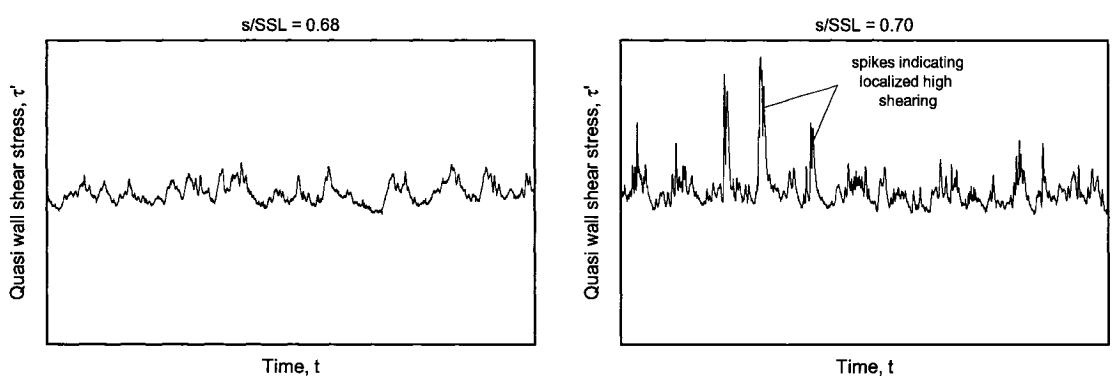

Figure 4.21: **Quasi-Wall Shear Stress Traces for** $Re = 50000$, $FSTI = 3.9\%$ **and** $\Lambda/B_x = 0.11$

at the location of maximum bubble displacement. The location of maximum RMS is approximately 82% and 76% of SSL for Reynolds numbers of 25000 and 50000, respectively, and 70% of SSL for Reynolds numbers of 100000 and 150000. These locations correspond with the knee of the surface pressure distribution, within the spatial resolution of the static pressure taps and hot-film sensors.

4.4.2.6 Point of Reattachment

The separated shear layer reattaches to the surface of the blade for all cases examined in the current study. Although the reattachment point occurs at a location where the wall shear stress is zero, the corresponding quasi-wall shear stress reaches a local maximum. As described by Mahallati (2003), this is due to a breakdown in the Reynolds Analogy at a reattachment point. The Reynolds Analogy, as described by White (1991), relates the heat transfer from the surface to the wall shear stress through similarity of the temperature and velocity fields. The location downstream of separation where the quasi-wall shear stress reaches a local maximum is at approximately 84% of SSL for Reynolds numbers of 25000 and 50000, respectively, and at approximately 72% of SSL for a Reynolds number of 150000. Although not visible in Figure 4.20, it is expected based on the pressure distribution that the reattachment point, and therefore the position of maximum quasi-wall shear stress, for a Reynolds numbers of 100000 is between 72% and 77% of SSL, but due to a damaged hot-film sensor, there is no data available in this region. The location of reattachment for a Reynolds number of 25000 is further upstream than that suggested by the surface static pressure measurements.

4.4.2.7 End of Transition

Although zero skewness is expected for a fully turbulent boundary layer, positive skewness is observed upstream of the the trailing edge for all cases examined. Mahallati (2003) interprets a positive plateau in the skewness as a fully turbulent boundary layer. It is difficult to distinguish a plateau in the current measurements. From visual inspection of the quasi-wall shear stress traces, transition is estimated to end at approximately 95% of SSL for the Reynolds number of 50000 case, and at 79% of SSL for Reynolds numbers of 100000 and 150000. For the Reynolds number of 25000, the boundary layer is still intermittent at the trailing edge, resulting in no regions of fully turbulent flow over the suction surface.

The interpretation of hot-film measurement described in this section will be used in Chapter 6 to compare the effects of turbulent length scale on the transition process over the Pak-B suction surface.

4.4.3 Summary of Pak-B Cascade Performance

The performance and aerodynamic characteristics of the Pak-B LPT airfoil have been examined in this chapter for Reynolds numbers ranging from 25000 to 150000 at an FSTI of 3.9% and an integral length scale of 11% of axial chord.

Surface static pressure measurements have shown the effects of Reynolds number on the blade loading, and in particular, on the extent of the suction surface separation bubble. The suction surface boundary layer separates at approximately the same surface location for all Reynolds numbers examined and the length of the separation bubble increases with decreasing Reynolds number. Downstream wake profiles, measured with a three-hole pressure probe at mid-span of the cascade, show a significant growth of the downstream wake with decreasing Reynolds number. This increase in wake size is primarily due to the

Table 4.3: **Separation/Transition Characteristics Based on Hot-Film Measurements**

Re	SSL_{sep}	SSL_{trans}	SSL_{reat}	SSL_{comp}
25000	0.63	0.72	0.84†	–
50000	0.63	0.70	0.84	0.95
100000	0.63	0.63	0.72 – 0.77‡	0.79
150000	0.63	0.63	0.72	0.79

† large uncertainty, ‡ estimated region

increase in the size of the separation bubble over the airfoil suction surface, and results in increased profile losses and deviation angles.

The separated-flow transition characteristics of the Pak-B airfoil have been examined using surface-mounted hot-film sensors. The estimated locations of suction surface separation (*sep*), transition onset (*trans*), reattachment (*reat*), and transition completion (*comp*) are tabulated in Table 4.3. These locations are given as distance from the leading edge normalized by the suction surface length (SSL).

The results and interpretation methods presented in this chapter are used as a basis for discussing the results in Chapter 6, which examines the influence of turbulent length scale on the performance of the Pak-B airfoil, and in Chapter 7, which presents the results for the Pak-B flow control study.

Chapter 5

Boundary Layer Traverse Measurements

5.1 Introduction

The study of boundary layer transition, as applied to low-pressure turbines, requires detailed measurements from which the state of the boundary layer can be inferred. In Chapter 4, surface static pressure and surface-mounted hot-film measurements were used to infer the state of the boundary layer over the Pak-B airfoil. Uncertainty arises from using these surface measurements to interpret the state of the boundary layer flow field, in particular the transition process within the separated shear layer. A more effective means of studying the boundary layer state is through hot-wire traverse measurements through the boundary layers. This chapter describes some such measurements performed during the current experimental study.

At the outset of the Pak-B study in the Low-Speed Turbomachinery Laboratory at

Carleton University, boundary layer traverse measurements using a hot-wire were not planned due to the relatively small size of the cascade blades (axial chord of 75mm), which results in boundary layer thicknesses on the order of a few millimeters. During the Pak-B flow control study, described in Chapter 7, calibration of the wall jet injection-flow was accomplished using hot-wire traverse measurements. It was found that the test-section traverse mechanism was usable for measuring the wall jet velocity profile at the injection slot with a hot-wire (slot width of approximately 0.3mm). This led to the use of hot-wire measurements to examine the boundary layer growth over the aft portion of the suction surface. One drawback to the current measurements is that the traverse mechanism is currently only able to move in the pitchwise and spanwise directions. This results in traverse planes inclined approximately 30° from the surface near the blade trailing edge. The results presented in this chapter are used to demonstrate the effectiveness of using boundary layer traverses to charactere the boundary layer flow field and associated transition processes.

This chapter presents the measurements made with a hot-wire for a Reynolds number of 50000 at FSTIs of 0.4% and 3.9%. First, the cascade performance for these cases is reviewed, followed by presentation of the hot-wire measurements, including the overall velocity field and detailed boundary layer profiles. The chapter concludes with a summary of the hot-wire measurements with recommendations for future boundary layer traverse measurements.

5.2 Cascade Performance for Hot-Wire Traverse Cases

A Reynolds number of 50000 was selected for the hot-wire measurements since the performance of the Pak-B airfoil is significantly different at this Reynolds number for the two FSTIs considered. At low FSTI (0.4%), the separation bubble over the aft portion of the suction surface does not reattach, resulting in high losses and reduced flow turning. At high FSTI (3.9%), the suction surface separation bubble undergoes transition and reattaches to the surface resulting in much lower losses, as described in the previous chapter. The data presented in this section for the low FSTI case are from Mahallati (2003).

Figure 5.1 shows the loading distributions over the Pak-B airfoil for the two cases examined. The overall loading for the low FSTI case is reduced due to the open separation bubble, identified by the pressure plateau which starts at approximately 60% of axial chord.

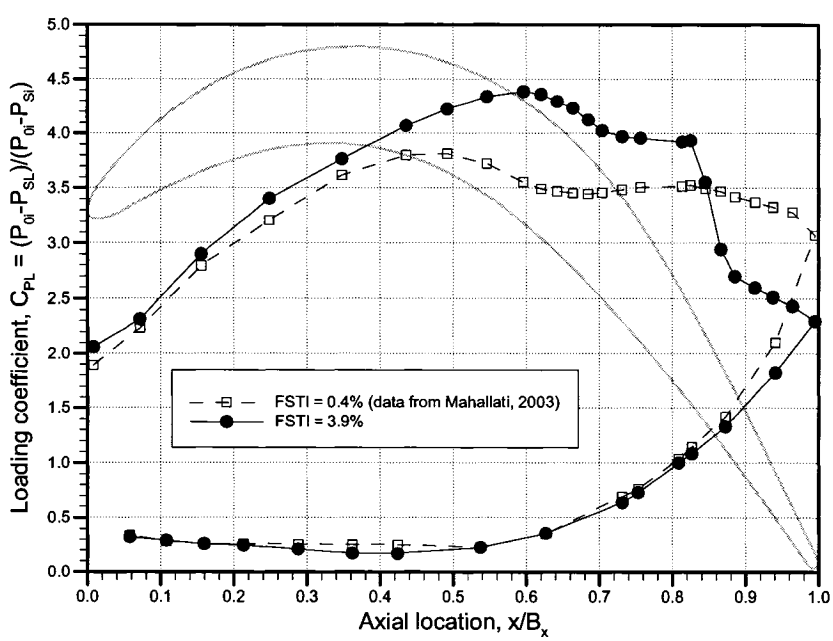

Figure 5.1: **Loading Distributions for Hot-Wire Traverse Cases** ($Re = 50000$)

The high FSTI case shows a reattached separation bubble. The mixed-out profile losses and mixed-out deviation angles are shown in Figure 5.2 over a range of Reynolds numbers for the two FSTIs considered. The left-hand graph of Figure 5.2 presents the mixed-out profile loss coefficients and the right-hand graph presents the mixed-out deviation angles. At a Reynolds number of 50000, the profile loss for low FSTI is four times that at high FSTI, and the deviation angle is about three times that at high FSTI.

The cases with Reynolds number of 50000 were chosen due to the significant differences in performance between low and high FSTI, while they have flow velocities high enough to avoid significant hot-wire measurements errors which occur at velocities below 5 m/s (Bruun, 1995).

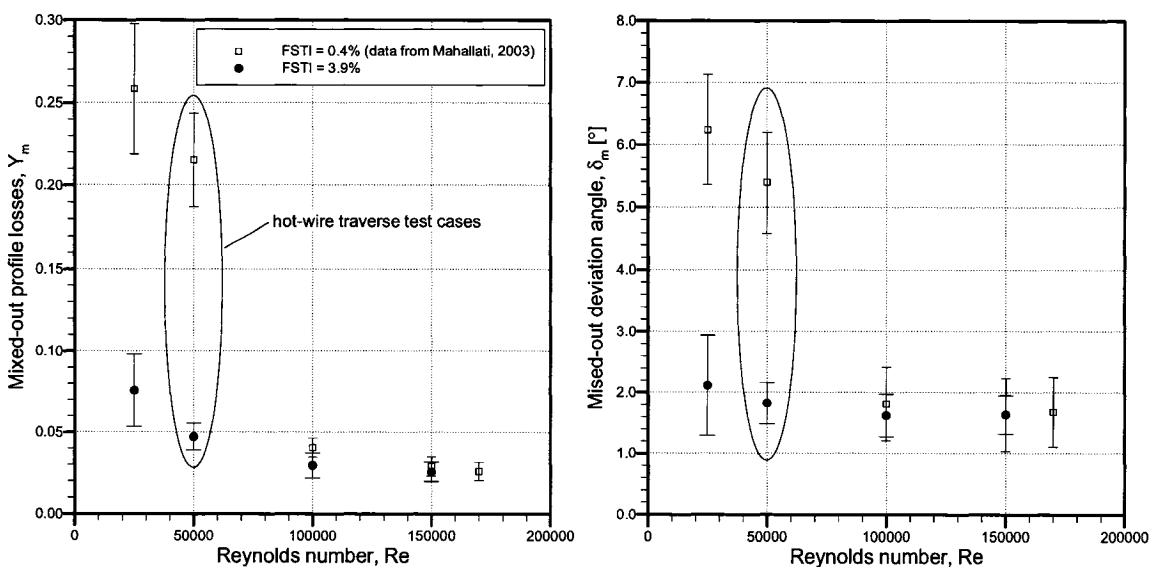

Figure 5.2: **Performance of Hot-Wire Traverse Cases**

5.3 Velocity Field Measurements

The flow field over the aft-suction surface region of the Pak-B airfoil has been measured using a hot-wire. The traverse measurement planes for the two FSTI cases are shown in Figure 5.3. These traverse planes were selected to capture the separated flow regions over the blade suction surface, and each consists of 98 measurement points. Each measurement point consists of 65536 samples, sampled at 30kHz, resulting in approximately 2 seconds of data. The resulting velocity fields for the low and high FSTI measurements are shown as colour-flood contour plots in Figures 5.4 and 5.5, respectively. These figures present

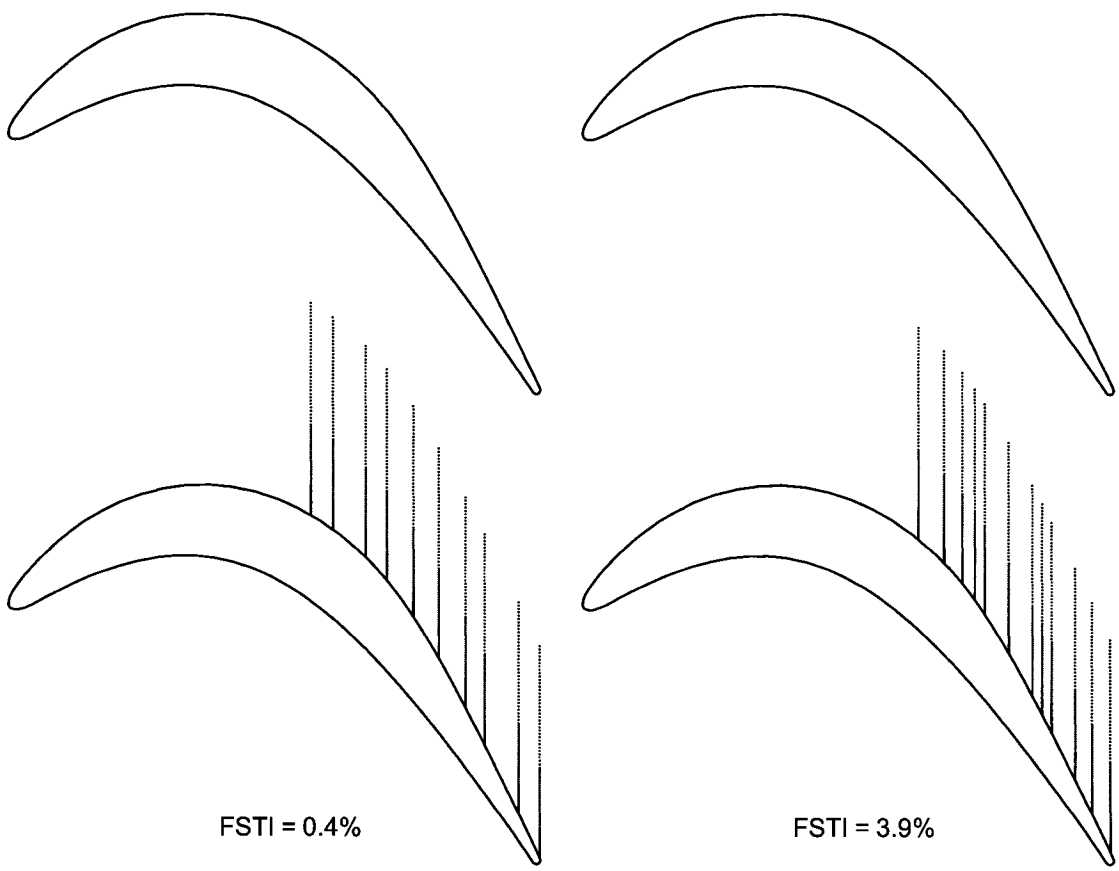

Figure 5.3: **Hot-Wire Traverse Measurement Planes**

the mean velocity field (left-hand side) and the velocity fluctuation field (right-hand side). The fluctuation level is represented by the root-mean-square (RMS) of the instantaneous velocity traces. Both mean and fluctuation quantities are normalized by the mixed-out outlet velocity, U_m. The uncertainties in mean velocity and RMS fluctuation levels are below 5% of the calculated value, except when the mean velocity is below 5m/s, where the uncertainties can be as high as 10% of the calculated value. The uncertainty in turbulence intensity (RMS divide by local mean velocity) is below 10% of the calculated value, except when the mean velocity is below 5m/s, where the uncertainty can be as high as 20%. These uncertainties have been estimated based on the method of Yavuzkurt (1984) as described in Appendix C.

The low FSTI case (0.4%), presented in Figure 5.4, shows a large separated shear layer that does not reattach to the surface. The discontinuities in the contours are a result of interpolation errors due to the highly skewed measurement grid. The estimated edge of the shear layer is shown as a solid line, along which the velocity remains relatively constant as the bubble grows. Initially, the fluid under the separation bubble is relatively stagnant, identified by the low velocities and low fluctuations (dark blue regions), and is sometimes referred to as the "dead-air" region (Hatman and Wang, 1999). Downstream of the "dead-air" region, both mean velocity and fluctuations increase under the separated shear layer, represented by the light blue and green regions, respectively. The increased velocities and fluctuations may be due to a large recirculation region, which cannot be distinguished because a single hot-wire can only measure magnitude, not direction. The line of maximum shear, shown as the dashed line, is where the inflection point in the shear layer occurs. The highest fluctuations in the flow field occur along this line (red regions), suggesting that transition has been initiated, but entrainment is not sufficient to reattach the shear layer. The fully separated shear-layer described for the case of 0.4% FSTI can be classified as a "long separation bubble" (Tani, 1964, and Hatman and Wang, 1999), for which Malkiel and

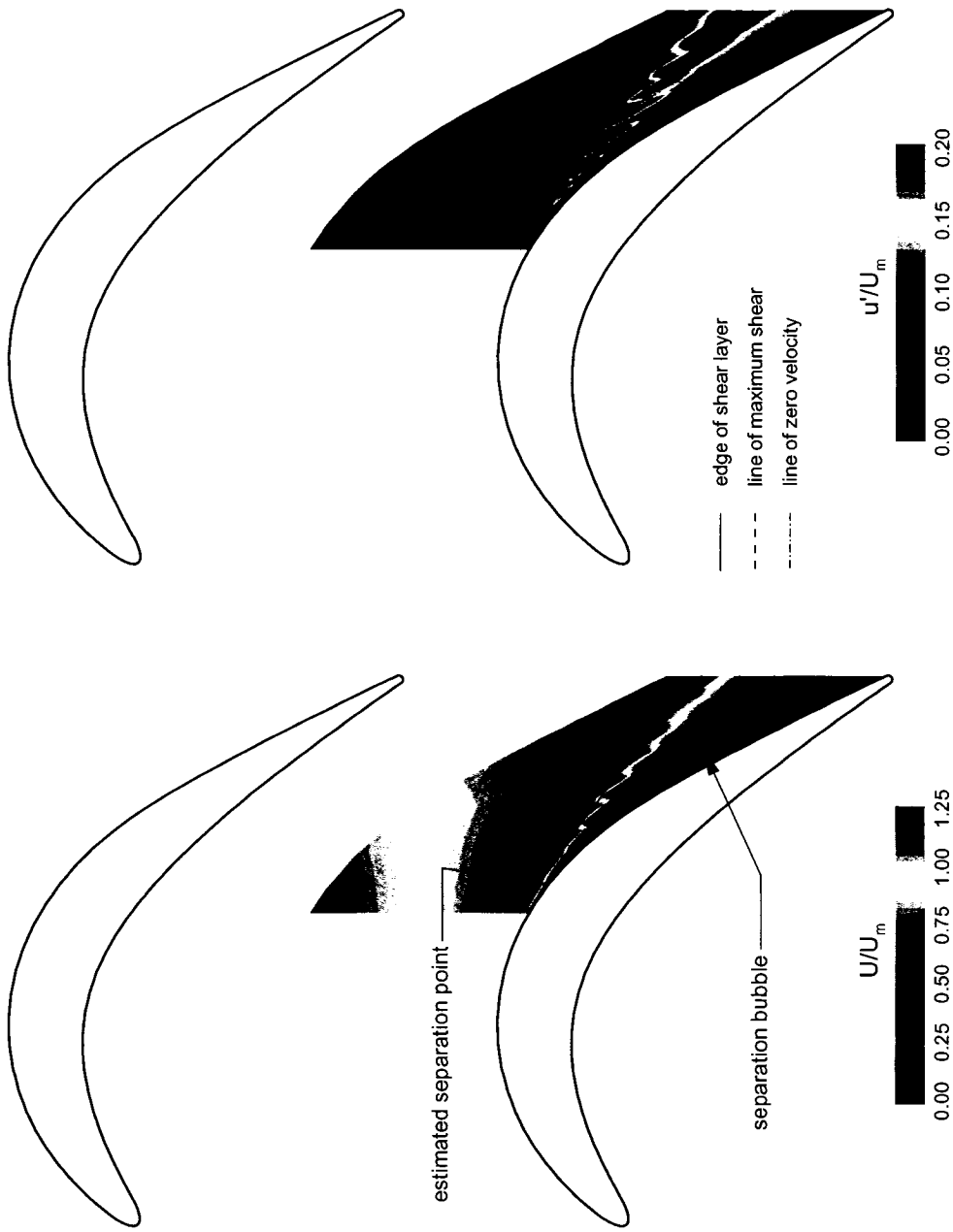

Figure 5.4: **Velocity Field Measurements for** $FSTI = 0.4\%$

Mayle (1996) state that transition is complete well before the end of the constant pressure region and reattachment occurs when the turbulent shear layer entrains enough momentum to overcome the strong adverse pressure gradient. For the case described above, the high fluctuations in the separated shear layer indicate that transition may be complete, but entrainment of freestream fluid is still insufficient to cause reattachment.

The high FSTI case (3.9%), presented in Figure 5.5, shows a reattached separation bubble over the aft section of the suction surface. As with the low FSTI case, the estimated edge of the shear layer is shown as a solid line and the line of maximum shear is shown as a dashed line. The estimated line of zero velocity within the bubble is shown by a dashed-dotted line, and shows the extent of the separation bubble. These lines have been extracted from the velocity profiles presented in the next section. Within the separation bubble, a "dead-air" region is initially present (dark blue regions), as with the low FSTI case, but as transition begins fluctuations grow due to the highly disturbed outer flow (green region below the zero velocity line of the right-hand plot). Transition begins along the line of maximum shear and is indicated by the high turbulent fluctuation levels present in the region of bubble reattachment (red region). After reattachment, the fluctuation level decreases and a thick turbulent boundary layer develops. Hatman and Wang (1999) discuss the mechanisms involved in separated-flow transition and their basic conclusion, for reattached bubbles, is that transition occurs as a result of two different instability mechanisms. The first is Tollmein-Schlichting (T-S) instability, which is the dominant mechanism in attached-flow boundary layer transition and occurs in the forward shallow region of the bubble. The second is Kelvin-Helmholtz (K-H) instability, which is a highly three-dimensional instability that typically occurs in free-shear layer transition, such as in jets, wakes, and mixing layers. For separated-flow transition, K-H instability occurs in the aft-region of the bubble away from the surface.

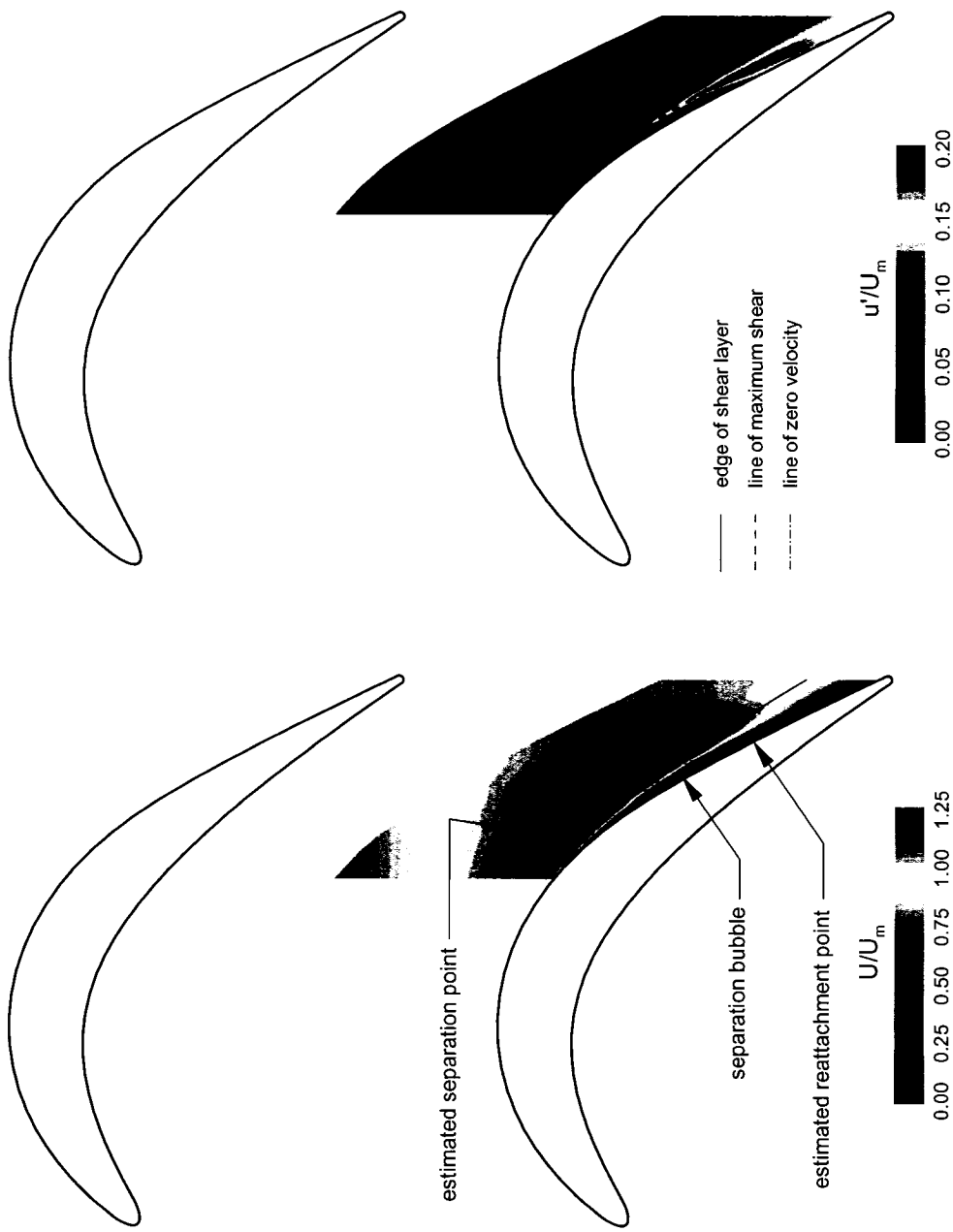

Figure 5.5: **Velocity Field Measurements for** $FSTI = 3.9\%$

The contour plots of Figures 5.4 and 5.5 give an overall picture of the flow field. The next section presents the measured hot-wire data in the form of velocity profiles, which give additional insight into the shear layer development over the Pak-B airfoil.

5.4 Velocity Profiles

5.4.1 Limitations and Extracted Data

Velocity profiles can be helpful for studying the transition process over airfoils. Details of the developing boundary layer can be obtained and used to validate surface measurement interpretation techniques, such as those presented in Chapter 4. One limitation of the current measurements is the inclination of the traverse planes to the blade surface. To account for this inclination, the positions of the measurement points have been corrected, using Equation 5.1, to represent the distance normal to the surface.

$$y_{normal} = y_{traverse} \sin(\phi) \tag{5.1}$$

In Equation 5.1, ϕ is the inclination angle of the traverse plane to the surface. Although the boundary layer profiles presented in this form do not represent the profile at a specific surface location, they are representative of the profiles in the region of the quoted surface location.

Boundary layer integral parameters have also been extracted from the hot-wire traverse measurements. The inability of single hot-wires to distinguish direction results in differences between the calculated and the true values when reverse flow is present. For the current measurements, which represent the velocity magnitude only, the integral parameters are distinguished from the true parameters by an apostrophe ($'$). When reverse flow is not

present, the integral parameters described below represent the true definition.

The displacement thickness, $\delta^{*\prime}$, which represents the mass deficit in the boundary layer, is given by

$$\delta^{*\prime} = \int_0^{\delta} (1 - \left|\frac{U}{U_e}\right|)dy \tag{5.2}$$

where δ is the boundary layer thickness, U is the local mean velocity, and U_e is the local freestream velocity. The momentum thickness, θ', which represents the momentum deficit in the boundary layer, is given by

$$\theta' = \int_0^{\delta} \left|\frac{U}{U_e}\right| (1 - \left|\frac{U}{U_e}\right|)dy. \tag{5.3}$$

These length scales have been expressed as Reynolds numbers based on the local freestream velocity, U_e, giving

$$Re_{\delta^{*\prime}} = \frac{U_e \delta^{*\prime}}{\nu} \tag{5.4}$$

and

$$Re_{\theta'} = \frac{U_e \theta'}{\nu}. \tag{5.5}$$

The shape factor, H', represents the fullness of the boundary layer profile, and is given by

$$H' = \frac{\delta^{*\prime}}{\theta'}. \tag{5.6}$$

The measured velocity profiles and their associated integral parameters are discussed in the next sections for the two FSTI cases (0.4% and 3.9%) at a Reynolds number of 50000.

5.4.2 Low FSTI

The measured boundary layer profiles for an FSTI of 0.4% at a Reynolds number of 50000 are presented in Figure 5.6. The traverse quantities for the top three graphs are mean velocity, turbulence intensity, and RMS fluctuation level, respectively. The mean and RMS quantities are normalized by the local freestream velocity, where what is referred to here as turbulence intensity is the RMS fluctuation normalized by the local mean velocity.

At the first traverse location ($\sim 46\%SSL$), the boundary layer is laminar and has low fluctuation levels. An inflectional mean velocity profile is present at station 2 ($\sim 49\%SSL$) and separation is clearly present at station 3 ($\sim 55\%SSL$). The boundary layer remains separated past the trailing edge. Up to station 5 ($\sim 65\%SSL$) the near-zero velocities and low fluctuations below the separated shear layer represent the "dead-air" region of the separation bubble. At station 6 ($\sim 71\%SSL$), mean velocity and fluctuation levels increase within the separation bubble. In this region, the inability of hot-wires to distinguish flow direction, coupled with high turbulence intensities, results in mean velocity measurements greater than the actual mean velocity level. This effect is show in Figure 5.7 for an idealized sinusoidal hot-wire signal. The fluctuating component of a zero-mean velocity trace (Figure 5.7a) is measured by a hot-wire as always positive (Figure 5.7b), resulting in a calculated mean velocity greater than the actual mean. The increased fluctuation levels at station 6 indicate that transition may have begun within the separated shear layer, and that a reverse-flow vortex may be present. This trend in the profiles is present up to the last traverse plane.

The shear layer is identified in Figure 5.6 by the regions of high RMS fluctuations, as seen in the graph of u'/U_e. The locus of maximum u'/U_e seems to coincide with the inflection points in the mean velocity profiles. The locus of inflection points was also marked on the contour plot of Figure 5.4 and designated there as the line of maximum shear. It is

difficult to distinguish the locations of zero velocity from the hot-wire data, but the profiles of turbulence intensity, u'/U, give an estimate of where this occurs. Since any fluctuations present at near-zero velocity would result in extremely high turbulence intensity, the locus of maximum u'/U is assumed the line of zero velocity under the shear layer.

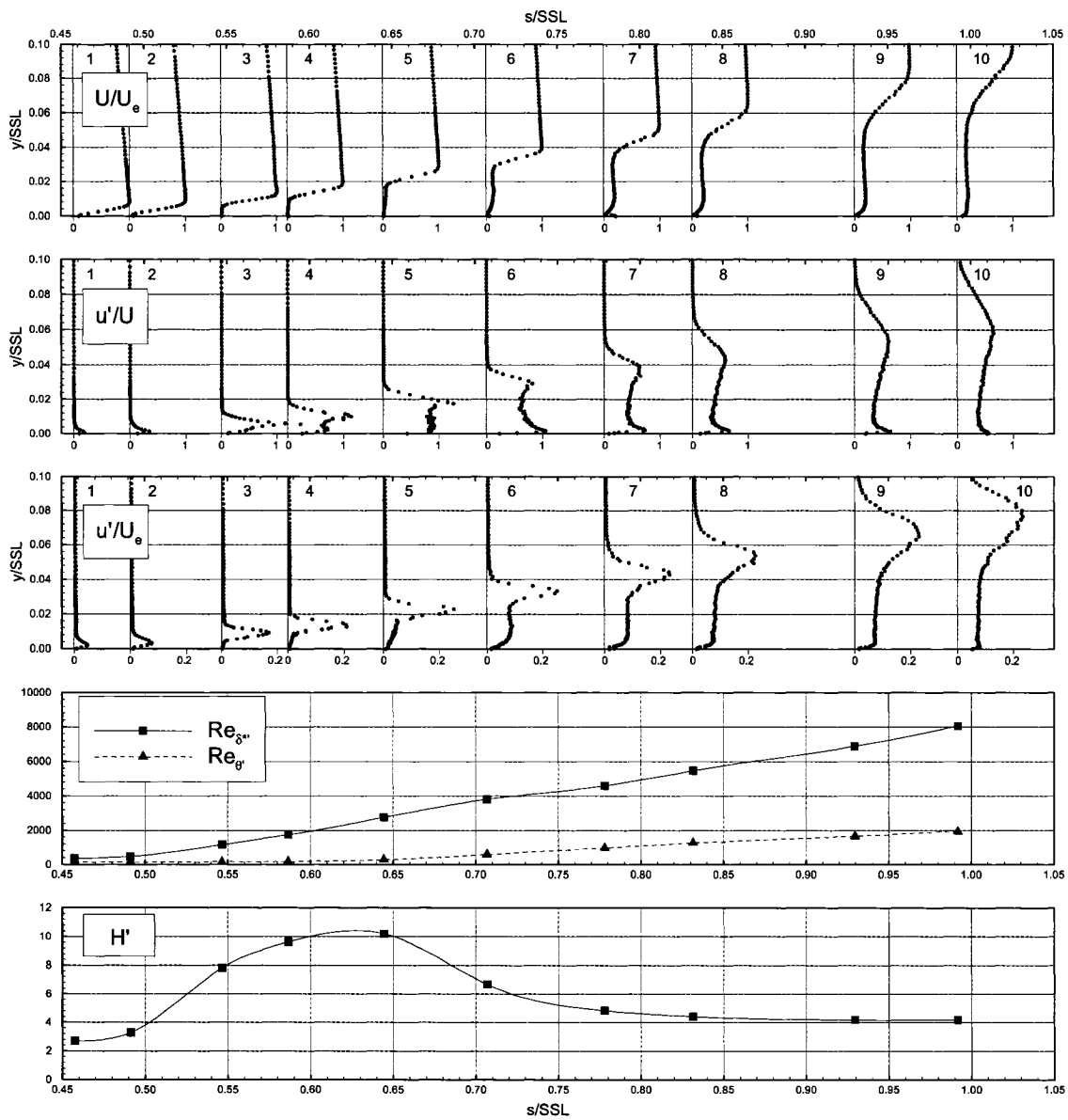

Figure 5.6: **Boundary Layer Profile Measurements for** $FSTI = 0.4\%$

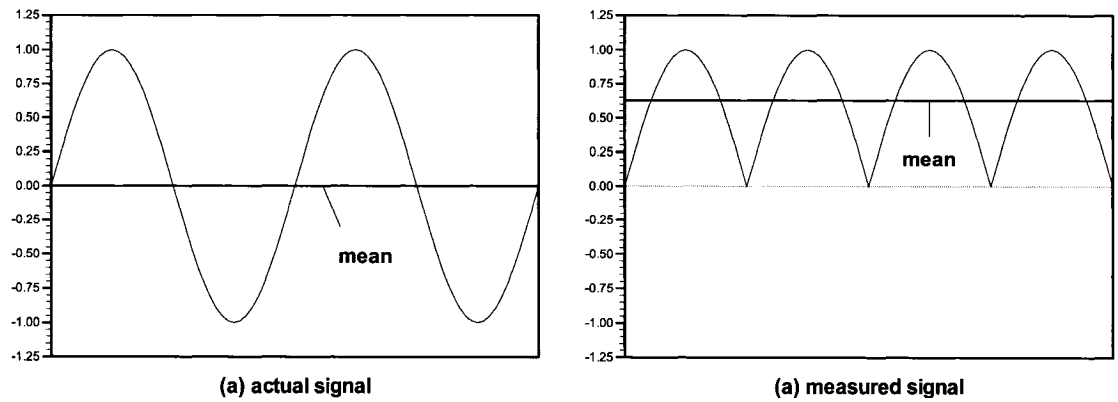

Figure 5.7: **Representation of Mean Velocity Errors for Single Hot-Wire**

The two lower graphs in Figure 5.6 show the boundary layer integral parameters extracted from the mean velocity profiles. Although, due to possible reverse flow, the calculated integral parameters do not have the same physical significance normally associated with them, they may give insight to the transition process. A monotonic increase in both the displacement thickness and momentum thickness is present due to the growth of the separated shear layer. The shape factor shows an initial increase up to station 5 ($\sim$ 65%SSL), after which it decreases and levels-off. The decrease in H', present after station 5, is due to the apparent increase in mass and momentum under the separated shear layer. Although this increased mass and momentum may be due to hot-wire measurement errors, the drop in H' indicates that transition may have begun within the separated shear layer.

The boundary layer profiles for an FSTI of 0.4% give some indications of the transition process within a fully separated shear layer. The transition process for a reattached shear layer is discussed in the next section.

5.4.3 High FSTI

As described in the previous section, boundary layer profiles can give an indication of the transition process for separated flow. The boundary layer profiles and integral parameters for a Reynolds number of 50000 at an FSTI of 3.9% are shown in Figure 5.8.

At station 1 ($\sim$ 51%SSL), the boundary layer is laminar with low fluctuation levels. By station 2 ($\sim$ 56%SSL), an inflection point is visible in the velocity profile, and the fluctuations are higher than at station 1. The increased fluctuations may be caused by the inviscid instability associated with an inflection point (White, 1991). At station 3 ($\sim$ 59%SSL) the inflectional velocity profile is clearly seen and the boundary layer is separated at station 4 ($\sim$ 62%SSL). Up to station 6 ($\sim$ 70%SSL), both the mean velocity and RMS fluctuation levels are low near the surface, indicating the "dead-air" region below the separated shear layer. At station 6, increased RMS fluctuations underneath the separated shear layer indicate that transition may have begun. A large increase in both mean velocity and RMS fluctuation levels are observed underneath the shear layer at station 7 ($\sim$ 76%SSL), which could be due to turbulent fluctuations within the shear layer, indicating the start of transition. The separated shear layer appears to be reattaching near station 8 (79%SSL) and may be reattached by station 9 ($\sim$ 81%SSL). As the boundary layer develops downstream of reattachment, the velocity profile grows and fills-out near the surface. At the last traverse plane ahead of the trailing edge, the lack of inflection points and the relatively constant level of RMS fluctuations normal to the surface indicate a turbulent boundary layer.

As with the low FSTI case, the line of zero velocity is extracted from the positions of maximum turbulence intensity, u'/U, at each traverse plane and marked on the contour plots of Figure 5.5. The lack of a peak in turbulence intensity at station 10 ($\sim$ 89%SSL) indicates that the shear layer has reattached to the surface. Since the peaks in RMS

fluctuation level, u'/U_e, appear to coincide with the inflection points of the laminar and separated shear layers, the locus of inflection points was also marked on Figure 5.5 and designated there as the line of maximum shear. The lack of a peak in u'/U_e at station 10 also indicates that the shear layer has reattached to the surface as a turbulent boundary

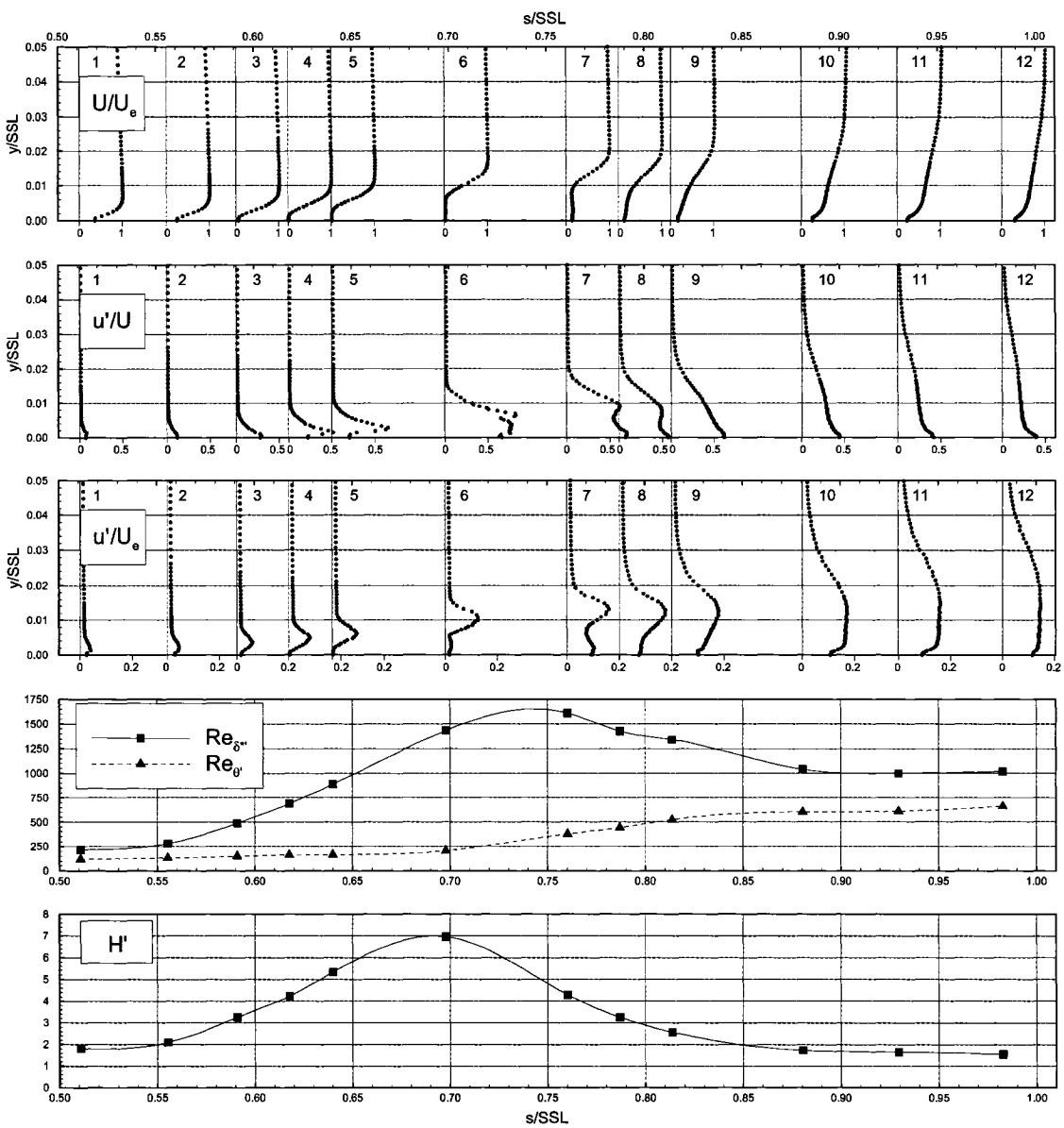

Figure 5.8: **Boundary Layer Profile Measurements for** $FSTI = 3.9\%$

layer.

The integral parameters calculated from the mean velocity profiles are shown in the two lower graphs of Figure 5.8. The displacement thickness increases quickly after separation, whereas the momentum thickness remains low until transition begins at approximately station 6 (70%SSL). The displacement thickness reaches a maximum at station 7 ($\sim$ 76%SSL) which, based on observations of Yaras (2002) for a simulated LPT flat-plate experiment, may indicate the start of reattachment. This location corresponds with the knee of the surface static pressure distribution. Downstream of reattachment, the displacement thickness and momentum thickness both increase. The shape factor grows quickly after separation and reaches a maximum near the estimated start of transition (station 7), which is also seen in the data of Yaras (2002). Near the trailing edge, the shape factor drops to approximately 1.5, which is typical of a turbulent boundary layer in a strong adverse pressure gradient.

The mean velocity and fluctuation level profiles presented in Figure 5.8 are very similar to those presented by Volino and Hultgren (2001) for a flat-plate experiment with a simulated Pak-B pressure distribution, and those by Volino (2002) for a large scale, single passage Pak-B experiment. In these studies, intermittency was extracted from the hot-wire measurements. From their intermittency profiles, it is seen that at the location where transition begins in the separated shear layer, RMS fluctuation levels increase inside the bubble. These increases are very similar to the near-wall increases in Figure 5.8, where transition is assumed to begin.

Figure 5.9 compares the mean velocity and RMS fluctuation profiles with the surface static pressure and surface-mounted hot-film measurements from Chapter 4. The separation point ($\sim$ 60%SSL) agrees for all measurements, within the resolution of the measurement locations, as do the locations of transition onset ($\sim$ 70%SSL) and reattachment ($\sim$ 81%SSL).

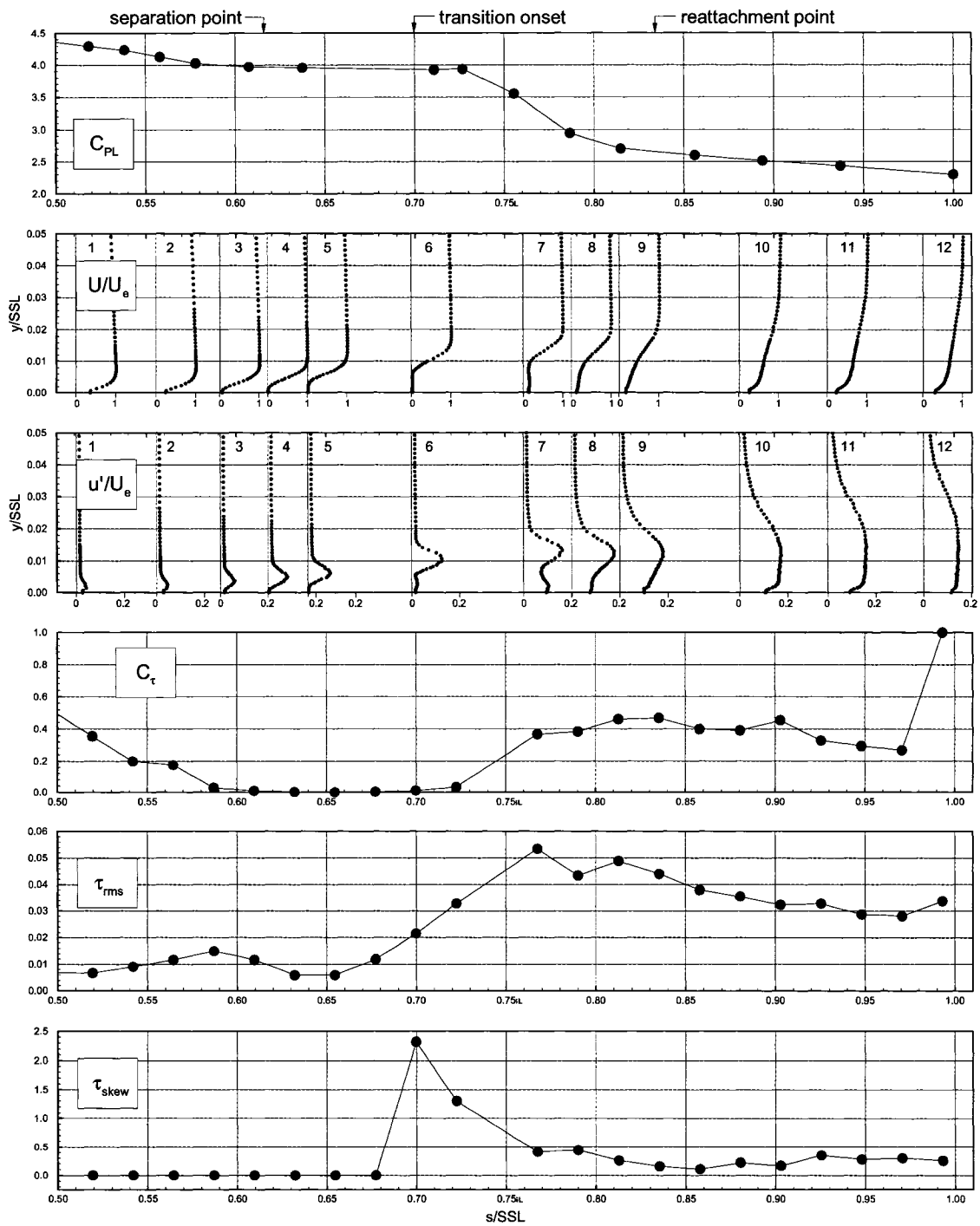

Figure 5.9: **Pressure, Hot-Wire, and Hot-Film Measurements for** $FSTI = 3.9\%$

The increased RMS fluctuation levels within the separation bubble correspond with the first location of positive skewness of quasi-wall shear stress, which has been interpreted in Section 4.4.2 as the location of transition onset. The hot-wire traverse measurements presented in this section add additional confidence to the surface-mounted hot-film interpretation method of Mahallati (2003) for reattached separation bubbles.

5.5 Summary of Boundary Layer Traverse Measurements

Boundary layer measurement techniques using a hot-wire have been developed for the Low-Speed Turbomachinery Laboratory at Carleton University. Although there are some limitations in extracting boundary layer profiles from the current data, the initial measurements show promise for future studies of boundary layer transition over LPT airfoils. The accuracy of the test-section traverse mechanism has allowed detailed measurements within the boundary layer over the aft section of the Pak-B suction surface. A relatively simple modification to the test-section will allow traverse measurements more nearly normal to the blade surface. This would involve a two-degree of freedom linear traverse mechanism mounted to the bottom tailboard (tailboard shown in Figure 3.2 of Section 3.2.2). This modification will give an additional degree of freedom to allow movement normal to the blade surface.

Boundary layer traverse measurements have been made for a Reynolds number of 50000 at FSTIs of 0.4% and 3.9%. The separated shear layer characteristics for both FSTI cases have been examined in terms of the mean and fluctuating components of velocity in the form of colour-flood contour plots and velocity profiles. For the low FSTI case, transition appears to begin in the separated shear layer but insufficient entrainment of freestream fluid prevents reattachment to the surface. This open separation bubble results in high profile losses and decreased flow turning. High FSTI promotes transition and reattachment

of the shear layer which results in low profile losses and the desired flow turning. The high FSTI hot-wire measurements agree well with the surface static pressure distribution and surface-mounted hot-film measurements, and add confidence to the hot-film interpretation techniques developed by Mahallati (2003) for separated-flow transition.

The hot-wire traverse techniques described here have also been used in the Pak-B flow control study described in Chapter 7.

Chapter 6

Influence of Turbulent Length Scale on the Pak-B Cascade

6.1 Motivation

In the absence of incoming upstream wakes, it is generally accepted that Reynolds number, pressure gradient history, and freestream turbulence are the dominant parameters affecting transition over low-pressure turbine (LPT) airfoils for attached (Solomon *et al.*, 1996, Roberts and Yaras, 2003) and separated (Yaras, 2001, Yaras, 2002) flows. Most studies have focused on the effects of freestream turbulence level without regard for the spectrum of turbulence. Recently, a series of three papers have discussed the importance of the freestream turbulence spectrum on laminar heat transfer and pre-transitional flow in gas turbines (Dullenkopf and Mayle, 1995, Mayle and Schultz, 1997, Mayle *et al.*, 1998). Mayle *et al.* (1998) proposed a unified spectrum for freestream turbulence which can be described by the level of turbulence and any turbulent length scale. To account for the spectrum of turbulence, Butler *et al.* (2001) studied the heat transfer distribution over a

turbine airfoil at low-Reynolds number with varying levels of turbulent integral length scale and found that for the levels of integral length scale examined, no effect on the transition onset location was observed for an attached boundary layer.

During the course of the current experimental program, a new turbulence generating grid was designed and manufactured to produce high-FSTI, similar to that of the previous study by Mahallati (2003) (grid H1), but with a smaller turbulent length scale. This new grid, designated "grid H3", was described in Section 4.2. The freestream turbulence intensities and integral length scales at the inlet of the cascade are tabulated in Table 6.1 for the two grids.

In this chapter, the effects of turbulent length scale on separated-flow transition over the Pak-B airfoil are examined by comparing the measurements of Mahallati (2003) using grid H1 with the measurements of the current author using grid H3 (grid H3 results presented in Chapter 4). Four Reynolds numbers have been examined: 25000, 50000, 100000, and 150000. First, differences in the axial velocity ratio between the two sets of data are presented. Then, comparisons between the loading distribution, the downstream wake profiles, the mixed-out profile losses, the outlet flow deviation angles, and the surface-mounted hot-film measurements are presented. The chapter concludes with a summary of the influence of turbulent length scale on the aerodynamics of the Pak-B airfoil.

Table 6.1: **Cascade Inlet Turbulence Characteristics for Grids H1 and H3**

Grid	$FSTI$	Λ/B_x
H1	3.8 ± 0.5	0.32 ± 0.07
H3	3.9 ± 0.5	0.11 ± 0.04

6.2 Axial Velocity Ratio

Before discussing the influence of turbulent length scale on the Pak-B cascade, one difference in the cascade flow between the two grids used must be highlighted. The close proximity of grid H3 to the cascade has an effect on the axial velocity ratio (AVR), which defines the spanwise convergence ($AVR > 1$) or divergence ($AVR < 1$) of the mid-span flow through the cascade. Figure 6.1 shows the cascade AVR for grids H1 and H3 over the range of Reynolds numbers examined. It is desired to achieve an AVR close 1.0 to simulate two-dimensional flow. The AVR for grid H3 is slightly low ($\approx$ 0.97 to 0.99), whereas the AVR for grid H1 is slightly high ($\approx$ 1.00 to 1.02). The values of AVR for grid H1 are typical of values observed for turbine cascades.

Data of Rodger *et al.* (1992) show that for a turbine cascade, losses and deviation angle are a function of AVR, with losses increasing as AVR drops below 1, and flow deviation

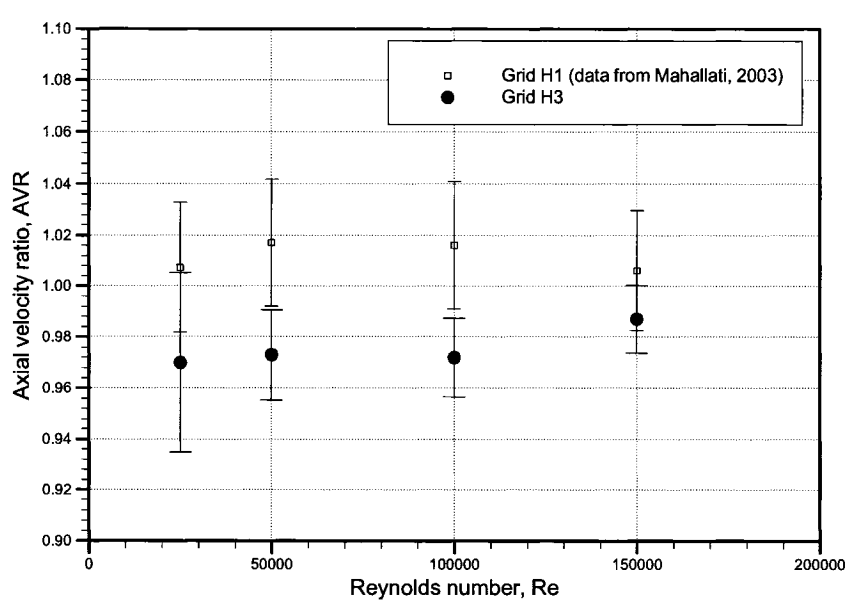

Figure 6.1: **Axial Velocity Ratio of Pak-B Cascade for Grids H1 and H3**

angle decreases slightly with decreasing AVR. Rodger *et al.* (1992) observed an increase in losses of approximately 50% between $AVR = 1.0$ and $AVR = 0.97$. This suggests that the low AVR of grid H3 may have an undesired effect on the losses when comparing against the data for grid H1. The cascade of Rodger *et al.* (1992) had an aspect ratio of approximately 1.0 and the current cascade has an aspect ratio of 2.4. The endwall boundary layers and secondary flows affect the mid-span flow more so when the aspect ratio is small, therefore any difference in losses between the current study and that of Mahallati (2003) are not expected to be as significant as for the case of Rodger *et al.* (1992). The following sections compare the cascade measurements made for the two grids.

6.3 Loading Distributions

Figure 6.2 shows the loading distributions for an FSTI of approximately 4% with integral length scales of 11% and 32% of axial chord, for all Reynolds numbers examined.

There is very little difference in the pressure surface loading distribution for the two different length scales, at all Reynolds numbers. As for the suction surface, there are a few differences between the two cases. First, the loading over the forward part of the blade is slightly higher for the small length scale cases. Also, the location of the suction peak is slightly different, with the small length scale location ahead of the large length scale location by approximately 2% to 3% of axial chord. These observations are believed not related to the difference in length scales, but to the difference in grid location for the two sets of data. The small length scale cases have an imposed adverse pressure gradient across the cascade due to the reduced AVR. Data of Rodger *et al.* (1992) show a similar increase in the forward suction surface loading for reduced AVR (≈ 0.97) at design incidence. The non-uniformities present in the cascade inlet flow for grid H3 (described in Section 4.3.3) may also have an effect on the loading distribution.

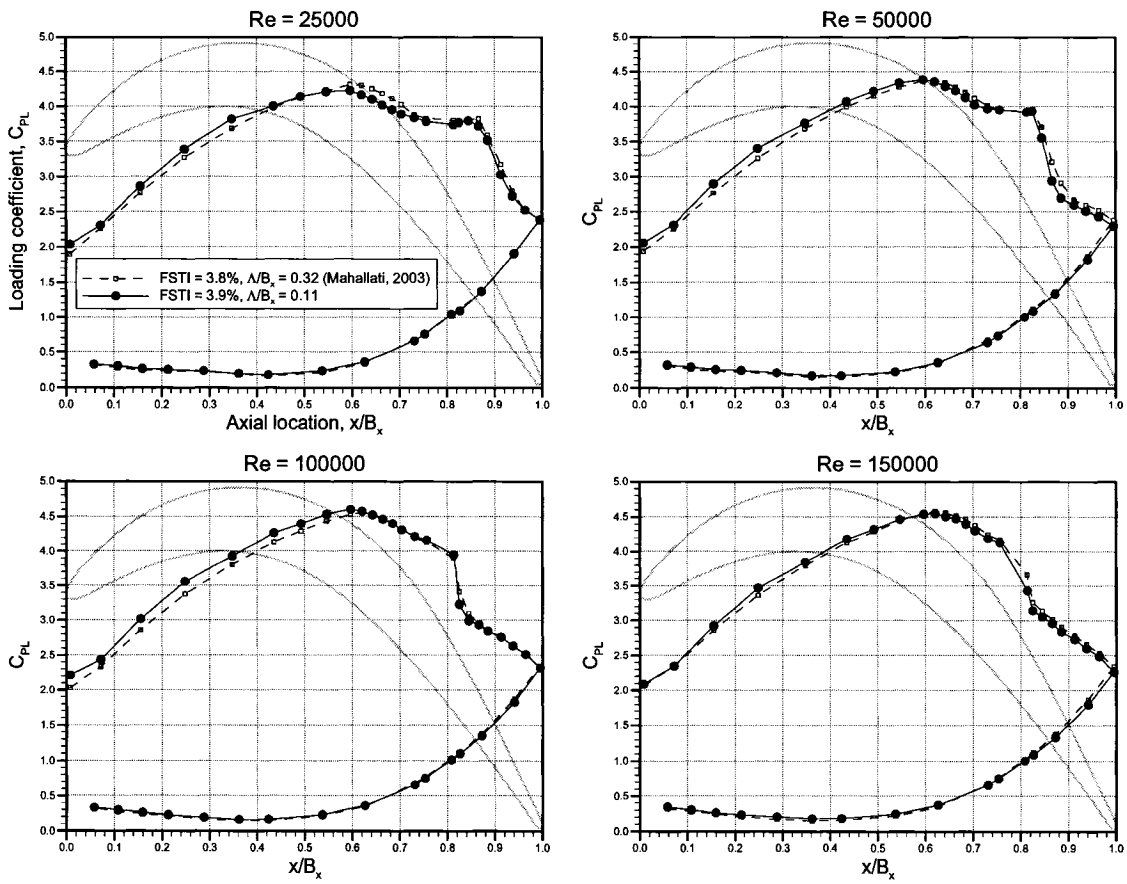

Figure 6.2: **Influence of Turbulent Length Scale on Loading Distributions**

The location of separation for the two length scale cases is essentially the same, within the resolution of the static pressure tap locations. The location of transition also appears to coincide for all Reynolds numbers, as inferred by the knee of the separation bubble. The reattachment point, on the other hand, appears to have moved slightly upstream by approximately 1% to 2% of axial chord (2% to 3% of suction surface length) for the small length scale cases. In the study by Roberts and Yaras (2003) for attached flows, transition was affected by variations in turbulent length scale, but only when the integral length scale was of the same order as the boundary layer thickness near transition. The locations of separation, transition onset, and reattachment will be discussed further in Section 6.7, where

the surface mounted hot-film data will be discussed. The following section will discuss the influence of turbulent length scale on the downstream wake profiles.

6.4 Wake Profiles

The wake profiles for both turbulent length scales investigated are shown in Figure 6.3. It is clear that the wakes for the small length scale cases are deeper than their corresponding large length scale cases, and that, except at a Reynolds number of 25000, the small length scale wakes are thinner. Both sets of measurements were made at the same distance downstream of the cascade.

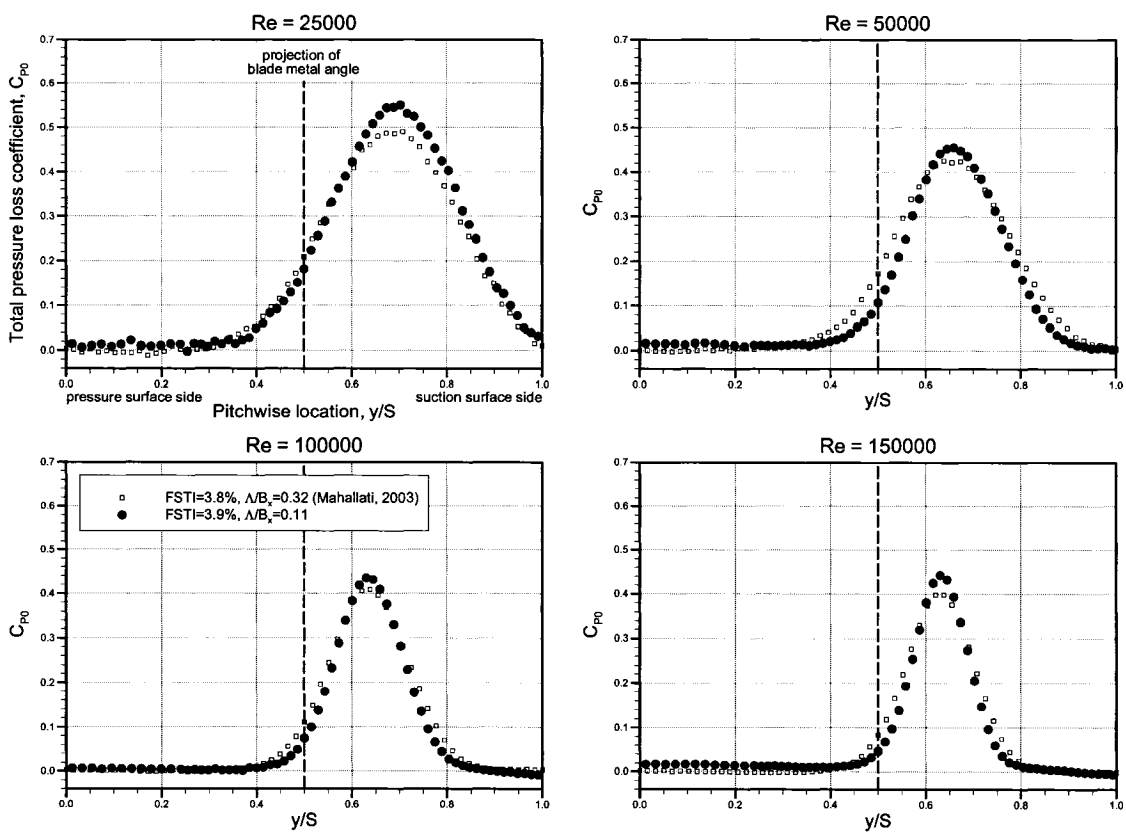

Figure 6.3: **Influence of Turbulent Length Scale on Wake Profiles**

The wakes in Figure 6.3 appear to diffuse more quickly for larger length scales. This has also been observed by Ames and Plesniak (1995) who made measurements downstream of a first-stage nozzle cascade at elevated levels of FSTI. Their experiments included two cases with nearly identical FSTI of approximately 8% but with length scales of 11% and 30% of blade chord. The wakes for their small length scale measurements were deeper and thinner than the larger length scale case. Although no direct explanation is given by Ames and Plesniak for the differences in the wakes, two-dimensional hot-wire measurements downstream of their cascade shed some light on the observations. In the downstream wakes, the large-length scale case has slightly higher turbulent shear stress levels, which leads to an increase in the wake growth rate. In the downstream "loss-free" regions between the wakes, the streamwise velocity fluctuations have the same level for both cases, but the cross-stream velocity fluctuations for the large length scale case are approximately 30% greater than those for the small length scale case. The current author believes that the larger cross-stream fluctuations promote higher entrainment of freestream fluid into the wake, causing the increased turbulent shear stresses, and enhancing the wake decay rate. This of course has not been documented for the current study and it is recommended that the turbulence field downstream of the cascade be examined with a two-component hot-wire (X-wire).

As already mentioned, the momentum deficit downstream of a cascade airfoil is a measure of the total pressure losses across the cascade. The following section discusses the mixed-out profile losses for both levels of integral length scale examined.

6.5 Mixed-Out Profile Losses

Figure 6.4 presents the comparison of profile losses for the two turbulent length scales investigated. The losses are higher for the small length scale experiments by approximately 25%. Some of this increased loss may be a result of the close proximity of the turbulence generating grid to the cascade, with increased losses due to the decay of inlet flow non-uniformities through the blade passages. However, this would not appear to account fully for the difference in losses between the two length scales. Recalling the discussion in Section 6.4 regarding the downstream wake profiles, it is seen in Figure 6.3 that, apart from at a Reynolds number of 25000, the momentum deficit within the wakes for the two length scale cases is approximately the same. Another possible reason the difference in losses arises from the differences in AVR across the cascade for the two grids (described in Section 6.2). A decrease in AVR results in an adverse pressure gradient across the cascade, which enhances the adverse pressure gradients over the blade surfaces. Measurements presented by Rodger

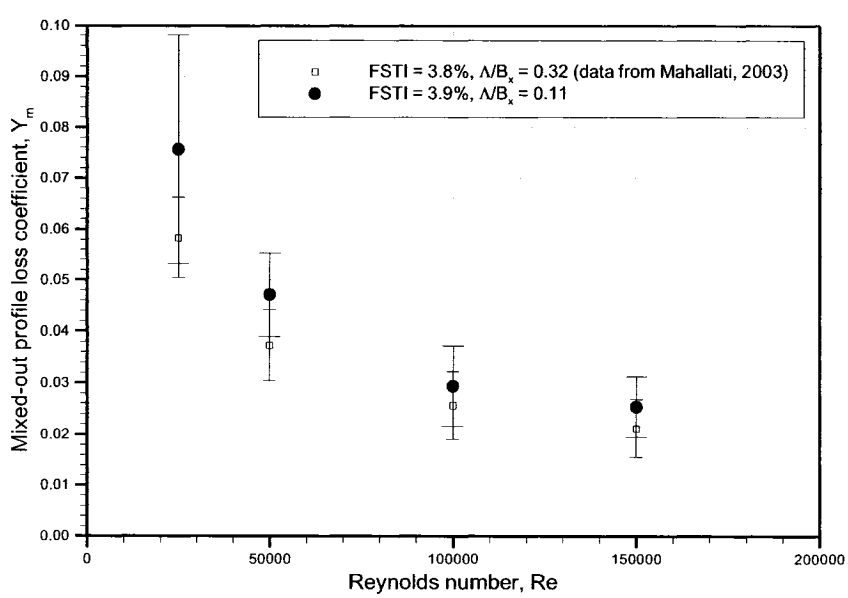

Figure 6.4: **Influence of Turbulent Length Scale on Mixed-Out Profile**

et al. (1992) in a turbine airfoil cascade show an increase in losses as AVR is decreased. Although these differences in losses are present in the current measurements, the trend with Reynolds number is similar.

The flow deviation angle is also an important performance parameter in cascade studies, and the influence of length scale on deviation is described in the next section.

6.6 Mixed-Out Deviation Angles

The mixed-out deviation angles for the two length scale cases are shown in Figure 6.5. The influence of turbulent length scale on deviation is minimal resulting in similar flow turning. As the Reynolds number is decreased below a value of 100000, the deviation angle increases slightly for both levels of length scale investigated.

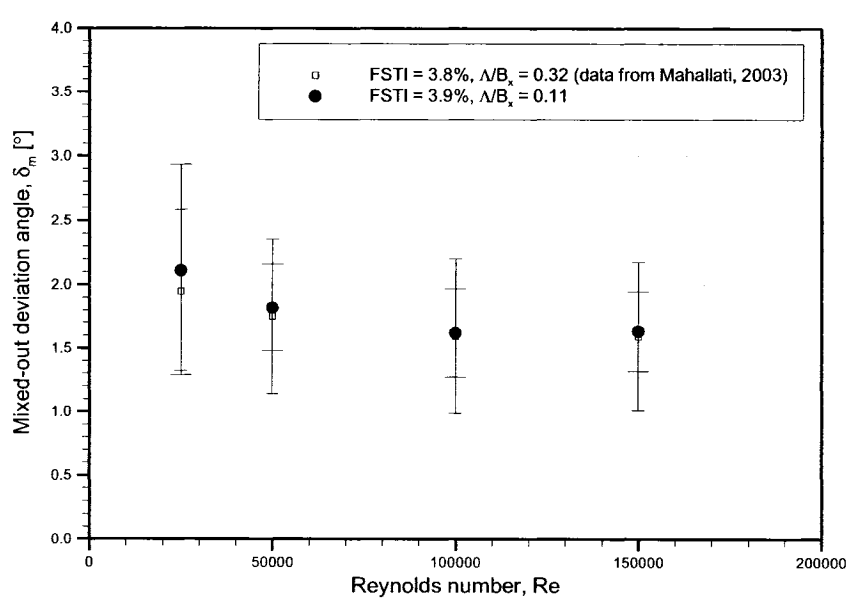

Figure 6.5: **Influence of Turbulent Length Scale on Mixed-Out Deviation Angles**

6.7 Transition Process Over Suction Surface

As discussed in Chapter 4, surface mounted hot-film measurements are a useful technique for examining the transition process over the suction surface of the Pak-B airfoil. This section compares the mean, RMS, and skewness of the quasi-wall shear stress signals for similar FSTI but with two different levels of integral length scale. Figures 6.6 and 6.7 show the distributions of statistical quantities of the quasi-wall shear stress over the suction surface length (SSL) for the two cases, along with the surface static pressure distribution measurements. Reynolds numbers of 25000 and 50000 are shown in Figure 6.6 and Reynolds numbers of 100000 and 150000 are shown in Figure 6.7.

The locations of separation, transition onset, maximum bubble height, and reattachment are indicated in Figures 6.6 and 6.7, and are are inferred based on the hot-film interpretation method described in Section 4.4.2. The location of separation is indicated by the first sensor where the quasi-wall shear stress is approximately zero. Transition onset is indicated by the first sensor where the skewness becomes a positive non-zero value. The location of maximum bubble height has been inferred from the location of maximum RMS, and reattachment is indicated by the first local maximum in mean quasi-wall shear stress downstream of the separation point (except at $Re = 100000$ where this is estimated to occur between 72% and 77% SSL).

The inferred locations of separation, transition onset, maximum bubble height, and reattachment are all approximately the same for both length scales examined, within the resolution of the sensor spacing. One discernible difference between the two length scales is a slightly higher RMS levels for the larger length scale cases downstream of the suction peak, ahead of and after the separation bubble. This is likely due to the larger freestream eddies that have a stronger buffeting effect on the boundary layer, in particular the laminar boundary layer between the suction peak and the separation point. Also, there appears to be

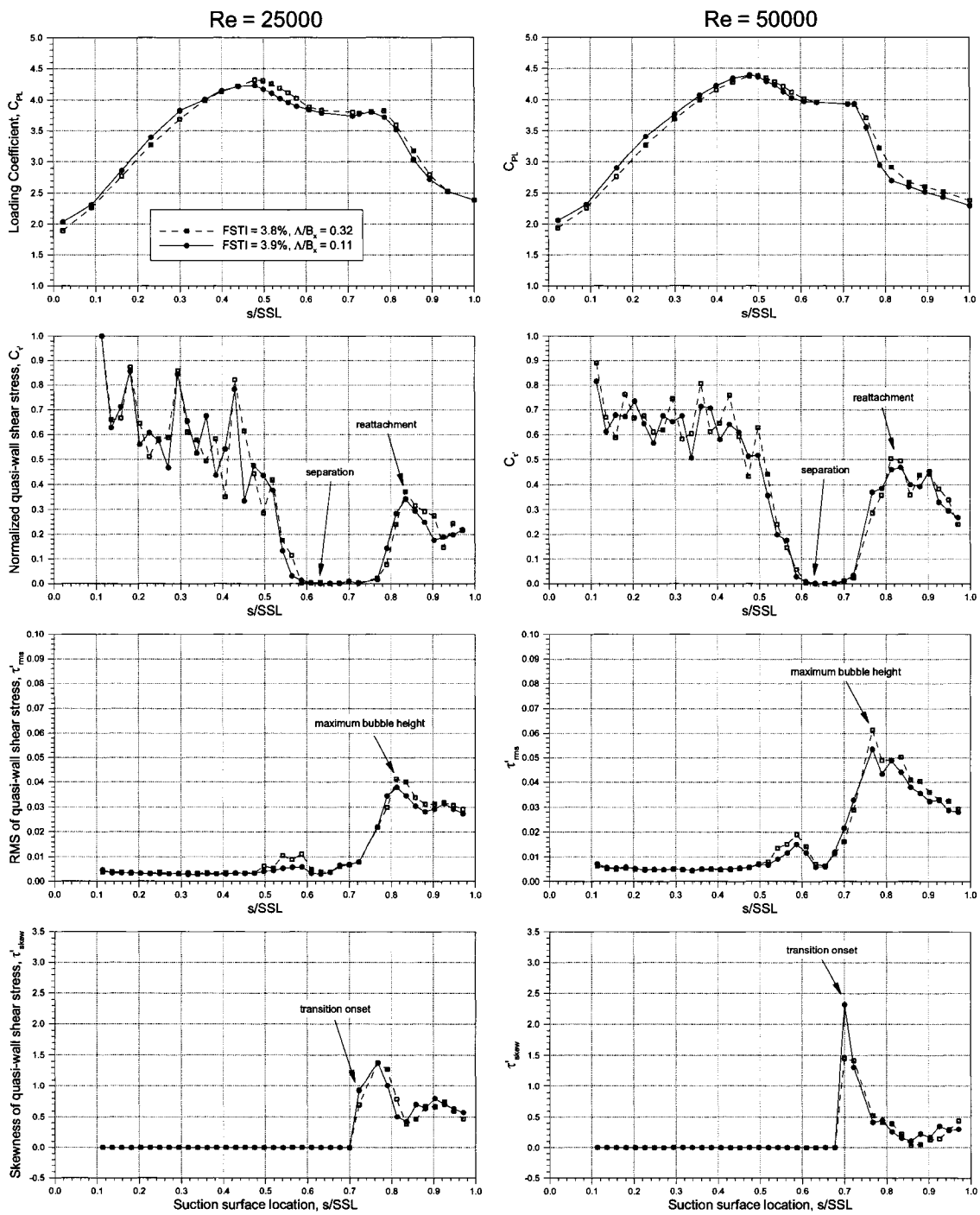

Figure 6.6: **Hot-Film Measurements for** $Re = 25000$ **and** $Re = 50000$

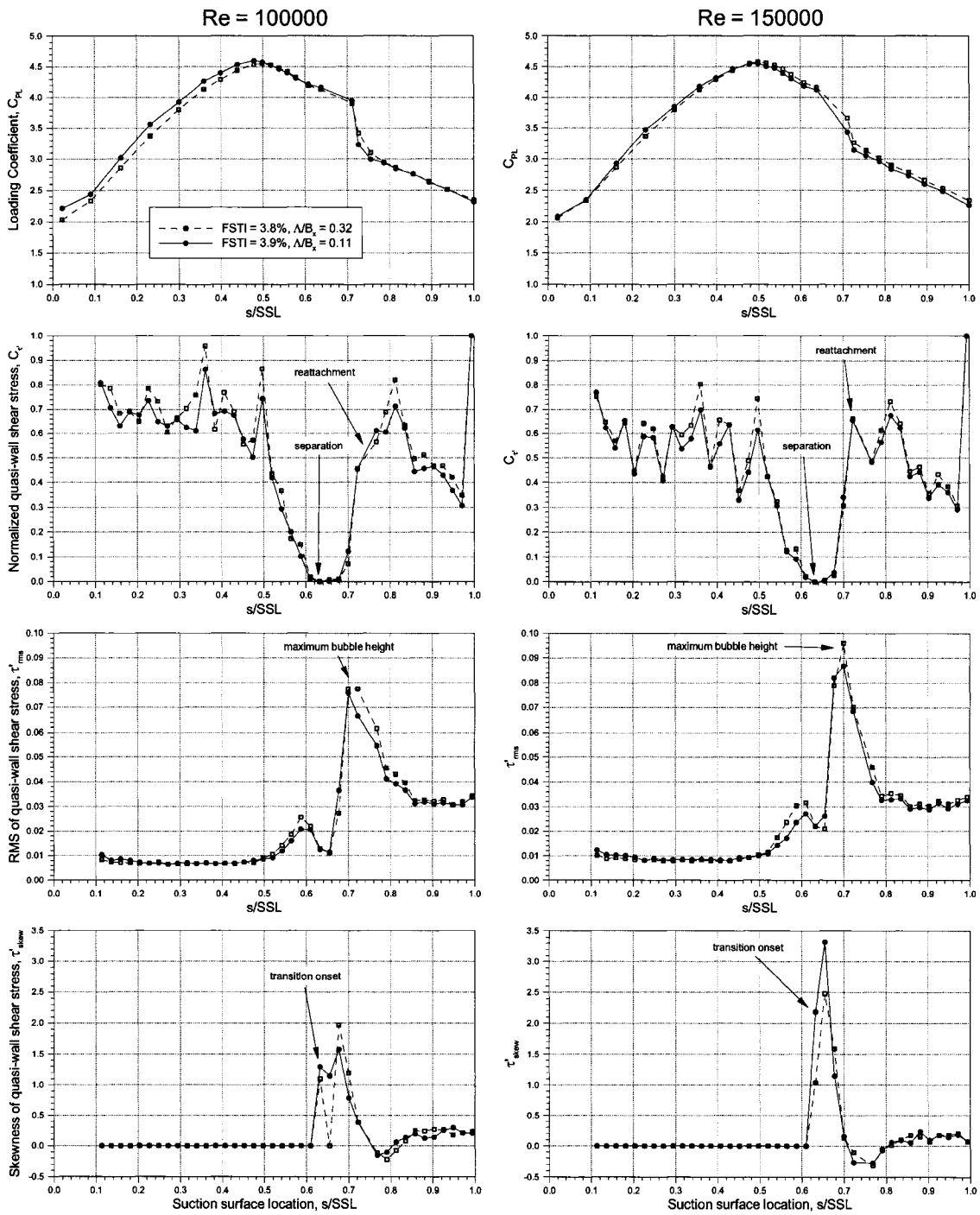

Figure 6.7: **Hot-Film Measurements for** $Re = 100000$ **and** $Re = 150000$

a slight downstream shift in the skewness distribution for the larger length scale cases. This shift is approximately the same length as the apparent shift in the reattachment location inferred from the pressure distribution. This could be due to the difference in AVR between the two grid arrangements.

6.8 Summary of Length Scale Study

This chapter has presented measurements made for the Pak-B cascade for two different levels of freestream turbulent length scale with similar levels of freestream turbulence intensity. In general, the separation and transition characteristics are similar for both levels of turbulent length scale examined.

The surface static pressure measurements show higher loading in the forward acceleration region of the suction surface, and show a slight upstream shift in the suction peak for the small length scale cases. The mixed-out profile losses for the small length scale cases are approximately 25% higher than those for the larger length scale cases. Deviation is essentially the same for both levels of length scale. The surface-mounted hot-film measurements show very little difference in the transition process for the two length scales examined. The larger freestream integral length scale cases show a slightly delayed transition onset location and reattachment location over the suction surface. The differences observed for the two levels of integral length scale examined are assumed primarily due to the differences in AVR between the two cascades, and not the level of turbulent length scale.

Chapter 7

Flow Control Measurements

7.1 Introduction

Low-pressure turbines in modern aero-engines operate under low Reynolds number conditions at cruise altitude. As discussed in Chapter 2 and shown in Chapter 5, a typical high-lift turbine airfoil can stall under these conditions, resulting in increased losses and decreased engine efficiency. This chapter examines a flow control concept that can be used to suppress stall in an LPT cascade.

There are two general methods of flow control, each characterized by the energy expenditure required by the flow control device. Passive flow control requires no auxiliary energy and no control loop. Active flow control requires energy expenditure and may use a control loop (Gad-el-Hak, 2001). For active flow control there are two general control strategies. The first is known as "predetermined" control, in which steady or unsteady energy input is applied without regard to the state of the flow. The second is known as "reactive" control, in which a control loop is continually adjusted based on measurements of the flow, using either an open feedforward or a closed feedback control loop. More details

of these control methods are given in Section 2.7.

Although passive flow control devices require no energy input, these devices may be effective only at operating conditions where control is required, and may have a negative impact on performance at operating conditions where control is not required. The benefit of active flow control is that the control device can be turned on only when needed. The current study evaluates a method of active flow control for separation control in an LPT cascade. A predetermined control strategy is used for the present experiments, but the implementation of a reactive control loop might be desirable for practical use.

The current control strategy consists of localized fluid injection by means of an inclined plane wall jet, at a location upstream of the nominal suction surface separation point. This blowing technique has been used by Fottner (1979), Sturm *et al.* (1992) and Culley *et al.* (2003) for separation suppression of highly-loaded compressor blades. The wall jet supplies energy to the decelerating boundary layer downstream of the suction peak. This injected fluid can increase the momentum in the near-wall region of the boundary layer, which is then expected to resist stronger pressure gradients and which may, therefore, delay or even suppress separation. For the current investigation in which a laminar boundary layer separates from the surface, the injected fluid is also expected to have an effect on the transition process.

The flow control configuration under investigation also acts as a passive flow control device. With no fluid injection, the wall jet injection slot acts as a spanwise recessed groove at a location just upstream of separation. Lake *et al.* (2000) examined two types of recessed surface modifications on the suction surface of the Pak-B airfoil: streamwise V-grooves and a spanwise row of dimples. Both of these passive flow control devices were found to improve the low-Reynolds number performance of the airfoil without affecting the higher-Reynolds number performance. Lake *et al.* (2000) found that a row of dimples located at 65% of the

Pak-B axial chord (53% suction surface length) resulted in the best overall performance enhancement.

This chapter presents experimental results for the Pak-B flow control study using the above mentioned flow control technique. The flow control configuration and test matrix are presented first, followed by a discussion of the wall jet injection characteristics. The suction surface pressure measurement results are then discussed, as well as the inlet and outlet three-hole pressure probe traverses. The hot-wire traverse measurements in the aft-suction surface region are then discussed. Finally, a summary of the flow control study is given.

7.2 Flow Control Configuration and Test Matrix

An inclined plane wall jet is used as the flow control device for the current study. The wall jet injection slot is located at approximately 52% of suction surface length ($\sim$ 64% of the Pak-B axial chord), with an inclination of approximately 38° to the surface, as shown in Figure 3.4. Details of the internal arrangement were presented in Section 3.2.4. The earlier figure is repeated here as Figure 7.1, for reference. The slot width, b, is approximately 0.3mm (0.4% B_x or 0.3% SSL) and covers the middle 78% of the blade span. The slot location is at approximately the optimum dimple location of Lake *et al.* (2000) for their passive flow control study of the Pak-B airfoil, and is also at approximately the optimum vortex generator jet (VGJ) location of Bons *et al.* (2001) for their active flow control study of the Pak-B airfoil.

The flow control device, as well as the Pak-B blade profile, have been designed by Pratt & Whitney. The slot is located slightly downstream of the suction peak of the airfoil, the region in which the developing laminar boundary layer encounters a strong adverse pressure gradient. This location is consistent with the results of Fottner (1979) for a similar flow

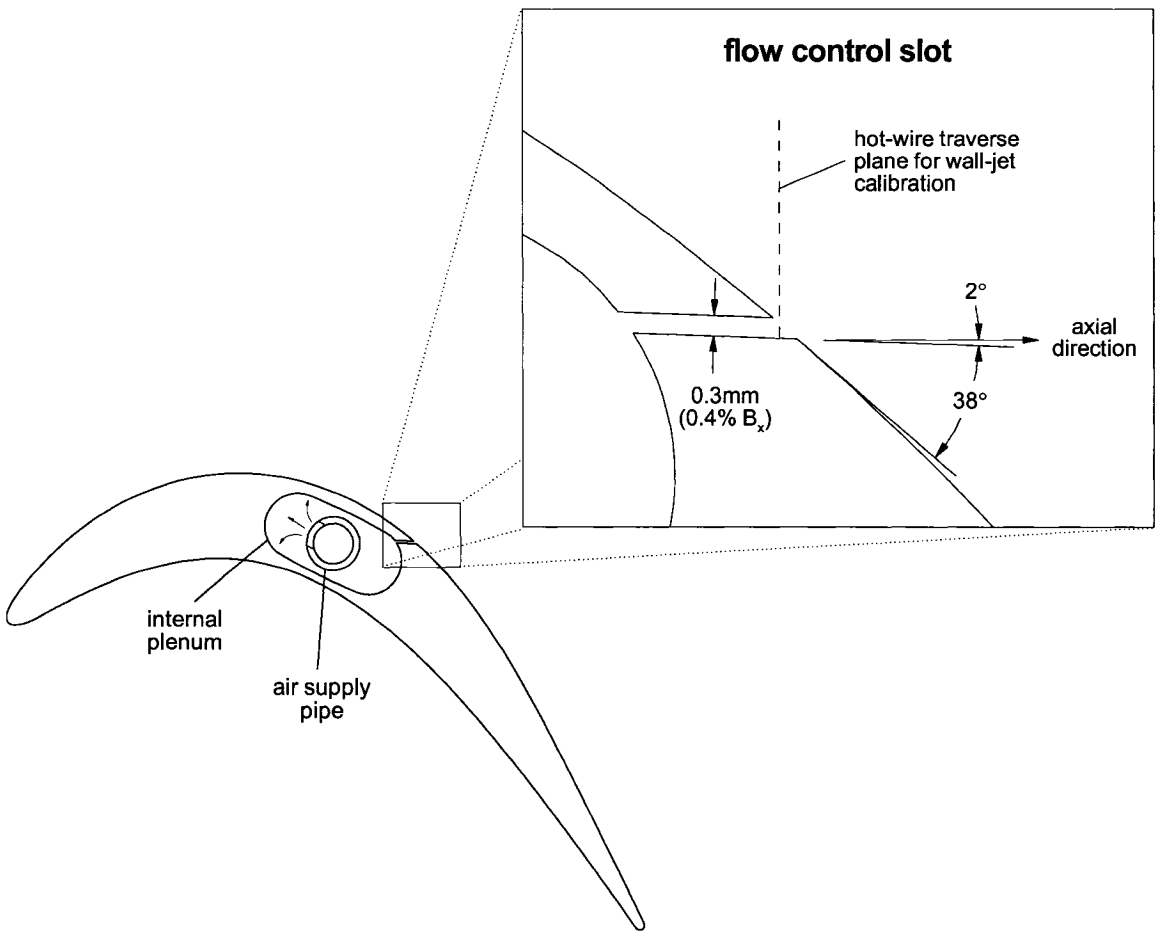

Figure 7.1: **Pak-B Flow Control Blade Configuration**

control configuration on a highly-loaded compressor blade, which concluded that the slot should be located just upstream of separation. The optimum surface location should allow sufficient mixing of the wall jet with the boundary layer ahead of the separation point. Fottner (1979) also found that the dominant jet parameter that influences separation is the jet velocity. The optimum jet velocity was found to be largely independent of the jet mass flow rate, or slot width. This indicates that the slot width should be as small as possible to reduce the required secondary air supply. For the present configuration, the high inclination angle of the slot relative to the surface is due to manufacturing restrictions.

In the current experiments, the blowing ratio, B, has been used as the characteristic jet velocity parameter, and is defined as

$$B = \frac{\rho_j U_{j_{max}}}{\rho_e U_e}$$

where $U_{j_{max}}$ is the maximum jet velocity at the injection slot outlet, U_e is the local freestream velocity, ρ_j and ρ_e are the densities of the jet and freestream flows, respectively. This parameter has been used by Fottner (1979) and Sturm *et al.* (1992) for similar studies on compressor blades, and by Bons *et al.* (1999) for separation control on an LPT blade using vortex generator jets. The blowing ratio is also typically used as a characteristic parameter for turbine film cooling. For the current study, the flow is assumed incompressible and since the measured temperature difference between the jet and freestream flows was less than $2° - 3°C$, the density ratio is assumed to be 1.0. The blowing ratio, as used in the current study, is then

$$B = \frac{U_{j_{max}}}{U_e}. \tag{7.1}$$

The test matrix for the current study consists of a range of blowing ratios for various cascade operating conditions, as summarized in Table 7.1. The focus of the study is on the

Table 7.1: **Pak-B Active Flow Control Test Matrix (Range of Blowing Ratios)**

	FSTI = 0.4%			**FSTI** = 3.9%		
Re	**3HP** *	**Loading** *	**HWT**	**3HP** *	**Loading** *	**HWT**
25000	0 → 2.0	0 → 2.0	-	0 → 1.25	0 → 1.25	-
50000	0 → 2.0	0 → 2.0	0, 0.5, 1.0, 2.0	0 → 1.0	0 → 1.25	0, 0.5, 1.0
100000	0 → 1.25	0 → 1.25	-	0	0	-
150000	0	0	-	-	-	-

3HP - three-hole probe measurements, HWT - hot-wire traverse measurements, * increments in B of ~ 0.25

low FSTI cases for which the baseline suction surface flow is fully separated at Reynolds numbers of 25000 and 50000. The high FSTI cases are used to examine the effects of flow control for cases where the separated flow normally reattaches. Surface static pressure measurements over the aft-suction surface are used to estimate the location and size of any associated separation bubbles. Performance characteristics including profile losses, deviation angles, and flow control effectiveness are calculated from three-hole pressure probe measurements. Hot-wire traverse measurements have also been made over the suction surface downstream of the slot to examine the effects of the wall jet on the boundary layer development. Before the detailed measurements were made, the characteristics of the wall jet injection flow were measured, and these measurements are discussed in the next section.

7.3 Wall Jet Characteristics

Since the blowing ratio, B, is the parameter used to describe the level of secondary fluid injection, it was required to set this parameter during the experiments. To do so, a hot-wire was traversed across the jet injection plane and the local boundary layer. The traverse plane is in the pitchwise direction and, as shown in Figure 7.1, is within 2° of being normal to the jet emerging from the injection slot.

The wall jet and corresponding local boundary layer profiles for various blowing ratios are shown in Figures 7.2 and 7.3 for an FSTI of 0.4% at Reynolds numbers of 25000 and 50000, respectively. The blowing ratio was calculated from the maximum measured velocity within the jet divided by the maximum velocity measured at the edge of the boundary layer. The influence of Reynolds number on the growth of the upstream laminar boundary layer is clearly seen from Figures 7.2 and 7.3: at a Reynolds number of 25000, the boundary layer is much thicker at the slot location than at a Reynolds number of 50000. The local boundary layer profiles also show a dependence on the blowing ratio, particularly at a

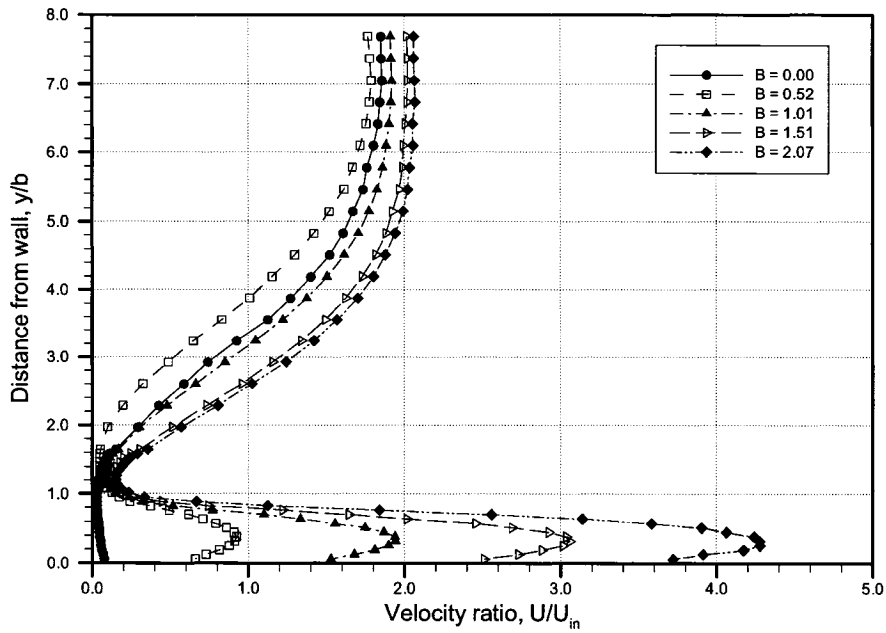

Figure 7.2: **Jet and Boundary Layer Profiles for Re = 25000 and $FSTI$ = 0.4%**

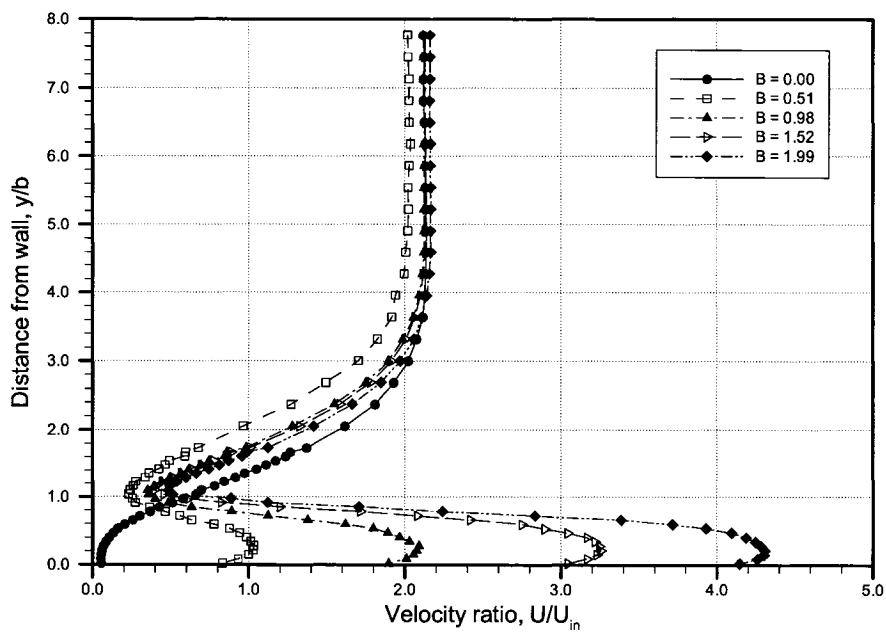

Figure 7.3: **Jet and Boundary Layer Profiles for Re = 50000 and $FSTI$ = 0.4%**

Reynolds number of 25000. At low blowing ratios, the velocity at the edge of the boundary layer is lower than for high blowing ratios. These effects are discussed further in later sections when the blade performance and aerodynamic characteristics are presented.

In order to set the blowing ratio during the subsequent measurements, the blowing ratio for the middle blade of the cascade was calibrated against the internal plenum pressure, as described in Appendix E. This pressure was measured by a static pressure tap located inside the blade plenum. During initial trials, the blowing ratio across the blade span was adjusted by adjusting the two manifold valves controlling the flow into the two ends of each blade plenum. The variation in blowing ratio across the blade span was adjusted to be within 10% of the mid-span value. The blowing ratios of the two adjacent flow control blades were adjusted using the manifold valves to be the same as that for the cascade middle blade, to within ±10%.

It is desired to minimize the required secondary air supply to the flow control device since, for future practical applications in an engine, it is important to keep the compressor bleed-air requirements to a minimum. A mass flow ratio, M, is defined as

$$M = \frac{\int_0^b d\dot{m}_j}{\int_0^S d\dot{m}_i} = \frac{\int_0^b (\rho u_j)_{MS} dy}{\int_0^S (\rho u_i \cos\alpha_i)_{MS} dy} = \frac{b}{S\cos\alpha_i}\int_0^1 (\frac{u_j}{u_i}) d(\frac{y}{b}). \tag{7.2}$$

where $\dot{m}_j$ and $\dot{m}_i$ are mass flow rates per unit span, measured at mid-span. M describes the mid-span mass flow rate of secondary air, $\dot{m}_j$, compared to the mid-span passage inlet mass flow rate, $\dot{m}_i$. The relationship between the mass flow ratio (Equation 7.2) and the blowing ratio (Equation 7.1) is shown in Figure 7.4. Assuming similar velocity profiles for the jet and the blade-to-blade flow at different operating conditions, the relationship between M and B is expected to be linear, which is seen in Figure 7.4 to be approximately the case. A maximum jet mass flow rate of approximately 1.3% of blade passage inlet mass flow rate is found for the range of blowing ratios considered.

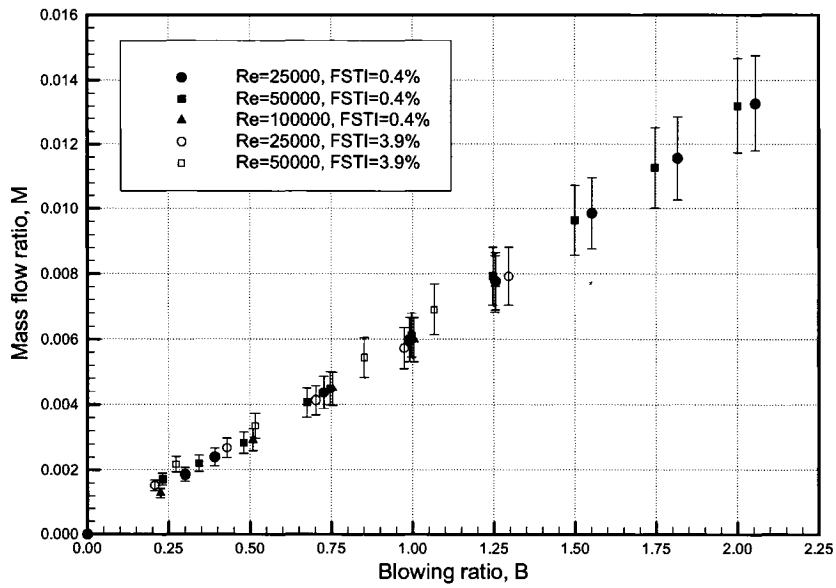

Figure 7.4: **Mass Flow Ratio vs. Blowing Ratio for Current Study**

The data presented in Figure 7.4 includes all the cases for which downstream three-hole pressure probe measurements have been made. In the next section the cascade flow quality, including inlet flow uniformity, outlet flow periodicity, two-dimensionality, and jet blowing steadiness, is presented.

7.4 Cascade Flow Quality

7.4.1 Inlet Uniformity and Outlet Periodicity

In steady-inflow cascade experiments, it is important to achieve uniform inlet flow and periodic outlet flow, as discussed in Section 4.3.3. Due to the significant differences in downstream flow pattern between stalled and unstalled conditions, multiple flow control blades are required to achieve periodic flow downstream of the cascade. Three flow control blades, mounted in the three middle positions of the cascade, were used to achieve relatively

periodic downstream flow.

Three-hole pressure probe traverse measurements have been made at midspan at $1.2B_x$ upstream and $0.5B_x$ downstream of the three flow control blades. These measurement planes are shown in Figure 4.10 on page 80. The measurements are shown in Figures 7.5 and 7.6 for two different flow conditions. These two cases are typical of the uniformity and periodicity achieved for all cases examined.

Figure 7.5 shows the inlet and outlet measurements for a Reynolds number of 50000, a freestream turbulence intensity of 0.4%, and a blowing ratio of 1.0. The flow upstream of the cascade (left-hand plots) is relatively uniform. The flow incidence angle is slightly low ($\sim$ 1.5° lower than design inlet flow angle of 35°). It was found that this could not be corrected for using the test section flow control flaps without sacrificing uniformity in the static and dynamic pressure. The measurements downstream of the cascade (right-hand plots) show slight differences in flow angle, dynamic pressure and static pressure distributions between the blade passages. This results from the lack of periodicity across the entire cascade, due to the lack of flow control on the upper and lower pairs of blades.

Figure 7.6 shows the inlet and outlet measurements for a Reynolds number of 50000, a freestream turbulence intensity of 3.9%, and a blowing ratio of 0.5. The high FSTI was achieved using turbulence generating grid H3 (discussed in Chapter 4). This grid is located close to the cascade where the disturbed flow from the grid does not have time to mix-out fully before entering the cascade, as discussed in Section 4.3.3. The non-uniformities present in the inlet flow (left-hand plots) are a result of the close proximity of the grid. The measurements downstream of the cascade (right-hand plots) show some differences in deviation angle, dynamic pressure and static pressure distributions between the blade passages, as also seen for the low FSTI case presented in Figure 7.5. The effects of the close proximity grid are also seen in the total pressure loss coefficient, C_{P0e}, where the upper

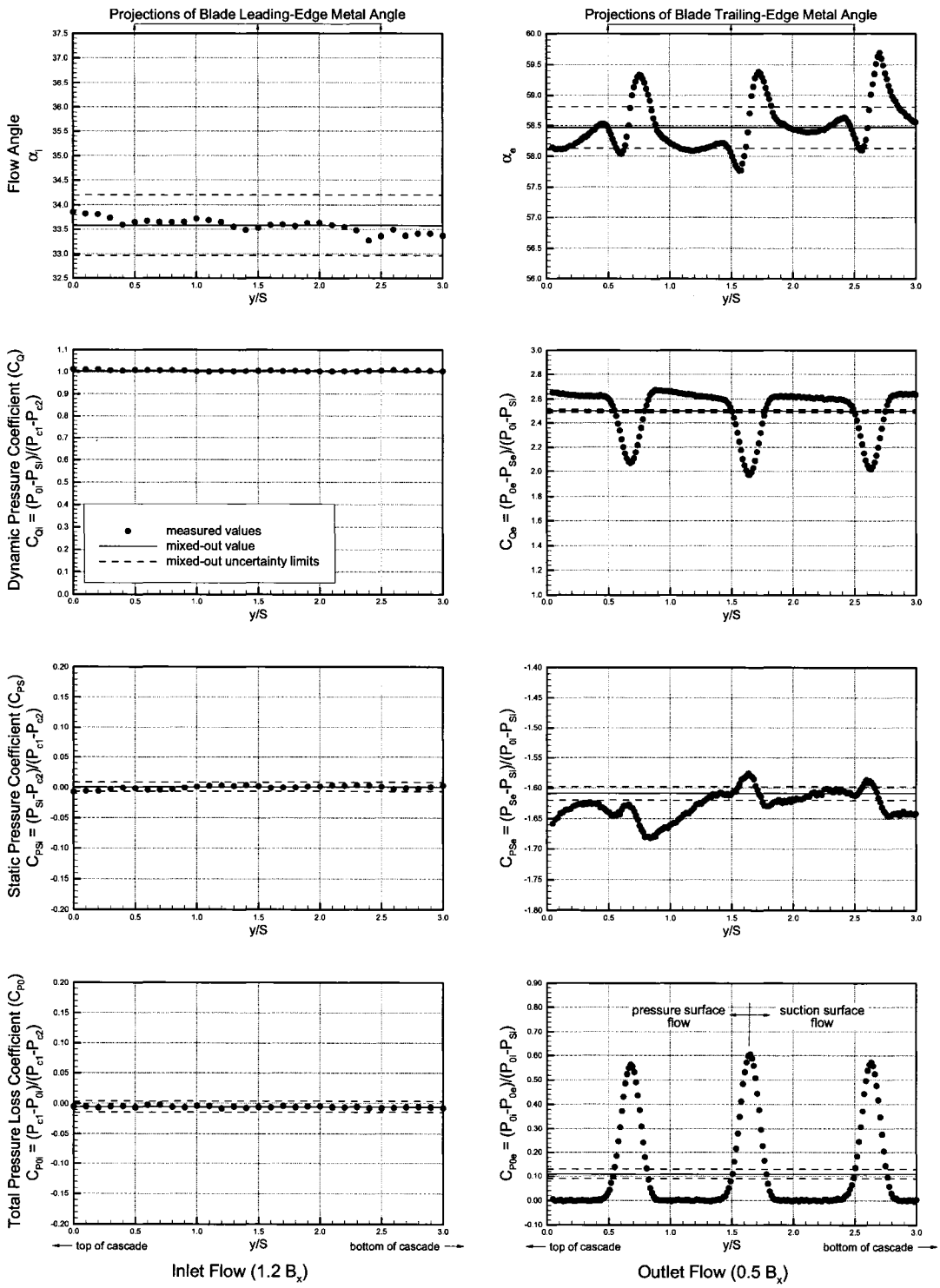

Figure 7.5: **Cascade Flow Quality for $Re = 50000$, $FSTI = 0.4\%$, $B = 1.0$**

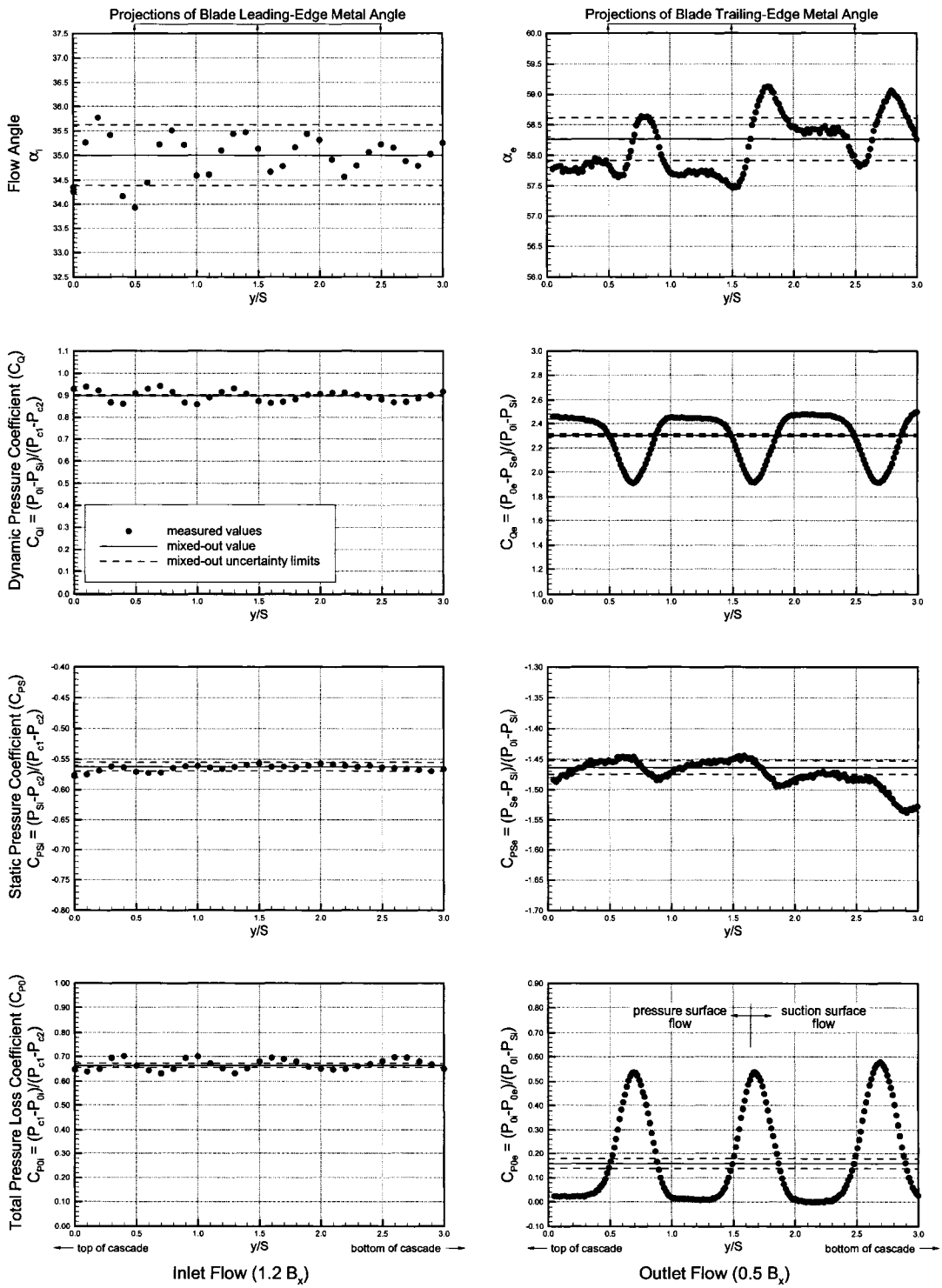

Figure 7.6: **Cascade Flow Quality for** Re **= 50000,** $FSTI$ **= 3.9%,** B **= 0.5**

blades show slight losses in the "loss-free" fluid between the wakes.

All three-hole pressure probe results presented in the cascade pressure measurements section, Section 7.5, are calculated from the measurements downstream of the cascade middle blade only (from $\sim$ 1.3 to 2.3 y/S).

7.4.2 Axial Velocity Ratio

Due to the injected mass of the jet, the measured axial velocity ratio (AVR) defined in Section 4.3.2 (Equation 4.23) does not represent the correct ratio of outlet-to-inlet mid-span mass flow rates, per unit area. Accounting for the mass injected into the blade passage through the flow control slot, which is considered inlet flow, a corrected axial velocity ratio is defined as

$$AVR' = \frac{\int_0^1 C_{Ve} \cos\alpha_e d(\frac{y}{S})}{\cos\alpha_i + \frac{b}{S}\int_0^1 \left(\frac{u_j}{u_i}\right) d(\frac{y}{b})} = \frac{AVR}{1+M} \tag{7.3}$$

which reduces to the previous definition, Equation 4.23, for zero-blowing. M is the mass flow ratio (Equation 7.2). At a blowing ratio of 2, the difference between AVR and AVR' is approximately 0.01.

The axial velocity ratio for the flow control experiments is shown in Figures 7.7 and 7.8 for FSTIs of 0.4% and 3.9%, respectively. These values are corrected for the additional jet mass flow using Equation 7.3. The AVR' for an FSTI of 0.4% (Figure 7.7) is lower than 1.0 ($\sim$0.95-1.00) for all Reynolds numbers and blowing ratios examined, which indicates a spanwise expansion of the mid-span flow. The AVR for the baseline blade cases are higher than 1.0 (Mahallati, 2003). It is assumed that the low AVR' for the flow control experiments is due to the lack of periodicity across the cascade, resulting from the difference in flow pattern between the three middle flow control blades and the outer clean blades. The presence of the flow control slot, which spans the middle 78% of the blade, may also

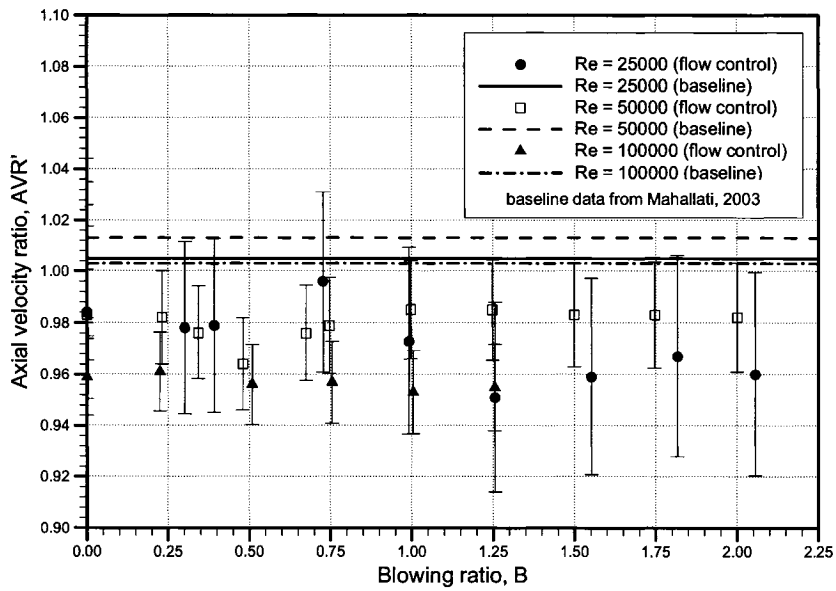

Figure 7.7: **Axial Velocity Ratios for Flow Control Experiments** ($FSTI$ = **0.4%**)

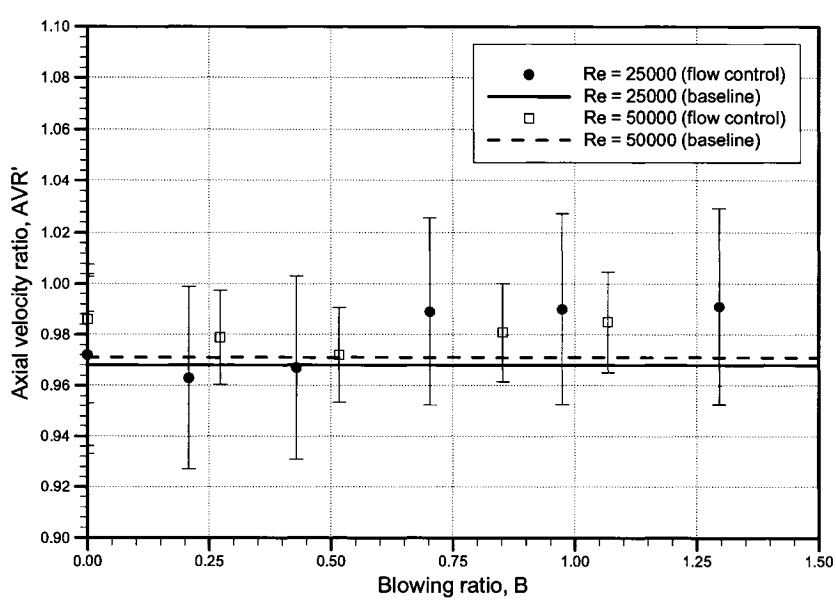

Figure 7.8: **Axial Velocity Ratios for Flow Control Experiments** ($FSTI$ = **3.9%**)

affect the end-wall and secondary flows, which largely determine the AVR. Similar AVR' characteristics are observed for an FSTI of 3.9% (Figure 7.8).

7.4.3 Wall Jet Steadiness

For the current flow control experiments, another important characteristic of the flow quality is the steadiness of the jet blowing ratio. It was found that a low-frequency oscillation in the air supply pressure was present. The measured oscillations in blowing ratio with time are shown in Figure 7.9 for the low FSTI measurements at Reynolds numbers of 25000 and 50000. Each period of oscillation is characterized by a relatively linear increase in blowing ratio, followed by a sudden drop. These oscillations are more pronounced at low Reynolds number where the required supply pressure is low. For increased blowing ratio and Reynolds number, the frequency increases and the magnitude of the fluctuations decrease. At even higher Reynolds numbers than those shown in Figure 7.9, the fluctuations are present but

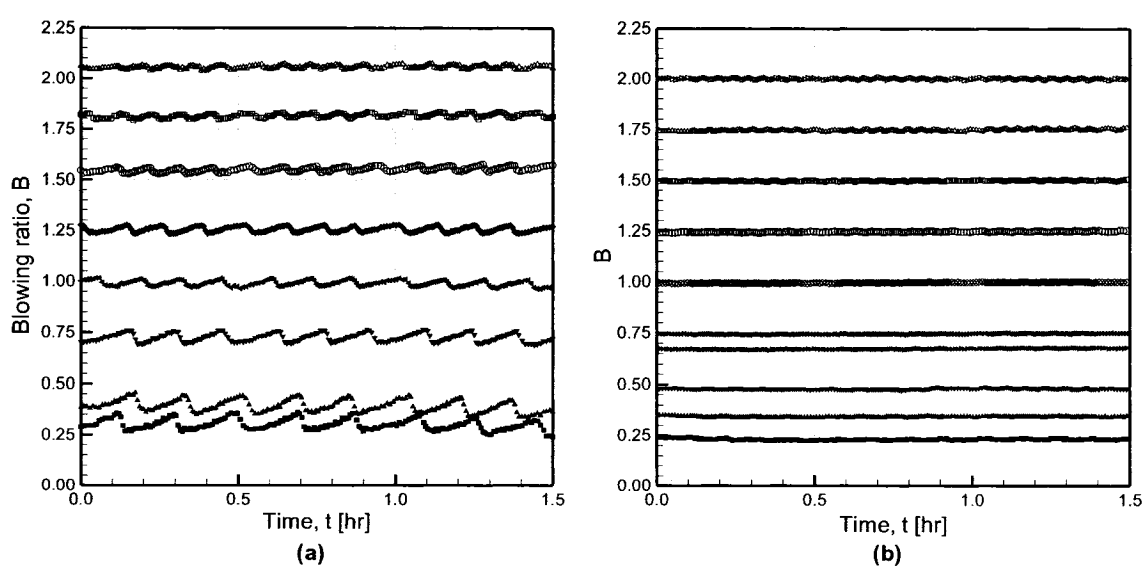

Figure 7.9: **Blowing Ratio Steadiness for (a) Re = 25000, (b) Re = 50000**

with a very low magnitude.

The next section presents the surface static pressure and three-hole pressure probe measurements for the flow control experiments.

7.5 Cascade Pressure Measurements

7.5.1 Introduction to Pressure Measurements for Current Study

To examine the aerodynamic characteristics of the Pak-B airfoil with active flow control, blade surface static pressure (loading) measurements and downstream three-hole pressure probe measurements have been made. The test matrix for these measurements was summarized in Table 7.1.

Surface static pressure measurements have been made over the aft section of the blade suction surface, downstream of the injection slot. One static pressure tap is located ahead of the slot in the acceleration region of the suction surface. The pressure tap locations were shown in Figure 3.10 on page 54.

Three-hole pressure probe measurements were made downstream of the cascade to measure the mid-span cascade performance. Detailed measurements, consisting of 65 points per pitch, were made at 0.5 B_x downstream of the three flow control blades to examine the wake characteristics. The measurement plane for these measurements has been shown in Figure 4.10 on page 80. From these downstream measurements, profile losses, flow control effectiveness, and deviation angles were calculated.

Before presenting the surface static pressure and three-hole probe measurements, an extension to the downstream mixed-out flow calculation procedure is presented, which accounts for the injection of mass and momentum through the blowing slot.

7.5.2 Extension to Mixed-Out Flow Calculation Procedure

7.5.2.1 Jet Injection Considerations

The general data reduction procedures for calculating cascade performance characteristics from three-hole pressure probe measurements have been discussed in Chapter 4 (Section 4.3.2). The calculation of profile losses assumes that the mass flow rate and total pressure into the blade passage are those calculated from the cascade inlet flow measurements. For the current flow control study, mass is injected through the flow control slot with a total pressure that may differ from the cascade inlet total pressure. This must be taken into account in the loss calculations. The following sections describe an extension to the procedures of Section 4.3.2 to account for the injected momentum of the jet.

7.5.2.2 Mass Flow Rate Into Blade Passage

The total mass flow rate of air into the control volume consisting of the blade passage, $\dot{m}_{i_{tot}}$, is the mass flow rate through the blade passage inlet plane, $\dot{m}_i$, plus the mass flow rate of the injected jet, $\dot{m}_j$:

$$\dot{m}_{i_{tot}} = \dot{m}_i + \dot{m}_j.$$

The mass flow rates are taken as being per unit blade span, since the current measurements are assumed two-dimensional. The mass flow rate through the blade passage inlet plane is

$$\dot{m}_i = \int_0^S d\dot{m}_i = \int_0^S \rho u_i \cos\alpha_i dy = \rho u_i \cos\alpha_i S \tag{7.4}$$

since the flow is assumed incompressible and u_i and α_i are the mean values obtained from the inlet flow measurements (Section 4.3.2). The mass flow rate of the jet is

$$\dot{m}_j = \int_0^b d\dot{m}_j = \int_0^b \rho u_j dy = \rho b \int_0^1 u_j d(\frac{y}{b}) \tag{7.5}$$

where the integral is evaluated from the jet profile measurements discussed in Section 7.3.

7.5.2.3 Total Pressure Into Blade Passage

Total pressure is a measure of the mechanical energy of a flow. For the flow control measurements, it is necessary to quantify the total mechanical energy input to the blade passage. This is done by use of the first law of thermodynamics, which states that the energy of a system must be conserved (Moran and Shapiro, 1996).

The conservation of energy equation for a control volume, as given by White (1994), is

$$\frac{dE}{dt} = \frac{dQ}{dt} - \frac{dW}{dt} = \frac{d}{dt}\left(\int_{CV} e\rho dV\right) + \int_{CS} e\rho(\vec{U}\cdot\vec{n})dA \tag{7.6}$$

where E is the energy contained within the control volume, Q is the heat transferred to the control volume, W is the work output of the control volume, and e is the specific energy of the fluid. The work term, W, includes shaft work, pressure work, and work due to viscous stresses. The specific energy is defined as

$$e = u + \tfrac{1}{2}U^2 + gz$$

where u is the specific internal energy, $1/2U^2$ is the kinetic energy per unit mass, and gz is the potential energy per unit mass of the fluid.

To calculate the total mechanical energy into the blade passage, a simplified control

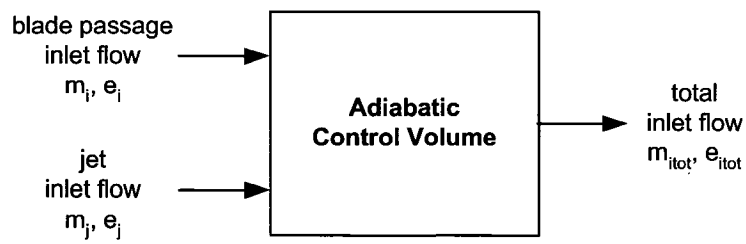

Figure 7.10: **Idealized Control Volume for Inlet Flow Energy Balance**

volume is used (shown in Figure 7.10). Equation 7.6 is applied to this control volume with some general assumptions. The system is assumed steady ($d/dt = 0$) and adiabatic, with no shaft or viscous work. With these assumptions, Equation 7.6 becomes

$$0 = \int_{CS} \left(u + \frac{P}{\rho} + \tfrac{1}{2}U^2 + gz \right) \rho(\vec{U} \cdot \vec{n}) dA.$$

For the current study, potential energy changes (Δgz) can be neglected since the working fluid is air, and the equation given above can be further rearranged, resulting in

$$0 = \int_{CS} u\rho(\vec{U} \cdot \vec{n}) dA + \int_{CS} (\frac{P}{\rho} + \tfrac{1}{2}U^2)\rho(\vec{U} \cdot \vec{n}) dA$$

in which the second integral is a mass-averaged total mechanical energy term. Assuming that the air is an ideal gas, the internal energy, u, can be assumed a function of temperature only. Since the measured differences in freestream and jet temperature are only 2° to 3°C, and the temperature changes due to irreversibilities are going to be small, the first integral containing the specific internal energy term can be neglected. Multiplying by the density, ρ, since the fluid is assumed incompressible, the second integral becomes

$$0 = \int_{CS} (P_0)\, \rho(\vec{U} \cdot \vec{n}) dA \tag{7.7}$$

which is a mass average of the total pressure in and out of the control volume.

Applying Equation 7.7 to the control volume of Figure 7.10, the mass-averaged total pressure balance becomes

$$\int_{i_{tot}} P_0 d\dot{m}_{i_{tot}} = \int_{i} P_0 d\dot{m}_i + \int_{jet} P_0 d\dot{m}_j$$

from which the mass-averaged total pressure into the blade passage, $\bar{P}_{0i_{tot}}$ is

$$\bar{P}_{0i_{tot}} = \frac{\dot{m}_i}{\dot{m}_{i_{tot}}} \bar{P}_{0i} + \frac{1}{\dot{m}_{i_{tot}}} \int_{jet} P_0 d\dot{m}_j. \tag{7.8}$$

The inlet plane total pressure, $\bar{P}_{0i}$, is the mass averaged value for the fluid passing through the inlet plane of the cascade. The mass-averaged total pressure of the jet is

$$\int_{jet} P_0 d\dot{m}_j = \int_0^b (P_{Sj} + \tfrac{1}{2}\rho u_j^2)\rho u_j dy. \tag{7.9}$$

Substituting expressions for the mass flow rates (Equations 7.4 and 7.5) and the jet total pressure (Equation 7.9) into Equation 7.8, the mass-averaged total pressure into the blade passage is

$$\bar{P}_{0i_{tot}} = \frac{\rho u_i \cos\alpha_i S}{\rho u_i \cos\alpha_i S + \rho b \int_0^1 u_j d(\frac{y}{b})} \bar{P}_{0i} + \frac{\rho b \int_0^1 P_{Sj} u_j d(\frac{y}{b}) + \rho b \int_0^1 \frac{1}{2}\rho u_j^3 d(\frac{y}{b})}{\rho u_i \cos\alpha_i S + \rho b \int_0^1 u_j d(\frac{y}{b})}. \tag{7.10}$$

This reduces to $\bar{P}_{0i}$ for zero jet momentum.

The analysis given above assumes instantaneous mixing of the jet with the flow through the cascade inlet plane and does not represent an actual mixing process. The result though is used in the downstream mixed-out flow calculation to account for the addition of mechanical energy from the jet.

For use with the mixed-out conservation relations of Section 4.3.2, Equation 7.10 is rearranged slightly and divided by the inlet plane dynamic pressure, $^1/_2\rho u_i{}^2$, resulting in

$$\frac{\bar{P}_{0i_{tot}}}{\frac{1}{2}\rho u_i^2} = \frac{\cos\alpha_i}{\cos\alpha_i + \frac{b}{S}\int_0^1 \left(\frac{u_j}{u_i}\right) d(\frac{y}{b})} \left(\frac{\bar{P}_{0i}}{\frac{1}{2}\rho u_i^2}\right) + \frac{\frac{b}{S}\int_0^1 \frac{P_{Sj}}{\frac{1}{2}\rho u_i^2}\left(\frac{u_j}{u_i}\right) d(\frac{y}{b}) + \frac{b}{S}\int_0^1 \left(\frac{u_j}{u_i}\right)^3 d(\frac{y}{b})}{\cos\alpha_i + \frac{b}{S}\int_0^1 \left(\frac{u_j}{u_i}\right) d(\frac{y}{b})}. \quad (7.11)$$

Equation 7.11 is used in the following section to account for the jet momentum in the total pressure loss calculations.

7.5.2.4 Total Pressure Loss Coefficient

Using the calculated total pressure into the blade passage described in the previous section (Equation 7.10), a total pressure loss coefficient can be defined which accounts for the additional mechanical energy, or total pressure, of the jet. This coefficient is calculated from three-hole pressure probe measurements (α_i, α_e, C_{Ve}, C_{Qe}, and C_{PSe}) and hot-wire measurements of the jet velocity profile (u_j/u_i). This calculated pressure loss will include losses due to viscous dissipation within the blade boundary layers, trailing edge losses, mixing losses within the downstream wake, and losses due to mixing of the injected jet with the boundary layer and freestream.

The new mixed-out total pressure loss coefficient, based on inlet dynamic pressure, is

$$C'_{P0m} = \frac{\bar{P}_{0i_{tot}} - \bar{P}_{0m}}{\frac{1}{2}\rho u_i^2} = \frac{\bar{P}_{0i_{tot}}}{\frac{1}{2}\rho u_i^2} - \frac{\frac{1}{2}\rho u_m^2}{\frac{1}{2}\rho u_i^2} - \frac{P_{Sm}}{\frac{1}{2}\rho u_i^2} \quad (7.12)$$

where $^1/_2 u_m^2$ and P_{Sm} are the mixed-out dynamic and static pressures downstream of the cascade, respectively, and their corresponding terms in the above equation are defined by Equations 4.19 and 4.15 of Section 4.3.2. In the following, a total pressure loss correction term, $\Delta C'_{P0m}$, is derived which corrects the calculated total pressure loss coefficient, C_{P0m}

(Equation 4.21), as follows

$$C'_{P0m} = C_{P0m} + \Delta C'_{P0m}. \tag{7.13}$$

The main assumption involved in the derivation of the correction term, $\Delta C'_{P0m}$, is that the static pressure is constant across the jet injection plane, and is equal to the static pressure at the edge of the local boundary layer. The local static pressure can be defined based on the loading coefficient at the slot location, C_{PLj}, as:

$$\begin{aligned} P_{Sj} &= P_{0i} - \tfrac{1}{2}\rho u_i^2 C_{PLj} \\ &= P_{Si} + \tfrac{1}{2}\rho u_i^2 (1 - C_{PLj}) \end{aligned}$$

The loading coefficient, C_{PLj}, is inferred from the edge-of-the boundary layer velocity, u_{je}, using Bernoulli's Equation. Assuming inviscid, incompressible flow outside the blade boundary layer, the local static pressure can be expressed in terms of the local velocity. Equating the total pressure at the cascade inlet plane, P_{0i}, with the edge-of-the boundary layer total pressure, P_{0e}, Bernoulli's Equation gives

$$\begin{aligned} P_{0i} &= P_{0e} \\ P_{0i} &= P_{Se} + \tfrac{1}{2}\rho u_e^2 \\ P_{0i} - P_{Se} &= \tfrac{1}{2}\rho u_e^2 \end{aligned}$$

from which the local pressure coefficient at the edge of the boundary layer, C_{Pe}, is

$$C_{Pe} = \frac{P_{0i} - P_{Se}}{\frac{1}{2}\rho u_i^2} = \frac{\frac{1}{2}\rho u_e^2}{\frac{1}{2}\rho u_i^2} = (\frac{u_e}{u_i})^2.$$

With the assumption that the jet static pressure, P_{Sj}, is the same as the local edge of the boundary layer static pressure, P_{Se}, then $C_{PLj} = C_{Pe}$ and the jet static pressure can

be expressed as

$$P_{Sj} = P_{Si} + \tfrac{1}{2}\rho u_i^2 \left[1 - \left(\frac{u_{je}}{u_i}\right)^2\right]. \tag{7.14}$$

The velocity ratio, u_{je}/u_i, is found from the jet profiles presented in Section 7.3.

Inserting Equation 7.14 into Equation 7.11, and then combining the result with Equations 4.19 and 4.15 in Equation 7.12 results in a total pressure loss coefficient which takes into account the injected jet momentum. This new parameter is called the "corrected" total pressure loss coefficient, and given by

$$\begin{aligned} C'_{P0m} = {} & \frac{\frac{b}{S}\int_0^1 \left(\frac{u_j}{u_i}\right) d(\frac{y}{b})}{\cos\alpha_i + \frac{b}{S}\int_0^1 \left(\frac{u_j}{u_i}\right) d(\frac{y}{b})} \left[1 - \left(\frac{u_{je}}{u_i}\right)^2\right] + \frac{\cos\alpha_i + \frac{b}{S}\int_0^1 \left(\frac{u_j}{u_i}\right)^3 d(\frac{y}{b})}{\cos\alpha_i + \frac{b}{S}\int_0^1 \left(\frac{u_j}{u_i}\right) d(\frac{y}{b})} \\ & - \int_0^1 C_{PSe}\, d(\frac{y}{S}) + \left[\int_0^1 C_{Ve}\cos\alpha_e\, d(\frac{y}{S})\right]^2 - 2\int_0^1 C_{Qe}\cos^2\alpha_e\, d(\frac{y}{S}) \\ & + \left[\frac{\int_0^1 C_{Qe}\sin(2\alpha_e)\, d(\frac{y}{S})}{2\int_0^1 C_{Ve}\cos\alpha_e\, d(\frac{y}{S})}\right]^2 . \end{aligned} \tag{7.15}$$

Subtracting the standard loss coefficient, C_{P0m} (Equation 4.21), from Equation 7.15 gives the total pressure loss correction term:

$$\Delta C'_{P0m} = \frac{\frac{b}{S}\int_0^1 \left(\frac{u_j}{u_i}\right) d(\frac{y}{b})}{\cos\alpha_i + \frac{b}{S}\int_0^1 \left(\frac{u_j}{u_i}\right) d(\frac{y}{b})} \left[1 - \left(\frac{u_{je}}{u_i}\right)^2\right] + \frac{\cos\alpha_i + \frac{b}{S}\int_0^1 \left(\frac{u_j}{u_i}\right)^3 d(\frac{y}{b})}{\cos\alpha_i + \frac{b}{S}\int_0^1 \left(\frac{u_j}{u_i}\right) d(\frac{y}{b})} - 1 \tag{7.16}$$

which reduces to zero when there is no jet momentum addition. The integrals in Equation 7.16 are evaluated from the jet velocity profiles as discussed in Section 7.3.

7.5.2.5 Profile Loss Coefficient

The mixed-out profile loss coefficient has also been modified to account for the additional momentum of the jet. The "corrected" mixed-out profile loss coefficient is

$$Y'_m = Y_m + \frac{\Delta C'_{P0m}}{C_{Qm}} \tag{7.17}$$

where Y_m is the mixed-out profile loss coefficient as calculated from the outlet traverse measurements, described in Section 4.3.2 (Equation 4.22), C_{Qm} is the mixed-out dynamic pressure coefficient (Equation 4.19), and $\Delta C'_{P0m}$ is the total pressure loss correction coefficient (Equation 7.16).

7.5.2.6 Flow Control Effectiveness Coefficient

One purpose of the current study is to examine the effectiveness of the active flow control device at reducing losses due to flow separation. An effectiveness coefficient is proposed, which represents the performance gain obtained using the flow control device in relation to the momentum input of the device.

The performance gain of the flow control device is defined as the difference between the baseline airfoil total pressure loss, $\Delta P_0|_{BAS} = (\frac{1}{2}\rho u_m^2\, Y_m)_{BAS}$ and the "corrected" flow control airfoil total pressure loss, $\Delta P_0|_{AFC} = (\frac{1}{2}\rho u_m^2\, Y'_m)_{AFC}$. The momentum input of the flow control device is defined as the momentum flux rate through the outlet plane of the flow control slot, $\rho\overline{u_j}^2 b$, where $\overline{u_j}$ is the mean velocity of the jet:

$$\overline{u_j} = \int_0^b u_j d(\frac{y}{b}).$$

The momentum flux rate calculated using the mean jet velocity, $\overline{u_j}$, is of similar magnitude

to the actual momentum flux rate calculated by integrating the momentum flux across the jet injection plane:

$$\rho\overline{u_j}^2 b \approx \rho b \int_0^b u_j^2 d(\frac{y}{b}).$$

For the current measurements, the errors introduced by this simplification are estimated to be ±5% of the actual momentum flux rate.

The proposed effectiveness coefficient, ζ, is defined as

$$\zeta = \frac{[(\frac{1}{2}\rho u_m^2\ Y_m)_{BAS} - (\frac{1}{2}\rho u_m^2\ Y_m')_{AFC}]S}{\rho\overline{u_j}^2 b} \tag{7.18}$$

where S is the blade spacing. An effectiveness coefficient of this form allows comparison with other injection-type flow control and cascade configurations.

Using parameters measured in the current experiments, Equation 7.18 can be defined as follows:

$$\zeta = \frac{(C_{Qm}Y_m')_{BAS} - (C_{Qm}Y_m')_{AFC}}{2\frac{b}{S}(\int_0^b \frac{u_j}{u_i} d\frac{y}{b})^2}. \tag{7.19}$$

The effectiveness coefficient presented in this section and the "corrected" profile loss coefficient defined in the previous section are used to examine the performance of the active flow control airfoil and compare it to the performance of the baseline Pak-B airfoil. These results are presented in the following sections discussing the surface static pressure and three-hole pressure probe measurements made for the flow control cascade. First, the measurements for low FSTI (0.4%) are presented, followed by those for high FSTI (3.9%).

7.5.3 Loading and Three-Hole Probe Measurements for FSTI=0.4%

7.5.3.1 Baseline Airfoil Results for FSTI = 0.4%

This section briefly presents the baseline Pak-B airfoil loading distributions and losses for an FSTI of 0.4%. These measurements are from Mahallati (2003).

Figure 7.11 shows the loading measurements for Reynolds numbers of 25000, 50000, 100000, and 150000. Separation is indicated by a pressure plateau in the surface static pressure distribution. At low FSTI and low Reynolds numbers (25000 and 50000), the suction surface boundary layer separates and does not reattach to the surface, resulting in reduced flow turning and high losses. At higher Reynolds numbers (100000 and 150000), the suction surface flow separates but transition within the separated free shear layer promotes reattachment, resulting in the desired flow turning and lower losses.

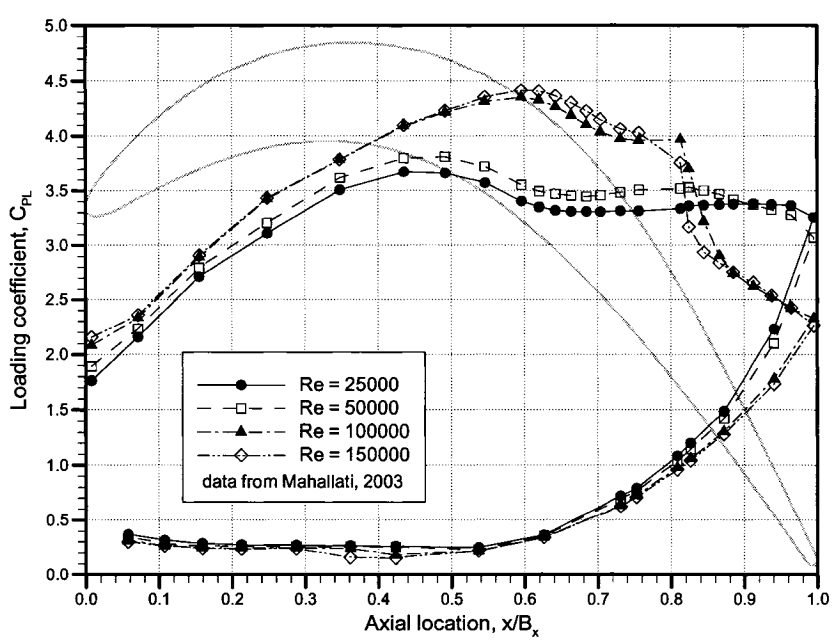

Figure 7.11: **Baseline Pak-B Loading Distributions for** $FSTI$ **= 0.4%**

Figure 7.12 shows the mixed-out profile losses. At low Reynolds numbers (25000 and 50000) the losses are high due to the fully-separated suction surface boundary layer. At higher Reynolds numbers (100000 and 150000) the losses are low due to reattachment of the separated shear layer over the suction surface.

Flow control is desired for the Pak-B airfoil at low Reynolds numbers and low FSTI to prevent full separation of the suction surface boundary layer. The following sections present the results of the Pak-B flow control study for an FSTI of 0.4%. First, the suction surface pressure distribution downstream of the flow control slot is presented, followed by a discussion of the downstream wake profiles, the mixed-out profile losses, the flow control effectiveness, and finally the mixed-out deviation angles.

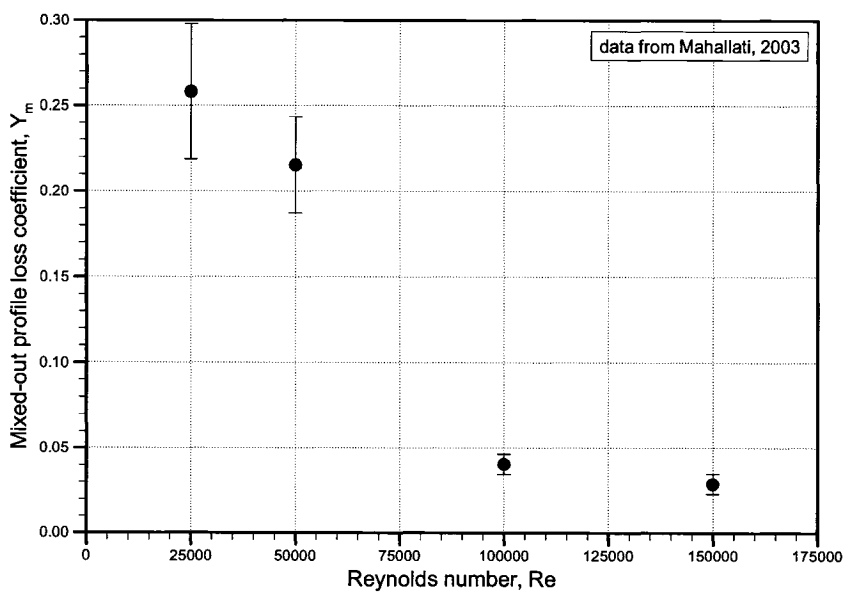

Figure 7.12: **Baseline Pak-B Profile Losses for $FSTI$ = 0.4%**

7.5.3.2 Loading Distributions for FSTI = 0.4%

The aft suction surface of the Pak-B airfoil is the region where separation occurs, and hence is a region of interest for assessing the effects of the current flow control technique. Surface static pressure measurements have been made downstream of the flow control slot and are shown in Figure 7.13 for an FSTI of 0.4% at Reynolds numbers of 25000, 50000, 100000, and 150000. One static pressure tap is located upstream of the injection slot and the measurements are presented based on suction surface length. The blowing ratio range is from approximately 0.00 to 2.00 for Reynolds numbers of 25000 and 50000, and from approximately 0.00 to 1.25 for a Reynolds number of 100000. Increments in blowing ratio are approximately 0.25. Only the zero-blowing case ($B = 0.00$) has been examined for a Reynolds number of 150000.

For a Reynolds number of 25000, the suction surface flow remains fully-separated up to a blowing ratio of approximately 1.00. At a blowing ratio of 1.23, the blade loading near the slot is increased and separation occurs at approximately 65% SSL. At this blowing ratio, the separation bubble appears reattached ahead of the trailing edge, but the reattachment point is difficult to locate. For blowing ratios above 1.23, the boundary layer appears attached over the entire aft-suction surface. For low blowing ratios at this Reynolds number, there is evidently insufficient momentum in the injected wall jet to re-energize the boundary layer and the blade remains stalled. As the blowing ratio is increased, the injected flow re-energizes the boundary layer which is then able to overcome the strong adverse pressure gradient, resulting in an attached suction surface boundary layer.

For a Reynolds number of 50000 at zero-blowing ($B = 0.00$), the separated shear layer reattaches to the surface resulting in increased loading and the absence of stall, whereas the baseline airfoil is stalled at this operating condition. This was an unexpected effect due to the presence of the flow control slot. It is suggested that the flow control slot acts as

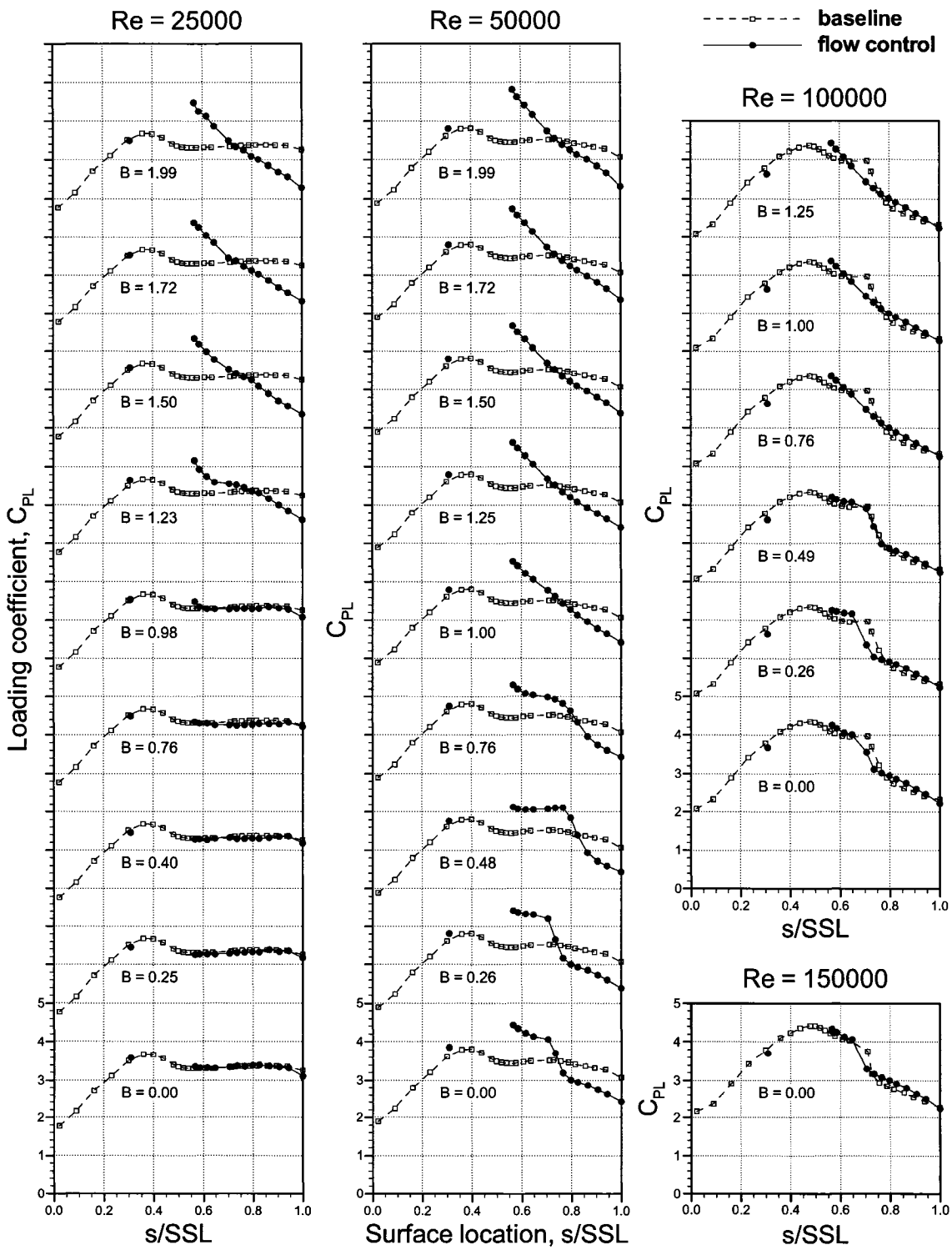

Figure 7.13: **Flow Control Loading Distributions for $FSTI$ = 0.4%**

a boundary layer trip, which promotes earlier transition and therefore reattachment ahead of the trailing edge. At this Reynolds number, the spanwise slot behaves as a passive flow control device. For zero-blowing, the separation point is at approximately 65%SSL. For low-momentum addition ($B = 0.26$ and $B = 0.48$), the boundary layer separates earlier (before 60%SSL) than for zero-blowing, and the separation bubble is longest at $B = 0.48$. At $B = 0.76$, the separation point returns to approximately the same location as for zero-blowing, but the separation bubble is longer, reattaching around 90%SSL, as opposed to approximately 80%SSL for zero-blowing. For $B = 1.00$ and higher, the boundary layer remains attached over the entire aft-suction surface. As the blowing ratio is increased for the attached boundary layer cases, the pressure coefficient at the first pressure tap downstream of the slot increases as well. At $B = 1.00$, the pressure coefficient at the first pressure tap downstream of the slot is approximately 4.75, which increases to approximately 4.90 at $B = 1.99$. This change is probably due to acceleration of the freestream fluid downstream of the slot, and is also seen in the data of Fottner (1979) and Sturm *et al.* (1992) for a similar wall jet device on a compressor airfoil. In general, at a Reynolds number of 50000, low momentum injection promotes earlier separation and a larger separation bubble. The suction surface boundary layer remains attached for blowing ratios greater than 1.00.

At a Reynolds number of 100000, the flow control characteristics are similar to those at a Reynolds number of 50000. For zero-blowing, the separation bubble is smaller than for the baseline airfoil, and for low B (0.26 and 0.49), the separation point moves forward and the separation bubble length increases. For $B = 0.76$ and higher, the suction surface boundary layer remains attached.

The zero-blowing case for a Reynolds number of 150000 shows a shorter separation bubble than for the baseline case, similar to what is seen at a Reynolds number of 100000.

The separation characteristics over the blade surface have a direct impact on the shape

and size of the boundary layer at the airfoil trailing edge, and hence has a direct effect on the downstream wake profiles. The wake profiles for an FSTI of 0.4% are presented in the next section.

7.5.3.3 Wake Profiles for FSTI = 0.4%

The boundary layers that develop over the blade surfaces merge into a wake of low-momentum fluid downstream of the cascade. These wake profiles give an indication of the total pressure losses across the cascade.

Figure 7.14 presents the wake profiles downstream of the middle flow control blade for a Reynolds number of 25000. For zero blowing, the wake is large and significantly shifted from the extended trailing edge ($y/S = 0.5$), indicating a fully-separated flow, but is smaller and less shifted than for the baseline case. As the blowing ratio is increased to 0.39 the

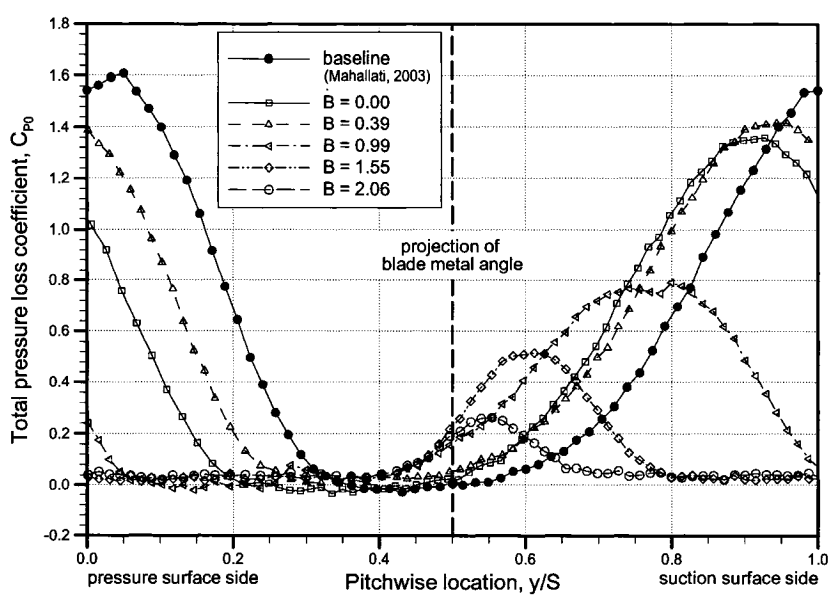

Figure 7.14: **Wake Profiles for Re = 25000 and $FSTI$ = 0.4%**

wake becomes larger, indicating higher losses than for zero blowing. At $B = 0.99$ the wake size is reduced but is still relatively large, spanning approximately 50% of the blade pitch. The small dip in the total pressure at $y/S \approx 0.8$ for $B = 0.99$ is due to oscillations in the jet supply pressure (discussed in Section 7.4.3). A drop in the blowing ratio of approximately 0.05 occurred just before this measurement point, and the dip in total pressure indicates the blowing ratio sensitivity of the separation bubble near $B \approx 1.00$. As B is increased above 1.00, the wake continually decreases in size due to two effects. The first is the elimination of the separation bubble and the second is the increased injection of momentum. Above a blowing ratio of approximately 1.00, the injected flow has a higher total pressure than the cascade inlet flow.

The downstream wake profiles for a Reynolds number of 50000 are presented in Figure 7.15. The zero-blowing wake is much smaller, and much less shifted than the baseline wake, indicating a reattached separation bubble, in agreement with the loading data in Figure

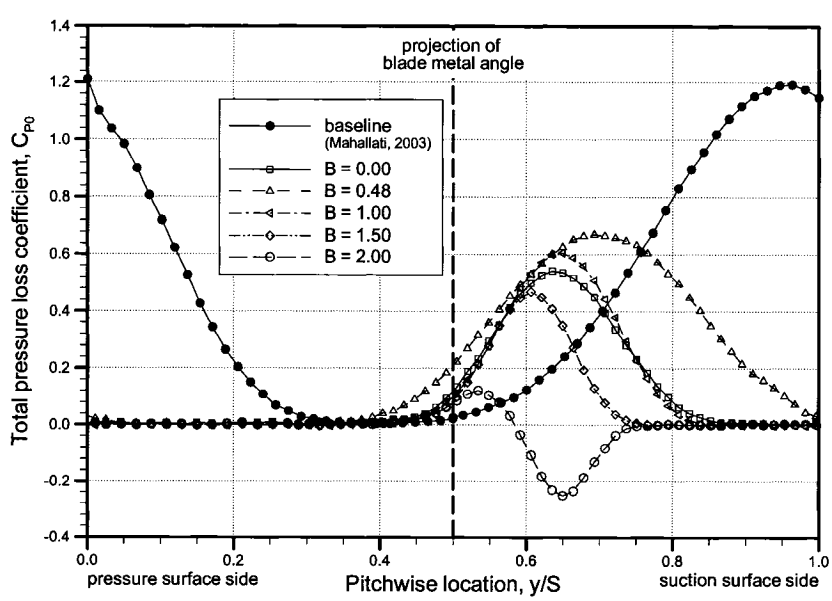

Figure 7.15: **Wake Profiles for Re = 50000 and $FSTI$ = 0.4%**

7.13. As the blowing ratio increases from 0.00 to 0.48, the wake increases significantly in size. The loading measurements presented in the previous section showed an increase in separation bubble length at low B, with a maximum near $B = 0.50$. At $B = 1.00$, where the separation bubble is eliminated, the wake has approximately the same width as, but is deeper than, the zero-blowing case. The suction surface side of the wake continually decreases in size as B is increased, and at $B = 2.00$ the wall jet persists downstream of the trailing edge, resulting in a negative total pressure loss peak.

Figure 7.16 presents the wake profiles for a Reynolds number of 100000. The suction surface side of the zero-blowing wake is smaller than for the baseline case, which is likely due to the reduction in separation bubble size. For the range of blowing ratios presented, the wake profiles are similar in size and shape, indicating very little effect of flow control on losses. For the cases of jet injection, the wakes are slightly deeper than for zero blowing.

The zero-blowing wake for a Reynolds number of 150000 is shown in Figure 7.17 along

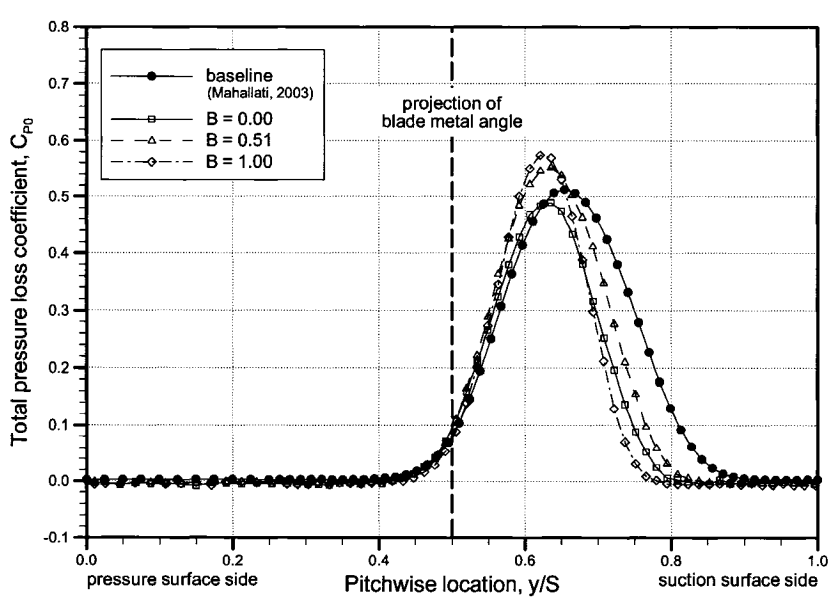

Figure 7.16: **Wake Profiles for Re = 100000 and $FSTI$ = 0.4%**

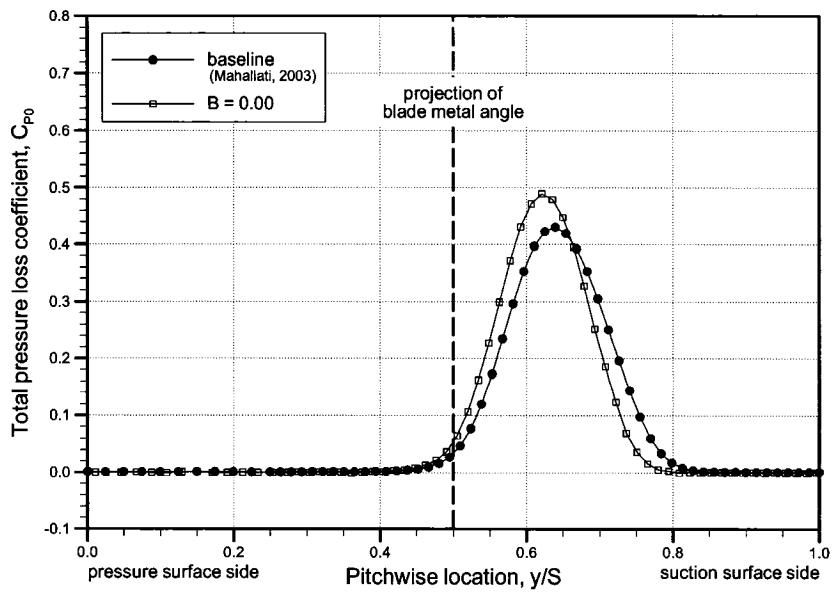

Figure 7.17: **Wake Profiles for Re = 150000 and $FSTI$ = 0.4%**

with the baseline airfoil wake for the same Reynolds number. The zero-blowing wake is slightly deeper than the baseline wake but appears to have a similar momentum deficit, which would result in similar losses for both cases. The zero-blowing wake is also less shifted towards the suction surface side of the passage indicating a smaller deviation from the blade metal angle.

The wake profiles presented in this section provide the background to the pressure loss characteristics of the flow control airfoil, which are presented in the next section.

7.5.3.4 Mixed-Out Profile Losses for FSTI = 0.4%

The mixed-out profile losses define the mid-span pressure losses across the cascade and are a result of viscous dissipation within the blade boundary layers and the downstream wakes, as well as losses due to a finite trailing edge thickness (Denton, 1993). In this section,

two forms of the mixed-out profile losses are presented: the mixed-out profile loss coefficient based on a mixing analysis of the downstream three-hole pressure probe measurements (designated "mixed-out", Equation 4.22), and the mixed-out profile loss coefficient which takes into account the momentum addition of the jet (designated "corrected", Equation 7.17). Although the "corrected" losses truly represent the aerodynamic losses across the cascade, the "mixed-out" losses might be useful in a mean-line analysis of a turbine stage since they give the resultant total pressures that downstream blade rows would experience. This section presents the flow control airfoil losses for Reynolds numbers of 25000, 50000, 100000, and 150000 at an FSTI of 0.4%.

The profile loss coefficients for a Reynolds number of 25000 are presented in Figure 7.18. For $B < 1.00$, the losses are high due to the fully separated shear layer, seen in the loading measurements of Figure 7.13, and of similar magnitude to the baseline Pak-B losses. At $B \approx 1.00$, the separated shear layer reattaches just ahead of the trailing edge resulting in

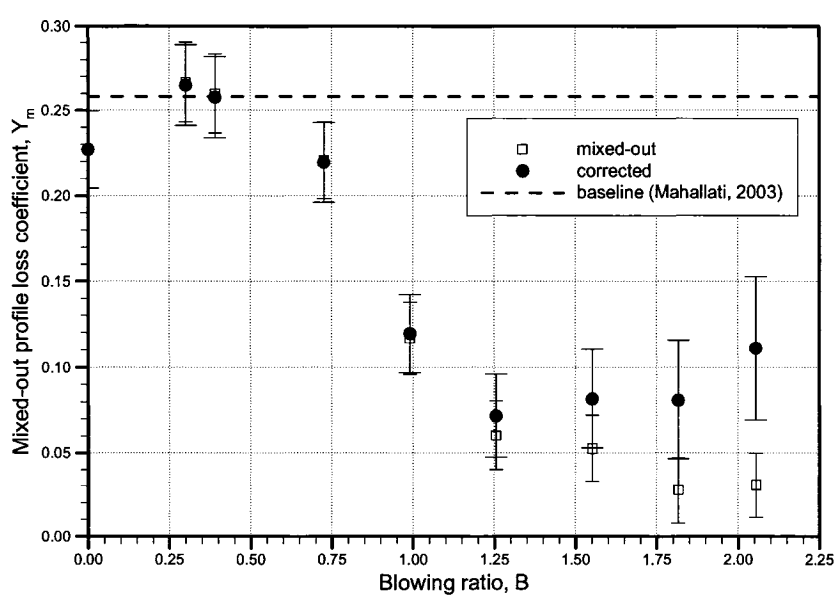

Figure 7.18: **Profile Losses for Re = 25000 and $FSTI$ = 0.4%**

reduced losses. For $B > 1.00$, the "mixed-out" losses continually decrease until $B \approx 1.80$. The "corrected" losses, which account for all losses generated within the blade passage and downstream wake, remain relatively constant between $B = 1.25$ and $B = 1.80$, above which increase, perhaps due to increased mixing between the jet and the passage flow.

The mixed-out profile loss coefficients for a Reynolds number of 50000 are presented in Figure 7.19. The zero-blowing case has significantly lower losses than the baseline case, suggesting again that the presence of the slot acts as a boundary layer trip, promoting earlier transition and reattachment of the separated shear layer. A maximum in losses is present at $B \approx 0.50$, where the separation bubble appears longest (Figure 7.13). The mechanism for this increase in bubble length is described later in Section 7.6.4, with reference to hot-wire traverse measurements. Above $B \approx 0.50$ the "mixed-out" losses continually decrease and become negative at $B = 2.00$. As the momentum of the jet is increased, a strong wall jet develops over the entire aft-suction surface, past the trailing edge. The high-momentum

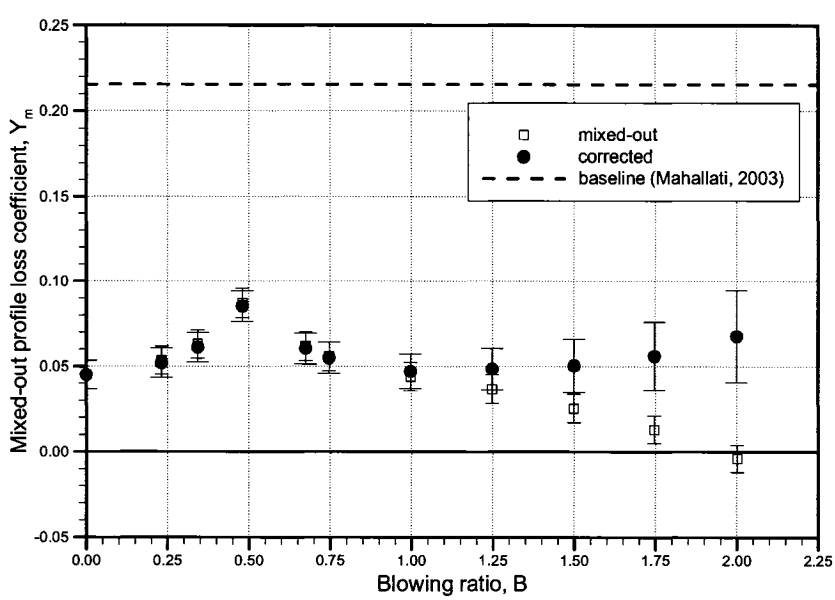

Figure 7.19: **Profile Losses for Re = 50000 and $FSTI$ = 0.4%**

of the wall jet, present in the wake profiles of Figure 7.15, results in negative "mixed-out" profile losses. If corrections are made for the jet momentum addition, as discussed in Section 7.5, the "corrected" losses plateau between $B \approx 1.00$ and 1.50, above which they increase due to mixing between the jet and the freestream.

Finally, The mixed-out profile loss coefficients for a Reynolds number of 100000 are presented in Figure 7.20. The losses over the selected blowing ratio range are all lower than for the baseline Pak-B airfoil. The increase in losses for $0.00 < B < 1.00$, seen for the Reynolds number of 50000 case, is also apparent at this Reynolds number. The losses peak at $B \approx 0.50$, after which they decrease.

The effects of passive flow control on the loss coefficients are summarized in Figure 7.21 for the low FSTI zero-blowing cases, and compared to the baseline airfoil cases. For all Reynolds numbers examined, the zero-blowing flow control losses are lower or equal to the baseline losses. It is assumed that disturbances are generated within the boundary layer due

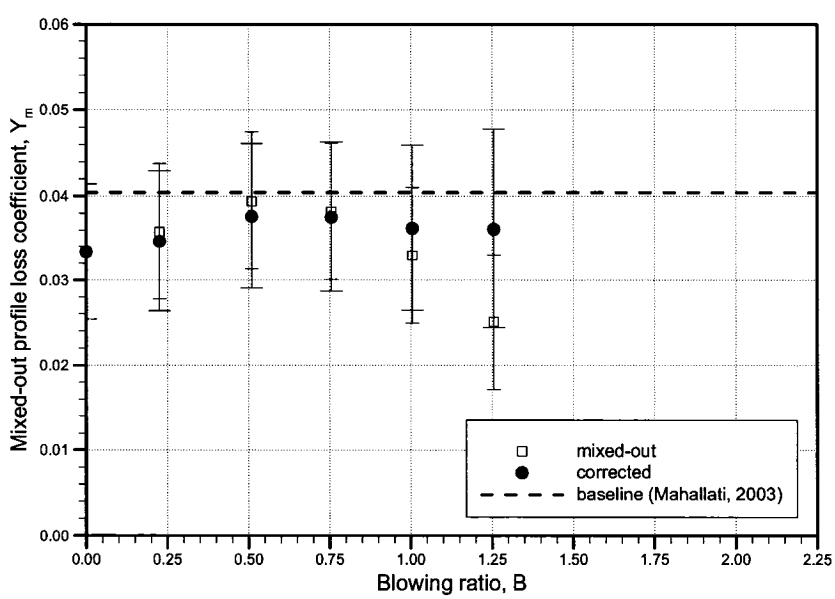

Figure 7.20: **Profile Losses for Re = 100000 and $FSTI$ = 0.4%**

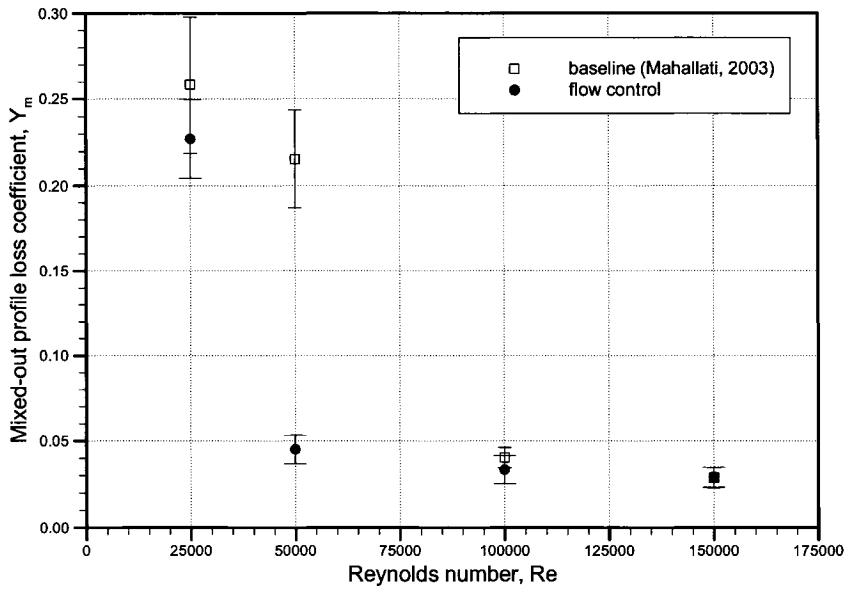

Figure 7.21: **Zero-Blowing Profile Losses for $FSTI$ = 0.4%**

to the presence of the slot, and that these disturbances promote earlier transition within the separated shear layer. At a Reynolds number of 50000, the presence of the slot results in reattachment of the separated shear layer ahead of the trailing edge and a significant reduction in the profile loss.

The "corrected" profile loss coefficients for all low FSTI cases are summarized in Figure 7.22. The figure shows that for the flow control airfoil, active flow control is only effective at reducing losses for a Reynolds number of 25000 where the flow is fully separated at zero-blowing. The blowing ratio that gives the lowest "corrected" losses for this Reynolds number is approximately 1.25. For higher Reynolds numbers, the losses are highest at low blowing ratios ($B \approx 0.50$), and remain higher or equal to the zero-blowing cases for all examined blowing ratios. The next section discusses the effectiveness of this blowing flow control technique, based on an effectiveness coefficient.

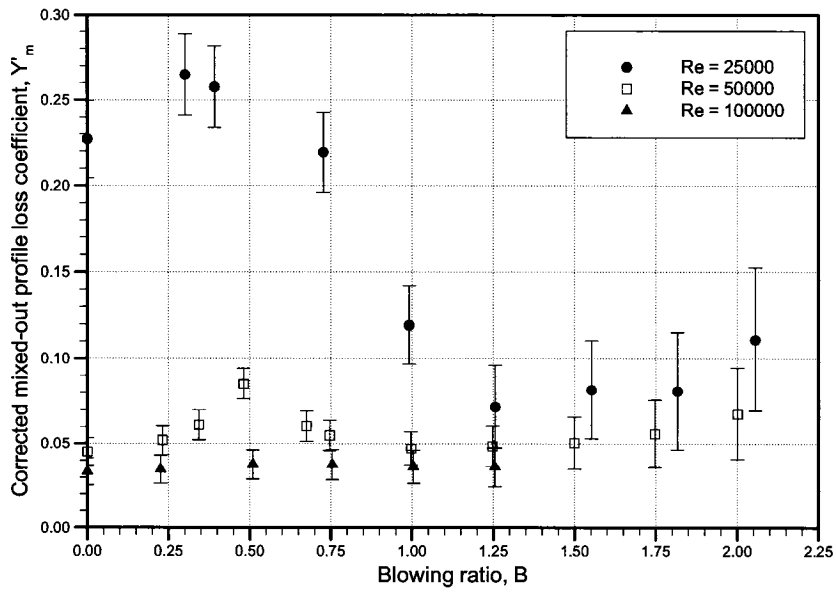

Figure 7.22: **Profile Losses for $FSTI$ = 0.4%, Corrected for Jet Momentum**

7.5.3.5 Flow Control Effectiveness for FSTI = 0.4%

An effectiveness coefficient, ζ, proposed in Section 7.5.2.6, relates the flow control airfoil loss reduction, as compared to the baseline airfoil, to the momentum input of the flow control device. Figure 7.23 presents this effectiveness coefficient for the current low-FSTI study. Based on the definition of ζ, a negative value signifies an increase in losses from the baseline case. A maximum positive value of ζ corresponds to the optimum case for which the use of the jet momentum is maximized in reducing the losses.

For a Reynolds number of 25000, the effectiveness is negative for low blowing ratios ($B < 0.50$), indicating higher losses than the baseline airfoil. A maximum in ζ occurs at $B \approx 1.00$, which signifies the optimum blowing ratio. It is perhaps not surprising that the optimum occurs at $B \approx 1.00$, since the jet momentum is essentially the same as the local freestream momentum at this condition and results in minimum mixing losses between the

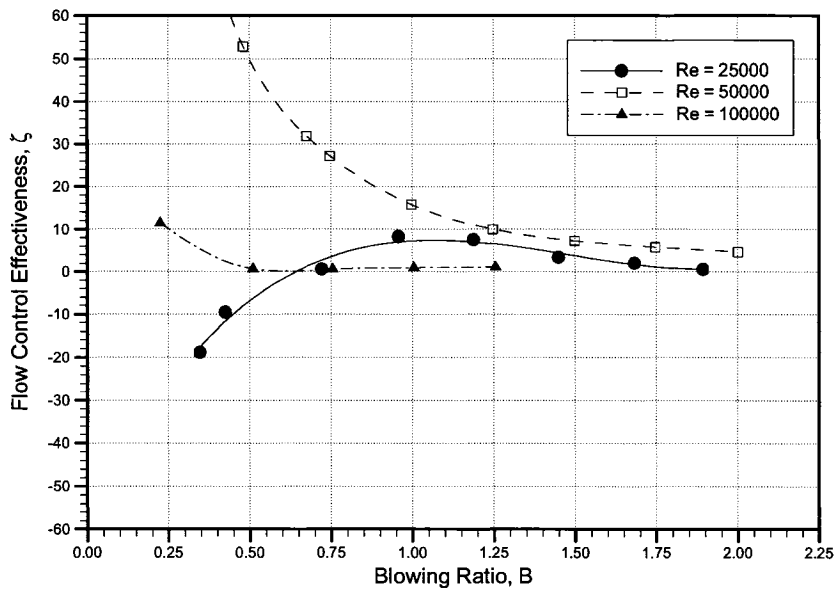

Figure 7.23: **Active Flow Control Effectiveness for $FSTI$ = 0.4%**

jet and the freestream flow. For Reynolds numbers of 50000 and 100000, the maximum in ζ occurs at very low blowing ratios, tending towards infinity as B approaches zero, signifying the effectiveness of the injection slot as a passive flow control device.

7.5.3.6 Mixed-Out Deviation Angles for FSTI = 0.4%

The deviation of the outlet flow from the trailing edge metal angle is important in turbine design. A designer must estimate the deviation in order to match the blade row characteristics to the desired velocity triangles. The mixed-out deviation angles for the low FSTI flow control study are presented in Figure 7.24, and compared to the baseline Pak-B measurements.

For a Reynolds number of 25000, the mixed-out deviation angle is high for low blowing ratios ($B < 1.00$), indicating decreased flow turning due to the fully-separated suction

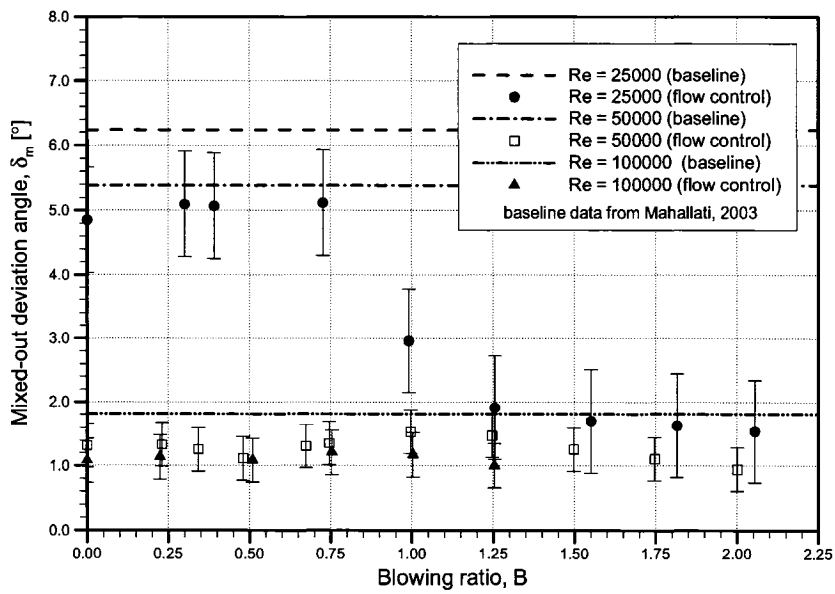

Figure 7.24: **Mixed-Out Deviation Angles for $FSTI$ = 0.4%**

surface boundary layer. At $B \approx 1.00$, the deviation angle decreases and for higher B the flow turning is typical of a well-designed turbine blade row at design incidence ($\delta_m \approx 1.3°$ for the Pak-B airfoil based on the correlation of Islam and Sjolander (1999)). For Reynolds numbers of 50000 and 100000, the deviation angle is lower than the corresponding baseline airfoil case for all blowing ratios examined.

The effects of passive flow control (zero blowing) on the variation of deviation angle with Reynolds number are summarized in Figure 7.25. The mixed-out deviation angles for zero blowing show a similar trend with Reynolds number as the profile losses, which were shown in Figure 7.21, since both high deviation and high losses are associated with large-scale separation on the airfoil. The zero-blowing deviation angles are lower than all corresponding baseline airfoil cases, with significant differences at a Reynolds number of 50000.

The method of active flow control investigated prevents stall of the Pak-B airfoil at low

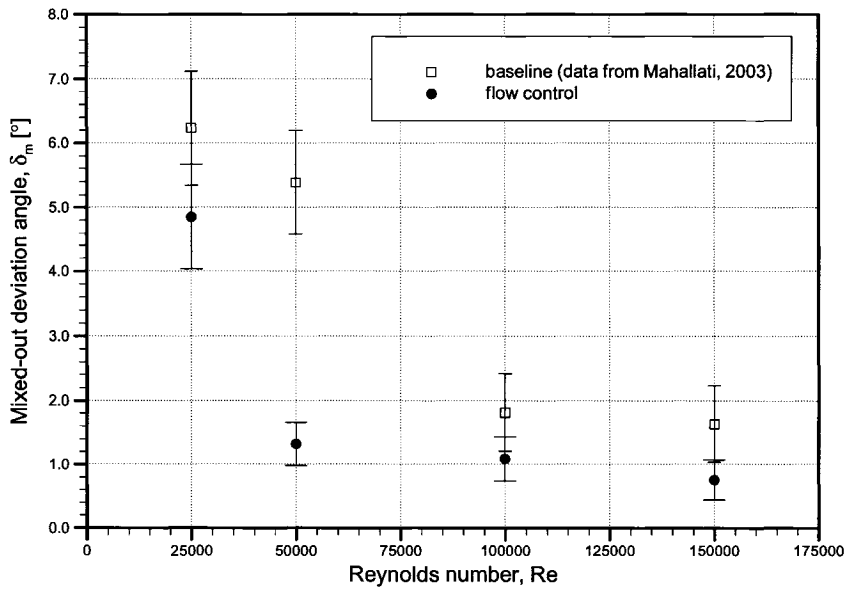

Figure 7.25: **Zero-Blowing Mixed-Out Deviation Angles for $FSTI$ = 0.4%**

Reynolds number (25000) and low-FSTI (0.4%). Passive control, obtained by the presence of the slot with no blowing, resulted in equal or better performance at all Reynolds numbers examined, in particular at a Reynolds number of 50000 where stall is prevented. Low-pressure turbines typically operate under conditions with higher FSTI, where the Pak-B airfoil is un-stalled for the range of Reynolds numbers examined, as described in Chapter 4. It is therefore desired to assess the effects of this flow control technique under these conditions. The next section examines the performance of the flow control airfoil for an FSTI of 3.9%.

7.5.4 Loading and Three-Hole Probe Measurements for FSTI=3.9%

7.5.4.1 Baseline Airfoil Results for FSTI = 3.9%

This section briefly repeats the baseline Pak-B airfoil loading distributions and losses for an FSTI of 3.9%. These measurements were initially presented in Chapter 4.

Figure 7.26 shows the loading measurements for Reynolds numbers of 25000, 50000, 100000, and 150000. For all Reynolds numbers examined, the suction surface flow separates but transition within the free shear layer promotes reattachment before the trailing edge. The location of separation is approximately the same for all cases, but the length of the separation bubble varies inversely with the Reynolds number.

Figure 7.27 shows the mixed-out profile losses. The losses decrease with increasing

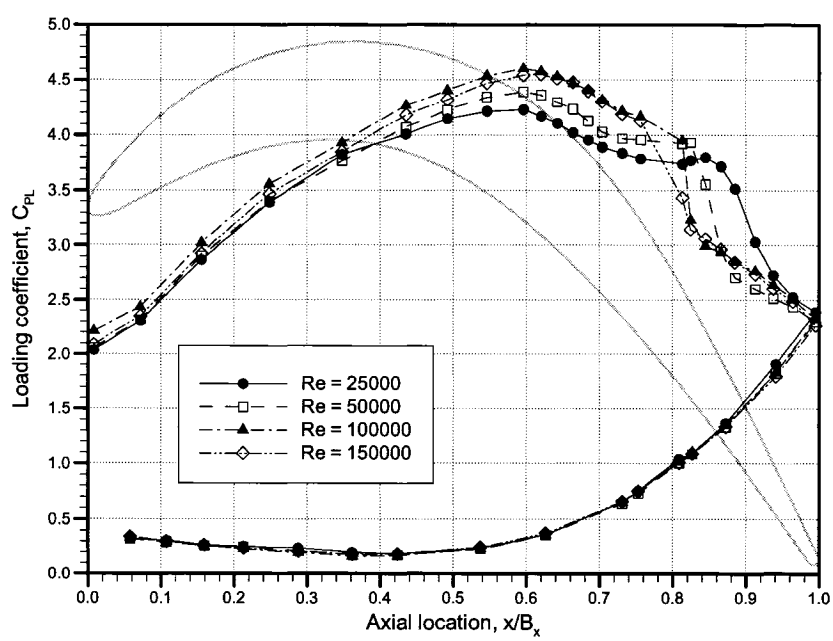

Figure 7.26: **Baseline Pak-B Loading Distributions for** $FSTI$ **= 3.9%**

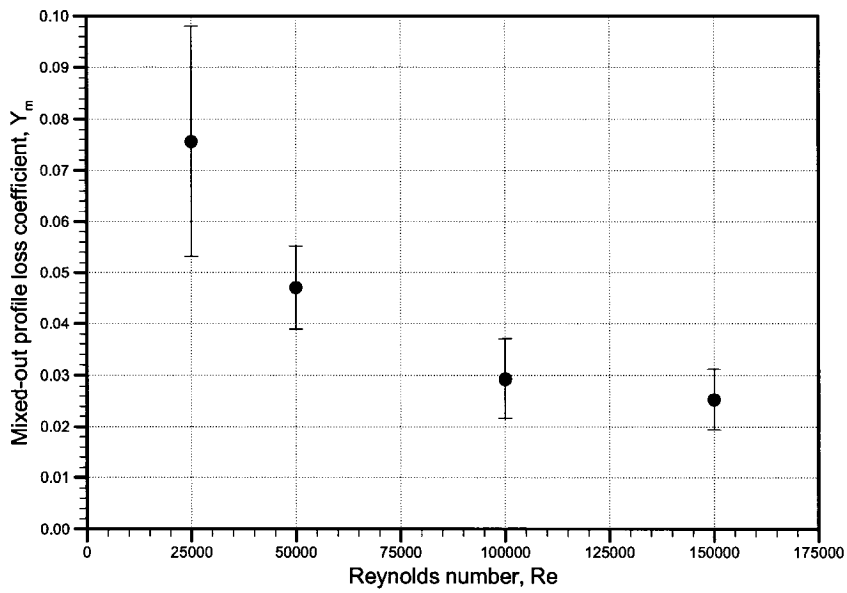

Figure 7.27: **Baseline Pak-B Profile Losses for $FSTI$ = 3.9%**

Reynolds number due primarily to the reduction in separation bubble size.

At this level of freestream turbulence, which is typical of what is encountered in an LPT environment, stall of the Pak-B airfoil does not occur for the range of Reynolds numbers examined. This suggests that realistically, flow control is not needed for the Pak-B airfoil. The flow control measurements presented in this chapter are intended to provide background for the design of more highly loaded LPT airfoils that may stall under the low Reynolds number, high FSTI conditions of an engine at altitude. The measurements presented in the following sections, for an FSTI of 3.9%, are intended to examine the effects of this flow control technique for unstalled low-Reynolds number conditions. First, the suction surface pressure distributions downstream of the flow control slot are presented, followed by a discussion of the downstream wake profiles, the mixed-out profile losses, the flow control effectiveness, and finally the mixed-out deviation angles.

7.5.4.2 Loading Distributions for FSTI=3.9%

The purpose of the current high-FSTI experiments is to assess the effects of the flow control device for cases where the separated shear layer reattaches to the surface for the baseline airfoil. The aft suction surface of the blade is the region where separation occurs, and hence is a region of interest for assessing the effects of the flow control device. As for the lower value of FSTI, surface static pressure measurements have been made downstream of the flow control slot. They are shown in Figure 7.28 for an FSTI of 3.9% at Reynolds numbers of 25000, 50000, and 100000. One static pressure tap is located upstream of the injection slot and, as before, the measurements are presented based on suction surface length. The blowing ratio range is from 0.00 to 1.47 for a Reynolds numbers of 25000, and 0.00 to 1.25 for a Reynolds number of 50000. Increments in blowing ratio are approximately 0.25. Only the zero-blowing case has been examined for a Reynolds number of 100000.

For a Reynolds number of 25000, there is very little difference in the aft-suction surface pressure distribution between the baseline and zero-blowing cases. At blowing ratios of 0.17 and 0.46, the separation bubble length remains similar to the zero-blowing case and as the blowing ratio increases above ≈ 0.50, a larger separation bubble forms. For blowing ratios greater than 0.79, the separation bubble decreases in size and at $B = 1.47$, the bubble is very small.

For a Reynolds number of 50000, the separation bubble characteristics with blowing ratio are similar to those at 25000, except that the separated shear layer reattaches well ahead of the trailing edge in all cases. For $B \approx 1.00$ and higher, the injected momentum appears to suppress separation, resulting in a smooth deceleration up to the trailing edge.

The zero-blowing case for a Reynolds number of 100000 shows a shorter separation bubble than for the baseline airfoil. This is similar to what was seen at low FSTI (0.4%)

for the same Reynolds number (Figure 7.13).

The downstream wake profiles also give insight into the effects of the current flow control technique, and are discussed in the next section.

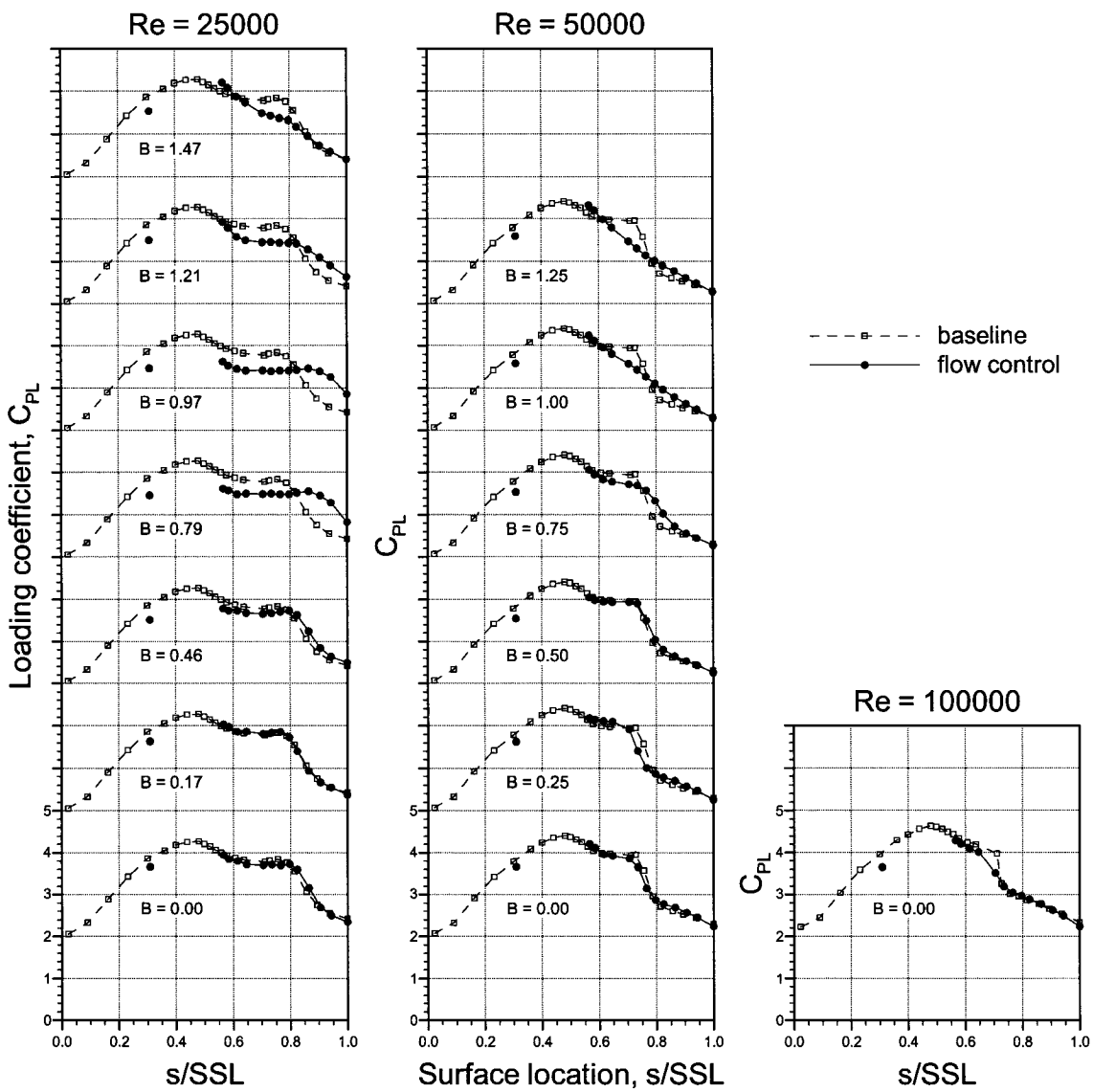

Figure 7.28: **Flow Control Loading Distributions for $FSTI$ = 3.9%**

7.5.4.3 Wake Profiles for FSTI=3.9%

This section presents the wakes profiles measured at $0.5B_x$ downstream of the Pak-B flow control airfoil for an FSTI of 3.9%.

Figure 7.29 shows the downstream wake profiles for a Reynolds number of 25000. For zero-blowing, the wake spans approximately 70% of the blade pitch. As B increases to 0.43, the wake becomes wider and deeper, indicating larger separation, as is also seen in the loading measurements of the last section (Figure 7.28). For $B = 0.97$, the wake decreases in width and depth but does not quite return to the zero-blowing size.

Figure 7.30 shows the wake profiles for a Reynolds number of 50000. The wake characteristics are similar to those at a Reynolds number of 25000, with larger wakes when the flow control device is active.

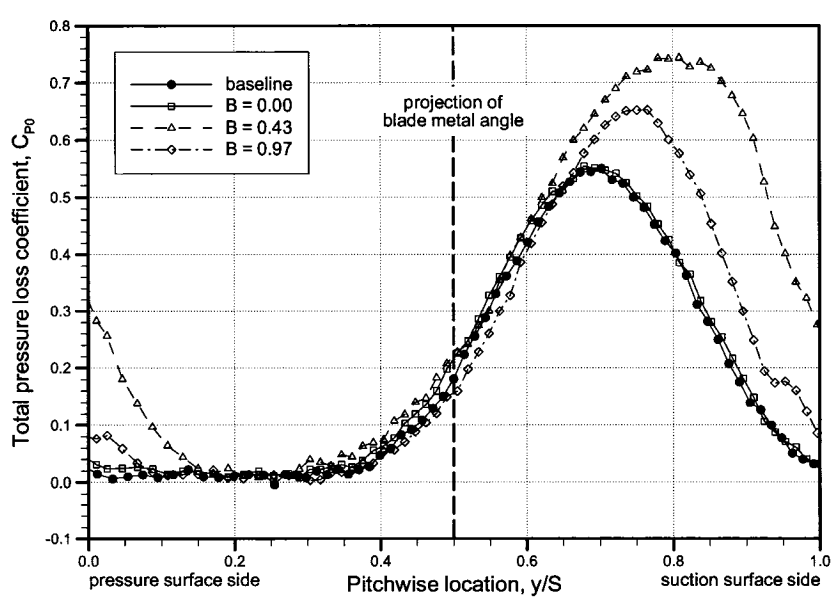

Figure 7.29: **Wake Profiles for Re = 25000 and $FSTI$ = 3.9%**

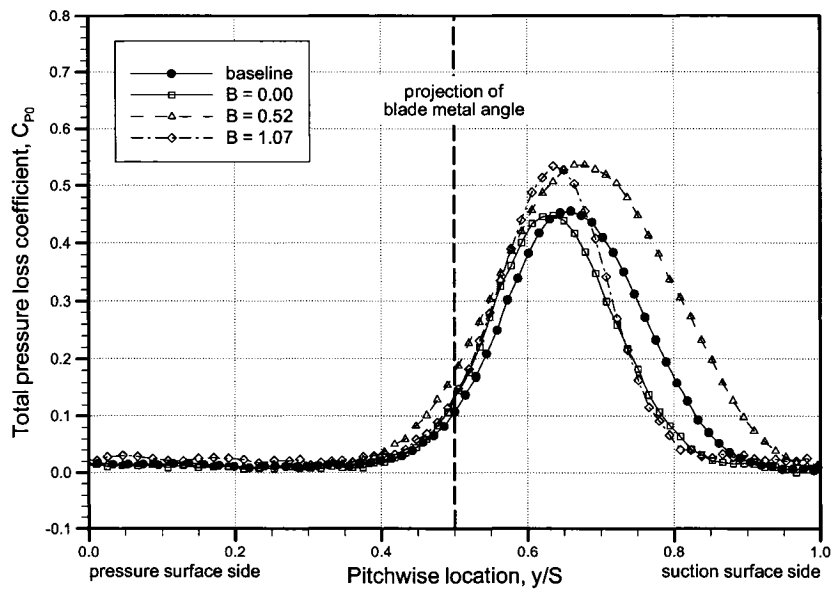

Figure 7.30: **Wake Profiles for Re = 50000 and $FSTI$ = 3.9%**

The wake profile for zero blowing at a Reynolds number of 100000 is shown in Figure 7.31 compared to the baseline airfoil case for the same Reynolds number. The zero-blowing wake is of similar depth and width as the baseline wake, but is less shifted towards the suction surface side of the passage indicating a smaller deviation from the blade metal angle. The pressure losses associated with the wake profiles are presented in the next section.

7.5.4.4 Mixed-Out Profile Losses for FSTI=3.9%

In this section, both the "mixed-out" losses, integrated from the downstream wake profiles, and the losses "corrected" for jet momentum addition are presented for Reynolds numbers of 25000, 50000, and 100000 at an FSTI of 3.9%.

The profile loss coefficients for a Reynolds number of 25000 are shown in Figure 7.32. The zero-blowing loss is similar to the baseline airfoil loss, indicating a minimal effect of

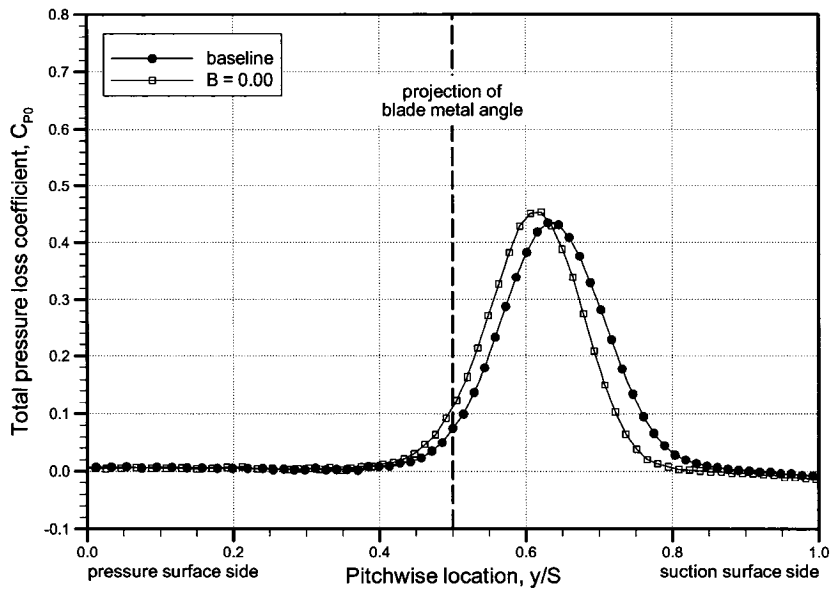

Figure 7.31: **Wake Profiles for Re = 100000 and $FSTI$ = 3.9%**

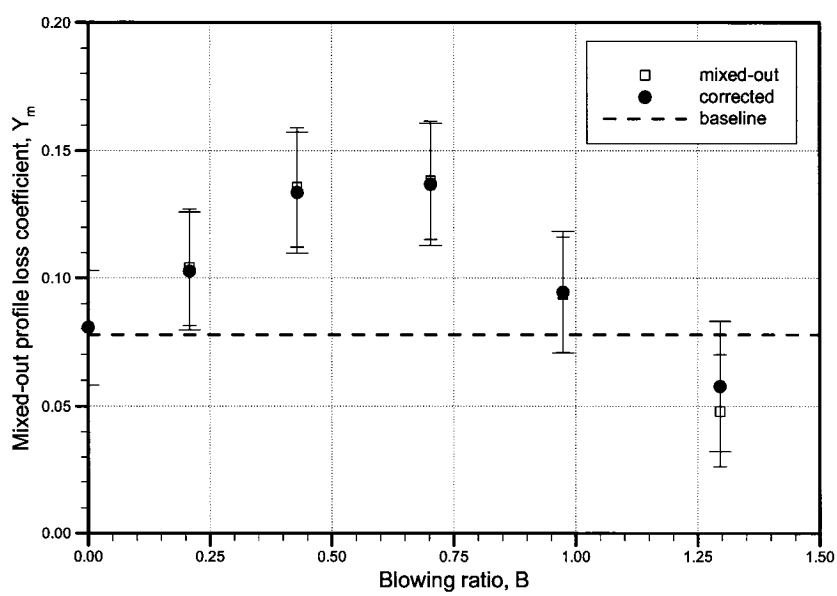

Figure 7.32: **Profile Losses for Re = 25000 and $FSTI$ = 3.9%**

the flow control slot on the blade performance. As B is increased up to $B \approx 0.70$, the losses increase and are almost double those at zero blowing. The loading measurements (Figure 7.28) show a large separation bubble for B lower than 1.00, which results in larger wakes and hence, higher losses. For $B \approx 1.30$ the separation bubble is small and the losses decrease below the baseline airfoil level.

The profile loss coefficients for a Reynolds number of 50000 are presented in Figure 7.33. The zero-blowing losses are slightly lower than the baseline case, indicating a small effect of the flow control slot on the separation characteristics. The losses reach a maximum near $B = 0.50$, as seen for most Reynolds numbers and FSTIs at which the zero-blowing case has a reattached bubble. As B increases to approximately 0.80, the losses decrease to a value similar to the baseline case, after which a slight increase in losses is observed. For all blowing ratios examined at a Reynolds number of 50000, the losses are higher than the zero-blowing case.

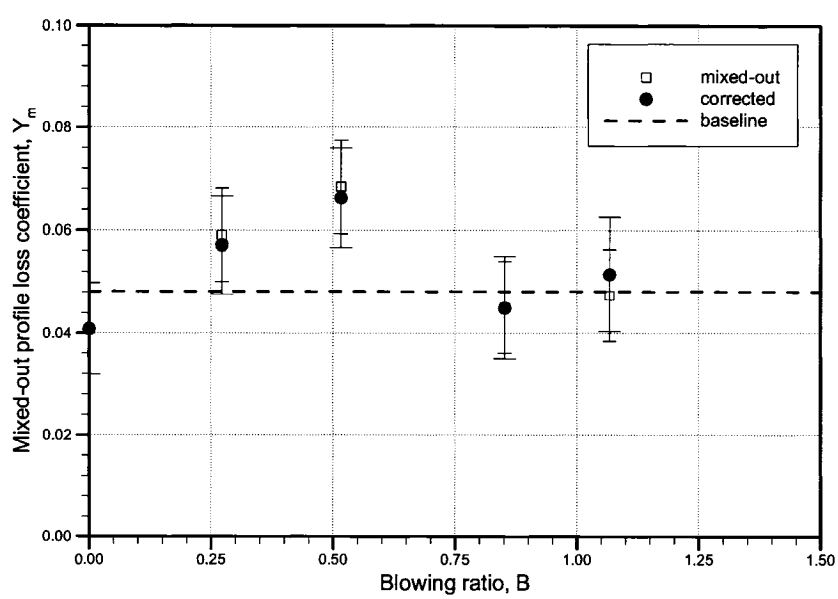

Figure 7.33: **Profile Losses for Re = 50000 and $FSTI$ = 3.9%**

The effects of passive flow control by means of a spanwise groove are summarized in Figure 7.34. The similarity in the zero-blowing wake profiles compared to the baseline cases, as discussed in the previous section, result in very similar profile losses at all Reynolds numbers examined. A small reduction in losses is present for Reynolds numbers of 50000 and 100000.

The "corrected" profile loss coefficients for all high-FSTI cases are shown in Figure 7.35. It is apparent in Figure 7.35 that the active flow control device is not effective at high FSTI when the zero-blowing case has a reattached separation bubble. The only case where losses are reduced is for $B = 1.30$ at a Reynolds number of 25000. For blowing ratios greater than those examined, a further reduction in losses may be possible, but at the expense of greater injected jet momentum.

The mixed-out profile losses for high-FSTI show that the current flow control configuration causes a decrease in performance when the baseline airfoil losses are already low. This

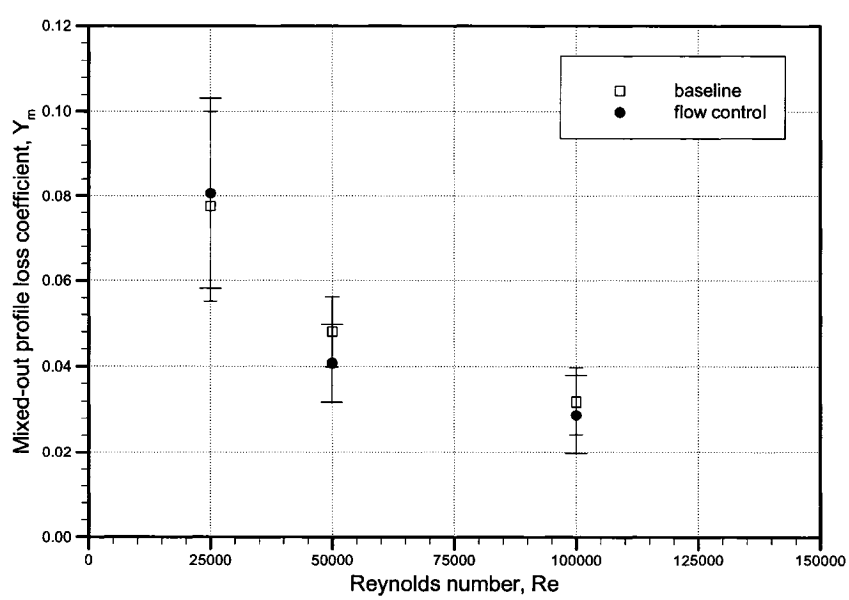

Figure 7.34: **Zero-Blowing Profile Losses for $FSTI$ = 3.9%**

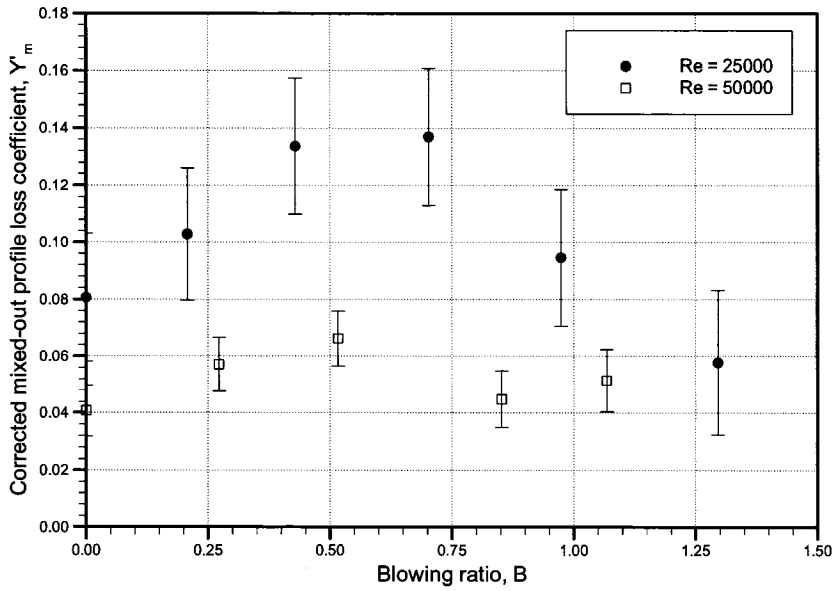

Figure 7.35: **Profile Losses for $FSTI$ = 3.9%, Corrected for Jet Momentum**

is confirmed by the flow control effectiveness coefficient, discussed in the next section.

7.5.4.5 Flow Control Effectiveness for FSTI=3.9%

The effectiveness of the active flow control device at high FSTI is shown in Figure 7.36 in terms of the proposed effectiveness coefficient, ζ (Equation 7.18). Based on the definition of ζ, a negative value signifies an increase in losses from the baseline case. It is clearly seen in Figure 7.36 that the current active flow control device is not effective at low blowing ratios, where the profile losses are higher than for the baseline airfoil. The cases where the flow control device reduces the losses show very small positive values of the effectiveness coefficient, much smaller than those achieved for the low FSTI cases (Figure 7.23).

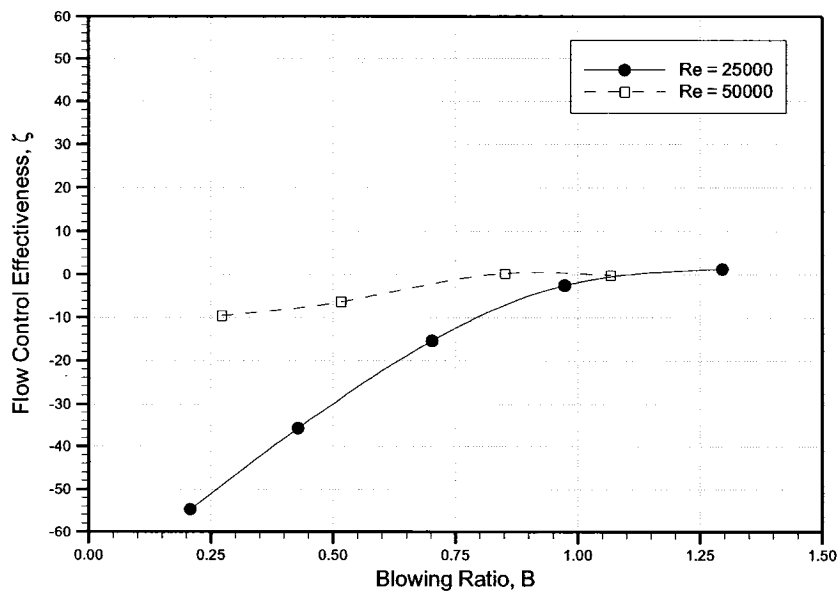

Figure 7.36: **Active Flow Control Effectiveness for $FSTI$ = 3.9%**

7.5.4.6 Mixed-Out Deviation Angles for FSTI=3.9%

At high FSTI, the baseline Pak-B airfoil achieves good flow turning with low outlet flow deviation from the trailing edge metal angle, as discussed in Section 4.3.7. Figure 7.37 shows the mixed-out deviation angles for the current high-FSTI flow control study. For a Reynolds number of 25000, the deviation angle is similar to the baseline case for low-blowing ratios (0.00 and 0.20). At this Reynolds number, deviation reaches a maximum at $B \approx 0.70$, above which it returns to a value similar to the baseline case. The increased deviation is probably due to the large separation bubble that forms over the suction surface, as seen in the loading distribution (Figure 7.28).

For a Reynolds number of 50000, the deviation angle remains relatively constant for all blowing ratios examined, and similar to the baseline case.

The zero-blowing deviation angles for all Reynolds numbers examined are shown in

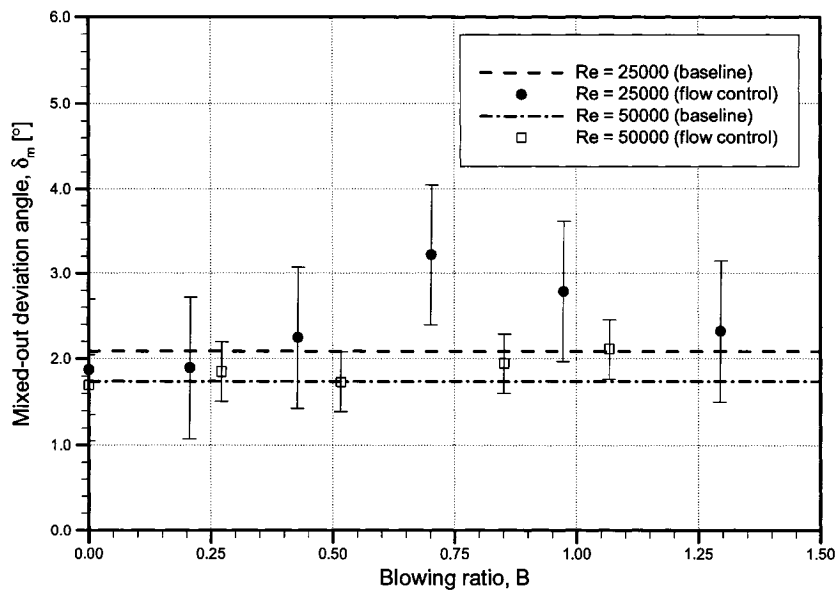

Figure 7.37: **Mixed-Out Deviation Angles for $FSTI$ = 3.9%**

Figure 7.38 and compared to those for the baseline airfoil. Figure 7.38 shows very little difference in the flow deviation between the flow control airfoil and the baseline airfoil, indicating very little effect of the passive flow control device (spanwise groove) on deviation for high FSTI.

So far, in the current chapter, the discussions have focussed on the performance of the flow control cascade and how the mid-span cascade flow reacts to the presence of blowing flow control. To gain a better understanding of how the flow control technique affects the flow field, boundary layer traverses have been made with a hot-wire and are presented in the following sections.

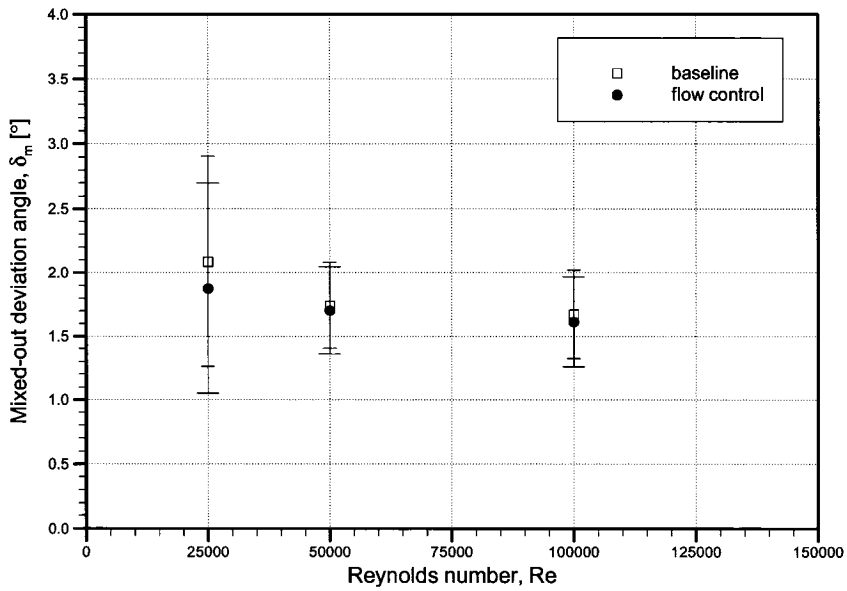

Figure 7.38: **Zero-Blowing Mixed-Out Deviation Angles for $FSTI$ = 3.9%**

7.6 Discussion of Hot-Wire Traverse Measurements

7.6.1 Motivation

This chapter has thus far presented the pressure measurements and performance characteristics for the Pak-B flow control airfoil. Surface static pressure measurements have shown the separation bubble characteristics, and downstream three-hole pressure probe measurements have been used to extract cascade performance parameters such as profile losses and deviation angle. These measurements show the effects of the flow control device but do not directly indicate the ways in which this flow control method affects the flow field. To examine this, hot-wire traverse measurements have been made in the aft-suction surface region of the flow control blade. The following sections present the hot-wire measurements for selected flow control conditions.

7.6.2 Hot-Wire Traverse Cases

Hot-wire traverse measurements have been made over the aft-suction surface of the flow control Pak-B airfoil at a Reynolds number of 50000 for FSTIs of 0.4% and 3.9%. This Reynolds number was selected based on the observed effectiveness of both the passive and active flow control techniques. Various blowing ratios were examined at each FSTI.

At an FSTI of 0.4%, measurements have been made for blowing ratios of 0.0, 0.5, 1.0, and 2.0. This selection of blowing ratios was chosen to examine most of the observed effects on performance at low FSTI. The pressure measurements for these cases have been presented in Section 7.5.3. At an FSTI of 3.9%, measurements have been made for blowing ratios of 0.0, 0.5, and 1.0. These blowing ratios were selected to enable comparison with the low FSTI measurements. The pressure measurements for these cases have been presented in Section 7.5.4.

The hot-wire traverse planes for both FSTIs examined are shown in Figure 7.39. Each of the 14 traverse planes for each FSTI consists of 98 measurements points. At each measurement point, 16384 samples were taken at a sampling rate of 30kHz.

7.6.3 Velocity Field Measurements

The mean velocity field in the aft-suction surface region of the airfoil shows the extent of any separated region and the fluctuations in the velocity also give an indication as to where transition occurs. In Chapter 5, which discussed similar hot-wire measurements for the baseline Pak-B airfoil, the mean velocity and velocity fluctuation fields were presented in the form of colour-flood contour plots, in which the regions of separation and transition were visible. Due to the large number of flow control cases examined (7 cases), these contour plots are not presented in the main body of this chapter, but are included as Appendix

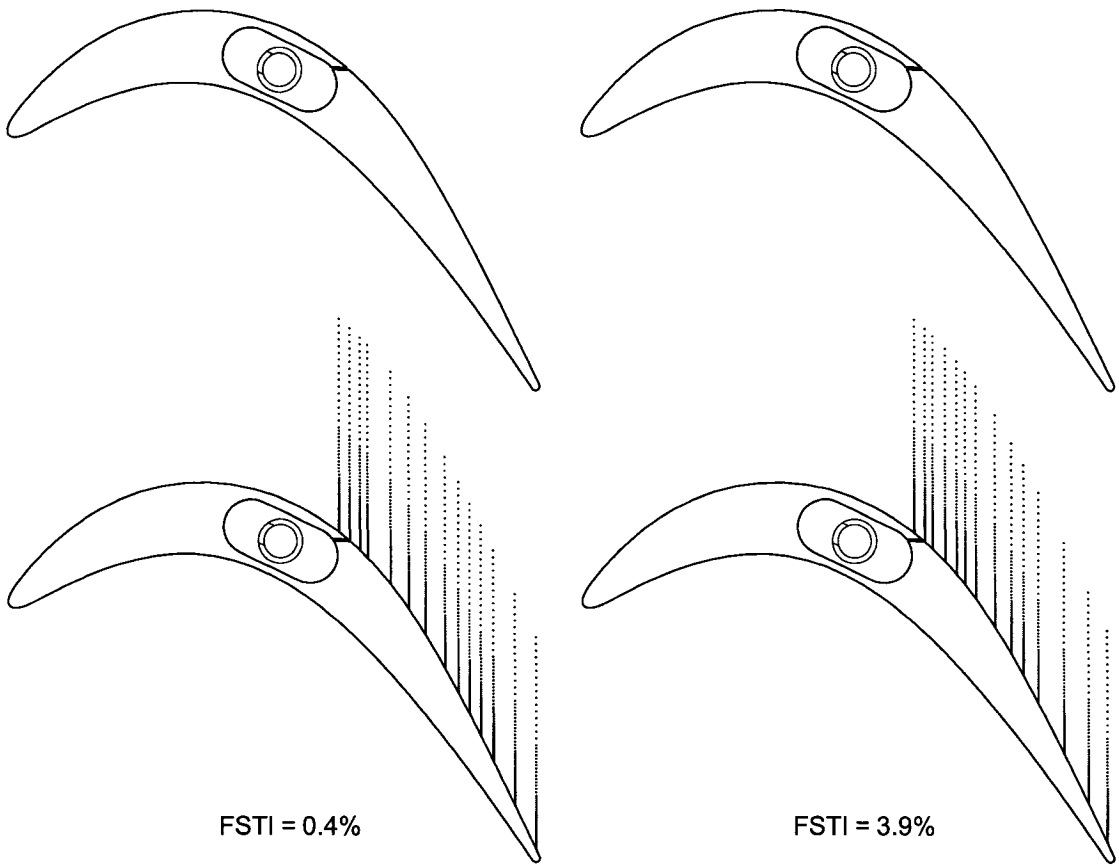

Figure 7.39: **Hot-Wire Traverse Measurement Planes for Flow Control Study**

F. All of the important information contained in the contour plots are also visible in the velocity profiles, which are presented in the following section.

7.6.4 Velocity Profiles

7.6.4.1 Limitations and Extracted Data

The development of the aft-suction surface shear layer is presented in the form of profiles of mean velocity, U, and velocity root-mean-square fluctuation level (RMS), u'. One limitation of the current measurements is the inclination of the traverse planes to the

blade surface, which is on the order of 45°, as seen in Figure 7.39. To account for this inclination, the positions of the measurement points have been corrected, using Equation 5.1 on page 122, to represent the distance normal to the surface. Thus, the velocity profiles presented represent only the approximate profiles at a specific surface location.

Boundary layer integral parameters have been extracted from the hot-wire traverse measurements. The displacement thickness Reynolds number, $Re_{\delta^{*\prime}}$, the momentum thickness Reynolds number, $Re_{\theta'}$, and the shape factor, H', are defined in Chapter 5 on page 122. These integral parameters do not take into account the sign of the velocity in regions of reverse flow since the measured velocities represents the magnitude only. This is due to the inability of hot-wires to distinguish flow direction.

Both mean and fluctuation quantities are normalized by the local edge-of-the-boundary-layer velocity, U_e. The uncertainties in mean velocity and RMS fluctuation levels are below 5% of the calculated value, except when the velocity is below 5 m/s were the uncertainties can be as high as 10% of the calculated values. These uncertainties have been estimated based on the method of Yavuzkurt (1984) as described in Appendix C.

The mean and fluctuating velocity profiles are first presented for an FSTI of 0.4%, followed by those for an FSTI of 3.9%.

7.6.4.2 Measurements for FSTI = 0.4%

The purpose of the hot-wire traverse measurements is to gain more insight into the interaction between the wall jet and the boundary layer. The region of interest is that slightly downstream of the injection slot where the wall jet begins mixing with the boundary layer. Figure 7.40 shows the boundary layer profiles for the first four measurement planes in the region of the slot for an FSTI of 0.4% and blowing ratios of 0.0, 0.5, 1.0, and 2.0.

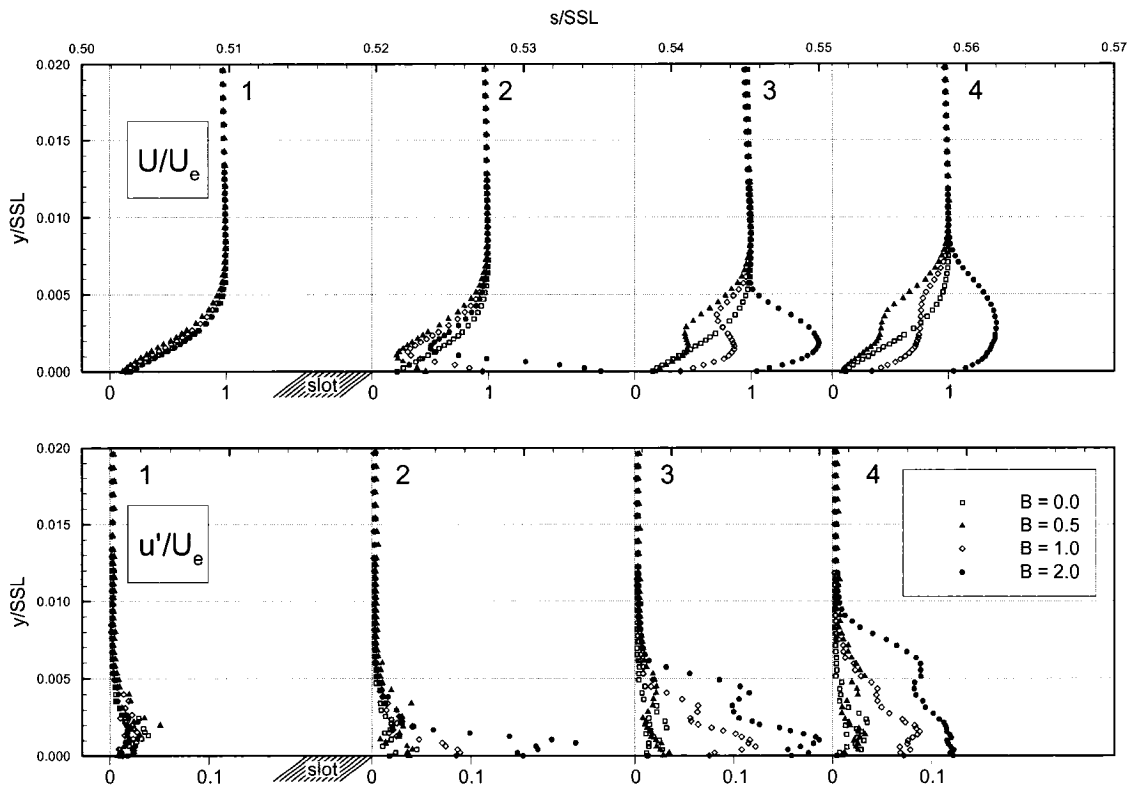

Figure 7.40: **Boundary Layer Profiles in Vicinity of Slot for $FSTI$ = 0.4%**

The slot is located between $\approx 51.5\%SSL$ and $\approx 52\%SSL$, with traverse plane 2 located at the downstream slot edge.

At Station 1 in Figure 7.40 there are slight differences in the mean velocity profiles for all values of B examined. This is due to the effects of the downstream separation on the overall flow field. There is a visible inflection point in the profile for $B = 0.5$ (triangular red symbols). All fluctuation profiles at Station 1 show low level fluctuations within the boundary layer, which is therefore interpreted as laminar.

At Station 2, which is located at the downstream edge of the slot, there is a distinct shift of the laminar boundary layer away from the surface due to the injected mass. This is the region where mixing between the wall jet and the boundary layer begins. High

fluctuations near the surface indicate a turbulent wall jet. There is also an increase in near-wall fluctuations for the zero-blowing case, indicating a disturbance due to the presence of the "passive flow control" spanwise groove.

The velocity profiles at station 3 show the effects of mixing between the wall jet and the laminar boundary layer. For $B = 0.0$, an inflection point is present in the mean velocity profile due to the strong adverse pressure gradient, and near-wall fluctuations are still present. For $B = 0.5$, the mean velocity profile shows the reason for an increased downstream separation bubble. The wall jet lifts the laminar boundary layer away from the surface, but contains insufficient momentum to entrain high energy fluid towards the wall, resulting in a thick boundary layer with a higher momentum deficit than the zero-blowing case. The mean velocity profiles for $B = 1.0$ and $B = 2.0$ show a fuller near-wall profile than the zero-blowing case, which results in a boundary layer less prone to separation. The high-momentum jet at $B = 2.0$ entrains boundary layer and freestream fluid resulting in a thick wall jet profile with minimal momentum deficit between the jet and freestream. The fluctuation profiles for $B = 0.5$, 1.0, and 2.0 show a double peak. The peak nearest the wall is a result of turbulence in the wall jet flow. The second peak is in the region of highest shear in the outer mixing layer and may be interpreted as the onset of transition.

The profiles at Station 4 are similar to those at Station 3. The mean velocity profiles for $B = 0.0$ and 0.5 show near-wall inflection points indicating susceptibility to separation. The higher blowing ratios have a full near-wall profile, with a strong wall jet present at $B = 2.0$. The fluctuation profiles for $B > 0.0$ still show the double peak in the near-wall and outer mixing layer regions.

Downstream of the initial jet-boundary layer mixing region, the effects of the injected momentum are pronounced. Figure 7.41 presents the mean and fluctuation velocity profiles measured over the full aft-suction surface region of the flow-control airfoil. The surface static

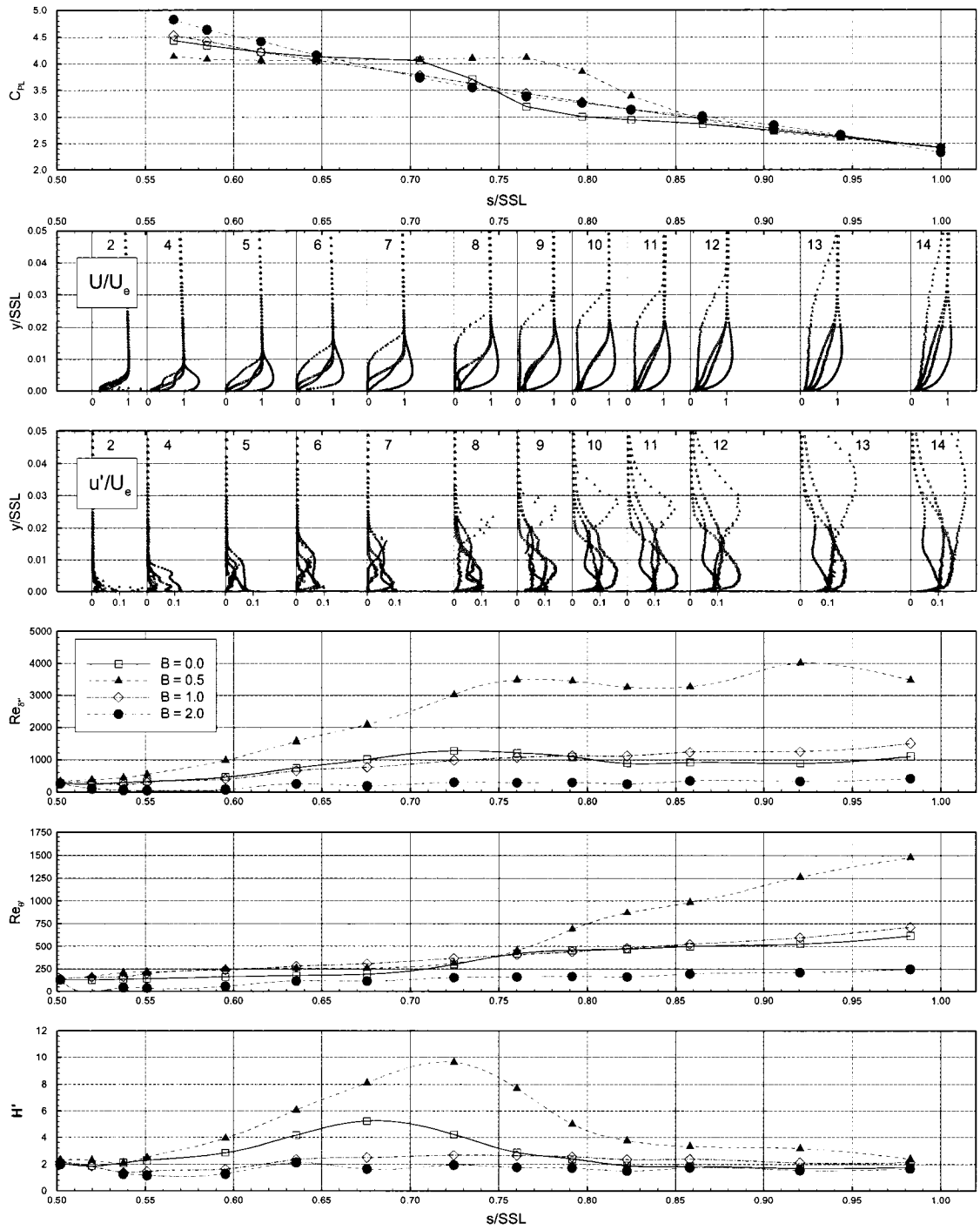

Figure 7.41: **Aft-Suction Surface Boundary Layer Profiles for $FSTI$ = 0.4%**

pressure distribution expressed in terms of the loading coefficient, C_{PL}, is also presented at the top of Figure 7.41, and the boundary layer integral parameters at the bottom.

The mean velocity profiles for the zero-blowing case ($B = 0.0$) show a separated shear layer at Station 6 ($\approx 64\%SSL$) with reattachment by Station 10 ($\approx 79\%SSL$). It is estimated that transition begins around Station 8 ($\approx 72\%SSL$), indicated by the increase in mean and fluctuating velocity below the separated shear layer. High near-wall fluctuations downstream of the slot are the likely cause of stall prevention. These high fluctuations are caused by the presence of the slot which acts as a disturbance to the laminar boundary layer.

At a blowing ratio of 0.5, separation is present at Station 5 ($\approx 60\%SSL$) due to the thick low-momentum boundary layer caused by the low-momentum jet. The separation bubble at $B = 0.5$ is thicker and longer than that at $B = 0.0$, with reattachment occurring near Station 12 ($\approx 86\%SSL$). Transition is estimated to begin near Station 8 ($\approx 72\%SSL$), indicated by the increase in fluctuation levels below the separated shear layer and by the maximum in shape factor, H'. The high fluctuations present within the separated shear layer indicate that strong mixing occurs. The location of maximum bubble height, or maximum displacement thickness, occurs near Station 9 ($\approx 76\%SSL$) and corresponds to the "knee" in the pressure distribution over the bubble. A very thick boundary layer is present at the trailing edge, resulting in increased losses as compared to the zero-blowing case.

Separation is not present at a blowing ratio of 1.0. The fuller profile downstream of the slot inhibits separation over the entire aft-suction surface. High fluctuations across the profiles indicate a fully turbulent boundary layer. Near the trailing edge, the displacement and momentum thicknesses are higher than the zero-blowing case, indicating that although separation is prevented, the fluid injection does not result in a reduction in losses. This is

likely due to the losses resulting from the mixing between the wall jet and the shear layer.

At $B = 2.0$, the wall jet is present up to the trailing edge and the flow is attached over the entire suction surface. Fluctuations are highest in the inner region of the wall jet, below the velocity peak, but downstream of Station 8 ($\approx 72\%SSL$) the outer layer fluctuations are lower than most other blowing ratios examined. This results from lower shear in the outer layer of the wall jet. The mean and fluctuation velocity profiles are similar to those presented by Ramaprian (1975) for wall jets in an adverse pressure gradient. For $B = 2.0$, the integral parameters presented in Figure 7.41 are calculated from the surface up to the point of maximum wall jet velocity. Calculation across the entire wall jet/shear layer would result in negative displacement and momentum thicknesses, which although represent the high entrainment of freestream fluid into the wall jet, are not directly comparable to the other cases examined. The shape factor, which represents the fullness of the inner wall jet, is below a value of 2.0 for most stations. In an adverse pressure gradient, a shape factor below 2.0 is indicative of a turbulent boundary layer that is still well short of separation (Fottner, 1979).

The hot-wire measurements presented in this section have given insight into the mechanism by which separation is either promoted or prevented by the injected jet momentum. For low-momentum injection ($B \approx 0.5$), the laminar boundary layer is lifted away from the wall and a thick low-momentum shear layer results in a larger separation bubble and higher losses than the zero-blowing case. For blowing ratios on the order of 1.0 and higher, separation is prevented by the higher momentum injected in the near-wall region. At high-blowing ratios ($B \approx 2.0$), the high momentum injected from the slot entrains freestream fluid resulting in a wall jet over the entire aft-suction surface. The next section presents similar measurements for high-FSTI conditions where the separated shear layer reattaches without flow control.

7.6.4.3 Measurements for FSTI = 3.9%

As described in the previous section, the region of interest for studying the effects of the injected fluid is that downstream of the injection slot. Figure 7.42 shows the boundary layer profiles for the first four measurement planes in the region of the slot for an FSTI of 3.9% and blowing ratios of 0.0, 0.5, and 1.0.

At Station 1, located ahead of the slot, the mean velocity profiles for all blowing ratios examined are very similar, as are the fluctuation profiles. The zero-blowing case shows a slightly thinner boundary layer. The thicker boundary layers at $B > 0.0$ are due to the downstream lifting effect of the wall jet.

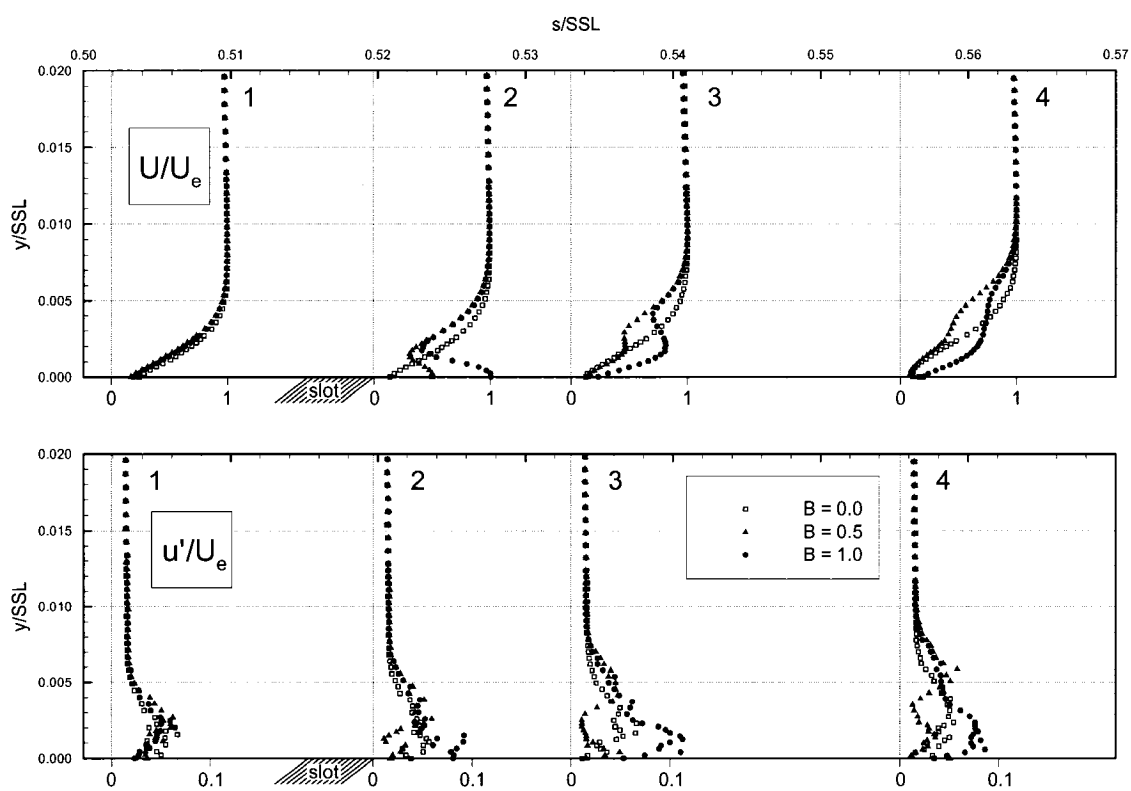

Figure 7.42: **Boundary Layer Profiles in Vicinity of Slot for $FSTI$ = 3.9%**

The mean velocity profiles at Station 2 show the lifting effect of the wall jet on the laminar boundary layer. The profiles outside the jet region for $B > 0.0$ are very similar. The fluctuation profiles show higher near-wall fluctuations for $B = 0.0$ as compared to $B = 0.5$. At $B = 0.5$, the turbulent fluctuation level in the jet is in fact lower than the laminar fluctuation level generated within the upstream laminar boundary layer. The high near-wall fluctuations for $B = 1.0$ indicate a turbulent wall jet flow.

At Station 3, the $B = 0.5$ case shows a thick low-momentum boundary layer, similar to the low-FSTI case discussed in the previous section. The zero-blowing case not only has a lower momentum deficit than the $B = 0.5$ case, but also has higher maximum fluctuations. At $B = 1.0$, the high near-wall momentum and high near-wall fluctuations indicate a shear layer that is less susceptible to separation than the zero-blowing case.

The profiles at Station 4 are similar to those at Station 3. The $B = 0.0$ and $B = 0.5$ cases have a distinct inflection point in the mean velocity profile.

The development of the shear layer over the full aft-suction surface with flow control is shown in Figure 7.43 for an FSTI of 3.9% and blowing ratios of 0.0, 0.5, and 1.0. The surface static pressure distribution expressed in terms of the loading coefficient, C_{PL} is also presented at the top of Figure 7.43, and the boundary layer integral parameters at the bottom.

The zero-blowing case ($B = 0.0$) is similar to the corresponding low-FSTI case described in the previous section. Separation is present at Station 6 ($\approx 60\%SSL$), with reattachment by Station 11 ($\approx 77\%SSL$). Transition is estimated to begin near Station 9 ($\approx 70\%SSL$), indicated by the increased fluctuations below the separated shear layer and the maximum in the shape factor, H'. Reattachment begins near Station 10 ($\approx 73\%SSL$), as indicated by the local maximum in displacement thickness. The location and length of the separation bubble inferred from these measurements agrees well with the surface static pressure distribution.

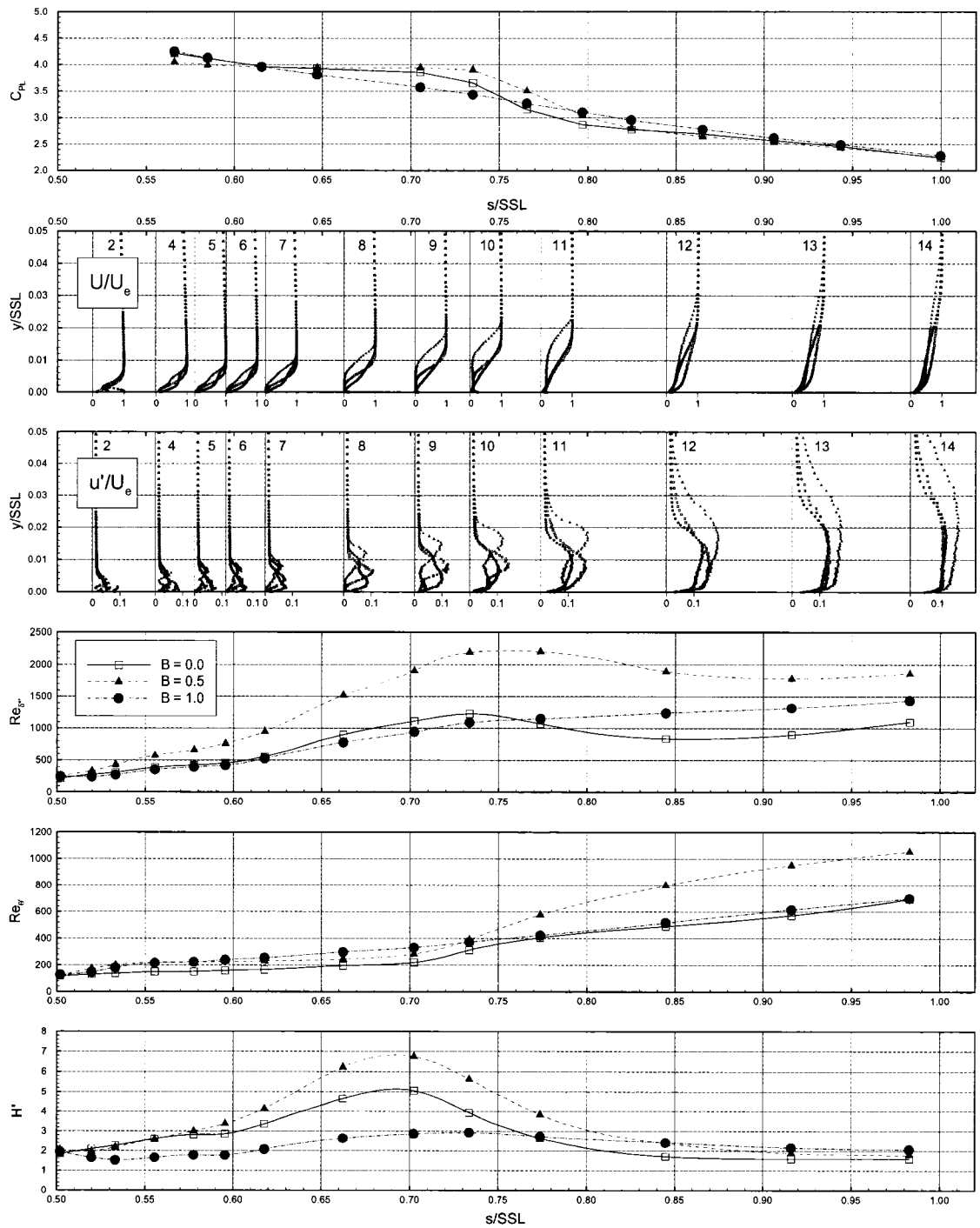

Figure 7.43: **Aft-Suction Surface Boundary Layer Profiles for $FSTI$ = 3.9%**

As compared to the corresponding baseline case presented in Chapter 5, the separation bubble has approximately the same length but is slightly thinner. This thinning of the separation bubble is likely due to increased fluctuations caused by the slot disturbance, which results in earlier transition and thus slightly higher entrainment towards the surface ahead of separation.

At $B = 0.5$, the separation bubble is larger than for $B = 0.0$, both in thickness and length, due to the higher momentum deficit downstream of the flow control injection slot. Separation is present at Station 6 ($\approx 60\%SSL$) with transition onset estimated near Station 9 ($\approx 70\%SSL$). Reattachment begins after Station 11 ($\approx 77\%SSL$) and the separated shear layer is reattached to the surface at Station 12 ($\approx 85\%SSL$). The thick trailing edge boundary layer results in the increased losses discussed in Section 7.5.4.4.

Separation is prevented at $B = 1.0$ due to higher-momentum near-wall fluid provided by the wall jet. The trailing edge boundary layer profile has a higher displacement thickness than the zero-blowing case, but the momentum thickness is similar.

The boundary layer traverses presented for an FSTI of 3.9% show that blowing through the flow control slot can either prevent or promote separation, depending on the level of momentum addition. The zero-blowing case has a small separation bubble that does not adversely affect the blade performance as compared to the non-separated boundary layer seen at $B = 1.0$. The presence of the slot with zero-blowing also reduces the thickness of the separation bubble.

7.7 Summary of Flow Control Study

This chapter has presented results for the Pak-B flow control study. A method of active flow control, consisting of an inclined plane wall jet, has been used to inject momentum in the near-wall region of the boundary layer in hopes that the additional high-energy fluid will reduce or suppress separation. When no blowing is present, the flow control slot also acts as a passive flow control device, consisting of a spanwise groove.

It has been found that the use of active flow control is only useful when the baseline (clean blade) airfoil is stalled. Stall occurs at low-Reynolds numbers (25000 and 50000) and low freestream turbulence intensity (0.4%). At a Reynolds number of 25000 and an FSTI of 0.4%, a blowing ratio greater than 1.0 is required to suppress stall and reduce profile losses to an acceptable level. At a Reynolds number of 50000 and an FSTI of 0.4%, the active flow control device is effective at preventing stall, but the presence of the flow control slot without any blowing also results in stall suppression and acceptable losses. This passive flow control device appears to be an effective method of increasing the performance of the Pak-B airfoil, and may be a future avenue of study for LPT stall control. For cases where the baseline airfoil has a reattached separation bubble, the active flow control device does not significantly improve performance. In many cases, mainly at low-blowing ratios, the current method of active flow control increases the profile losses of the Pak-B airfoil, whereas the passive flow control device results in equal or decreased losses for all cases examined.

To examine the interaction between the jet and the surface shear layer, hot-wire traverse measurements made over the aft-suction surface region of the airfoil have been presented. At high blowing ratios, separation is prevented by injection of high-momentum turbulent fluid in the near-wall region, which "fills-up" the boundary layer. At low-blowing ratios, the low-momentum addition, coupled with the lifting effect of the injected fluid on the laminar boundary layer, results in a boundary layer profile with higher momentum deficit than the

zero-blowing case. This low-momentum profile is more prone to separation.

The current study has demonstrated that both passive and active flow control can be used to improve the performance of a low-pressure turbine airfoil. Active flow control has been found to prevent stall of the Pak-B airfoil for low freestream turbulence intensity (0.4%), a level much lower than would be expected in an engine. Although the examined method of active flow control does not benefit the Pak-B airfoil at engine conditions (freestream turbulence intensity of 4%), the results suggest that a more highly loaded airfoil that stalls at high freestream turbulence levels may benefit from this flow control technique. One advantage of active flow control is that the control scheme can be activated only when required, and the disadvantages of the current control technique for un-stalled conditions could be avoided.

Chapter 8

Conclusions and Recommendations

8.1 Conclusions

A decrease in performance of the low-pressure turbine (LPT) of modern high bypass ratio turbofan engines has been observed at low-Reynolds numbers, typical of the conditions encountered during high-altitude flight. This decrease in performance is due to laminar separation of the suction surface boundary layer and subsequent stall of the LPT airfoils. The stall characteristics of LPT airfoils are influenced by the Reynolds number and level of freestream turbulence, both of which affect the transition process within the separated shear layer.

The present research has examined the influence of turbulent length scale on the performance of a low-pressure turbine airfoil at low Reynolds numbers, and has examined a method of separation control for low-pressure turbines at low Reynolds numbers. These investigations have been performed in a low-speed linear cascade test section with a low-pressure turbine airfoil typical of current in-service designs. The airfoil profile is the Pratt & Whitney Pak-B airfoil, which is an industry supplied airfoil with a surface shape that

has been inverse-designed to achieve the same non-dimensional pressure distribution at low speed as is encountered in compressible flow conditions of an actual engine. Mid-span measurements have been presented for a range of Reynolds numbers and freestream turbulence levels. Detailed flow field measurements were made downstream of the cascade using a three-hole pressure probe, surface static pressure measurements were made to examine the loading distribution over the airfoil, and hot-wire traverse measurements were made to examine the development of the aft suction surface shear layer. Surface-mounted hot-film measurements were also made over the suction surface of the baseline (non-flow control) airfoil to examine the transition process within the separated shear layer.

To examine the influence of turbulent length scale on the performance of the Pak-B cascade, a new turbulence generating grid was designed and manufactured to achieve a similar level of freestream turbulence intensity as a previous study performed in the same facility (Mahallati, 2003), but with a smaller freestream turbulent length scale. The freestream turbulence intensity was approximately 4% at the leading edge of the cascade middle blade, and the corresponding level of integral length scale was on the order of 10% of the airfoil axial chord length, as compared to approximately 30% in the study of Mahallati (2003). First, measurements were performed with the new small length-scale grid to examine the performance and the separated-flow transition process of the Pak-B airfoil at elevated levels of turbulence intensity (Chapter 4). It was observed that for the Reynolds numbers examined (25000 to 150000), transition within the separated shear layer promoted reattachment to the suction surface ahead of the trailing edge. As the Reynolds number was decreased, transition onset was delayed and the length of the separation bubble increased. This resulted in an increase in profile losses with decreasing Reynolds number. A comparison of these results with those of Mahallati (2003) for the larger turbulent length scale measurements (Chapter 6) showed very little difference in the transition process over the airfoil suction surface. A slight downstream shift in the location of transition onset

and reattachment was observed for the larger length scale cases. The profile losses for the two levels of length scale showed similar trends with Reynolds number, but approximately 25% higher losses were observed for the small length scale cases. These increased losses may be due to the lower axial-velocity ratio (AVR) present for these cases. A low AVR imposes an additional adverse pressure gradient across the cascade that can influence the mid-span boundary layers. For the two levels of turbulent integral length scale examined, it is concluded that there is no significant effect of length scale on the transition process over the Pak-B airfoil.

During the course of the present experimental investigations, it was realized that sufficient precision could be achieved with the test section traverse mechanism to make detailed hot-wire traverse measurements of the aft suction surface shear layer. Chapter 5 presented these measurements for the baseline (non-flow control) airfoil at a Reynolds number of 50000 with freestream turbulence intensities of 0.4% and 3.9%. Profiles of mean and fluctuating velocity components were compared with surface-mounted hot-film measurements to examine the validity of interpreting separated-flow transition with surface measurements. Good agreement between the estimated locations of separation, transition onset, maximum bubble height, and reattachment was observed for the high-freestream turbulence measurements, adding confidence to the surface-mounted hot-film interpretation techniques.

A method of active separation control was examined for the Pak-B airfoil in Chapter 7. The flow control technique consisted of localized blowing through an inclined slot, located slightly upstream of the nominal separation location. The injected wall jet was expected to re-energize the near-wall boundary layer. The resulting shear layer was then expected to overcome the strong adverse pressure gradient and prevent separation. In general, active separation control using the present technique is only effective at reducing losses when the

baseline (non-flow control) airfoil is stalled. This occurs at Reynolds numbers of 25000 and 50000 with a freestream turbulence intensity of 0.4%. A blowing ratio greater than 1.0 was required to prevent stall and reduce losses to an acceptable level at a Reynolds number of 25000, whereas at a Reynolds number of 50000, the presence of the slot without blowing prevented stall and reduced profile losses. At all conditions examined, the flow control airfoil without blowing had losses either similar to or lower than the baseline airfoil, indicating that a recessed spanwise groove may be a possible method of passive flow control. For conditions at which the flow control airfoil with no blowing was un-stalled, an increase in the length of the separation bubble and an increase in losses was observed for low levels of blowing (blowing ratio of approximately 0.5). The advantage of active flow control is that the control method could be activated only when required, and the disadvantages of the current control technique for un-stalled conditions could be avoided. To examine the separation characteristics of the flow control airfoil with and without blowing, hot-wire traverse measurements were made over the suction surface downstream of the injection slot. At high levels of blowing (blowing ratios of 1.0 and 2.0), separation was prevented by injection of high-momentum turbulent fluid in the near-wall region, which "filled-up" the boundary layer and promoted transition in the outer shear layer. At low levels of blowing (blowing ratio of 0.5), the low-momentum addition, coupled with the lifting effect of the injected fluid on the laminar boundary layer, resulted in a velocity profile with high momentum deficit which promoted earlier separation and a larger separation bubble.

8.2 Recommendations for Future Work

From the results of the present experimental investigations, future avenues of research have been identified.

Some of the limitations of the hot-wire traverse techniques developed during the present

investigation can be eliminated by modifying the test section traverse mechanism. By attaching a two-axis traverse mechanism to the bottom tailboard of the test section, traverses normal to the airfoil surfaces could be performed. This would allow more accurate calculation of the shear layer integral parameters, and also allow comparison to previously published measurements over the Pak-B airfoil. Also, more detailed examination of hot-wire traverse measurements could be performed. For example, a spectral analysis of the hot-wire signals could be performed to attempt the identification of the dominant frequencies involved in separated-flow transition. Extraction of intermittency data could also be performed, using filtering techniques such as those used by Roberts and Yaras (2003) and Volino (2002).

The current study has demonstrated that active flow control can prevent stall of the Pak-B airfoil for low freestream turbulence intensity. Although the examined method of flow control does not benefit the Pak-B airfoil at levels of freestream turbulence typical of those encountered in an actual engine, the results suggest that a more highly loaded airfoil that stalls at high freestream turbulence levels may benefit from this flow control technique. One such airfoil is currently under investigation in the Low-Speed Turbomachinery Laboratory at Carleton University. Examples of unsteady blowing using vortex generator jets for separation suppression of the Pak-B airfoil have been demonstrated by Bons *et al.* (2002) and Volino (2003b). The main advantage of unsteady blowing is a reduction in the required secondary mass flow rate for a given level of loss reduction. Unsteady blowing techniques using a slot configuration could also be investigated, particularly with more highly loaded airfoils.

The investigation of Mahallati (2003) also examined the effects of unsteady wake induced transition on the separation characteristics of the Pak-B airfoil. It was demonstrated that the presence of incoming wakes prevents stall of the airfoil even at low freestream turbulence levels. For a more highly loaded airfoil, the unsteady wake induced transition process may no

longer be able to prevent stall, and blowing flow control may be a viable solution. Clocking of pulsed injection with the wake passing frequency could also be examined to reduce the required secondary air supply.

The present flow control investigation has also identified a possible means of passive flow control. The presence of the slot without injection has prevented stall for one combination of Reynolds number and freestream turbulence intensity. This suggests that passive separation control might be an economic means of flow control in gas turbine engines, and is recommended as the first step in future low-pressure turbine flow control studies.

References

Abu-Ghannam, B. J. and Shaw, R. (1980), "Natural Transition of Boundary Layers - The Effects of Turbulence, Pressure Gradient and Flow History," Journal of Mechanical Engineering Sciences, **22**, pp. 213–228.

Ainley, D. G. and Mathieson, G. C. R. (1951), "A Method of Performance Estimation for Axial Flow Turbines," British ARC, R&M 2974 .

Ames, F. E. and Plesniak, M. W. (1995), "The Influence of Large Scale, High Intensity Turbulence on Vane Aerodynamic Losses, Wake Growth, and the Exit Turbulence Parameters," ASME paper No. 95-GT-290, Houston, Texas.

Anderson, B. T., Meyer, R. R. and Chiest, H. R. (1991), "Techniques Used in the F-14 Variable-Sweep Transition Flight Experiment," AIAA Journal of Aircraft, **28**, pp. 622–629.

Back, L. and Cuffel, R. (1982), "Experimental Investigation of Turbulent Wall-Jets in the Presence of Adverse Pressure Gradients in a Rectangular Diffuser," International Journal of Heat and Mass Transfer, **25**, pp. 871–887.

Bearman, P. W. (1971), "Corrections for the Effect of Ambient Temperature Drift on Hot-Wire Measurements in Incompressible Flow," DISA Information, **11**, pp. 25–30.

Benner, M. W. (2003), "The Effects of Leading Edge Geometry on Profile and Secondary Losses in Turbine Cascades," Ph.D. thesis, Carleton University, Ottawa, Canada.

Bons, J. P., Sondergaard, R. and Rivir, R. B. (1999), "Control of Low-Pressure Turbine Separation Using Vortex Generator Jets," AIAA paper No. 99-0367, Reno, Nevada.

Bons, J. P., Sondergaard, R. and Rivir, R. B. (2001), "Turbine Separation Control Using Pulsed Vortex Generator Jets," Journal of Turbomachinery, **123**, pp. 198–206.

Bons, J. P., Sondergaard, R. and Rivir, R. B. (2002), "The Fluid Dynamics of LPT Blade Separation Control Using Pulsed Jets," Journal of Turbomachinery, **124**, pp. 77–85.

Brocher, E. F. (1961), "The Jet-Flap Compressor Cascade," Journal of Basic Engineering, pp. 401–407.

Bruun, H. H. (1995), *Hot-&Wire Anemometry: Principles and Signal Analysis*, Oxford University Press, New York.

Butler, R. J., Byerley, A. R., Treuren, K. V. and Baughn, J. W. (2001), "The Effect of Turbulence Intensity and Length Scale on Low-Pressure Turbine Blade Aerodynamics," International Journal of Heat and Fluid Flow, **22**, pp. 123–133.

Carter, C. J., Guillot, S. A., Ng, W. F. and Copenhaver, W. W. (2001), "Aerodynamic Performance of a High-Turning Compressor Stator with Flow Control," AIAA paper No. 2001-3973, Salt Lake City, Utah.

Chin, Y. T., Aiken, T. N. and Oates, G. S. (1975), "Evaluation of a New Jet Flap Propulsive-Lift System," AIAA Journal, **12**, pp. 605–610.

Culley, D. E., Bright, M. M., Prahst, P. S. and Strazisar, A. J. (2003), "Active Flow Separation Control of a Stator Vane Using Surface Injection in a Multistage Compressor Experiment," ASME paper No. GT2003-38863, Atlanta, Georgia.

Cumpsty, N. A. (1989), *Compressor Aerodynamics*, Longman Group, United Kingdom.

Curtis, E. M., Hodson, H. P., , Banieghbal, M. R., Denton, J. D., Howell, R. J. and Harvey, N. W. (1997), "Development of Blade Profiles for Low-Pressure Turbine Applications," Journal of Turbomachinery, **119**, pp. 531–538.

Denton, J. D. (1993), "Loss Mechanisms in Turbomachines," ASME Journal of Turbomachinery, **115**, pp. 621–656.

Dhawan, S. and Narasimha, R. (1958), "Some Properties of Boundary-Layer Flow During the Transition from Laminar to Turbulent Motion," Journal of Fluid Mechanics, **3**, pp. 418–436.

Dorney, D. J., Lake, J. P., King, P. I. and Ashpis, D. E. (2000), "Experimental and Numerical Investigation of Losses in Low-Pressure Turbine Blade Rows," AIAA paper No. 2000-0737, *AIAA 38th. Aerospace Sciences Meeting & Exhibit*, Reno, NV.

Dullenkopf, K. and Mayle, R. E. (1995), "An Account for Free-Stream-Turbulence Length Scale on Laminar Heat Transfer," ASME Journal of Turbomachinery, **117**, pp. 401–406.

Eriksson, J. G., Karlsson, R. I. and Persson, J. (1998), "An Experimental Study of a Two-Dimensional Plane Turbulent Wall Jet," Experiments in Fluids, **25**, pp. 50–60.

Fielder, R. A. and Gessner, F. B. (1972), "Influence of Tangential Fluid Injection on the Performance of Two-Dimensional Diffusers," Journal of Basic Engineering, **94D**, pp. 666–674.

Fottner, L. (1979), "Theoretical and Experimental Investigations on Aerodynamically Highly-Loaded Compressor Bladings with Boundary Layer Control," AIAA paper No. 79-7032, Lake Buena Vista.

Fraser, C. J., Milne, J. S. and Gardiner, I. D. (1988), "The Effect of Pressure Gradient and Freestream Turbulence Intensity on the Length of Transitional Boundary Layers," Proc Instn Mech Engrs, **202**, pp. 195–203.

Funazaki, K., Endo, T. and Tanuma, T. (1996), "Reduction of Secondary Flow Effects in a Linear Cascade by Use of Air Suction from the Endwall," ASME paper No. 96-TA-51, Jakarta, Indonesia.

Gad-el-Hak, M. (2000), *Flow Control: Passive, Active, and Reactive Flow Management*, Cambridge University Press, Cambridge, UK.

Gad-el-Hak, M. (2001), "Flow Control: The Future," Journal of Aircraft, **38**, pp. 402–418.

Goobie, S. M. (1989), "A Test Section for Investigating the Off-Design Performance of Planar Cascades," Ph.D. thesis, Carleton University, Ottawa, Canada.

Gostelow, J. P., Blunden, A. R. and Walker, G. J. (1994), "Effects of Freestream Turbulence and Adverse Pressure Gradients on Boundary Layer Transition," Journal of Turbomachinery, **116**, pp. 392–404.

Gostelow, J. P., Melwani, N. and Walker, G. J. (1996), "Effects of streamwise pressure gradients on turbulent spot development," Journal of Turbomachinery, **118**, pp. 737–743.

Harvey, N. W., Cox, J. C., Shulte, V., Howell, R. and Hodson, H. P. (1999), "The Role of Research in the Aerodynamic Design of an Advanced Low-Pressure Turbine," Proc IMechE, **213 Part A**, pp. 235–242.

Hatman, A. and Wang, T. (1999), "A Prediction Model for Separated-Flow Transition," ASME Journal of Turbomachinery, **121**, pp. 594–602.

Hinze, J. O. (1975), *Turbulence*, 2nd ed., McGraw-Hill, New York.

Hodson, H. P. (1985), "Measurements of Wake-Generated Unsteadiness in the Rotor Passage of Axial Flow Turbines," ASME Journal of Engineering for Gas Turbines and Power, **107**, pp. 467–476.

Hoheisel, H., Kiock, R., Lichtfuss, H. J. and Fottner, L. (1987), "Influence of Free-stream Turbulence and Blade Pressure Gradient on Boundary Layer and Loss Behavior of Turbine Cascades," Journal of Turbomachinery, **109**, pp. 210–219.

Hollon, B. and Jacob, J. (2001), "Experimental Investigation of Separation on Low Pressure Turbine Blades," AIAA paper No. 2001-0447, *AIAA 39th. Aerospace Sciences Meeting & Exhibit*, Reno, NV.

Hourmouziadis, J. (1989), "Aerodynamic Design of Low Pressure Turbines," AGARD Lecture Series 167, pp. 8:1–40.

Howell, R. J., Ramesh, O. N., Hodson, H. P., Harvey, N. W. and Schulte, V. (2001), "High Lift and Aft-Loaded Profiles for Low-Pressure Turbines," ASME Journal of Turbomachinery, **123**, pp. 181–188.

Islam, A. M. T. and Sjolander, S. A. (1999), "Deviation in Axial Turbines at Subsonic Conditions," ASME paper No. 99-GT-026, Indianapolis, IN.

Japikse, D. and Baines, N. C. (1994), *Introduction to Turbomachinery*, Concepts ETI & Oxford University Press, New York.

Johnson, M. W. and Dris, A. (2000), "The Origin of Turbulent Spots," Journal of Turbomachinery, **122**, pp. 88–92.

Kacker, S. C. and Okapuu, U. (1982), "A Mean Line Prediction Method for Axial Flow Turbine Efficiency," ASME Journal of Engineering for Power, **104**, pp. 111–119.

Kobayashi, R. and Fujisawa, N. (1982), "Turbulence Characteristics of Plane Wall Jets," Rep. Inst. High Speed Mech., **45**, pp. 95–113.

Kwong, A. H. M. and Dowling, A. P. (1994), "Active Boundary-Layer Control in Diffusers," AIAA Journal, **32**, pp. 2409–2414.

Lake, J. P., King, P. I. and Rivir, R. B. (1999), "Reduction of Separation Losses on a Turbine Blade with Low Reynolds Numbers," AIAA paper No. 99-0242, *AIAA 37th. Aerospace Sciences Meeting & Exhibit*, Reno, NV.

Lake, J. P., King, P. I. and Rivir, R. B. (2000), "Low Reynolds Number Loss Reduction on Turbine Blades with Dimples and V-Grooves," AIAA paper No. 00-0738, *AIAA 37th. Aerospace Sciences Meeting & Exhibit*, Reno, NV.

Launder, B. E. and Rodi, W. (1981), "The Turbulent Wall Jet," Progress in Aerospace Sciences, **19**, pp. 81–128.

Lewis, A. B. (1966), "Fixed-Direction Probes for Aerodynamics Measurements," Proc. Inst. Mech. Engrs, Pt.3J, **180**, pp. 141–152.

Lin, J. C. (2002), "Review of Research on Low-Profile Vortex Generators to Control Boundary-Layer Separation," Progress in Aerospace Sciences, **38**, pp. 389–420.

Lin, J. C., Howard, F. G., Bushnell, D. M. and Selby, G. V. (1990), "Investigation of Several Passive and Active Methods for Turbulent Flow Separation Control," AIAA paper No. 90-1598, *AIAA 21st Fluid Dynamics, Plasma Dynamics and Lasers Conference*, Seattle, WA.

Lin, J. C., Howard, F. G. and Selby, G. V. (1989), "Turbulent Flow Separation Control Through Passive Techniques," AIAA paper No. 89-0976, *AIAA 2nd Shear Flow Conference*, Tempe, AZ.

Lord, W. K., MacMartin, D. G. and Tillman, T. G. (2000), "Flow Control Opportunities in Gas Turbines," AIAA paper No. 2000-2234, *Fluids 2000*, Denver, CO.

Loth, J. L. and Boasson, M. (1984), "Circulation Controlled STOL Wing Optimization," AIAA Journal, **21**, pp. 128–134.

Mahallati, A. (2003), "Aerodynamics of a Low-Pressure Turbine Airfoil Under Steady and Periodically Unsteady Conditions," Ph.D. thesis, Carleton University, Ottawa, Canada.

Malkiel, E. and Mayle, R. E. (1996), "Transition in a Separation Bubble," ASME Journal of Turbomachinery, **118**, pp. 752–759.

Mayle, R. E. (1991), "The Role of Laminar-Turbulent Transition in Gas Turbine Engine," ASME Journal of Turbomachinery, **113**, pp. 509–537.

Mayle, R. E., Dullenkopf, K. and Schultz, A. (1998), "The Turbulent That Matters," ASME Journal of Turbomachinery, **120**, pp. 402–409.

Mayle, R. E. and Schultz, A. (1997), "The Path to Predicting Bypass Transition," ASME Journal of Turbomachinery, **119**, pp. 405–411.

Merchant, A. (2002), "Aerodynamic Design and Performance of Aspirated Airfoils," ASME paper No. GT2002-30369, Amsterdam, The Netherlands.

Mikolajczak, A. A., Weingold, H. D. and Nikkanen, J. P. (1970), "Flow Through Cascades of Slotted Compressor Blades," Journal of Engineering for Power, pp. 57–64.

Moffat, R. J. (1982), "Contributions to the Theory of Single-Sample Uncertainty," ASME Journal of Fluids Engineering, **104**, pp. 250–260.

Moran, M. J. and Shapiro, H. N. (1996), *Fundamentals of Engineering Thermodynamics*, 3rd ed., John Wiley & Sons, Inc., New York.

Murawski, C. G. and Vafai, K. (1999), "Effect of Variable Axial Chord on a Low-Pressure Turbine Blade," Journal of Propulsion and Power, **15**, pp. 667–674.

Murawski, C. G. and Vafai, K. (2000), "An Experimental Investigation of the Effect of Freestream Turbulence on the Wake of a Separated Low Pressure Turbine Blade at Low Reynolds Numbers," Journal of Fluids Engineering, **122**, pp. 431–433.

Muti Lin, J. C. and Pauley, L. L. (1996), "Low-Reynolds-Number Separation on an Airfoil," AIAA Journal, **34**, pp. 1570–1577.

Pack, L. G. and Roslin, R. D. (1998), "Overview of Active Flow Control at NASA Langley Research Center," Proceedings of SPIE - The International Society for Optical Engineering, **3326**, pp. 202–213.

Qui, S. and Simon, T. W. (1997), "An Experimental Investigation of Transition as Applied to Low Pressure Turbine Suction Surface Flows," ASME paper No. 97-GT-455.

Ramaprian, B. R. (1975), "Turbulence Measurements in an Equilibrium Axisymmetric Wall Jet," Journal of Fluid Mechanics, **71**, pp. 317–338.

Roach, P. E. (1987), "The Generation of Nearly Isotropic Turbulence by Means of Grids," International Journal of Heat and Fluid Flow, **8**, pp. 82–92.

Roberts, S. K. and Yaras, M. I. (2003), "Measurements and Prediction of Free-Stream Turbulence and Pressure-Gradient History on Attached-Flow Boundary-Layer Transition," ASME paper No. GT-2003-38261, Atlanta, GA.

Rodger, P., Sjolander, S. A. and Moustapha, S. (1992), "Establishing Two-Dimensional Flow in a Large-Scale Planar Turbine Cascade," AIAA paper No. AIAA-92-3066, Nashville, TN.

Rodger, P. W. (1992), "Establishing Two-Dimensional Flow in a Large Scale Planar Turbine Cascade," Master's thesis, Carleton University, Ottawa, Canada.

Schlichting, H. and Gersten, K. (2000), *Boundary-Layer Theory*, 8th ed., Springer-Verlag, Berlin.

Shyne, R. J., Sohn, K.-H. and DeWitt, K. J. (2000), "Experimental Investigation of Boundary Layer Behavior in a Simulated Low Pressure Turbine," Journal of Fluids Engineering, **122**, pp. 84–89.

Solomon, W. J. (2000), "Effects of Turbulence and Solidity on the Boundary Layer Development in a Low Pressure Turbine," ASME paper No. 2000-GT-0273, Munich, Germany.

Solomon, W. J., Walker, G. J. and Gostelow, J. P. (1996), "Transition Length Prediction for Flows With Rapidly Changing Pressure Gradients," Journal of Turbomachinery, **118**, pp. 744–751.

Sturm, W., Scheugenpflug, H. and Fottner, L. (1992), "Performance Improvements of Compressor Cascades by Controlling the Profile and Sidewall Boundary Layers," Journal of Turbomachinery, **114**, pp. 477–486.

Tani, I. (1964), "Low Speed Flows Involving Bubble Separation," Progress in Aeronautical Sciences, **5**, pp. 70–104.

Volino, R. J. (2002), "Separated Flow Transition Under Simulated Low-Pressure Turbine Airfoil Conditions: Part 1 - Mean Flow and Turbulence Statistics," ASME Journal of Turbomachinery, **124**, pp. 645–655.

Volino, R. J. (2003a), "Passive Flow Control on Low-Pressure Turbine Airfoils," ASME paper No. GT2003-38728, Atlanta, Georgia.

Volino, R. J. (2003b), "Separation Control on Low-Pressure Turbine Airfoils Using Synthetic Vortex Generator Jets," ASME paper No. GT2003-38729, Atlanta, Georgia.

Volino, R. J. and Hultgren, L. S. (2001), "Measurements in Separated and Transitional Boundary Layers Under Low-Pressure Turbine Airfoil Conditions," ASME Journal of Turbomachinery, **123**, pp. 189–197.

Walker, G. J. (1993), "The Role of Laminar-Turbulent Transition in Gas Turbine Engines: A Discussion," ASME Journal of Turbomachinery, **115**, pp. 207–217.

Walker, G. J. and Gostelow, J. P. (1990), "Effects of Adverse Pressure Gradient on the Nature and Length of Boundary Layer Transition," Journal of Turbomachinery, **112**, pp. 196–205.

Ward, J. W. (1963), "Behaviour and Effects of Laminar Separation Bubbles on Aerofoils in Incompressible Flow," Journal of the Royal Aeronautical Society, **67**, pp. 783–790.

White, F. M. (1991), *Viscous Fluid Flow*, 2nd ed., McGraw Hill, Inc., New York.

White, F. M. (1994), *Fluid Mechanics*, 3rd ed., McGraw Hill, Inc., New York.

Yaras, M. I. (2001), "Measurements of the Effects of Pressure-Gradient History on Separation-Bubble Transition," ASME paper No. 2001-GT-0193, New Orleans, Louisiana.

Yaras, M. I. (2002), "Measurements of the Effects of Freestream Turbulence on Separation-Bubble Transition," ASME paper No. GT-2002-30232, Amsterdam, The Netherlands.

Yavuzkurt, S. (1984), "A Guide to Uncertainty Analysis of Hot-Wire Data," Journal of Fluids Engineering, **106**, pp. 181–186.

Zhang, X. F. (2002), "Hot-Film Measurements of the Steady and Unsteady Boundary Layer Development on a Low-Pressure Turbine Airfoil," Master's thesis, Carleton University, Ottawa, Canada.

Zhou, M. D. and Wygnanski, I. (1993), "Parameters Governing the Turbulent Wall Jet in an External Stream," AIAA Journal, **31**, pp. 848–853.

Zweifel, O. (1945), "The Spacing of Turbo-Machine Blading Especially with Large Angular Deflection," The Brown Boveri Review, pp. 436–444.

Appendix A

Calibration of Pressure Transducers

The pressure transducers used in the current experiments convert a measured differential pressure to an analog electrical voltage. This appendix presents the calibrations of the pressure transducers used. Table A.1 lists the pressure transducers, their respective manufacturers and pressure ranges, and the number of transducers of each type.

The pressure standard used to calibrate the differential pressure transducers is a water micromanometer, as described by Benner (2003). Uncertainty in the measured differential height is $\pm 0.05mm$ of water ($\pm 0.5Pa$ at 20°). The Data Instrument transducers

Table A.1: **Differential Pressure Transducers**

Transducer	Manufacturer	Pressure Range	Quantity
DRAL501DN	Data Instruments	$\pm 250Pa$	4
DRAL505DN	Data Instruments	$\pm 1250Pa$	4
113LU20D-PCB	SensorTechnics	$\pm 5000Pa$	2

(DRAL501DN and DRAL505DN) have been calibrated on numerous occasions over a period of three years by the current author and Mahallati (2003). Based on these calibrations, the estimated uncertainties due to combined linearity, hysteresis and long-term stability, are $\pm 0.5Pa$ for the DRAL501DN's and $\pm 2Pa$ for the DRAL505DN's, with 95% confidence. The current author is the first to calibrate and use the SensorTechnics transducers. The estimated uncertainty for these transducers, based on two calibrations, is $\pm 5Pa$. A linear-fit regression analysis has been used to determine the calibration coefficients for all the above mentioned transducers. The linear regression takes the form

$$\Delta P = c_1 E + c_2.$$

where ΔP is the differential pressure, E is the transducer output voltage, and c_1 and c_2 are the linear calibration coefficients. The zero-offset voltage (voltage at zero pressure difference) has been found to drift from day-to-day, for all the transducers used. The c_2 coefficient was adjusted during the experiments for this zero-offset drift, since $c_2 = -c_1 E_{offset}$. Table A.2 lists the calibration coefficients for two separate calibrations performed during the course of the current experiments. The calibration data for the second calibration are shown in Figures A.1, A.2, and A.3 for the DRAL501DN's, the DRAL505DN's, and the 113LU20D-PCB's, respectively. The Data Instruments transducers have been calibrated over their specified range (see Table A.1), whereas the SensorTechnics transducers have been calibrated over the required range for the experiments ($\pm 2000Pa$).

Table A.2: **Pressure Transducer Calibration Coefficients**

	Calibration 1		Calibration 2	
Transducer	c_1	c_2	c_1	c_2
DRAL501DN-1	99.23	-351.51	99.05	-349.56
DRAL501DN-2	96.48	-336.01	96.35	-334.32
DRAL501DN-3	96.62	-336.18	96.47	-333.54
DRAL501DN-4	96.36	-335.88	96.25	-333.95
DRAL505DN-1	491.21	-1705.4	493.47	-1707.2
DRAL505DN-2	488.87	-1709.5	490.22	-1718.9
DRAL505DN-3	489.53	-1711.5	491.47	-1709.7
DRAL505DN-4	488.43	-1705.9	490.48	-1712.6
113LU20D-PCB-1	1991.9	-6967.3	1993.9	-6951.5
113LU20D-PCB-2	1989.4	-6951.3	1989.8	-6935.5

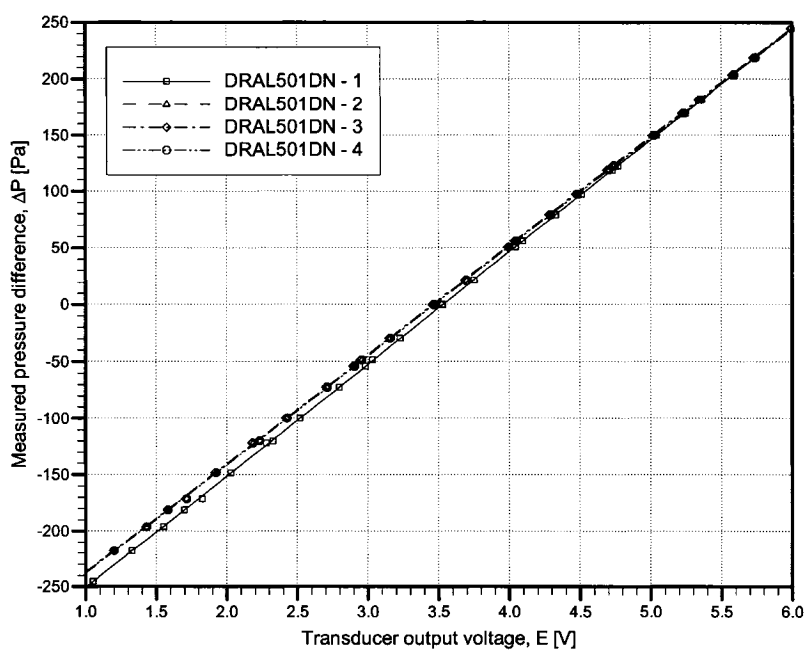

Figure A.1: **DRAL501DN Calibration Curves**

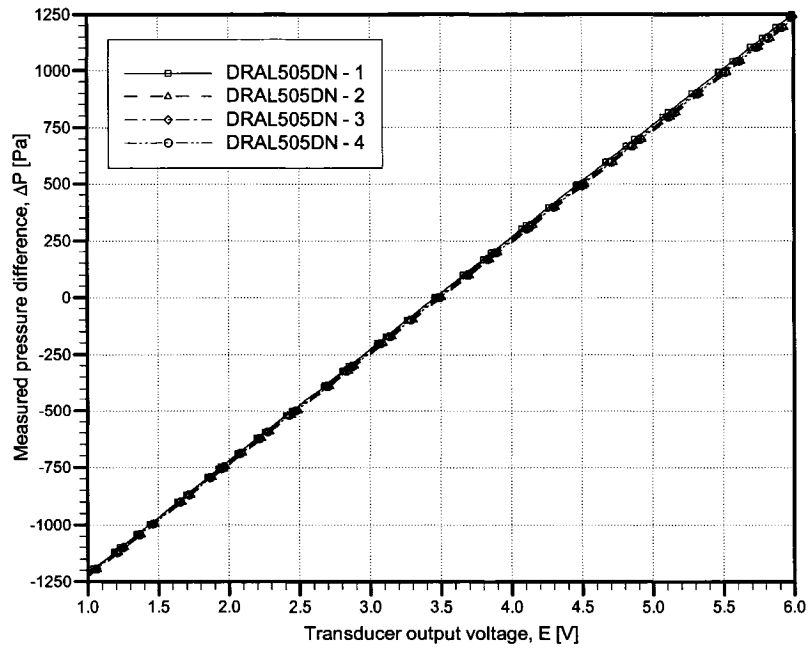

Figure A.2: **DRAL505DN Calibration Curves**

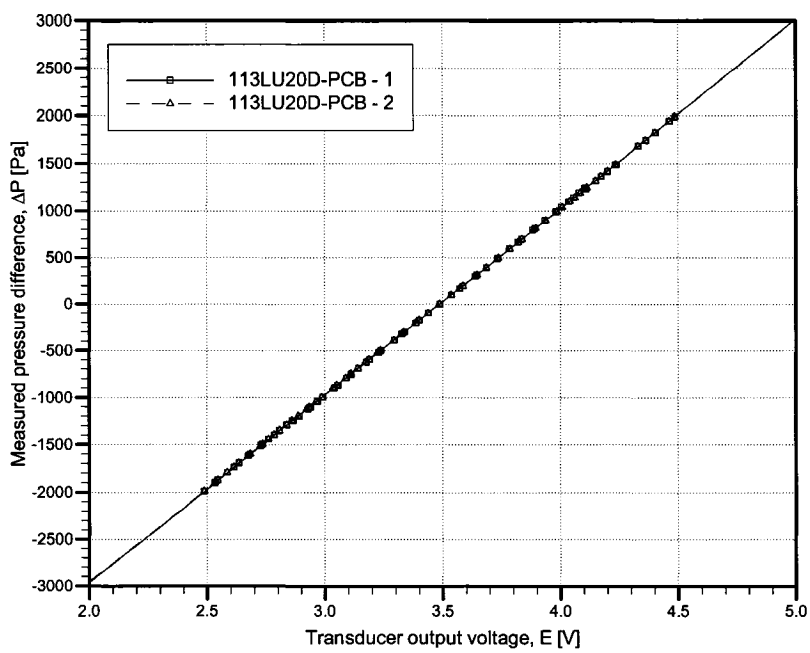

Figure A.3: **113LU20D-PCB Calibration Curves**

Appendix B

Calibration and Uncertainty Estimates of Three-Hole Pressure Probe

B.1 Calibrations

This appendix presents the calibration procedure and results for the three-hole pressure probe used in the current study. The calibrations have been performed in the calibration apparatus described in Section 3.3 and the form used for the calibration coefficients is that due to Lewis (1966). The probe geometry and port numbering are shown in Figure B.1.

The three-hole pressure probe has been calibrated in pitch over a range of $-10°$ to $+15°$ in increments of $0.5°$. Asymmetry in the range of pitch angles is due to the higher positive angles expected when the cascade stalls. The probe is aligned with the nozzle flow before

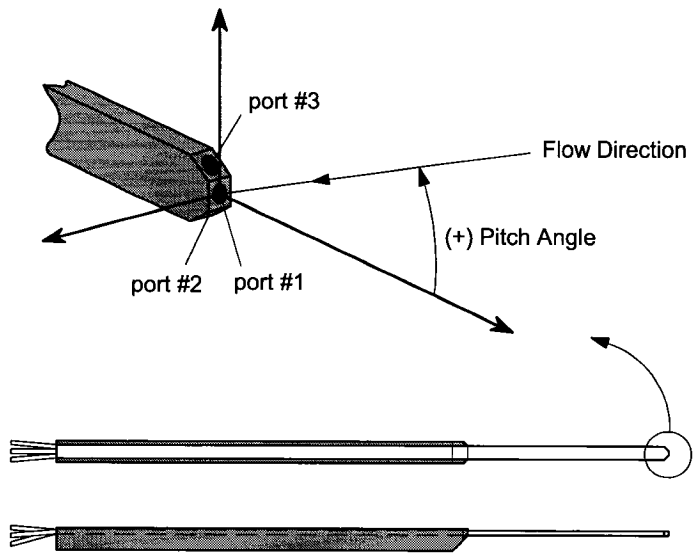

Figure B.1: **Geometry and Port Numbering of Three-Hole Pressure Probe**

each calibration. At each flow angle, the measured port pressure coefficients

$$C_{Pp} = \frac{P_p - P_S}{P_0 - P_S} \qquad (p = 1, 2, 3)$$

have been used to form 6 calibration coefficients, defined as:

$$\begin{aligned}
K_1 &= \frac{P_1 - P_S}{P_0 - P_S} = C_{P1} \\
K_{12} &= \frac{P_1 - P_2}{P_0 - P_S} = C_{P1} - C_{P2} \\
K_{13} &= \frac{P_1 - P_3}{P_0 - P_S} = C_{P1} - C_{P3} \\
K_{23} &= \frac{P_2 - P_3}{P_0 - P_S} = C_{P2} - C_{P3} \\
K_{\phi 2} &= \frac{P_1 - P_2}{P_1 - P_3} = \frac{K_{12}}{K_{13}} \\
K_{\phi 3} &= \frac{P_1 - P_3}{P_1 - P_2} = \frac{K_{13}}{K_{12}}
\end{aligned}$$

Calibrations have been performed at 7 different probe Reynolds numbers, Re_p, where

$$Re_p = \frac{Uw}{\nu}.$$

The probe width, w, is 2.0 mm. The Reynolds numbers at which the probe has been calibrated, and the corresponding cascade Reynolds number and measurement planes for which the calibration data is used, are given in Table B.1. The calibration coefficients for the three-hole probe are shown in Figures B.2 through B.5. A distinct Reynolds dependence is observed, particularly for K_{12} and K_{13} (Figure B.4). At low-Reynolds number, there is also significant scatter in the calibration data. This results from small pressure differences measured by the differential pressure transducers. Estimates of the uncertainty involved in the three-hole pressure probe measurements are discussed in the next section.

Table B.1: **Reynolds Numbers of Three-Hole Probe Calibrations**

Probe Reynolds Number	Cascade Reynolds Number	Measurement Plane
660	25000	inlet
1050	25000	outlet
1310	50000	inlet
2100	50000	outlet
2620	100000	inlet
4070	100000/150000	outlet/inlet
5460	150000	outlet

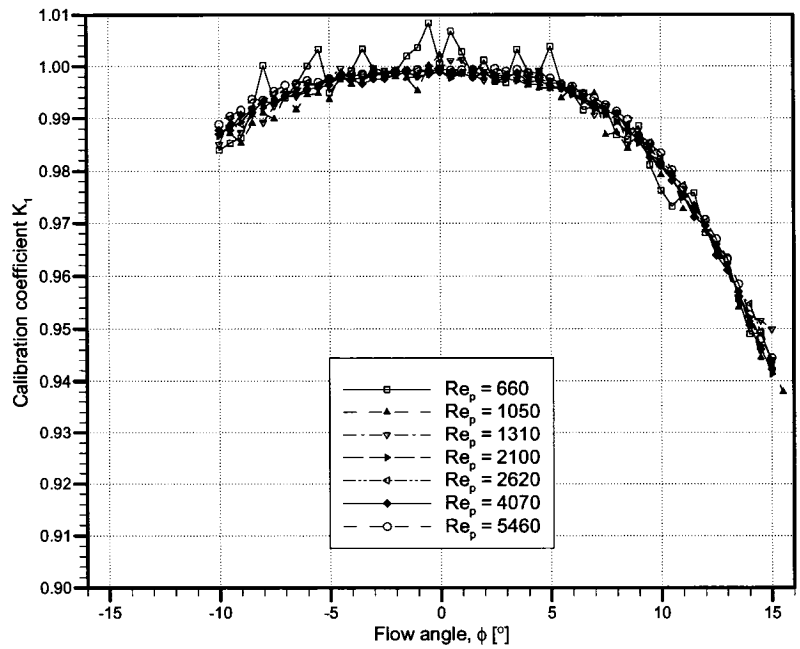

Figure B.2: **Variation of K_1 with Pitch Angle**

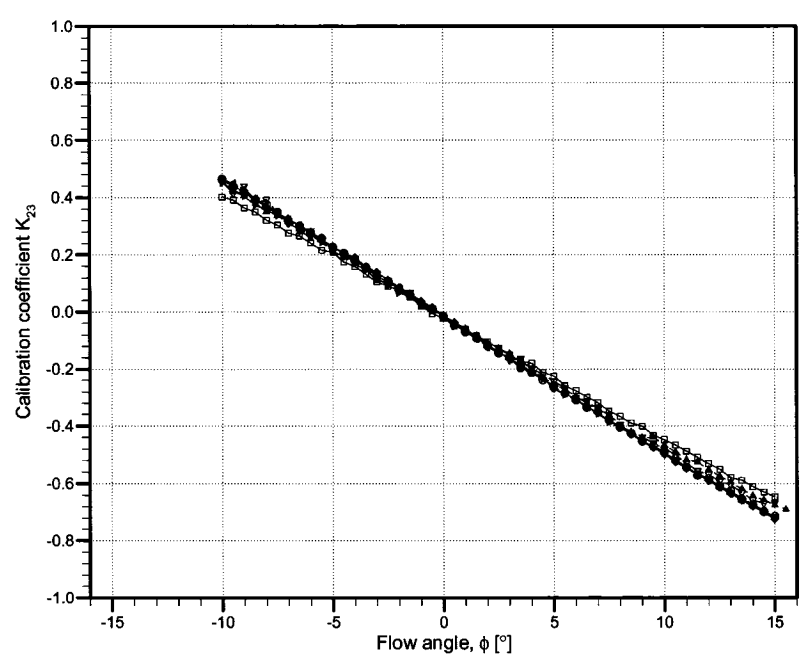

Figure B.3: **Variation of K_{23} with Pitch Angle**

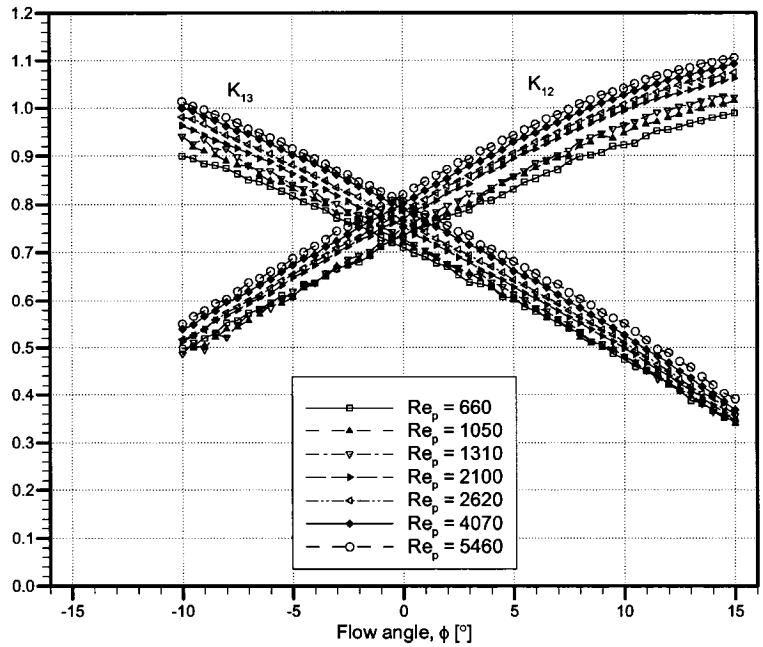

Figure B.4: **Variation of K_{12} and K_{13} with Pitch Angle**

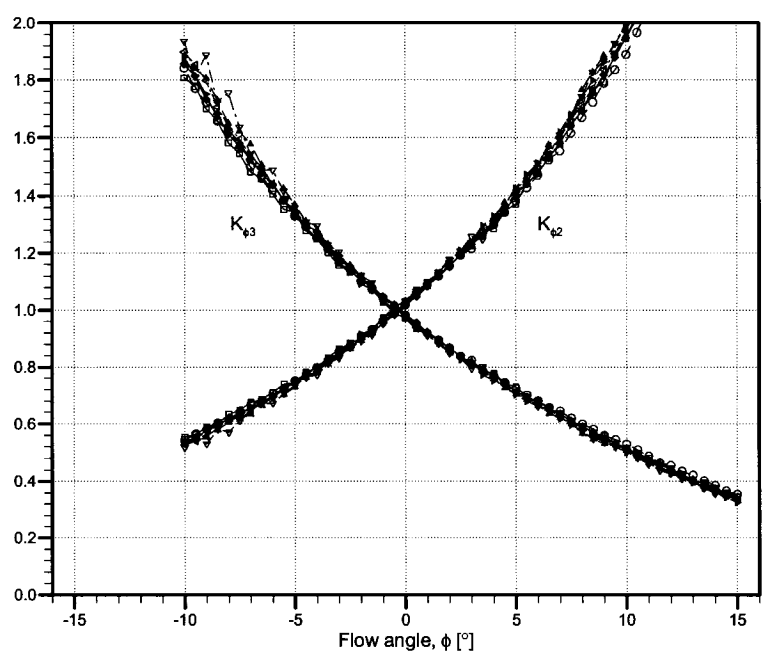

Figure B.5: **Variation of $K_{\phi 2}$ and $K_{\phi 3}$ with Pitch Angle**

B.2 Uncertainty Estimates

The uncertainty associated with three-hole pressure probe measurements can be significant at low-Reynolds number. To examine these uncertainties, a study was performed in the calibration apparatus described in Section 3.3, which provides a known flow.

For each probe Reynolds number examined, fifteen sets of measurements were performed and used to estimate the uncertainties in measured flow angle, ϕ, dynamic pressure coefficient, C_Q, velocity ratio, C_V, static pressure coefficient, C_{PS}, and total pressure loss coefficient, C_{P0} (all defined in Section 3.7.1). For each Reynolds number, a single calibration was used to reduce the data from the fifteen measurement sets. Three of the measurement sets were performed in the same manner as a calibration run, incrementing the pitch angle in increments of 0.5° from +15° down to −10°. The other twelve sets consisted of random traverse profiles from which hysteresis effects can be examined, half of which were performed with a specified pitch misalignment. A pitch misalignment of ±0.2° was used, based on the observed probe misalignment in the wind tunnel. The resulting uncertainties, with 95% confidence (twice the standard deviation), are shown in Figure B.6 and include uncertainty due to calibration error, transducer zero-offset error, alignment error, hysteresis, and repeatability. For probe Reynolds numbers between 660 and 2620, the DRAL501DN transducers have been used, and for probe Reynolds numbers between 2620 and 5460, the DRAL505DN transducers have been used.

The two uncertainties not accounted for are those due to shear flow and turbulence intensity. Within the wakes downstream of the cascade, the three-hole probe encounters a shear flow in which the dynamic pressure varies across the probe face. This results in a misinterpretation of flow angle, which has not been included in the uncertainty estimates. Also, the difference in turbulence intensity between the calibration apparatus and the wind tunnel has not been accounted for in the uncertainties of Figure B.6.

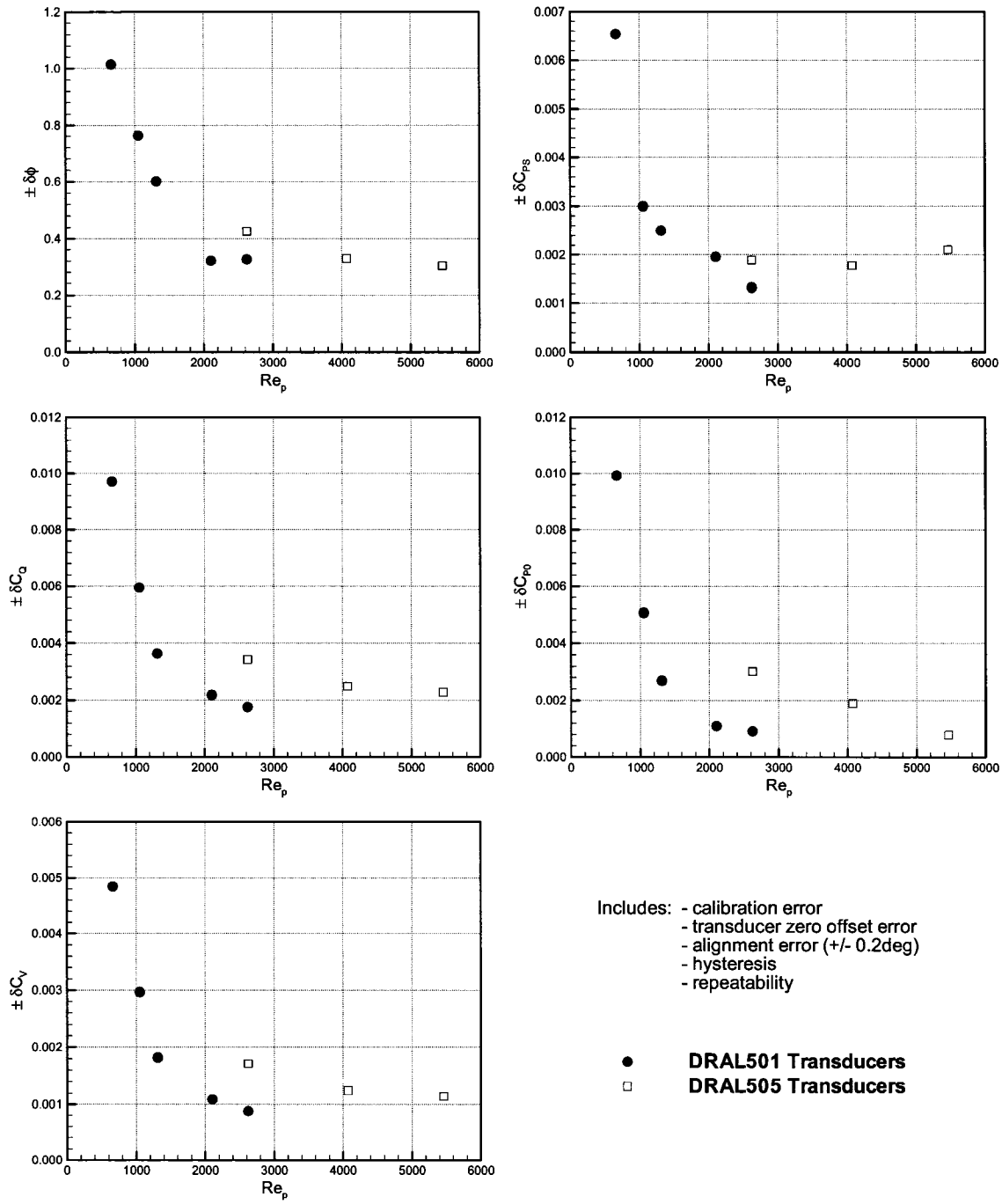

Figure B.6: **Uncertainty Estimates for Reduced Three-Hole Pressure Probe Data**

Appendix C

Calibration and Uncertainty Estimates of Hot-Wire Probes

C.1 Calibrations

This appendix presents the calibration procedures used and results obtained for the single-normal hot-wire probes used in the present study. Dantec type 55P01 plated hot-wire probes were used. Calibrations were performed on a semi-weekly basis during the course of the experiments.

The calibration procedure consisted of placing the hot-wire in a known flow, which for the current experiments was the calibration rig nozzle flow (described in Section 3.3). The probe was aligned with the nozzle flow to within 2°. For this level of misalignment, errors in the measured velocity should be insignificant (Bruun, 1995). Prior to the probe calibration, the anemometer channel was adjusted to give the desired overheat ratio, gain, offset, and frequency response. The velocity range for which the hot-wires were calibrated is 0 to 42

m/s. For each calibration velocity, 131072 samples were taken at a sampling rate of 30kHz, which results in approximately 4.4 seconds of data. A 14kHz low-pass filter was used for all measurements and calibrations.

The measured top-of-the-bridge anemometer voltage, E_{TOB}, is related to the flow velocity, U, by the general form of King's Law (Bruun, 1995):

$$E_{TOB}^2 = a + bU^n \tag{C.1}$$

where a, b, and n are the calibration coefficients. These calibration coefficients were determined based on a regression analysis. Calibration data with corresponding calibration curves are shown in Figure C.1 for two of the hot-wires used during the experiments (designated HW1 and HW2). Each of these calibrations is one of the many performed for each probe.

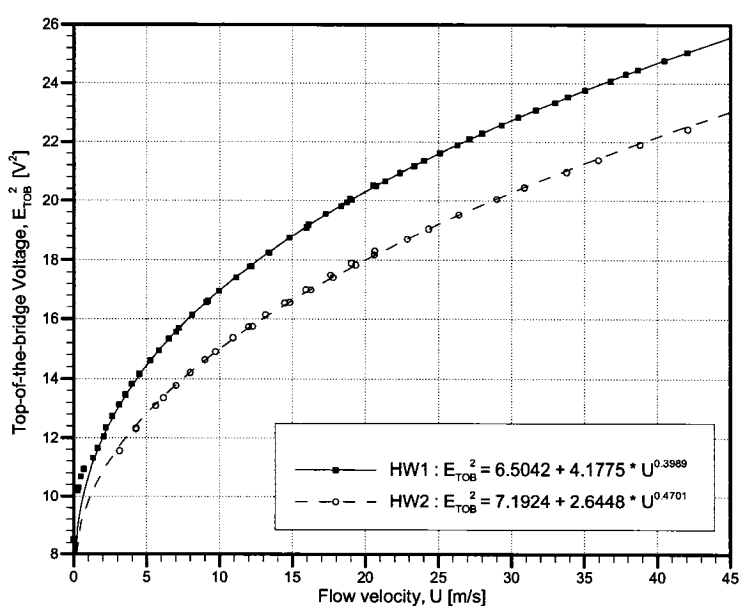

Figure C.1: **Representative Hot-Wire Calibration Curves**

C.2 Uncertainty Estimates

Uncertainties associated with the hot-wire measurements have been estimated based on the method of Yavuzkurt (1984).

Yavuzkurt (1984) describes two main uncertainties associated with hot-wire measurements. The first, δU_{cal}, is due to calibration error, and involves uncertainty in the known flow velocity, i.e. the calibration nozzle flow velocity. This uncertainty arises due to uncertainty in the nozzle contraction pressure measurement, uncertainty in the calculated air density, and uncertainty in the reference dynamic pressure coefficient at the measurement plane within the calibration rig. The second uncertainty, δU_{cf}, is due to curve-fitting uncertainties. This uncertainty is represented by the standard deviation of the the curve-fit regression analysis using King's Law (Equation C.1). The uncertainty of instantaneous hot-wire measurements is given by

$$\delta U_{HW} = \pm\sqrt{(\delta U_{cal})^2 + (\delta U_{cf})^2}.$$

Yavuzkurt (1984) shows that the calculated mean velocity, U, and the root-mean-square fluctuation level, u', will both have the same percentage error as the instantaneous velocity, and that the calculated turbulence intensity, u'/U, will have twice the percentage error of the instantaneous velocity.

For the current hot-wire measurements, uncertainties in the mean velocity, U, and the root-mean-square fluctuation level, u', are estimated to be below 5%, except at low velocity (<5m/s) where the uncertainties can be as high as 10%. The uncertainty in turbulence intensity, u'/U, is estimated to be below 10% of the calculated value, except at low velocity (<5m/s) where the uncertainty can be as high as 20% of the calculated value.

Appendix D

Flow Characteristics Downstream of Turbulence Generating Grid H2

Chapter 4 describes the design of a new turbulence generating grid for the wind tunnel (grid H3). The purpose of grid H3 was to generate a level of turbulence intensity (about 4%) similar to a grid previously used (grid H1), but with a smaller turbulent integral length scale at the cascade inlet. Mahallati (2003) had designed a grid for the same purpose, designated grid H2 in the current study, but significant non-uniformities in the cascade inlet flow were observed for grid H2. This appendix documents the flow downstream of grid H2.

Grid H2 has a tri-planar configuration, a schematic of which was shown in Figure 4.2 on page 70. The grid is comprised of two distinctly different meshes, one large mesh, square-bar grid overlayed on a small mesh woven-style grid. This grid is located at the same position in the wind tunnel as grid H3, much closer to the cascade than grid H1. Three-hole pressure probe measurements were made over one square blade pitch both upstream and downstream of the cascade middle blade at a Reynolds number of 50000 and upstream of the cascade at a Reynolds number of 25000. Two sets of measurements were made for

each of these three conditions. One set was made with the three hole probe in the standard orientation to measure the incidence/deviation angle, and the second set was made with the probe rotated 90° about its axis to measure flow angles in the spanwise direction. Since the observed spanwise flow angles were small ($< 5°$), the effects of yaw misalignment on the measurements was negligible. The two sets of flow angles, along with the measured velocity, were used to calculate and plot secondary flow vectors over top of a total pressure contour plot. These figures are discussed below. Secondary flow is referred to here as any flow in the spanwise direction.

Figure D.1 presents the secondary flow vectors and total pressure fields both upstream and downstream of the Pak-B cascade at a Reynolds number of 50000. For the total pressure coefficients, the reference static and total pressures are those measured at coordinates (0,0) of the inlet flow plane. The inlet measurements (left-hand plot) show strong total pressure non-uniformities entering the cascade. The jet-wake pattern emerging from the grid generates total pressure variations of 30% of the reference dynamic pressure over the observed region. The secondary flow vectors also show non-uniformities over the observed region. These inlet flow non-uniformities generate strong spanwise non-uniformities in the flow field downstream of the cascade (right-hand plot). A significant difference in the wake width is present over the observed region. Also, secondary flow patterns are present over the observed downstream region.

Figure D.2 presents the secondary flow vectors and total pressure field upstream of the Pak-B cascade at a Reynolds number of 25000. The total pressure field shows strong non-uniformities downstream of the grid, with a much stronger jet-wake pattern than at a Reynolds number of 50000.

After completing the measurements described above, it was decided to discontinue the use of grid H2 and commence the design of a new grid. The new grid (H3) also generates

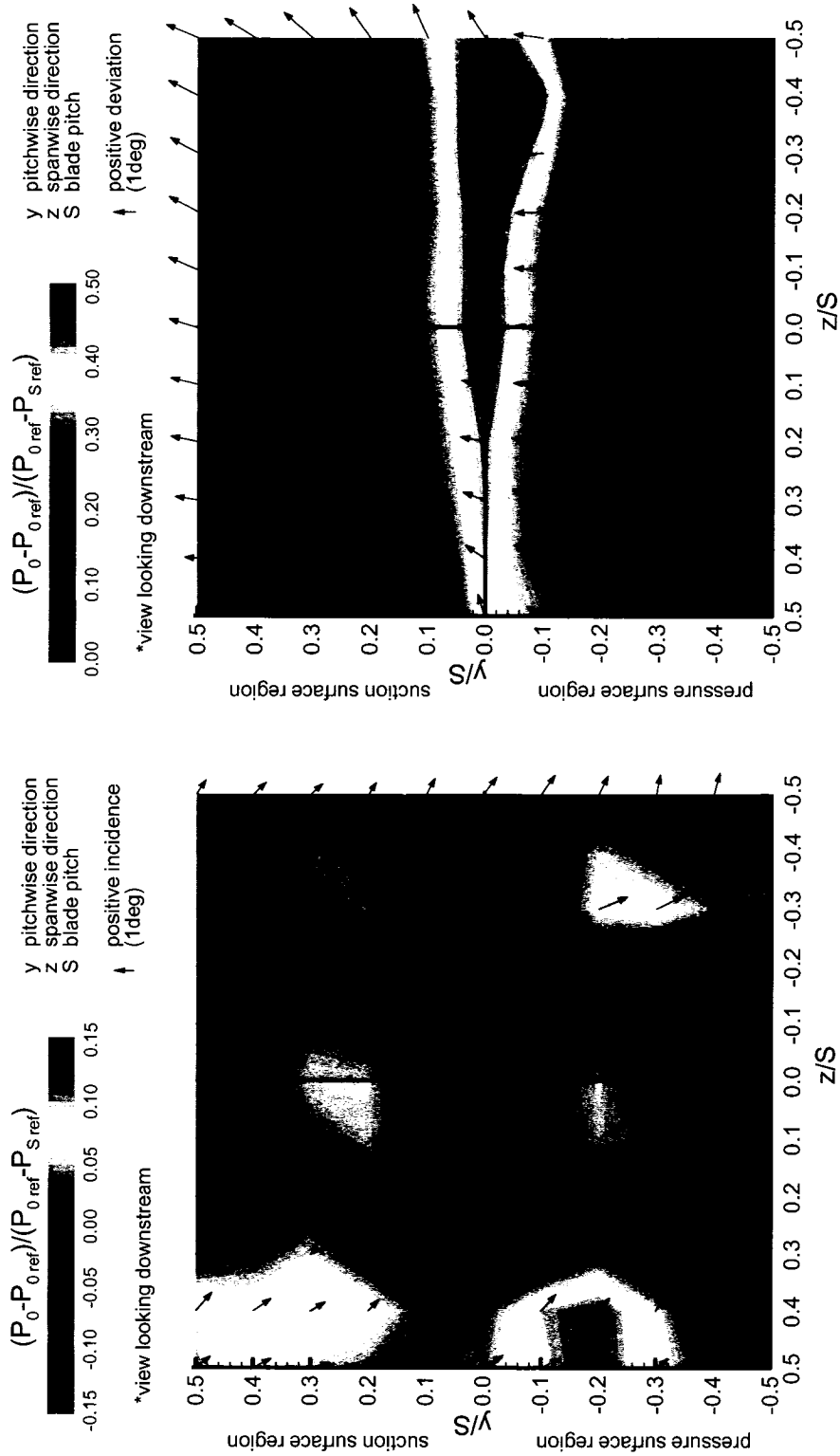

1.2 B_x Upstream of Cascade **0.5 B_x Downstream of Cascade**

Figure D.1: **Flow Field Upstream and Downstream of the Pak-B Cascade Using Grid H2 at Re=50000**

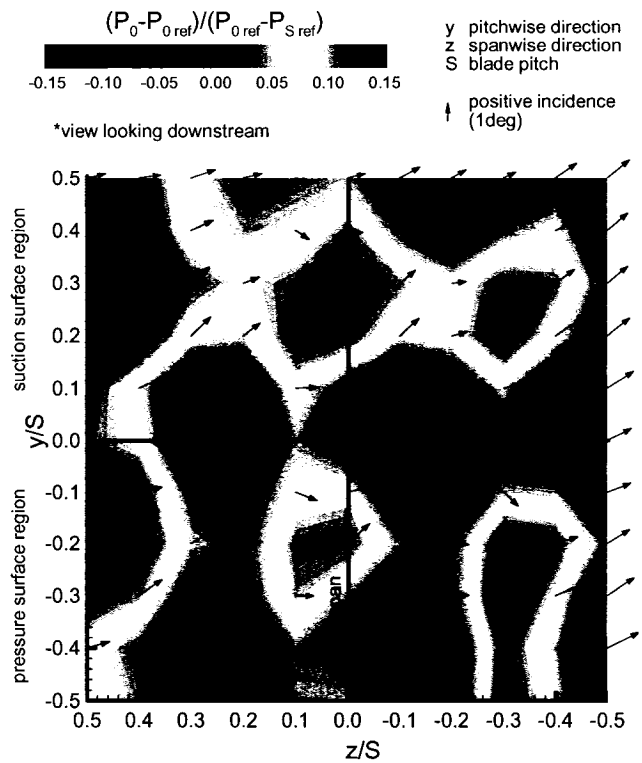

Figure D.2: **Flow Field Upstream of the Pak-B Cascade Using Grid H2 at** Re**=25000**

non-uniformities at the inlet of the cascade, due to the close proximity, but with a much lower magnitude. The small total pressure non-uniformities of grid H3 were also much more periodic than those of grid H2, enabling more accurate calculation of the upstream reference total pressure for the blade profile loss calculations.

Appendix E

Calibration of Flow Control Jet

During the flow control experiments, it was required to set the jet blowing rate to a specified value. This was accomplished by calibrating the wall jet before the experiments were performed. This appendix presents the wall jet calibrations for the middle flow control airfoil of the cascade.

The parameter of interest for characterizing the jet blowing rate is the blowing ratio, B, defined by

$$B = \frac{U_{j_{max}}}{U_e}$$

where $U_{j_{max}}$ is the maximum velocity in the wall jet profile at the injection slot outlet plane, and U_e is the local edge-of-the-boundary layer velocity. Hot-wire traverse measurements of the wall jet and local boundary layer have been used to obtain these two velocities, and calculate the blowing ratio. These measurements are discussed in Section 7.3. The jet blowing rate has been calibrated against the internal plenum pressure of the blade, P_b. The plenum pressure, which has been measured by a static pressure tap inside the blade plenum, is characterized by a blade plenum pressure coefficient. This blade plenum pressure

coefficient, C_{Pb}, is calculated from the plenum pressure, P_b, and the wind tunnel contraction pressures, P_{c1} and P_{c2}, and is given by

$$C_{Pb} = \frac{P_b - P_{c2}}{P_{c1} - P_{c2}}.$$

The wall jet calibration curves for the middle flow control airfoil are shown in Figures E.1 and E.2 for freestream turbulence intensities of 0.4% and 3.9%, respectively. Adjustment of the jet blowing ratio was accomplished by adjusting the air supply pressure regulator to achieve the required blade plenum pressure. Linear interpolation between the calibration data points was used to calculate the blade plenum pressure for a desired blowing ratio. The air supply manifold valves for the two adjacent flow control airfoils were adjusted to achieve similar blowing ratios for the three flow control airfoils, with the blowing ratio of the adjacent airfoils to within 10% of that for the middle airfoil.

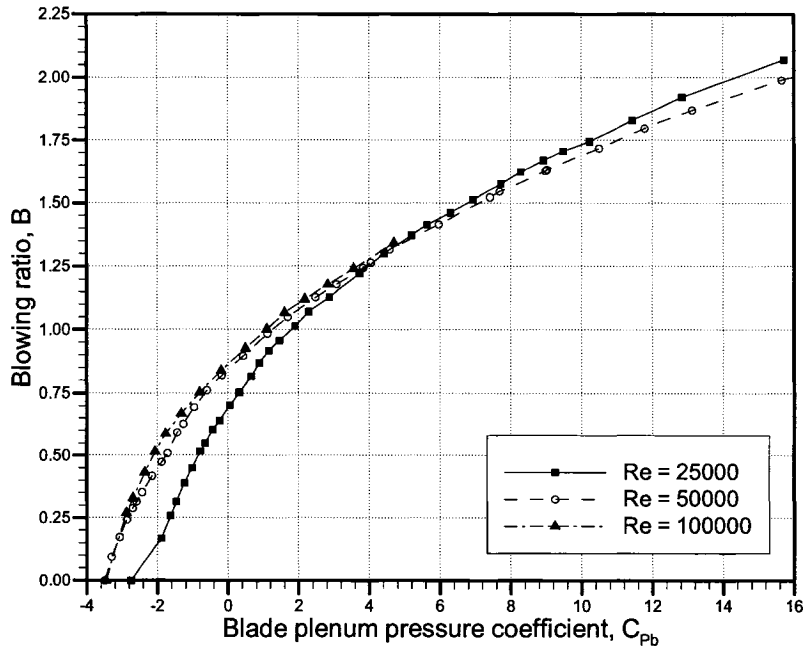

Figure E.1: **Flow Control Jet Calibrations for $FSTI$ = 0.4%**

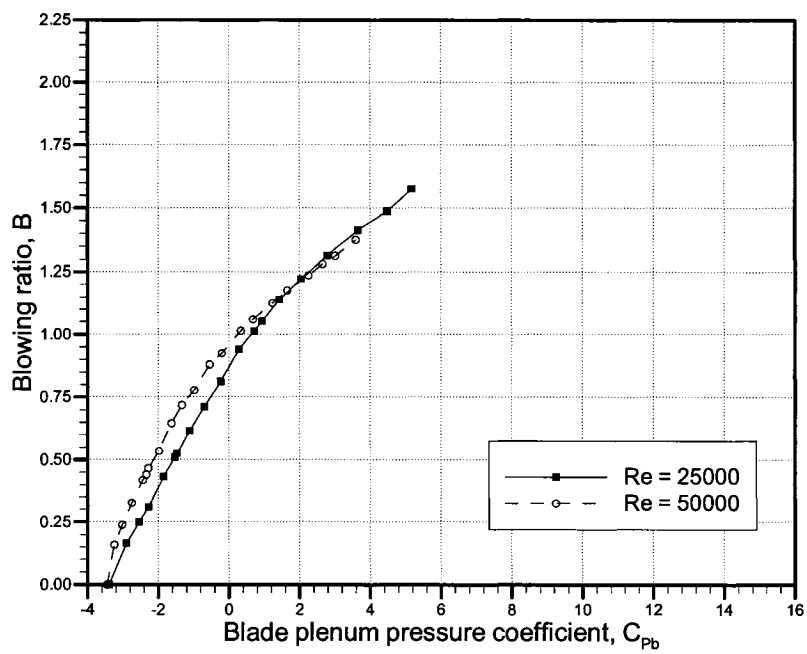

Figure E.2: **Flow Control Jet Calibrations for $FSTI$ = 3.9%**

Appendix F

Flow Control Velocity Field Contour Plots

This appendix presents the velocity field contour plots discussed in Chapter 7. Figures F.1 through F.7 show the mean and fluctuating velocity fields for the selected flow control cases. All hot-wire traverse cases were made at a Reynolds number of 50000, with blowing ratios of 0.0, 0.5, 1.0, and 2.0 examined at an FSTI of 0.4%, and blowing ratios of 0.0, 0.5, and 1.0 examined at an FSTI of 3.9%.

The hot-wire traverse planes are shown in Figure 7.39 of Chapter 7 (page 202). Each traverse plane consists of 98 measurements points, for which each consists of 16384 samples, sampled at 30kHz. The fluctuation level is represented by the root-mean-square (RMS) of the instantaneous velocity traces. Both mean and fluctuation quantities are normalized by the mixed-out outlet velocity. The uncertainties in mean velocity and RMS fluctuation levels are below 5% of the measured values, except when the mean velocity is below 5m/s, where the uncertainties can be as high as 10%. These uncertainties have been estimated based on the method of Yavuzkurt (1984), described in Appendix C.

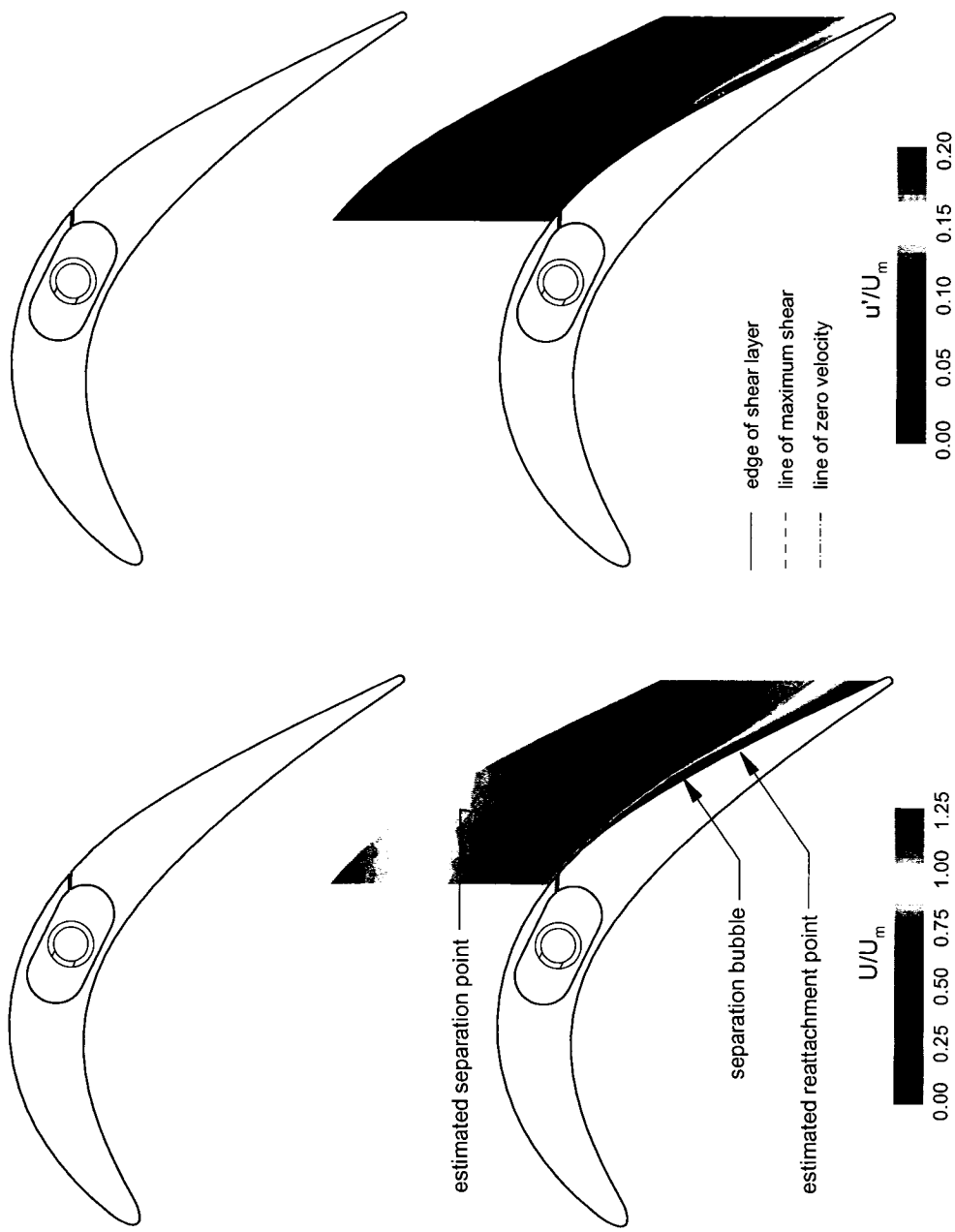

Figure F.1: **Velocity Field Measurements for $Re = 50000$, $FSTI = 0.4\%$, $B = 0.0$**

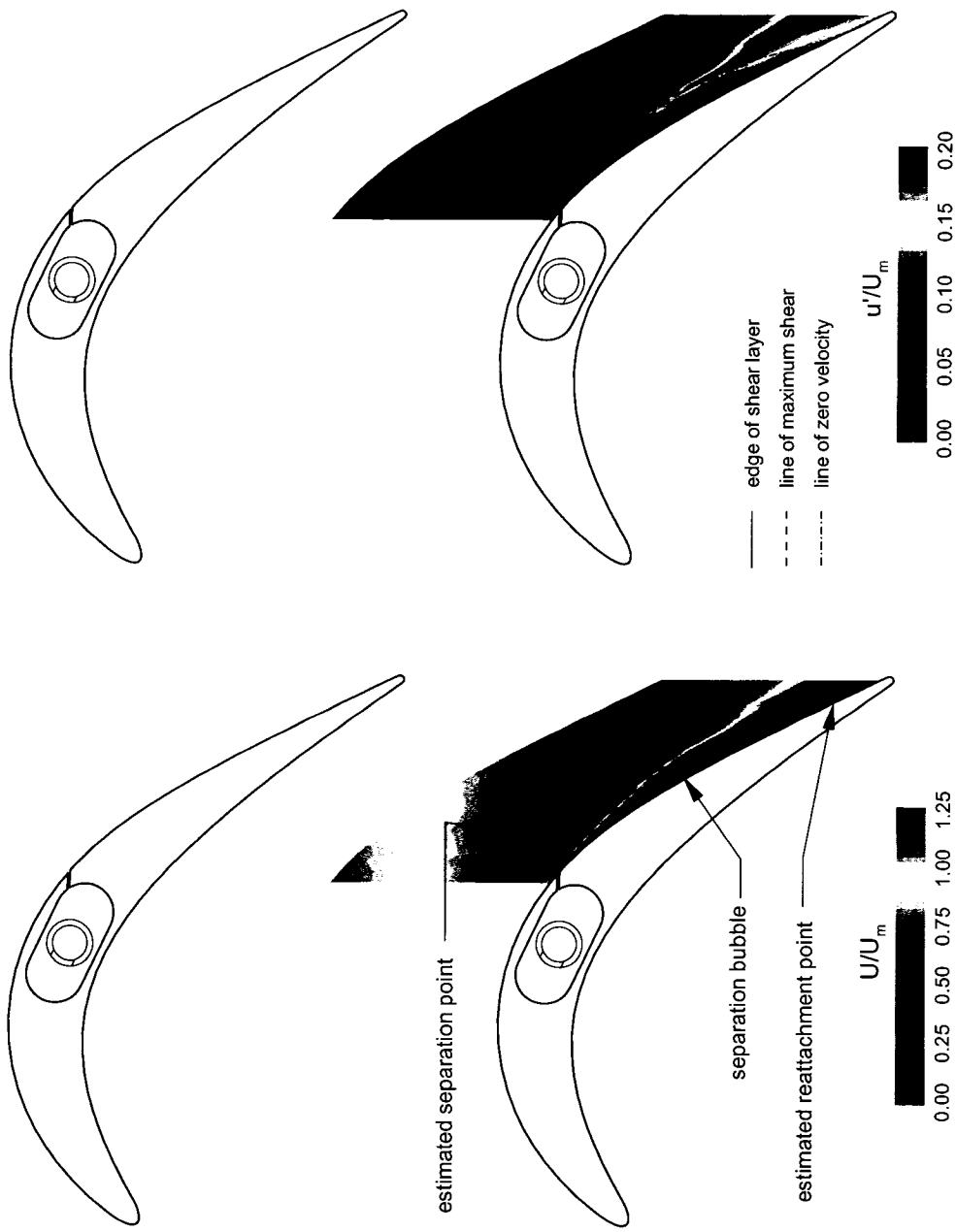

Figure F.2: **Velocity Field Measurements for $Re = 50000$, $FSTI = 0.4\%$, $B = 0.5$**

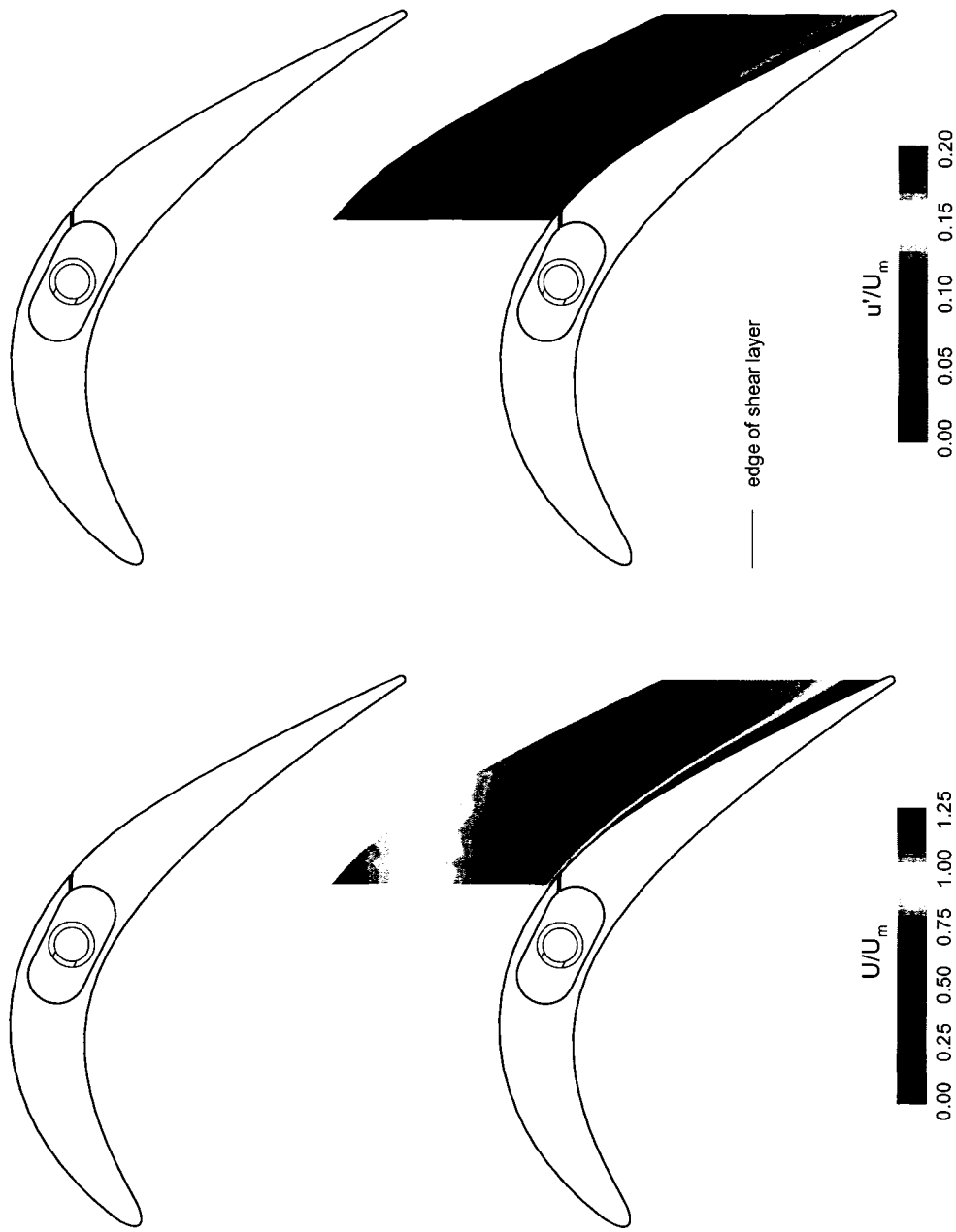

Figure F.3: **Velocity Field Measurements for $Re = 50000$, $FSTI = 0.4\%$, $B = 1.0$**

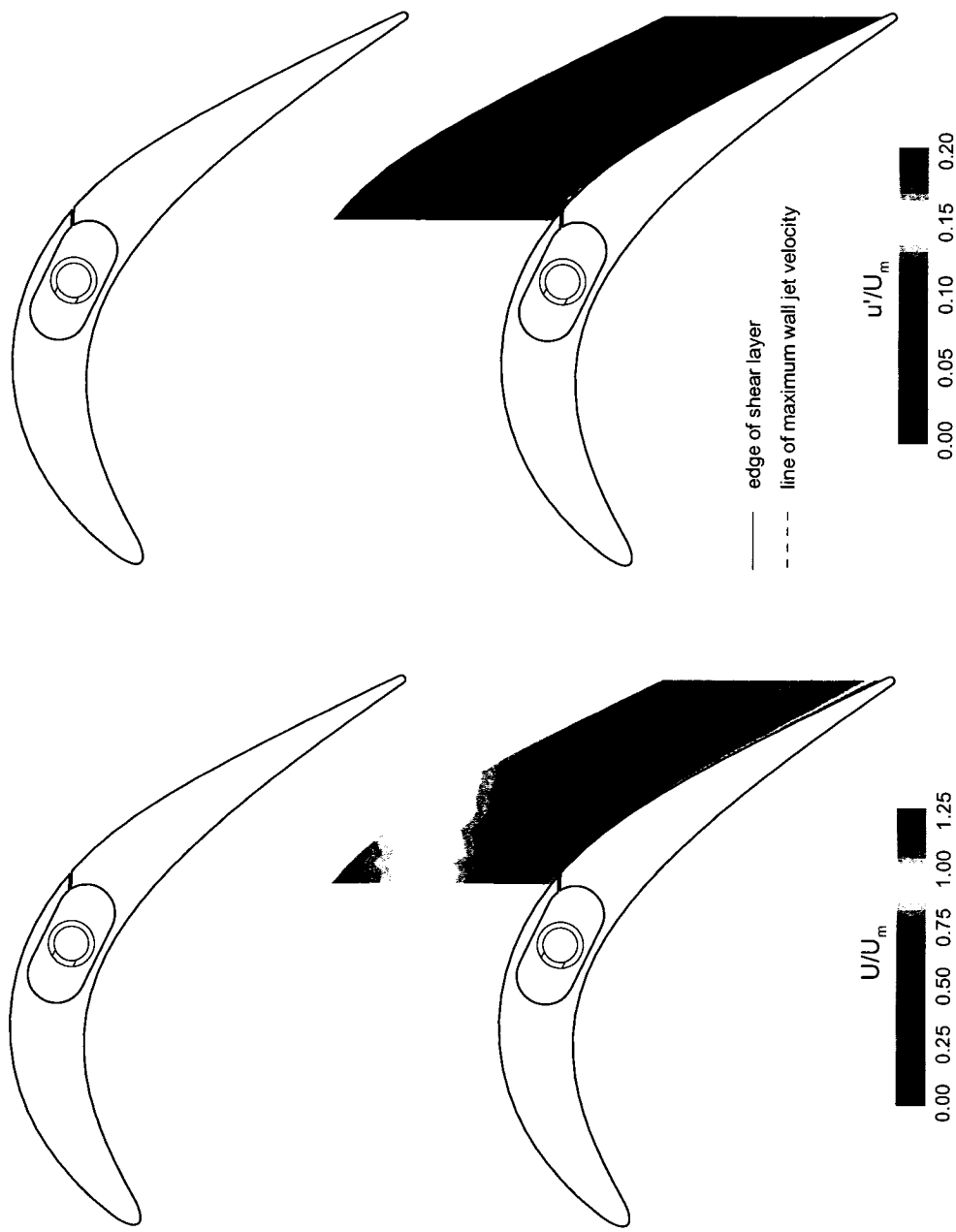

Figure F.4: **Velocity Field Measurements for $Re = 50000$, $FSTI = 0.4\%$, $B = 2.0$**

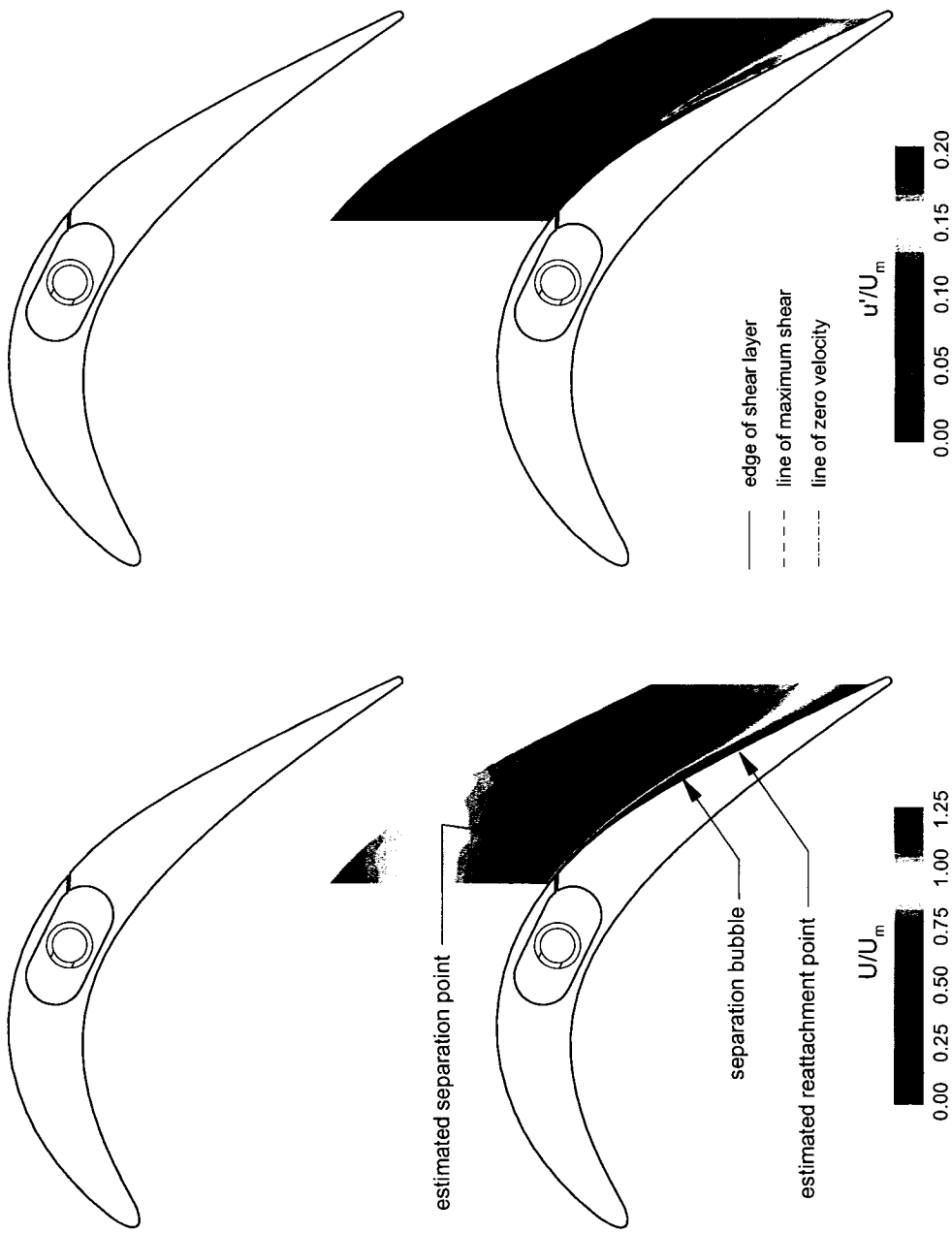

Figure F.5: **Velocity Field Measurements for $Re = 50000$, $FSTI = 3.9\%$, $B = 0.0$**

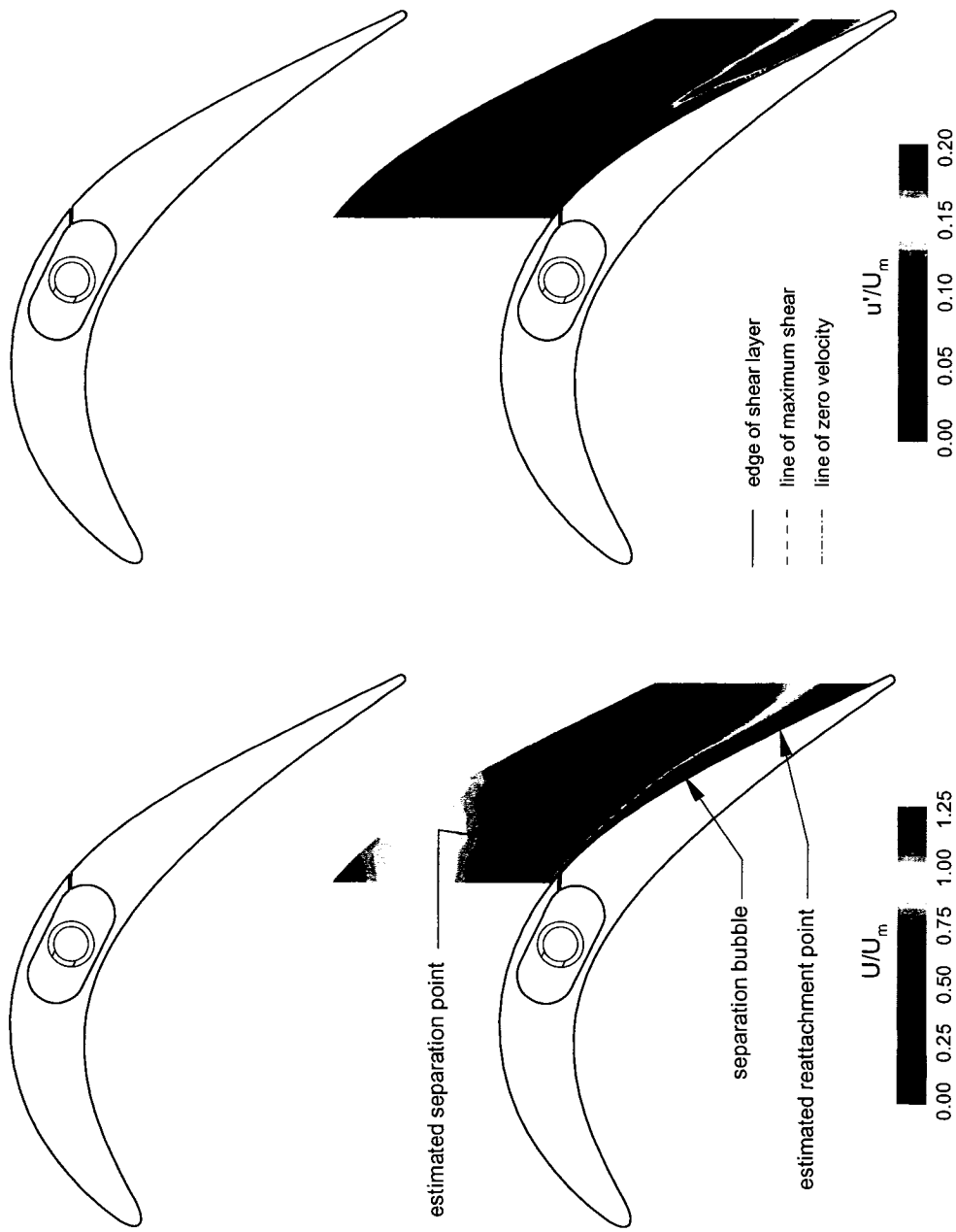

Figure F.6: **Velocity Field Measurements for $Re = 50000$, $FSTI = 3.9\%$, $B = 0.5$**

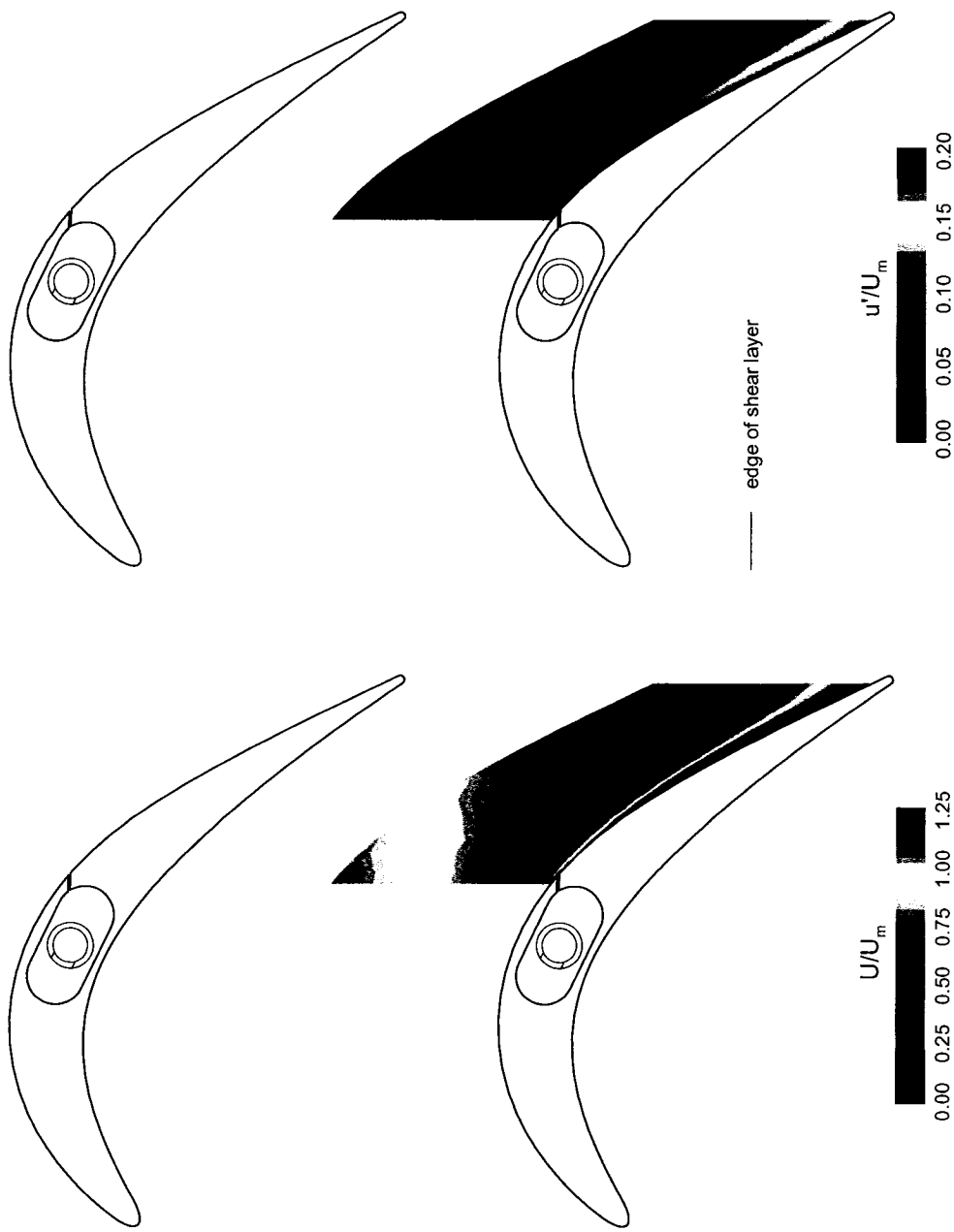

Figure F.7: **Velocity Field Measurements for $Re = 50000$, $FSTI = 3.9\%$, $B = 1.0$**